DEVELOPMENT AND BIODYNAMIC SIMULATION OF A DETAILED MUSCULO-SKELETAL SPINE MODEL

HUYNH KIM THO

(B.Eng)

A THESIS SUBMITTED

FOR THE DEGREE OF DOCTOR OF PHILOSOPHY

DEPARTMENT OF MECHANICAL ENGINEERING

NATIONAL UNIVERSITY OF SINGAPORE

2010

ACKNOWLEDGEMENTS

First of all, the author would like to express his deepest gratitude to Associate Professor Ian Gibson and Associate Professor Lu Wen Feng for their invaluable guidance, advice, patience, support and discussion throughout the last four years. It has been a rewarding research experience under their supervision.

The author would express his most sincere appreciation to Dr Gao Zhan for his invaluable help, sharing research experience and tricks of programming with MFC from the very first day the author comes to NUS.

The author would like to thank Dr Bhat Nikhil Jagdish for his useful discussions and advices during the last two years.

The author is very grateful to Lakshmanan Kannan Anand Natara for his assistance and maintenance of LifeMOD software.

The author would also like to thank Ms Wang JinLing, Ms Chevanthie H. A. Dissanayake, Ms Khatereh Hajizadeh, Ms Huang MengJie and all other fellow graduate students for their support and encouragement.

The author would also like to show his appreciation for the financial support in the form of a research scholarship from the National University of Singapore.

Finally, the author owes great thank to his parents for their love and support, and especially for his fiancée, Nguyen Huynh Diem Thanh, who is always by his side to constantly encourage him to overcome the most difficult time of the research. The author knows that no one will be happier than them to see this work completed.

TABLE OF CONTENTS

SUMMARY

The spine is one of the most important and indispensable structures in the human body. However, it is very vulnerable when suffering from external impact factors, resulting in spinal diseases and injuries such as whiplash injury, low back pain. In literature, spine models are extensively developed using either finite element or multi-body methods to find feasibly suitable solutions for treating these spinal diseases. However, these models are mainly used to investigate local biomechanical properties of a certain spinal region and do not fully take into account of muscles and ligaments. Hence, the aim of this thesis is to develop an entirely detailed musculo-skeletal muti-body spine model using LifeMOD Biomechanics Modeler and then simulate biodynamic behavior of the spine model in a haptically integrated graphic interface.

Initially, a default multi-body spine model is first generated by LifeMOD depending on the user's anthropometric input. Then, a completely discretized spine model is obtained by refining spine segments in cervical, thoracic and lumbar regions of the default one into individual vertebra segments, using rotational joints representing the intervertebral discs, building various ligamentous soft tissues between vertebrae, implementing necessary lumbar muscles and intra-abdominal pressure. To validate the model, two comparison studies are made with in-vivo intradiscal pressure measurements of the L4-L5 disc and with extension moments, axial and shear forces at L5-S1 obtained from experimental data and another spine model available in the literature. The simulation results indicated that the present model is in good correlation with both cases and matches well with the experimental data which

found that the axial forces are in the range of 3929 to 4688 N and shear forces up to 650 N.

To enhance more realistic interaction level between users (such as trainers, clinicians, surgeons) and the spine model during real-time simulation, a haptics technique is successfully integrated into a graphic environment named HOOPS in this research. Based on this new technique, the exploration process of the users for the spine model becomes much more realistic since the users can manipulate the haptic cursor to directly touch, grasp and feel geometric shape as well as rigidity of the spine through the force feedback of the haptic device. Moreover, they can even apply external forces in any arbitrary direction onto any certain vertebra to make the spine move. In such versatile simulation interface, the users can quickly and more conveniently study the locomotion and dynamic behaviour of the spine model.

Overall, this thesis has developed a bio-fidelity discretized multi-body spine model for investigating various medical applications. This spine model can be useful for incorporation into design tools for wheelchairs or other seating systems which may require attention to ergonomics as well as assessing biomechanical behavior between natural spines and spinal arthroplasty or spinal arthrodesis. Furthermore, the spine model can be simulated in the haptically integrated graphic interface to help orthepaedic surgeons understand the change in force distribution following spine fusion procedures, which can also assist in post-operative physiotherapy.

LIST OF TABLES

LIST OF FIGURES

LIST OF SYMBOLS

The important symbols used in this thesis are listed here. The other terms are described later when they appear in the thesis.

2D	Two Dimensional
3D	Three Dimensional
4D	Four Dimensional
C_i	The ith vertebra in cervical spine region
T_i	The ith vertebra in thoracic spine region
L_i	The ith vertebra in lumbar spine region
Si	The ith vertebra in sacrum region
DOF	Degree of Freedom
FFD	Free Form Deformation
FEM	Finite Element Model
MBM	Multi-Body Model
ADAMS	Auto Dynamic Analysis of Mechanical Systems
CAD	Computer Aided Design
CAE	Computer Aided Engineering
CAM	Computer Aided Manufacturing
NURBS	Non Uniform Rational B-Splines
IAP	Intra Abdominal Pressure
AABB	Axis Aligned Bounding Box
MSS	Mass Spring System
IVD	Intervertebral Disc

CHAPTER 1

INTRODUCTION

1.1. Overview of Clinical Spinal Problems

The human spine is one of the important and indispensable structures in the human body. It undertakes many functions, most importantly in providing strength and support for the remainder of the human body with particular attention to the heavy bones of the skull as well as in permitting the body to move in ways such as bending, stretching, rotating and leaning. Other functions include the protection of nerves, a base for rib growth and offering a means of connecting the upper and lower body via the sacrum which connects the spine to the pelvis. However, the human spine is also a very vulnerable part of our skeleton that is open to many spinal diseases and injuries such as whiplash injury, low back pain, scoliosis etc. Whiplash injury to the human neck is a frequent consequence of rear-end automobile accidents and has been a significant public health problem for many years. Soft-tissue injuries to the cervical spine are basically defined as injuries in which bone fracture does not occur or is not readily apparent. A whiplash injury is therefore an injury to one or more of the many ligaments, intervertebral discs, facet joints or muscles of the neck. Low back pain is the most common disease compared to others and strongly associated with degeneration of intervertebral discs (Luoma et al., 2000). The low back pain is usually seen in people with sedentary jobs who spend hours sitting in a chair in a relatively fixed position, with their lower back forced away from its natural lordotic curvature. This prolonged sitting causes health risks of the lumbar spine, especially for the three lower vertebrae

L3-L5. 80% of people in the United States will have lower back pain at some point in their life (Vallfors, 1985). As compared to lower back pain, scoliosis is a less common but more complicated spinal disorder. Scoliosis is a congenital three-dimensional deformity of the spine and trunk affecting between 1.5% and 3% of the population. In severe cases, surgical correction is required to straighten and stabilize the scoliosis curvature. Hence, studies into the treatment of these spinal diseases have played an important role in modern medicine. Many biomechanical models have been proposed to study dynamic behavior as well as biomechanics of the human spine, to develop new implants and new surgical strategies for treating these spinal diseases.

1.2. Biomechanical Models of Human Spine

Models in biomechanics can be divided into four categories: physical models, *in-vitro* models, *in-vivo* models and computer models. However, computer models have been extensively used due to its advantages over other ones in that these models can provide information that cannot be easily obtained by other models, such as internal stresses or strains. They can also be used repeatedly for multiple experiments with uniform consistency, which lowers the experimental cost, and to simulate different situations easily and quickly. In computer models, multi-body models and finite element models, or a combination of the two are the most popular simulation tools that can contribute significantly to our insight of the biomechanics of the spine.

Although a great deal of computational power is required, finite element models (FEMs) are helpful in understanding the underlying mechanisms of injury and dysfunction, leading to improved prevention, diagnosis and treatment of clinical spinal problems. These models often provide estimates of parameters that *in-vivo* or *in-vitro* experimental studies either cannot or are difficult to obtain accurately. Basically, FEMs are divided into two categories: the models for dynamic study and static study, respectively. The models developed for static study generally are more detailed in representing the spinal geometries. Although this type of model can predict internal stresses, strains and other biomechanical properties under complex loading conditions, they generally only consist of one or two motion segments and do not provide more insight for the whole column. The models for dynamic study generally include a series of vertebrae (as rigid bodies) connected by ligaments and disks modeled as springs. These models could only predict locally the kinematic and dynamic responses of a certain part of the spine under load. In addition to static and dynamic investigations, FEMs have also been widely used for years to study scoliosis biomechanics (Aubin, 2002). Thoroughly understanding the biomechanics of the spine deformation will help surgeons to formulate treatment strategies for surgery as well as design and development of new medical devices involving the spine. Due to the complexity of spine deformities, FEMs of scoliotic spines are usually restricted to two-dimensional models or sufficiently simplified into three-dimensional elastic beam element models. Although these models showed that the preliminary results achieved are promising, extensive validation is necessary before using the models in clinical routine.

Compared to FEMs, multi-body models have advantages such as less complexity, less demand on computational power, and relatively simpler validation requirements. Multi-body models (MBMs) possess the potential to simulate both the kinematics and kinetics of the human spine effectively. In multi-body models, rigid bodies are interconnected by bushing elements, pin (2D) and/or ball-and-socket (3D) joints. Multi-body models can also include many anatomical details while being computationally efficient. In these models, the head and vertebrae are modeled as rigid bodies and soft tissues (intervertebral discs, facet joints, ligaments, muscles) are usually modeled as massless spring-damper elements. Such multi-body models are capable of producing biofidelic responses. Generally, multi-body models can be broken down into two categories: car collisions and whole-body vibration investigations. In the former, displacements of the head with respect to the torso, accelerations, intervertebral motions, and neck forces/moments can provide good predictions for whiplash injury. In the latter, multi-body models are helpful for determining the forces acting on the intervertebral discs and endplates of lumbar vertebrae. In both cases, multi-body models are only focused either on the cervical spine or on the lumbar spine. Since these spine segments are partially modeled in detail, it is impossible to investigate the kinematics of the thoracic spine region. In other words, global biodynamic response of the whole spine has not been studied thoroughly.

1.3. Applications of Haptics into Medical Field

Although finite element models and multi-body models are the most powerful tools used to study intrinsic properties of injury mechanisms, many modern and novel techniques have been developed and integrated into these two models to obtain deeper understanding of biomechanical properties of medical diseases. One of these new techniques potentially used is computer haptics. The word haptics was introduced in the early 20th century to describe the research field that addresses human touch-based perception and manipulation. In the early 1990s, the synergy of psychology, biology, robotics and computer graphics made computer haptics possible. Much like computer graphics is concerned with rendering visual images, computer haptics is the art and science of synthesizing computer generated forces to the user for perception of virtual objects through the sense of touch. Thus, simulation with the addition of haptic techniques may offer better realism compared to those with only a visual interface. In recent years, haptic technique has been widely applied in numerous virtual reality environments to increase the levels of realism. Especially, haptics has been investigated at length for medical education and surgical simulations, such as for surgical planning and laparoscopic surgical training. For example, a lumbar puncture simulator developed by Gorman et al. (2000) uses haptic feedback to provide a safe method of training medical students for actual lumbar puncture procedures on a patient. Such procedures are complex and require precise control to obtain cerebro-spinal fluid from a patient for diagnostic purposes. Inadequate training can result in serious outcomes and so the haptic simulator hopefully provides good preliminary training for the lumbar puncture process. Later, the Virtual Haptic Back (VHB) project from University of Ohio developed a significant teaching aid in palpatory diagnosis (detection of medical problems via touch) (Robert L. Williams et al., 2004). The VHB simulates the contour and compliance properties of human backs, which are palpated with two haptic interfaces.

Although haptics has been widely utilized in medical fields, it seems that the haptic technique has not been applied to human spine models to study spinal diseases. Integrating the haptic technique into spine models has advantages in that surgeons can deeply investigate kinematic response of injury mechanisms in spinal diseases. In artificial disc design applications, this technique can be helpful in quickly verifying the suitability of material being used for components of artificial discs. Moreover, haptic technique can also be utilized to study in detail biodynamic responses of the whole human spine which either have not been investigated enough in the literature or are limited to partial spine segments. Understanding kinematic behaviors of whole human spine is beneficial to wheelchair design applications for the disabled. When applying forces to a certain vertebra of the spine under fixed constraints on sacrum and selected vertebrae, users such as surgeons or clinicians can feel force feedback from the spine as well as examine its locomotion. These results may be useful for designing suitable and comfortable wheelchairs for the disabled with specific abnormal spinal configurations. In addition, by simulating in a haptically integrated graphic environment, orthopaedic surgeons can gain insight into the planning of surgery to correct severe scoliosis. Different designs of rods and braces can for example be experimented with using this virtual environment. Furthermore, the surgeons may be able to understand the change in force distribution following spine fusion procedures, which can also assist in post-operative physiotherapy.

1.4. Research Objectives

The main objectives of this thesis were to develop a completely detailed musculo-skeletal muti-body spine model using LifeMOD Biomechanics Modeler and then simulate biodynamic behavior of the spine model in a haptically integrated graphic interface. The specific aims of this research were:

- Develop an entirely discretized musculo-skeletal multi-body spine model constructed in LifeMOD
- Validate the detailed spine model
- Propose a haptically integrated graphic interface
- Present a new tetrahedral mass-spring system model of intervertebral disc
- Study biodynamic behavior of the whole spine model as well as deformation response of intervertebral discs under external forces

Initially, a detailed spine model was obtained by step-by-step developing and discretizing a default multi-body spine model generated in LifeMOD. Subsequently, this detailed spine model was validated by comparing with experimental data, *in-vivo* measurements and other spine models in the literature. Then, biodynamic simulations of the spine model under external forces applying on different vertebrae were conducted and biomechanical properties of the spine such as displacement-force relationships were achieved. Next, these relationships were imported into a haptically integrated graphic environment. With this haptic interface, surgeons are able to interact more realistically with the spine model by touching, dragging or even applying external forces on a certain vertebra they desire. Under the external forces, the surgeons can investigate dynamic responses of the spine model computed via the displacement-force relationships. Since importing the geometry of the spine model in LifeMOD into the haptic interface is very difficult, a thoracolumbar spine model with complex geometry of vertebrae was used instead to observe better the locomotion of the spine. In addition, tetrahedral mass-spring system models of intervertebral discs were interposed between vertebrae of the spine and the surgeons can thoroughly understand deformation behavior of intervertebral disc in a certain spine segment during the haptic simulation. Moreover, running offline simulation of all intervertebral discs after the real-time haptic simulation of the thoracolumbar spine model can be useful for the surgeons to gain insight into the kinematics of the whole spine as well as deformation responses of all intervertebral discs globally.

In this thesis, it should be noted that the detailed spine model is developed based on multi-body method. Thus, using finite element method to build a fully detailed spine model is beyond the scope of this present study. In addition, since this research is mainly focused on investigating biodynamic behavior of the whole spine model, other properties such as stress and strain are not considered in the study as well.

1.5. Outline of the Thesis

This thesis consists of seven chapters which can be mentioned as follows. Chapter 1 introduces the background of research problems, the motivation for undertaking this research, the research objective and the outline of this thesis. Chapter 2 mentions an overview of human spine structure, the literature review on finite element models and multi-body models involving spine related injuries or diseases. In Chapter 3, an overview of LifeMOD software is presented. Then, a discretized musculo-skeletal muti-body spine model in LifeMOD software is developed in detail and validated by comparing results with experimental data and in-vivo measurements. Next, dynamic simulation and analysis of the spine model under external forces is shown. To interact with the spine model more realistically, a haptically integrated graphic interface is described thoroughly in Chapter 4. In this chapter, fundamentals of computer haptics are briefly introduced and the haptic rendering method used in the research is clearly presented. In Chapter 5, a new tetrahedral mass-spring system model of interverterbral disc is proposed to combine with the spine model. This combination will enable surgeons to better understand kinematics of the spine as well as deformation response of intervertebral discs at a specific spinal segment. Chapter 6 introduces some applications of the spine model developed in this thesis into medical areas and discusses some limitations encountered in the research. Chapter 7 draws some conclusions and suggests possible future works. Finally, the appendices give other relevant information including LifeMOD practical tutorials, step-by-step guideline process for developing a detailed spine model in LifeMOD, specific calculation of intra-abdominal pressure, dynamic database of the spine model in LifeMOD, relative displacements of all pairs of vertebrae under external forces in x- and z-axis directions and supplemental data.

CHAPTER 2

LITERATURE REVIEW

In this chapter, some fundamental backgrounds of human spine structure are briefly introduced to give sufficient understanding of the functionality of the components of the spine. Then, a survey of literature on finite element model and multi-body models used for studying clinical spinal problems such as whiplash injury, whole-body vibration and scoliosis is presented in detail. Finally, the potential drawbacks of the mentioned models are evaluated to highlight the rationale for a detailed musculo-skeletal multi-body spine model proposed in this current research.

2.1. Overview of Human Spine Structure

To be able to understand the causes of spinal disorders and find out the treatments for these diseases, some basic concepts and knowledge of human spine structure are required. In general, the human spine has three major components: the spinal column (i.e. bones and discs), neural elements (i.e. the spinal cord and nerve roots) and supporting structures (e.g. muscles and ligaments). These components play an important role in creating the normal movements of the spine.

2.1.1. Spinal column

The spinal column (Figure 2.1) extends from the skull to the pelvis and is made up of 33 individual bones termed vertebrae that are stacked on top of each other. The spinal column can break into 5 regions: 7 cervical vertebrae (C1-C7) in the neck, twelve thoracic vertebrae (T1–T12) in the upper back, five lumbar vertebrae (L1–L5) in the lower back, five bones (that are joined together in adults) to form the bony sacrum, and three to five bones fused together to form the coccyx or tailbone.

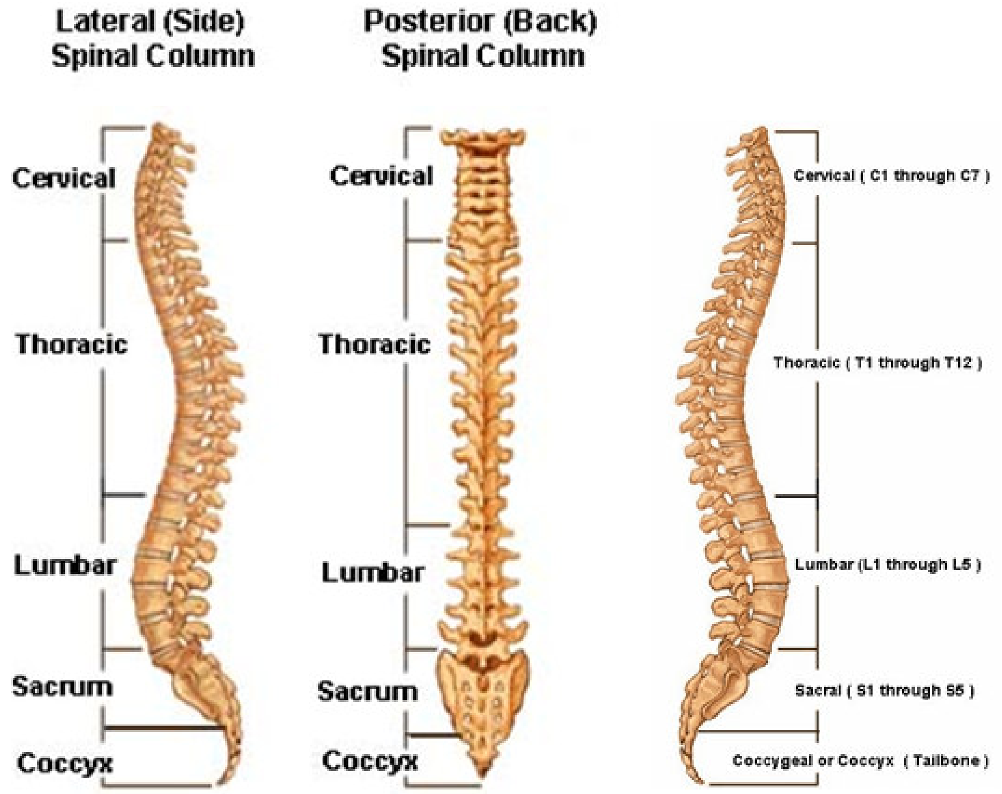

Figure 2.1 Spinal column (Spineuniverse)

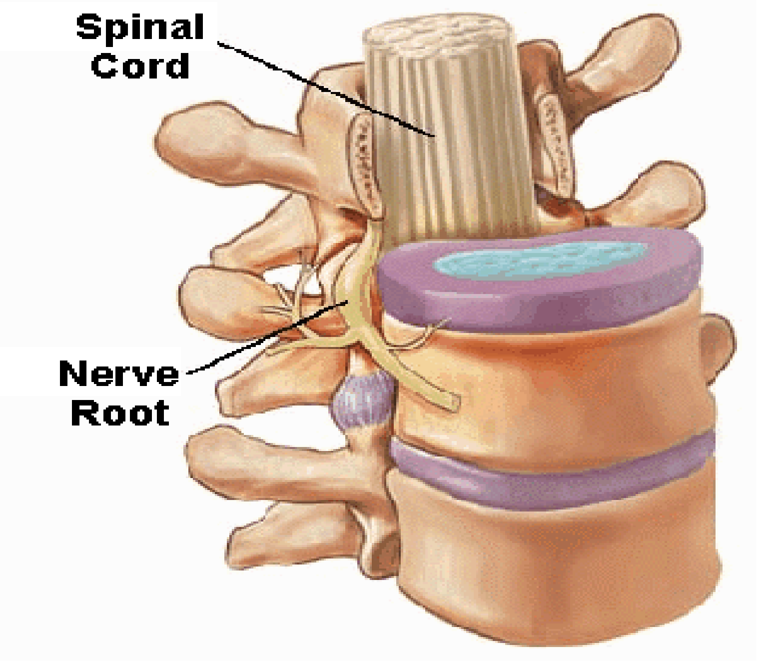

Figure 2.2 Nerve roots and spinal cords (TheWellingtonHospital)

2.1.2. Neural elements

The neural elements (Figure 2.2) consist of the spinal cord and nerve roots. The spinal cord runs from the base of the brain down through the cervical and thoracic spine. The spinal cord is surrounded by spinal fluid and by several layers of protective structures, including the dura mater, the strongest, outermost layer. At each vertebral level of the spine, there is a pair of nerve roots. These nerves go to supply particular parts of the body.

2.1.3. Supporting structures

The muscles and ligaments enable the spine to function in an upright position, and the trunk to assume a variety of positions for various activities. The spinal ligaments are extremely important for connecting the vertebrae and for keeping the spine stable. There are various ligaments attached to the spine, with the most important being the anterior longitudinal ligament and the posterior longitudinal ligament (Figure 2.3), which runs from the skull all the way down to the base of the spine (the sacrum). In addition to the ligaments, there are also many muscles attached to the spine, which further help to keep it stable. The majority of the muscles are attached to the posterior elements of the spine.

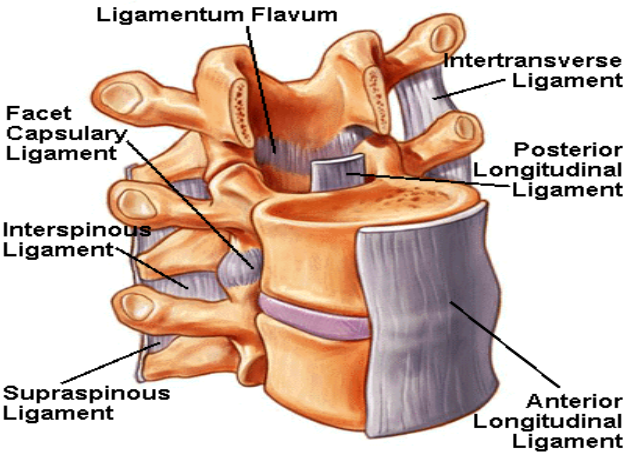

Figure 2.3 Ligaments of the spine (Spineuniverse)

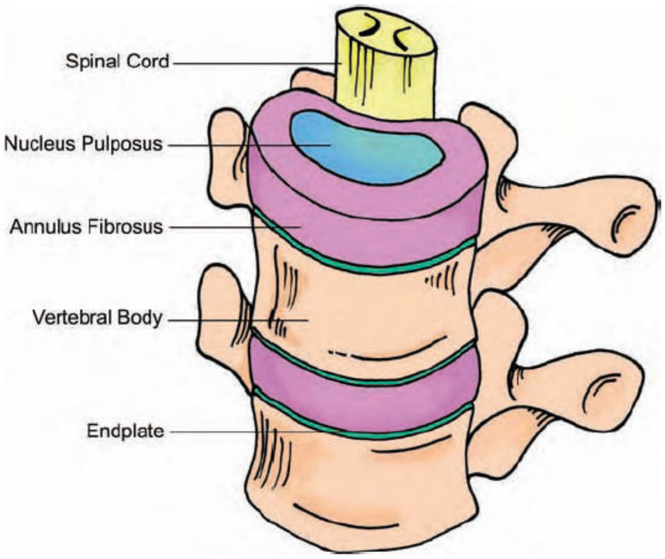

Figure 2.4 Intervertebral discs (Kurtz and Edidin, 2006)

2.1.4. Intervertebral disc structure

The intervertebral discs (Figure 2.4) are soft tissue structures situated between each of the 24 cervical, thoracic, and lumbar vertebrae of the spine. Their functions are to separate consecutive vertebral bodies. Once the vertebrae are separated, angular motions in the sagittal (forward, backward bending) and coronal planes (sideway bending) can occur.

The intervertebral disc consists of 3 main components: a nucleus pulposus surrounded by an annulus fibrosus (outer shell) both sandwiched between two cartilaginous vertebral endplates. The annulus fibrosus primarily bears the axial load on the disc. The lamellae of collagen fibers (Figure 2.5) that make up the annulus fibrosis are able to resist tension and support compressive loads, provided that it does not buckle. The nucleus pulposus, which contains a semi-fluid substance – proteoglycans, make up the core of the disc and serves to prevent buckling of the annulus. When it is compressed, the fluid is forced radially towards the inner surface of the annulus, forming a pressure that braces the annulus and prevents inwards buckling of the lamellae. Another role of the nucleus is that it acts as a shock absorber for the spine, preventing injury due to impact. The endplates cover 70% of the vertebral surface and the nucleus pulposus and inner annulus fibrosus. The outer 30% of the endplate surface is the only true cortical bone in the vertebral endplate. The central 70% is made of compressed cancellous bone. This is of significance to any implant design because for maximum stability of the implant the fixation should be on the dense cortical bone comprising the peripheral 30% of the endplates.

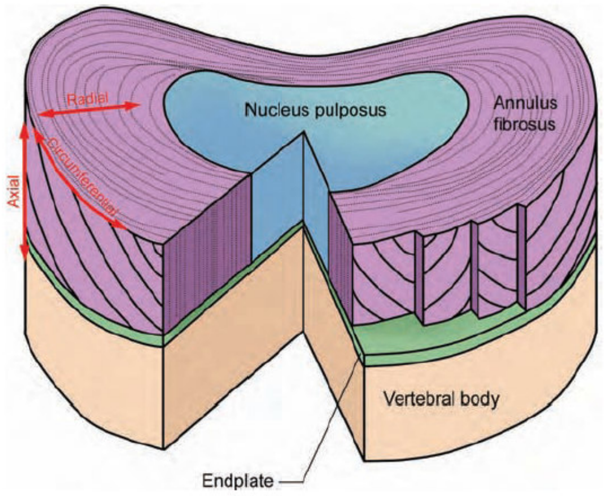

Figure 2.5 Structure of an intervertebral disc (Kurtz and Edidin, 2006)

2.2. Finite Element Model for Human Spine

2.2.1. Models for static studies

For the last decades, there are a multitude of researches conducted to study in depth various properties of each specific component of human spine such as vertebrae, ligaments, spinal cord, intervertebral discs etc. These researches will help surgeons to gain insight into underlying mechanism of these components and to find out suitable treatment solutions for spinal injuries or diseases.

In order to investigate cervical vertebral body stresses, Bozic et al. (1994) built an FEM that can represent the complex geometry and nonhomogeneous material properties of vertebra C4. The model can be useful for validating proposed fracture mechanisms in the cervical spine, as well as for examining the effects of varying loading conditions on bone remodeling. Then, Yoganandan et al. (1996) constructed a detailed, three-dimensional, anatomically accurate finite element model of the C4-C6 human vertical spine unit using close-up computer tomography to study biomechanical behavior of the spine under axial compressive loading and validated against experimental data. After that, Silva et al. (1998) used nine fresh-frozen thoracolumbar spines (32, 50, 51, 65, 71, 73, 84, 85 and 102 years old) with no obvious skeletal pathologies to build finite element models for predicting failure loads and fracture patterns for bone structures. Later, Teo et al. (2001) constructed a detailed 3D FEM of the human atlas (C1) with the geometrical data obtained using a three-dimensional digitizer to develop further understanding to the injury mechanisms of the atlas, which is important for the prevention, diagnosis, and treatment of spinal injuries. Afterwards, Nabhani et al. (2002) created three-dimensional models of the L4 and L5 vertebrae on a Silicon Graphics workstation, using the I-DEAS Master SeriesTM software package to identify areas that are subjected to the greatest stresses and which are more likely to be susceptible to degenerative diseases and injuries. Meanwhile, Pitzen et al. (2002) developed a FEM of a human spinal segment L3/L4 to predict the biomechanical behavior of the human lumbar spine in compression. Subsequently, Liebschner et al. (2003) introduced a novel finite element modeling technique combined with quantitative computed tomography-based modeling of trabecular properties and vertebral geometry to model the vertebral shell using a constant thickness of 0.35 mm and an effective modulus of 457 MPa. This modeling technique can accurately describe whole vertebral stiffness and strength, produce insight into vertebral body biomechanical behavior and may ultimately improve clinical indications of fracture risk of this cohort. Recently, Qiu et al. (2006) built an anatomically realistic 3D FEM of a T12–L1 motion segment based on embalmed vertebral specimens from a deceased 56-year-old male subject to investigate vertebral burst fracture mechanism at the thoracolumbar junction under dynamic vertical impact.

In addition to understanding biomechanics of vertebrae, there are also many researchers investigating intrinsic properties of ligaments, facets and spinal cord because these components are critical factors resulting in spinal injuries. Shirazi-Adl (1994) developed a detailed 3D FEM (L1-S1) to investigate the response of the whole ligamentous lumbar spine in axial torsion. Attention is focused on the inter-segmental variations, role of articular facets, presence of coupled movements, intervertebral stresses and the effects of a structural alteration at a level on the response. Then, Heitplatz et al. (1997) developed a 3D FEM of the C4-C7 human cervical spine structure using data from the Visible Human Project. The model was the first step in an attempt to simulate the three-dimensional movement of the cervical spine during whiplash accidents in order to predict the strain inside the spinal ligaments, with a view to supporting the development of car restraint systems. After that, Kumaresan et al. (1999) used the detailed, three-dimensional, anatomically accurate finite element model developed by Yoganandan et al. (1996) to study the effect of material property variations of such spinal components as cortical shell, cancellous core, endplates, intervertebral discs, posterior elements and ligaments on the human cervical spine biomechanics. Later, Teo et al. (2001) built a 3D FEM of the human lower cervical spine including the bony vertebrae, articulating facets, intervertebral disc, and associated ligaments. The present model was validated against published experimental and existing analytical results (Goel and Clausen, 1998, Heiplatz et al., 1998, Maurel et al., 1997, Moroney et al., 1988, Pelker et al., 1991, Shea et al., 1991, Yoganandan et al., 1996) under the same three load configurations: axial compression, flexion and extension. The FEM was further modified accordingly to investigate the role of disc, facets and ligaments in preserving cervical spinal motion segment stability in these load configurations. Recently, Greaves (2008) created a detailed three-dimensional and experimentally verified finite element model of a human cervical spine and spinal cord segment to investigate differences in cord strain distributions under various column injury patterns: contusion, distraction and dislocation.

Compared to vertebra, ligament and spinal cord studies, investigating intervertebal discs has attracted most attention of researchers because understanding insight into intervertebral discs is useful for surgeons to propose appropriate solutions in treating lumbar back pain, which is the most common among spinal injuries.

Different complex properties of intervertebral discs have been simulated and analyzed in detail. The very first study was conducted by Belytschko et al. (1974). The author developed an axisymmetric FEM for the study of the behavior of an intervertebral disc under axial loading. Then, Spilker et al. (1984) extended Belytschko’s model to investigate mechanical response of intervertebral disc under complex loading. Ahmed et al. (1986) improved the model developed by Shirazi-Adl et al. (1984) to analyze the lumbar L2-L3 motion segment subjected to sagittal plane moments. After that, Goel et al. (1995) created a three-dimensional FEM to investigate interlaminar shear stresses across the laminae of a ligamentous L3-L4 motion segment. Martinez et al. (1996) presented an experimental and finite element study of the biomechanical response of the intervertebral disc to static-axial loading in which classical consolidation theory was used to analyze its time-dependent response. Later, Kumaresan et al. (1999) developed an anatomically accurate, three-dimensional, nonlinear finite element model of the human cervical spine using close-up computer tomography images and cryomicrotome sections. The model was used to study the biomechanics of the cervical spine intervertebral disc by quantifying the internal axial and shear forces, which cannot determine directly from experimental studies, resisted by the ventral, middle, and dorsal regions of the disc under the above axial and eccentric loading modes. Subsequently, Natarajan et al. (2007) presented a poro-finite element model to predict the failure progression in a L4-L5 lumbar disc due to a physiologically relevant cyclic loading. And the model was validated by comparing the results with the in vivo measurements reported by Tyrrell and Reilly (1985). Further information on mechanical behavior of intervertebral discs can be found in these references (Shirazi-Adl et al. 1984, McNally et al. 1995, Lu et al., Wu et al. 1996, Todd et al. 1997, Templier et al. 1999, Lee et al. 2000, Kim 2000, Meakin et al. 2001, Baroud et al. 2003, Noailly et al. 2003, Yao et al. 2006, Denoziere et al. 2006).

While there are many researchers focused on studying mechanical response of intervertebral discs, some others have examined other properties such as linear, nonlinear, creep response etc. Firstly, Kulak et al. (1976) studied the nonlinear, rate-independent behavior of human intervertebral discs with a finite element model which incorporates a nonlinear elastic constitutive relation for the annulus fibrosis. Then, Laible et al. (1993) incorporated swelling process that occurs in soft tissue into a poroelastic FEM to analyze the dramatic effect of swelling on the load carrying mechanisms in the disc. After that, Argoubi et al. (1996) developed a nonlinear 3D poroelastic FEM to investigate the creep response of a lumbar motion segment under a constant axial compression (400, 1200, or 2000 N) for a period of 2h. Later, Bos et al. (2002) created an axisymmetric FEM to understand and describe the non-linear mechanical reactions of the intervertebral disc. Afterwards, Cheung et al. (2003) built a 3D FEM of the L4–L5 lumber motion segment to investigate the time-dependent responses of the intervertebral joint to static and vibrational loads. Subsequently, Kyureghyan et al. (2005) presented the prediction of the intervertebral disc creep during flexion using a combined approach of a human subject experiment and finite element model of the lumbar spine to calculate the deformations and stresses in the components of the lumbar spine. Recently, Schroeder et al. (2006) constructed a fibril-reinforced poro-viscoelastic swelling finite element model to compute the interplay of osmotic, viscous and elastic forces in an intervertebral disc under axial compressive load.

Besides the properties mentioned above, many authors also investigate deeply degeneration process of intervertebral discs. At first, Kurowski et al. (1986) utilized finite element method to study the influence of disc degeneration on the mechanism of load transmission through the lumbar vertebral body. Then, Kim et al. (1991) developed nonlinear three-dimensional finite element models of a ligamentous two motion segments spine specimen (L3-L4-L5) to investigate the effects of disc degeneration, simulated at the L4-L5 level, on the biomechanical behavior of the adjacent intact L3-L4 motion segment. After that, Shirado et al. (1992) conducted a biomechanical study performed using cadaveric spines to clarify the pathomechanism of thoracolumbar burst fractures and to evaluate the influence of disc degeneration and bone mineral density. Subsequently, Natarajan et al. (1994) developed a finite element model of a motion segment without posterior elements to study the disc degeneration process. The model was used to investigate the development of anular tears, nuclear clefts and subsequent propagation of these degenerative processes due to compressive and bending loads. Later, Kumaresan et al. (2001) used a validated intact finite element model of the C4-C6 cervical spine to simulate progressive disc degeneration at the C5-C6 level and investigate the basis for the occurrence of disc-related pathological conditions. Recently, Rohlmann et al. (2006) developed a 3-D nonlinear finite element model of the L3/L4 functional unit to study the influence of disc degeneration on motion segment mechanics. Schmidt et al. (2007) used finite element method to investigate load combinations that would lead to the highest internal stresses in a healthy and in degenerated discs.

In view of the results of the above studies, it is clear that FEMs developed for static studies generally are more detailed in representing the spinal geometries. Although this type of model can predict internal stresses, strains and other biomechanical responses under complex loading conditions, it generally only consists of one or two motion segments and can not provide more insight into biodynamics of the whole spine.

2.2.2. Models for dynamic studies

Goel et al. (1994) developed a nonlinear, three-dimensional finite element model of the ligamentous L4-S1 segment to analyze the dynamic response of the spine in the absence of damping under cyclic loads. The present model of the L4-L5 part of S1 lumbar segment is based on the three-dimensional finite element model of the L3-L5 segment earlier developed by the author's group (Goel et al., 1988). The model was validated by comparing the predicted data to the experimental values. The results of the model appeared to be in agreement with the in vivo data reported in the literature.

Maurel et al. (1997) constructed a three-dimensional parameterized finite element model of the complete lower cervical spine to investigate the influence of the posterior articular facets as their geometry is very different from those of the other spinal levels.

Kitazaki et al. (1997) introduced a two-dimensional model of human biomechanical responses to whole-body vibration by using the finite element method. In fact, the present model was evolved from those developed by Belytschko and Privitzer (1978). The geometry and material properties were based on those Belytschko and Privitzer used and also others. Some geometry and stiffness data were modified, comparing the vibration mode shapes of the model with the measurements obtained by Kitazaki and Griffin (1996). The results showed that an increase in contact area between the buttocks and the thighs and the seat surface, when changing posture from erect to slouched, may decrease the axial stiffness beneath the pelvis, with a non-linear forcedeflection relationship of tissue resulting in decreases in the natural frequencies.

Pankoke et al. (1998) presented a two dimensional dynamic finite element model of a sitting man to calculate internal forces acting on the lumbar vertebral disks under long term whole body vibration. The model is based on an anatomic representation of the lower lumbar spine (L3-L5). Geometry and inertial properties of the model are determined according to human anatomy. Stiffnesses of the spine model are derived from static in-vitro experiments in references (Schultz, 1979) and (Berkson, 1979). In short, the model can be used as a tool for estimating compressive forces and shear forces in the lumbar vertebral disks.

Buck et al. (1998) built a three dimensional dynamic finite element model of a sitting 50-percentile man based on a close representation of human anatomy with specific focus on the lumbar spine and muscles to evaluate the influence of muscles on whole-body dynamics and predict internal forces in the lumbar spine necessary to assess the potential risk of whole-body vibrations for the lumbar spine. Results showed that the influence of the muscle model is significant above about 6 Hz, which corresponds with the experimental results of Pope et al. (1990). It was also showed that the internal force-time-function in the disc L3-L4 is above the fatigue limit for elderly workers under static force of 411.6 N when the compression strength of 2000 N reported by Jager et al. (1996) is used.

Pankoke et al. (2001) introduced a simplified version of the three-dimensional detailed finite element model of Buck et al. (1998) adaptable to body height, body mass and posture of a specific subject to predict the dynamic spinal loads caused by whole-body vibrations.

Seidel et al. (2001) used a plane linear symmetric finite element model of the sitting man with an anatomic representation of the lumbar spine developed by Pankoke et al. (1998) to predict static and dynamic compression and shear forces acting on the S1-L5 segment during whole-body vibration for a variety of boundary conditions-body mass, height and posture.

Zander et al. (2002) created a 3-D nonlinear finite element model of the lumbar spine with internal spinal fixators and bone grafts to study mechanical behavior after mono- and bi-segmental fixation with and without stabilization of the bridged vertebra.

Guo et al. (2005) presented a detailed three-dimensional finite element model of the lower thorax-pelvis, T12-pelvis, based on actual vertebral geometry to predict the biomechanical behavior of the human spine at resonance frequency under whole-body vibration. The simulation results demonstrated that the human upper body mainly performed the vertical motion during whole-body vibration and the lumbar spine segment conducted translation and rotation in the sagittal plane. It can be seen that the anteroposterior motion of the L2-L3 segment was the largest, which is agreement with the findings of Kong et al. (2003).

Ng et al. (2005) developed a comprehensive, geometrically accurate, nonlinear C0-C7 finite element model based on a 68-year-old human cadaveric specimen. The model was used to investigate the biomechanical response of human neck under physiological static loadings, near-vertex drop impact and rear-end (whiplash) impact conditions and validated against the published experimental results. These findings are well compatible with the experimental observations (Panjabi et al., 2001).

Kang et al. (2005) constructed a three-dimensional finite element human whole body model-THUMS under the posterior-oblique impacts with angles of 15^0, 30^0, and 45^0 degrees to study the cervical spinal behaviors three-dimensionally and to analyze the stresses occurred in the facet joints considering the relationship with a whiplash disorders.

Ishikawa et al. (2005) designed a musculo-skeletal dynamic rigid link spine model to simulate the dynamic spinal motion and analyze the vertebral stress distribution with a role of functional electrical stimulation (FES) to the trunk extensor muscles.

Qiu et al. (2006) modified a detailed three-dimensional C0-C7 finite element model of the whole head-neck complex developed by Ng et al. (2005) to include T1 vertebra. Rear impact accelerations of different conditions were applied to T1 inferior surface to validate the simulated variations of the intervertebral segmental rotations of the cervical spine. In the same year, the author (2006) also built a nonlinear three-dimensional finite element model of thoracolumbar T11-L1 to explore the influence of bilateral facetectomy on spinal stability. The model was validated against published experimental results under various physiological loadings and evaluated under flexion, extension, lateral bending and axial rotation to determine alterations in kinematics. And it was concluded that removal of facets did not result in significant change in the sagittal motion in flexion and extension.

Pang (2006) generated and validated a seated whole human model, with special attention given to a finite element lower lumbar spine motion segment model (L3 to L5). The finite element lower lumbar spine model consisting of bony vertebrae and intervertebral discs would be able to predict stress distributions within the spinal components.

Hinz et al. (2007) extended the model developed by Hofmann et al. (2003) to describe the biodynamic response of different occupational groups of European workers exposed to whole-body vibration.

Zhang et al. (2007) used the detailed three-dimensional head-neck (C0-C7) finite element model developed by Teo et al. (2005) to investigate the kinematic responses of the head-neck complex under rear-end, front, side, rear-and front-side impact.

Guo et al. (2008) improved a three-dimensional finite element model comprising of the T12-pelvis spine unit developed by Teo et al. (2005, 2006) to determine the influence of antero-posterior (A-P) shifting of trunk mass from the upright sedentary posture on dynamic characteristics of the human lumbar spine.

Zhang et al. (2008) developed a comprehensive, geometrically accurate, nonlinear FE model of thoracolumbar spine multi-segment (T12-L5) to simulate the response of thoracolumbar spine under the mine blast condition with two initial postures.

Schmidt et al. (2008) created a FE model of a L4-L5 lumbar spinal segment under an axial compression preload of 500 N and pure unconstrained moments of 7.5 Nm to investigate the relationship between the rotation center and facet joint forces.

Based on the studies aforementioned, it is found that different from static studies which primarily examine biomechanics of one or two segments of the spine, FEMs for dynamic studies generally include a series of vertebrae (as rigid bodies) connected by ligaments and disks modeled as springs. These models can only predict locally the kinematic and dynamic responses of a certain part of the spine under load. Hence, global locomotion of the whole spine has not completely investigated yet.

2.2.3. Models for scoliotic spines

Several mathematical models of the spine have been developed and used to simulate scoliosis surgical correction. Belytschko et al. (1973) and Schultz et al. (1973) reported a comprehensive 3D deformable model of the thoraco-lumbar spine and used it to simulate the Harrington correction (Schultz and Hirsch, 1973, 1974). They compared corrections using lateral forces to those using longitudinal forces. These represented the very beginning of simulation, and no means of validation with respect to the 3D aspects were available.

Using a combined experimental/analytical method, the in vivo segmental properties of the scoliotic spine were determined in two studies: Vanderby et al. (1986) presented an optimization method based on preoperative radiographs of the spine loaded with a specific instrumented distractor; and Viviani et al. (1986) presented a method using frontal radiographs of the spine under traction. In both cases, models were developed in 2D, which limited their ability to represent correctly the complex 3D mechanism of scoliosis correction.

Stokes and Laible (1990) presented a 3D finite element model of the thoraco-lumbar spine and used it to simulate Harrington and Cotrel–Dubousset (CD) corrections. In both studies, geometry was personalized using stereo-radiographic reconstruction and Direct Linear Transformation technique, whereas mechanical properties were extracted from the literature concerning the behaviour of non-scoliotic specimens. The authors underlined that an identification of segmental stiffness was necessary to simulate the surgery correctly. The same conclusion was reported by Poulin et al. (1998) when simulating the CD correction with a rigid-body model of the spine.

Gignac et al (2000) presented a finite element model of the spine and rib cage and put forward an optimization approach to find optimal correction patterns for scoliotic spines. The method in this study is used to analyze the biomechanics of bracing, and may be beneficial in the design of new and more effective individualized braces. Nevertheless, the results are considered preliminary investigations, and the brace design work needs to be continued to address its clinical validity.

Lafage et al. (2004) simulated Cotrel–Dubousset scoliosis surgery for patients with idiopathic scoliosis using a 3D finite element model of the patient’s entire spine. However, the model showed that simulating specific mechanical behaviour of a given patient is limited since mechanical personalization has not been sufficiently investigated. Although the results of this method are promising, extensive validation is necessary before utilizing the model in clinical routine.

2.3. Multi-Body Model for Human Spine

2.3.1. Whole-body vibration and repeated shock investigation

Luo et al. (1991) extended the humanoid/neck/upper torso system with a numerical model and an instrumented physical model developed by Deng and Goldsmith (1987a, 1987b) by including the lower torso region to simulate the effect of a vehicular collision on a solely lap-belted occupant.

Fritz (1998) improved the biomechanical multi-body model developed by himself (1997) by including the arms to determine the forces on the lumbar spine and to study the effect of whole-body vibration on low back pain. Two year later, the author (2000) introduced a multi-body biomechanical model especially including the legs as active elements to predict forces in the lumbar spine and legs through computed transfer functions between the ground acceleration and the oscillating forces in the ankle, the knee, the hip, and the motion segment L3-L4 for the standing posture during whole-body vibration.

Some back disorders are caused by inappropriate loading of the spine that can be combined with other influential factors such as a body posture, whole-body vibration and shock. Hence, Seidel et al. (2001) summaries existing dynamic models of sitting man able to use in modeling the response of the spine system to whole-body vibration to provide a possibility to predict the forces acting on the disks and endplates of vertebrae.

Verver et al. (2003) developed a mathematical human body model in MADYMO validated for vertical vibrations based on volunteer experiments on a rigid seat and the standard car seat condition to predict spinal forces. The MADYMO model was constructed from RAMSIS anthropometry of the 50th percentile male with 1.74 m standing height and 75.7 kg total mass. The seat-to-human transmissibility of human model agrees reasonably with the volunteer responses for both the rigid seat and standard car seat experiments.

Yoshimura et al. (2005) built a simplified multi-body model of spinal column having 10 DOFs to assess vibration effects on the spine when a half-sine input was applied. The model was two-dimensional and performed only in sagittal plane. The analytical results indicated that the half-sine input affected the intervertebral disk between L4 and L5 most among the lumbar spine vertebrae.

2.3.2. Whiplash impact investigation

De Jager (1996) built a detailed three-dimensional mathematical model describing the dynamic behaviour of the human head and neck in accident situations without head contact. The model was suitable for studying neck injury mechanisms and neck injury criteria, since it revealed the loads and deformations of individual tissues of the neck.

Kroonenberg et al. (1997) developed a mathematical model of a seated car occupant to obtain insight into the biomechanical response of the spine and the occupant's interaction with the seat during rear-end collisions. And this model has the potential to become a powerful tool for parametric studies to aid in a seat design process.

Linder (2000) implemented a mathematical model of a new rear-end impact dummy neck using MADYMO. The main goal was to design a model with a human-like response of the first extension motion in the crash event. This mathematical model was used in the development phase of a mechanical dummy. And findings from this study have been used in the design of a new neck for the rear-end impact dummy.

Van Der Horst (2002) developed the detailed multi-body neck model built by De Jager (1996) to examine factors that might influence the risk of neck injury, such as the amount of activation of the neck muscles, the initial seating posture and the head restraint position. The results showed that the global kinematics like head, translational and angular, movements and accelerations as well as local kinematics such as vertebral rotations and tissue loads can be predicted with this neck model.

Garcia et al. (2003) presented a four-segment dynamic model in sagittal plane of human spine to analyze biomechanics of whiplash injury potential during the initial extension motion of the head in a rear-end collision. The model was validated against the experimental results from Ono et. al. (1997) (a human volunteer study), Luan et. al. (2000) (a cadaver study).

Stemper et al. (2004) built a MADYMO head-neck computer model to study the intrinsic biomechanical responses of cervical spine structures under different physiological, anatomical, and external impact conditions.

Jun (2006) developed a muscle-driven biomechanical model of the human head-neck system that could be used to simulate neck movements under muscle control. The development of the current head-neck model was based on a previous in vitro model of the sub-axial cervical spine that was developed within the rigid body dynamic simulation program, Visual Nastran 4D. The model can be used to explore muscle control strategies to simulate muscle force activation conditions in the future.

Esat et al. (2007) constructed a multi-body model of the whole human spine employing a similar methodology to the cervical spine multi-body model of Lopik and Acar (2004) to simulate whiplash traumas and analyses under various impact conditions and acceleration levels. The multi-body model devoid of muscles is validated against Panjabi et. al. (Panjabi et al., 1988, Panjabi et al., 1998) and colleagues' experiments conducted using a bench-top trauma sled and isolated cervical spine specimen. The model successfully reproduces the characteristic motion of the head and neck when subjected to rear-end crash scenarios.

Himmetoglu et al. (2007) developed a 50th percentile male multi-body head-and-neck model to analyze rear impact and the resulting whiplash injury effects. The volunteer sled tests performed by the Japanese Automobile Research Institute (JARI) had been used for the validation of the head-neck model for low-speed rear-impact scenarios. The model can simulate the rear-impact response of a human with a high degree of accuracy and, hence, it can be economically used as the head-neck section of a rear-impact human-body model to compare accurately crash scenarios and has the potential of predicting injury.

Lopik and Acar (2007) developed the detailed multi-body model of human head and neck comprising simplified but accurate representations of the nine rigid bodies representing the head, seven cervical vertebrae of the neck, and the first thoracic vertebra, as well as the soft tissues, i.e. muscles, ligaments, and intervertebral discs. It has been shown that the model can predict the loads and deformations of the individual soft-tissue elements making the model suitable for injury analysis.

Lately, by using LifeMOD, one of leading simulation tools for performing multi-body analysis, Kim et al. (2007) generated a human-wheelchair musculoskeletal model to analyze the cervical spine injury of wheelchair user regarding frontal and side impacts. However, the model is unable to determine internal forces as well as displacement of specific vertebrae since cervical, thoracic and lumbar spine regions are lumped into three rigid segments.

2.4. Summary

Based on the above review of both finite element models and multi-body models, it is clear that these two types of models are mainly focus on investigating biomechanical properties either of the cervical spine or of the lumbar spine region. There is a little research carried out so far to examine the influence of the thoracic spine segment on the biodynamic response of the whole spine column. In other words, modeling of a detailed whole human spine has not been completely investigated. In finite element models, the models developed for static study generally are more detailed in representing the spinal geometries. Although this type of model can predict internal stresses, strains and other biomechanical responses under complex loading conditions, it generally only consists of one or two motion segments and can not provide more insight into biodynamics of the whole column. The models for dynamic study generally include a series of vertebrae (as rigid bodies) connected by ligaments and disks modeled as springs. These models could only predict the local kinematic and dynamic responses of a certain part of the spine under loads. Although there are finite element models created for the whole spine to study scoliosis disorders, these scoliotic spine models are usually restricted to two-dimensional models or sufficiently simplified into three-dimensional elastic beam element models. In addition, extensive validation is necessary before using the models in clinical routine. In multi-body models, many authors have attempted to develop various human spine models for whiplash impact and whole-body vibration investigations. Although multi-body models are unable to gain insight into underlying mechanisms of injuries, they can provide more biofidelic and better kinematic responses of a certain spine region under loading. However, majority of these models have a shortcoming in that the lumbar spine or cervical spine region is modeled in detail whereas the thoracic spine region is usually oversimplified. Also, the influence of spinal muscles as well as ligaments was not fully taken into account in these models. Recently, LifeMOD Biomechanics Modeler has been popularly used as a multi-body dynamic simulation platform in numerous modeling researches. Many researchers have extensively utilized LifeMOD to create whole human spine models. But, their spine models are still quite basic and not fully discretized. Therefore, from orthopaedic surgeons' perspective, it is important to develop a completely detailed whole human spine model for studying global as well as local biodynamic behaviour of the spine. This detailed spine model can be useful for some medical applications such as spinal fusion investigation, wheelchair design, surgical planning etc. In next chapter of our research, this entirely discretized musculo-skeletal multi-body spine model using LifeMOD will be proposed and presented in detail.

CHAPTER 3

HUMAN SPINE MODEL DEVELOPMENT IN LIFEMOD

3.1. Introduction

In this chapter, an overview of LifeMOD is introduced to provide users with basic functionality of this simulation software. This chapter will also show users how to create a valid, appropriate and complex model for study. Then, the development process of a discretized musculo-skeletal multi-body spine model in various stages is described thoroughly. Validation of the detailed spine model is made by comparing results with those obtained from another spine model in the literature, experimental data as well as *in-vivo* measurements. Subsequently, dynamic behaviour simulation and analysis of the spine model is conducted under external forces applying on vertebrae in x, y, z directions. Based on these analyses, displacement-force relationships of all vertebrae are interpolated and expressed in term of polynomial functions which are later used in haptic simulation.

3.2. Overview of LifeMOD

3.2.1. Basic concepts of LifeMOD

Recently, many software applications have been developed for impact simulation, ergonomics, comfort study, biomechanical analysis, movement simulation and surgical planning. The software enables users to perform human body modeling and interaction with the environment where the human motion and muscle forces can be simulated. These tools are very useful for simulating the human-machine behavior simultaneously. LifeMOD from Biomechanics Research Group is a leading simulation tool that has been designed for this purpose.

The LifeMOD Biomechanics Modeler is a plug-in module to the ADAMS (Automatic Dynamic Analysis of Mechanical Systems) physics engine, produced by MSC Software Corporation to perform multi-body analysis. It provides a default multi-body model of the human body that can be modified by changing anthropometric sizes such as gender, age, height, weight etc. The created human body may be combined with any type of physical environment or system for full dynamic interaction. The results of the simulation are the human motion, internal forces exerted by soft tissues (muscles, ligaments, joints) and contact forces at the desired location of the human body. Further information on LifeMOD interface and some practical tutorials are shown in Appendix A. Full information on the LifeMOD Biomechanics Modeler can be found online (LifeMOD).

3.2.2. General human modeling paradigm

The creation of human models in LifeMOD begins by generating a base human segment set, followed by joints, soft tissues and contact elements between the model and the environment. Each human segment may be further discretized by creating single elements for each bone within the body segment. In general, dynamic analysis of the models in LifeMOD can be conducted in passive or active simulation. Executing passive or active simulation is based on the selected modeling method which is presented clearly in subsection 3.2.3. Figure 3.1 shows the simulation flowchart in LifeMOD.

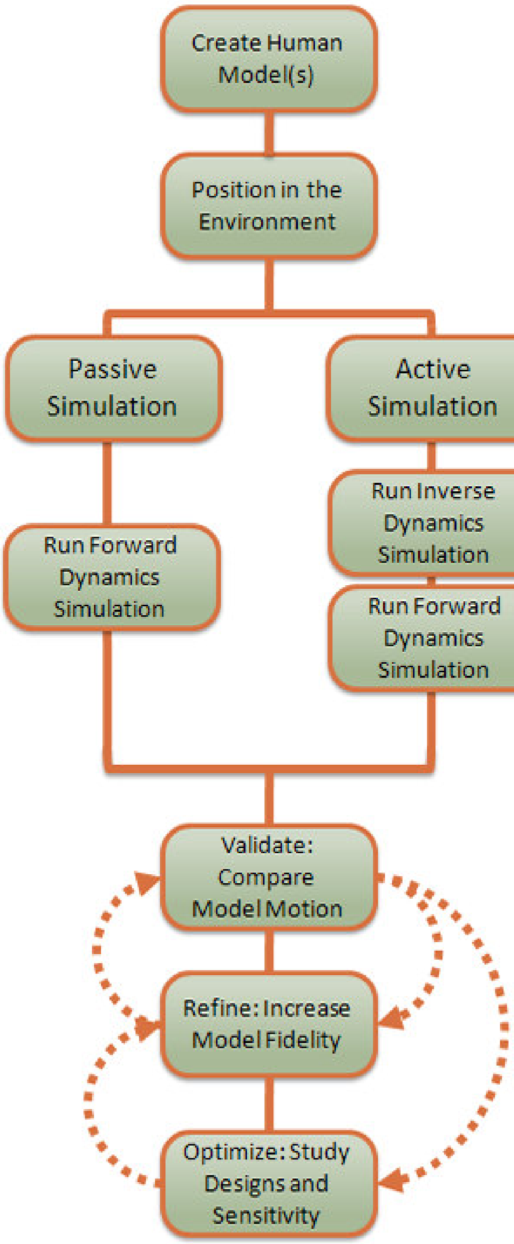

Figure 3.1 The simulation flowchart in LifeMOD

Active simulation requires inverse dynamics and forward dynamics processes whereas passive simulation needs only the forward dynamics process. An inverse dynamics simulation is run first to record joint angulation and muscle contraction histories for each body segment. Motion agents are positioned on the model to drive the movement and recorded in an inverse dynamics simulation. The compiled movement histories of joints and muscles are then used to drive the forward dynamics simulation.

Upon running the simulations, the user can import the test data and validate whether the desired results have been achieved. If the results do not meet expectations, the user can refine the model by changing the fidelity of the specific joints/segments/soft tissues or the environment before running the simulation again.

If the simulation achieves the desired results, it can then be optimized through studies in design sensitivity, experiment design that will help to improve the accuracy of the results.

3.2.3. Modeling methods

There are 3 basic modeling methods in LifeMOD as follows:

- Passive Jointed: These models are only used in passive simulation to evaluate passive injury activities such as car crash and sporting activities where the joints are built using properties from a Hybrid III crash dummy (LifeMOD_Manual).
- Recording Jointed: These models are used in active simulation to study any human activity. The segments of the model are moved in the desired motion pattern using user-input trajectories or motion capture data and the joint angle histories are then used to drive the joints with torques created from proportional-derivative controllers to enforce the recorded displacements (LifeMOD_Manual).
- Trainable Muscled: Similar to “Recording Jointed” models, these models are also used in active simulation to investigate any human activity. At first, the segments of the model are moved in the desired motion pattern using user-input trajectories or motion capture data. The joint angle and muscle contraction histories are then used to drive the joints and muscles

with torques and forces generated from proportional-derivative controllers to enforce the recorded displacements and contractions. During this process, the muscles are continually monitored to make sure the generated force does not exceed the specific muscle tissue force generating capabilities (LifeMOD_Manual).

In this research, the Trained Muscled model is adopted because it takes into account of the influence of muscles and joints. Using this type of model, dynamic results of human body obtained in the simulation will be more accurate and reliable.

3.3. Developing a Fully Discretized Musculo-Skeletal Multi-Body Spine Model

In this section, the developing process of a discretized musculo-skeletal spine model is presented thoroughly. This process includes five main stages such as generating a default human body model, discretizing the default spine segments, implementing ligamentous soft tissues, implementing lumbar back muscles and adding intra-abdominal pressure.

Initially, the modeling procedure takes place by first creating a base segment set, followed by generating default joints and muscle sets. Since the development is focused on spine regions, other components of human body such as legs, arms could be removed. After constraints are made between the spine model and its environment, trial simulations can be executed to test the stability performance of the spine model at each stage. These simulations will show defects of the model and provide the users some useful information for improving the model in subsequent stages. This improving process is continued and repeated until the spine model achieves the stability without occurring any errors. The complete step-by-step modeling procedure of the detailed spine model mentioned here can be found in Appendix B.

3.3.1. Generating a default human body model

The usual procedure of generating a human model is to create a complete set of body segments followed by redefining the fidelity of the individual segments. The body segments of a complete standard skeletal model are first generated by LifeMOD depending on the user's anthropometric input. The model used in this study was a median model with a height of 1.78 m and a weight of 70 kg created from the GeBod anthropometric database. By default, LifeMOD generates 19 body segments represented by ellipsoids. Then, some kinematic joints and muscles are generated for the human model. Figure 3.2 shows the base model in this study.

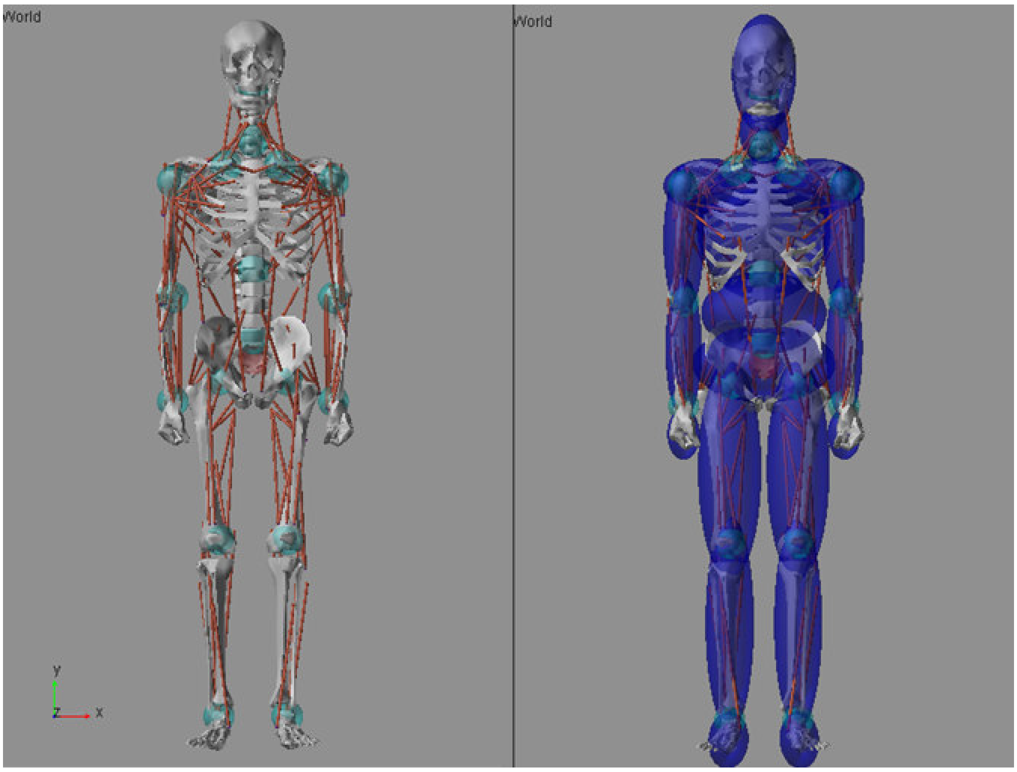

Figure 3.2 Default human body model

Before running the simulation to analyze dynamic properties of the spine, fixed constraints need to be imposed on the pelvis of the spine and external forces are applied on a certain spinal region. In this stage, the lower body and arms can be removed to observe locomotion of the spine more conveniently. Figure 3.3 shows dynamic characteristics obtained in three regions of the default spine model under forward force in sagittal plane. As can be seen in this figure, since the cervical, thoracic and lumbar regions of the default 19-segment multi-body model generated in LifeMOD are represented by three ellipsoidal segments, the movement of the spine cannot be depicted correctly and looks somewhat unrealistic. In addition, this default model is unable to accept external forces to a specific desired vertebra and to determine the load on each intervertebral disc as well as dynamic properties of each vertebra such as translation, rotation. Hence, discretizing the spine segments into individual vertebrae segments is necessary to describe the displacement behaviour of the spine more precisely and reliably.

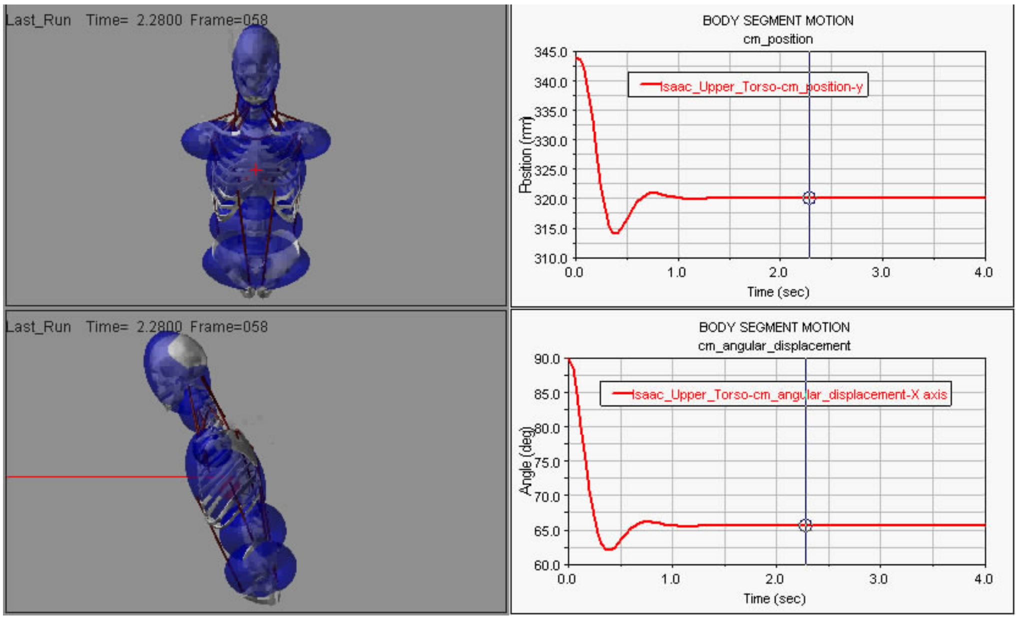

Figure 3.3 Default model under forward force on the thoracic region

3.3.2. Discretizing the default spine segments

To achieve a more detailed spine model, the improvement of the default spine model mentioned above is required and can be done in three following steps: refining the spine segments, reassigning muscle attachments and creating the spinal joints.

3.3.2.1. Refining the spine segments

From the base human model, the segments may be broken down into individual bones for greater model fidelity. Every bone in the human body is included in the generated skeletal model as a shell model. To discretize the spine region, the standard ellipsoidal segments representing the cervical (C1-C7), thoracic (T1-T12) and lumbar (L1-L5) vertebral groups are firstly removed. The individual vertebra segment is then given a name, CM location (designating the center of mass) and orientation (for the alignment of the inertia tensor to its reference axis system). The working grid of the model has to be established to allow more accurate estimation of CM location and orientation. Next, mass properties are estimated using ellipsoids. Figure 3.4 displays the refining process of the cervical region. Based on this procedure, the 24 vertebrae in the cervical, thoracic and lumbar regions are further discretized into individual ellipsoidal segments as can be seen in Figure 3.5.

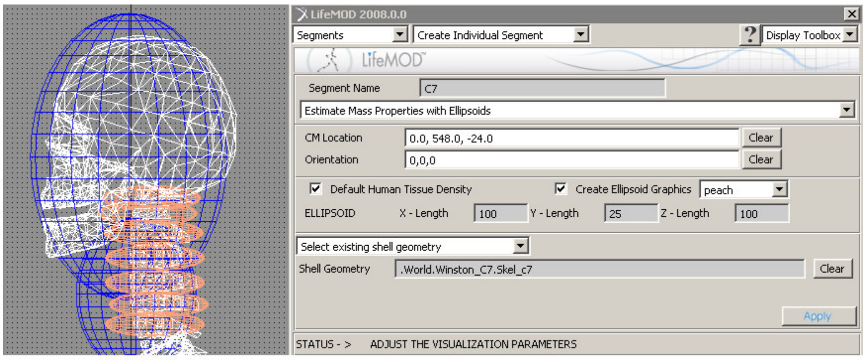

Segment Name: C7

Estimate Mass Properties with Ellipsoids

CM Location: 0.0, 548.0, -24.0

Orientation: 0,0,0

☑ Default Human Tissue Density

☑ Create Ellipsoid Graphics: peach

ELLIPSOID X - Length: 100 Y - Length: 25 Z - Length: 100

Select existing shell geometry

Shell Geometry: .World.Winston_C7.Skel_c7

STATUS - > ADJUST THE VISUALIZATION PARAMETERS

Figure 3.4 Refining process of the cervical spine

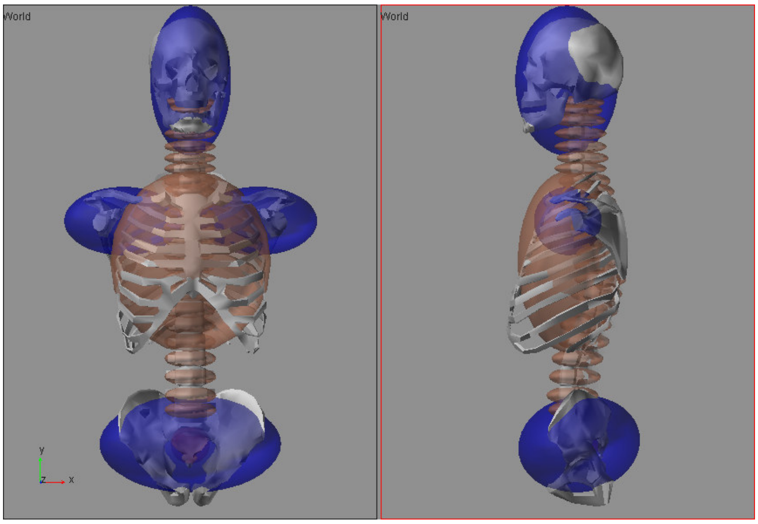

Figure 3.5 Front and side view of the complete discretized spine

3.3.2.2. Reassigning muscle attachments

The muscles are attached to the respective bones based on geometric landmarks on the bone graphics. With the new vertebra segments created, the muscle attachments to the original segment must be reassigned to be more specific to the newly created vertebra segments. The physical attachment locations will remain the same. Figure 3.6(a) and (b) shows the anterior and posterior view of several muscles in neck/trunk regions. Table 3.1 lists attachment locations of these muscles.

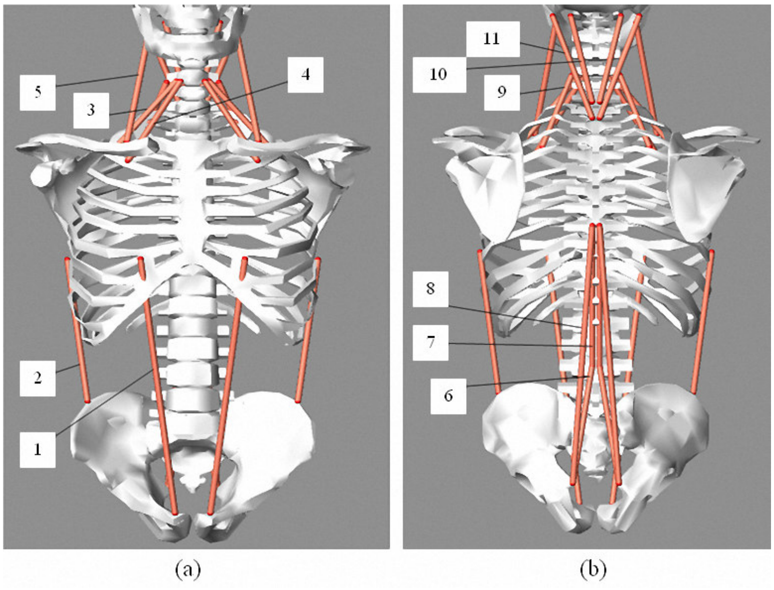

(a) (b)

Figure 3.6 Neck and trunk muscle set: (a) Anterior view; (b) Posterior view

Table 3.1 Attachment locations of neck and trunk muscle set

Index	Muscle	Attach proximal	Attach distal
1	Rectus abdominis	Sternum	Pelvis
2	Obliquus externus	Ribs	Pelvis
3	Scalenus medius	C5	Ribs
4	Scalenus anterior	C5	Ribs
5	Sternocleidomastiodeus	Head	Scapula
6	Erector spinae 2	L2	Pelvis
7	Erector spinae 3	T7	L2
8	Erector spinae 1	T7	Pelvis
9	Scalenus posterior	C5	Ribs
10	Splenius cervicis	Head	C7
11	Splenius capitis	Head	T1

3.3.2.3. Creating the spinal joints

It is necessary to create individual non-standard joints representing intervertebral discs between newly created vertebrae. The spinal joints are modeled as torsional spring forces and the passive 3 DOFs jointed action can be defined with user-specified stiffness, damping, angular limits and limit stiffness values. These joints are used in an inverse dynamics analysis to record the joint angulations while the model is being simulated. The properties of the joints can be found in the literature (Moroney et al., 1988, Panjabi et al., 1976, Schultz et al., 1979, Schultz and Ashton-Miller, 1991). The torsional stiffnesses of intervertebral discs and average segmental ranges of spinal motion are listed in Table 3.2 and Table 3.3, respectively. Figure 3.7 shows spinal joints representing intervertebral discs.

Table 3.2 Average torsional stiffness values for adult human spines (N.mm/deg) (Schultz and Ashton-Miller, 1991)

Spine level	Flexion/Extension	Lateral bending	Axial torsion
Occ-C1	40/20	90	60
C1-C2	60/50	90	70
C2-C7	400/700	700	1200
T1-T12	2700/3300	3000	2600
L1-L5	1400/2900	1600	6900
L5-S1	2100/3000	3600	4600

Table 3.3 Average segmental ranges of motion at each spine level (degree) (Schultz and Ashton-Miller, 1991)

Level	Flexion	Extension	Lateral bending	Torsion
Occ-C1	13	13	8	0
C1-C2	10	9	0	47
C2-C3	8	3	10	9
C3-C4	7	9	11	11
C4-C5	10	8	13	12
C5-C6	10	11	15	10
C6-C7	13	5	12	9
C7-T1	6	4	14	8
T1-T2	5	3	2	9
T2-T3	4	4	3	8
T3-T4	5	5	4	8
T4-T5	4	4	2	8
T5-T6	5	5	2	8
T6-T7	5	5	3	8
T7-T8	5	5	2	8
T8-T9	4	4	2	7
T9-T10	3	3	2	4
T10-T11	4	4	3	2
T11-T12	4	4	3	2
T12-L1	5	5	3	2
L1-L2	8	5	6	1
L2-L3	10	3	6	1
L3-L4	12	1	6	2
L4-L5	13	2	3	2
L5-S1	9	5	1	1

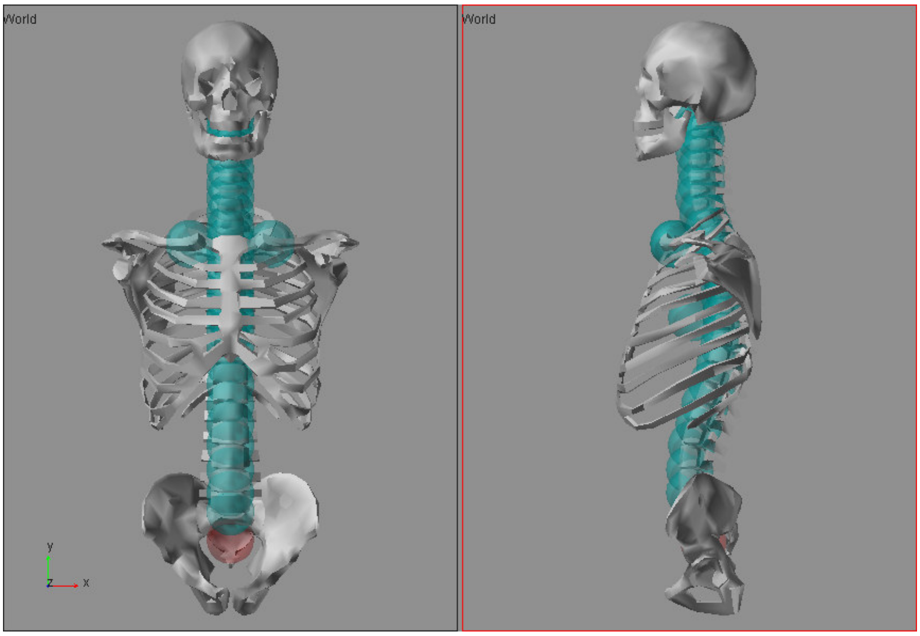

Figure 3.7 Front and side views of the spinal joints

After this step, simulations in second stage can be conducted to test the locomotion behavior of the discretized spine model. The boundary conditions are similar to the first simulation. However, different from the default one, it is possible to apply external forces to a specific vertebra of this discretized spine model in this stage. Figure 3.8 displays the dynamic properties of some vertebrae of the discretized spine model under forward force in the sagittal plane. In addition, comparing between the discretized and the default models can be observed in this figure. It is clear that the displacements of the discretized spine model are more flexible and realistic. Nevertheless, the discretized model seems to be quite loose because these displacements are excessive. The main reason is that the spine model has excluded all necessary ligaments connected between vertebrae. The ligaments play an important role in stabilizing the spine. Hence, building a detailed spine model will become more accurate if the influence of the ligaments is taken into account.

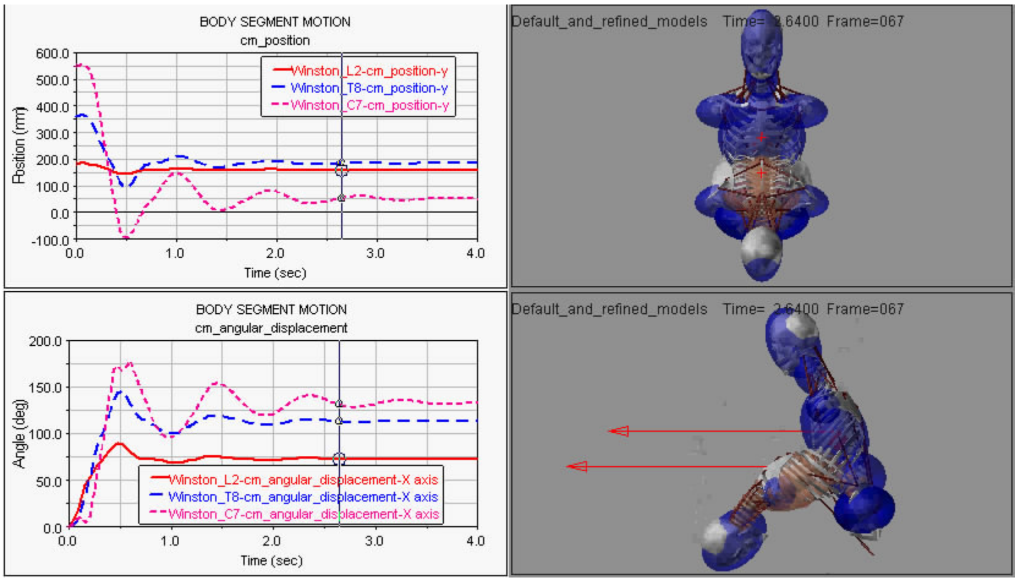

Figure 3.8 Comparison between default and refined models

3.3.3. Creating the ligamentous soft tissues

To stabilize the spine model, interspinous, flaval, anterior longitudinal, posterior longitudinal and capsule ligaments are created. Figure 3.9 displays various types of ligaments attached to vertebrae in the cervical spine region.

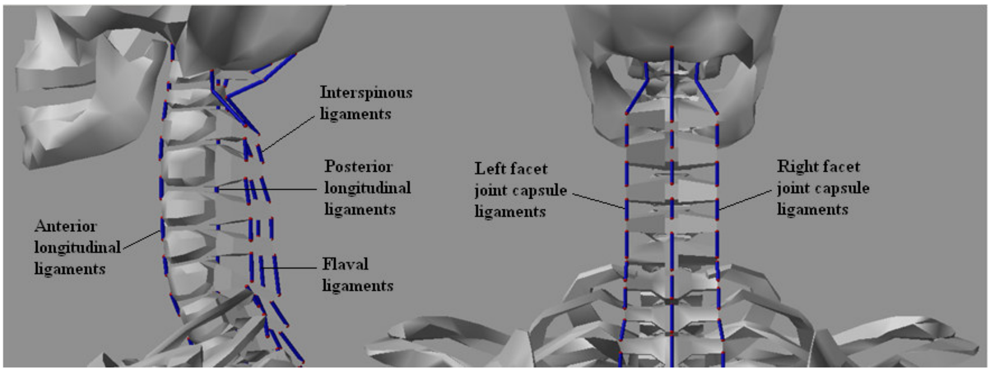

Figure 3.9 Various types of ligaments in the cervical spine

Figure 3.10 shows side and rear view of all ligaments of the whole spine running from skull down to the pelvis. These ligaments surrounding the spine will guide segmental motion and contribute to the intrinsic stability of the spine by limiting excessive motion. The stiffness of these ligaments is referenced from (Pintar et al., 1992, Yoganandan et al., 2001)

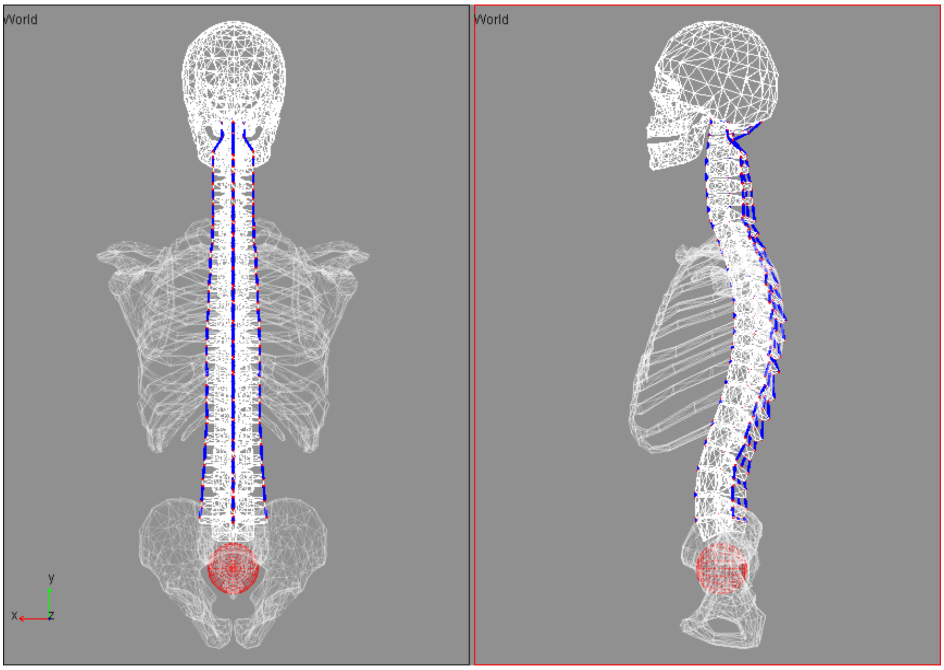

Figure 3.10 Back and side views of all ligaments attached to the spine model

After adding ligaments to the discretized spine model, simulations in the third stage will be executed to observe the effect of the ligaments on the locomotion of the spine. As can be seen in Figure 3.11, the displacements of the spine model without ligaments are more than those of the one with ligaments under forward forces in sagittal plane. It is obvious that the ligaments generate resultant forces to restrict excessive movement of the spine. However, when backward forces are applied on a certain vertebra, the spine is unable to achieve ultimate equilibrium as shown in Figure 3.12. It can only stabilizes in a short time, then lose the balance and twist aside. It is easily found that this instability is caused by lack of creating critical muscles in lumbar region of the spine. In addition to ligaments, lumbar muscles are vital for the spine not only in resisting flexion or extension motions but also in maintaining the stability. Therefore, it is required that all necessary lumbar muscles need to be created in the spine model in next stage.

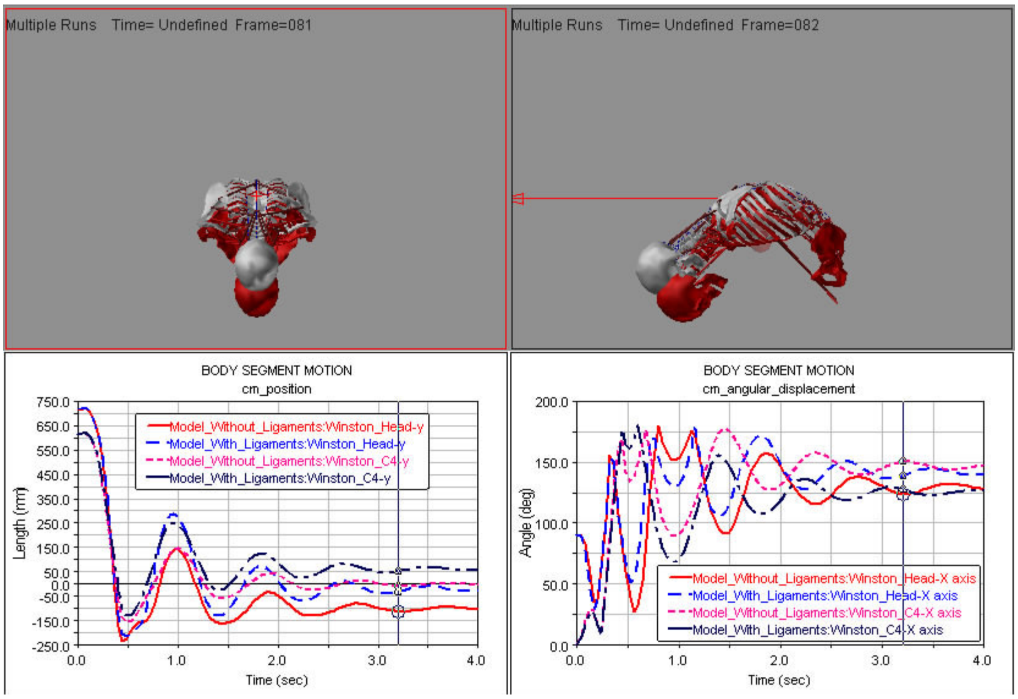

Figure 3.11 Comparison between with- and without-ligaments spine models

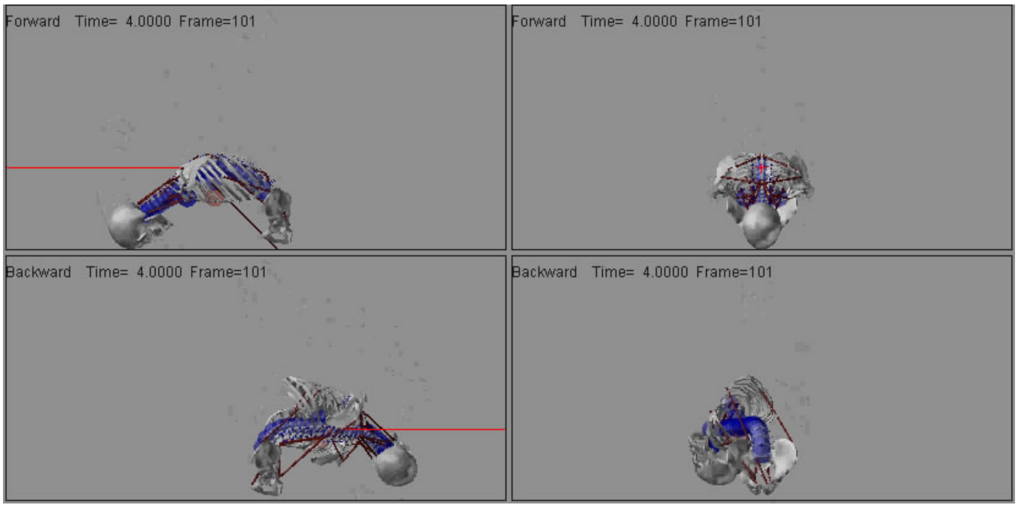

Figure 3.12 Instability of the spine model under backward force

3.3.4. Implementing lumbar muscles

Although LifeMOD provides many different types of muscles for users to build into a specific human body, there is still lack of some important muscles in the lumbar region of the spine such as multifidus, erector spinae, psoas major, quadratus lumbrorum, obliquus externus and obliquus internus. Skipping these muscles will lead to the instability of the spine as mentioned above. In this subsection, all these lumbar muscles will be described in detail to add into the spine model.

3.3.4.1. Multifidus muscle

The multifidus muscle is divided into 19 fascicles on each side according to descriptions by the group of Bogduk (Bogduk et al., 1992a, Macintosh and Bogduk, 1986). The multifidus can be modeled as three layers with the deepest layer having the shortest fibres and spanning one vertebra. The second layer spans over two vertebrae, while the third layer goes all the way from L1 and L2 to posterior superior iliac spine. The rather short span of the multifidus fascicles makes it possible to model them as line elements without via-points (Figure 3.13).

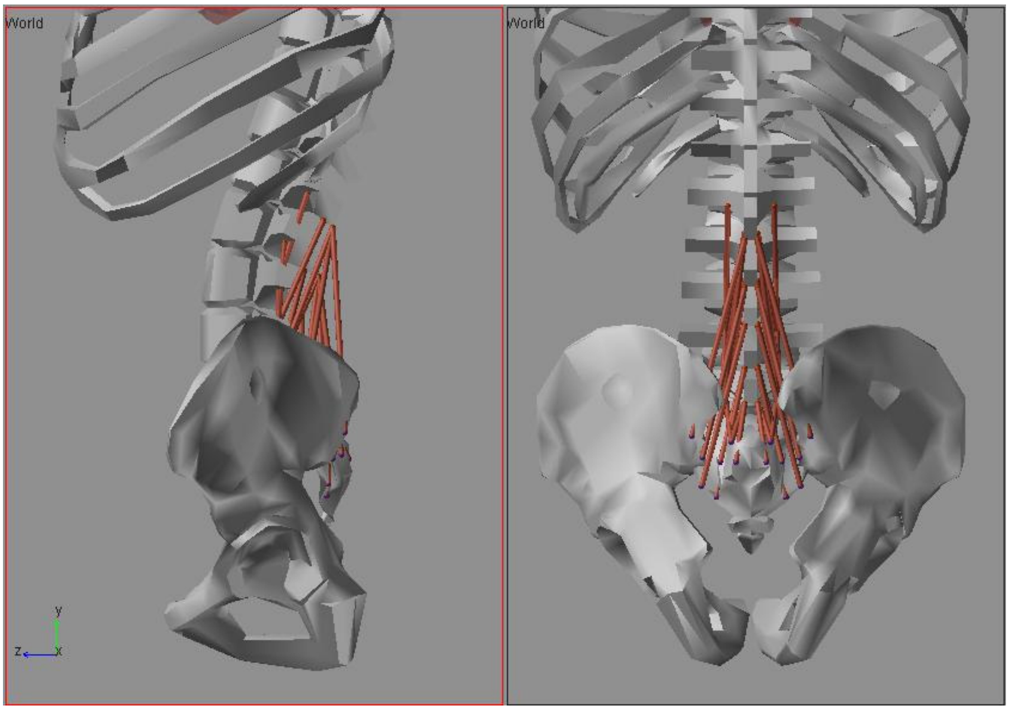

Figure 3.13 Side and back views of multifidus muscles in the spine model

3.3.4.2. Erector spinae muscle

According the descriptions by the group of Bogduk (Macintosh and Bogduk, 1987, 1991), there are four divisions of the erector spinae: longissimus thoracis pars lumborum, iliocostalis lumborum pars lumborum, longissimus thoracis pars thoracis and iliocostalis lumborum pars thoracis. The fascicles of the longissimus thoracis pars lumborum and iliocostalis lumborum pars lumborum originate from the transverse processes of the lumbar vertebrae and insert on the iliac crest close to the posterior superior iliac spine. The fascicles of the longissimus thoracis pars thoracis originate from the costae 1-12 close to the vertebrae and insert on the spinous process of L1 down to S4 and on the sacrum. The fascicles of the iliocostalis lumborum pars thoracis originate from the costae 5–12 and insert on the iliac crest. Since muscles of the two pars thoracis are automatically generated by LifeMOD, only muscles of the two pars lumborum need to be added to our model (Figure 3.14).

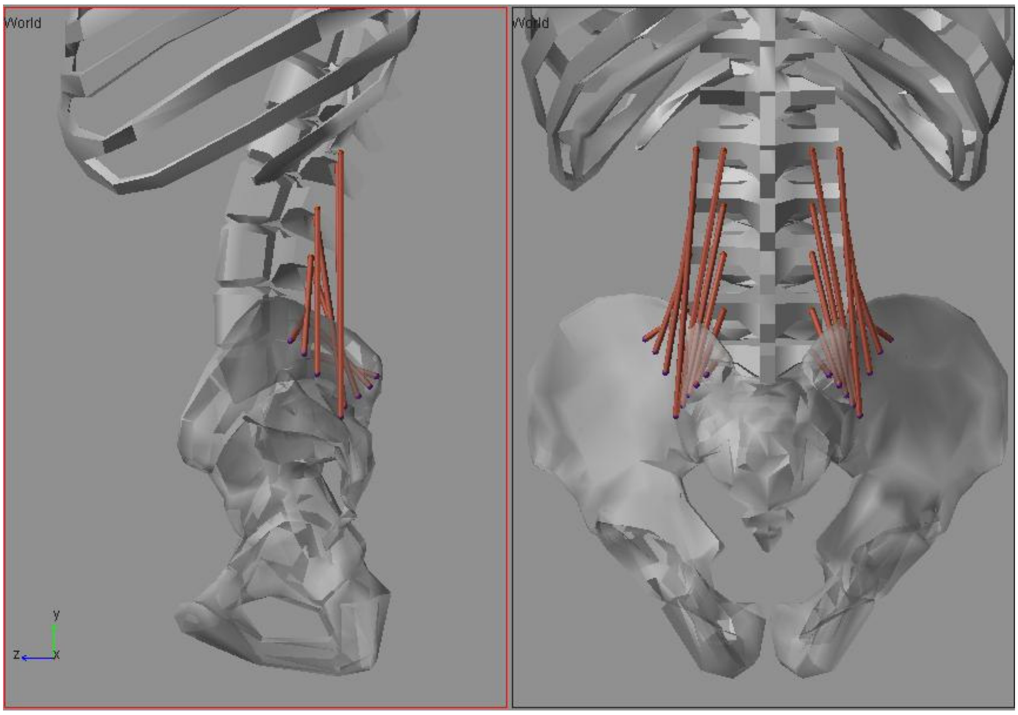

Figure 3.14 Erector spinae pars lumborum muscles in the spine model

3.3.4.3. Psoas major muscle

The psoas major is divided into 11 fascicles according to different literature sources (Andersson et al., 1995, Bogduk et al., 1992b, Penning, 2000). The fascicles originate in a systematic way from the lumbar vertebral bodies and T12 and insert into the lesser trochanter minor of the femur with a via-point on the pelvis (iliopubic eminence) as shown in Figure 3.15. Bogduk found that the psoas major had no substantial role as a flexor or extensor of the lumbar spine, but rather that the psoas major exerted large compression and shear loading on the lumbar joints. This implies that the moment arm for the flexion/extension direction is small and therefore the via-points for the path were chosen in such a way that the muscle path ran close to the centre of rotation in the sagittal plane.

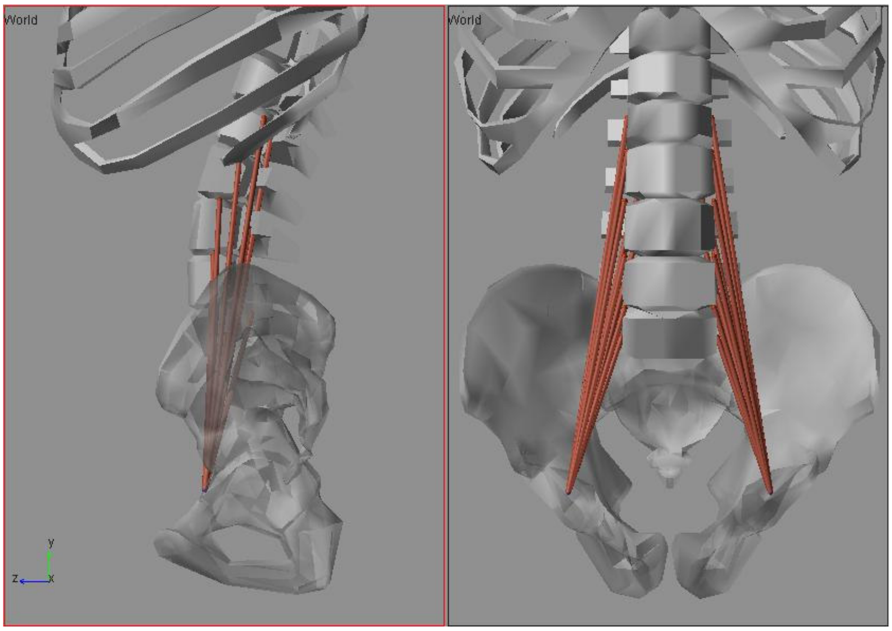

Figure 3.15 Side and front views of psoas major muscles in the spine model

3.3.4.4. Quadratus lumborum muscle

For modelling the quadratus lumborum, the description given by Stokes and Gardner-Morse (1999) was followed. They proposed to represent this muscle by five fascicles. The muscle originates from costa 12 and the anterior side of the spinous processes of the lumbar vertebrae and has in the model a common insertion on the iliac crest (Figure 3.16).

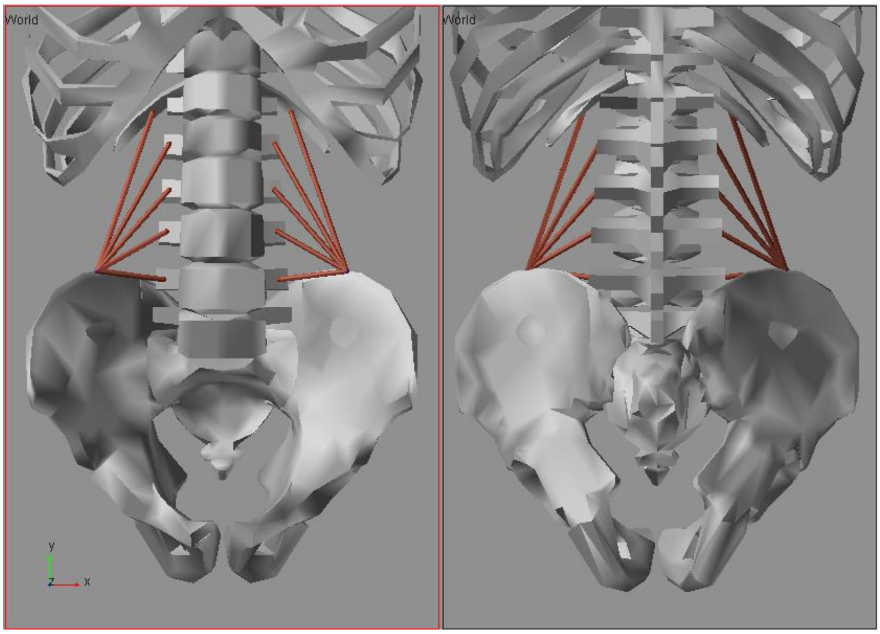

Figure 3.16 Anterior and posterior views of quadratus lumborum muscles

3.3.4.5. Abdominal muscles

Two abdominal muscles are included in the model: obliquus externus and obliquus internus. Modelling of these muscles requires the definition of an artificial segment with a zero mass and inertia. This artificial segment mimics the function of the rectus sheath on which the abdominal muscles can attach (Figure 3.17). The obliquus externus and internus are divided into 6 fascicles each (Stokes and Gardner-Morse, 1999). Two of the modeled fascicles of the obliquus externus run from the costae to the iliac crest on the pelvis, while the other four originate on the costae and insert into the artificial rectus sheath (Figure 3.18). Three of the modelled fascicles of the obliquus internus run from the costae to the iliac crest, while the other three originate from the iliac crest and insert into the artificial rectus sheath (Figure 3.19).

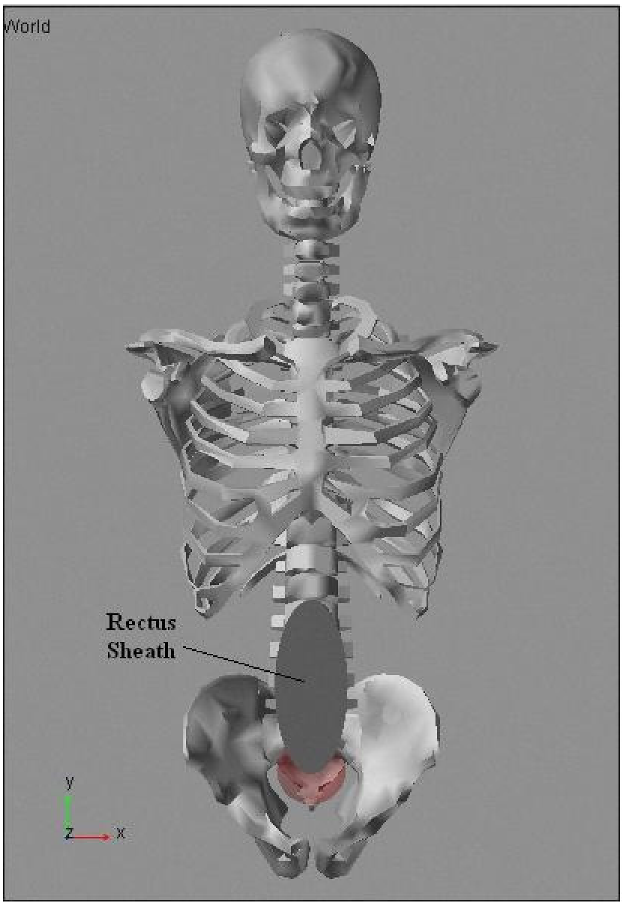

Figure 3.17 Artificial rectus sheath

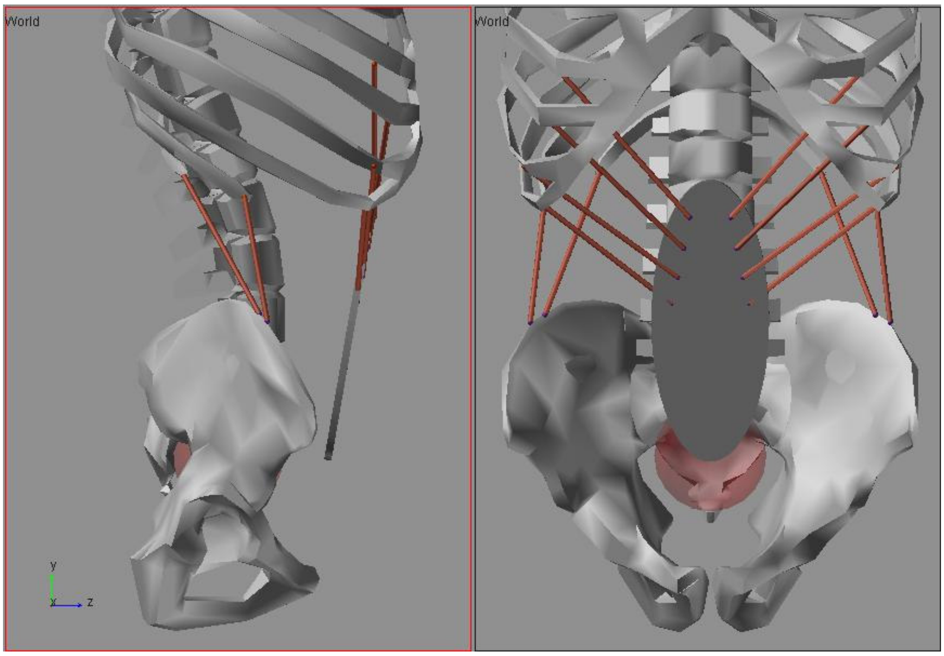

Figure 3.18 Side and front views of external oblique muscles

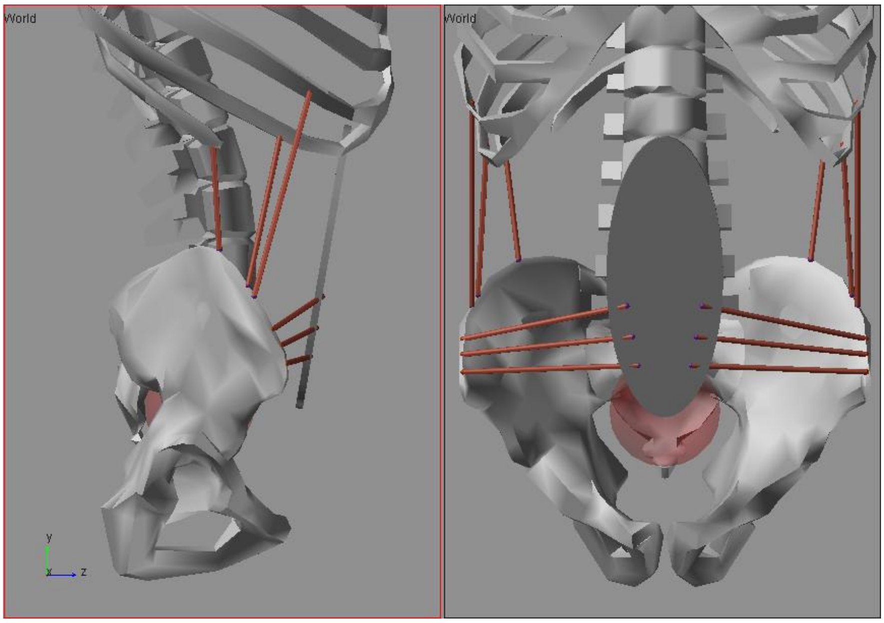

Figure 3.19 Side and front views of internal oblique muscles

In this fourth stage, after all lumbar muscles are implemented into the spine model, backward forces in sagittal plane are applied onto a specific vertebra and simulation results can be obtained. As can be seen in Figure 3.20, with the presence of necessary lumbar muscles, the spine finally achieves equilibrium. It is concluded that the detailed spine model at this stage can be stabilized in ultimate state under forward or backward forces in sagittal plane.

Nevertheless, the spine has not been achieved the stability in frontal plane under applying lateral forces in x direction. Figure 3.21 shows that many muscles are torn apart and the spine model lose its balance again. Although applied lateral forces are small, the resultant forces generated by lumbar muscles in this case are unable to maintain the balance of the spine. In other words, stabilizing the spine model in frontal plane is mainly affected by other components in human body rather than by lumbar muscles. There are many studies consistently shows that intra-abdominal pressure is key factor that mainly contributes to the stability of the lumbar spine besides muscles and ligaments (Arjmand and Shirazi-Adl, 2006, Cholewicki et al., 1999, Hodges et al., 2001). Thus, the instability of the spine model at this stage in this study is stem from the absence of intra-abdominal pressure. In next subsection, modeling process of intra-abdominal pressure will be presented clearly to solve the aforementioned instability.

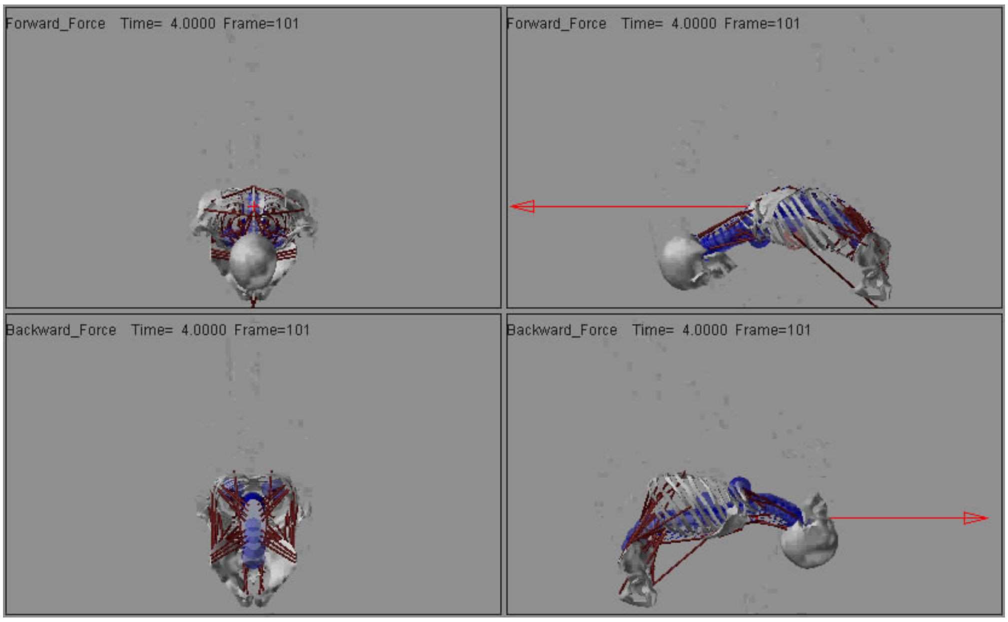

Figure 3.20 Stability of the spine model after adding lumbar muscles

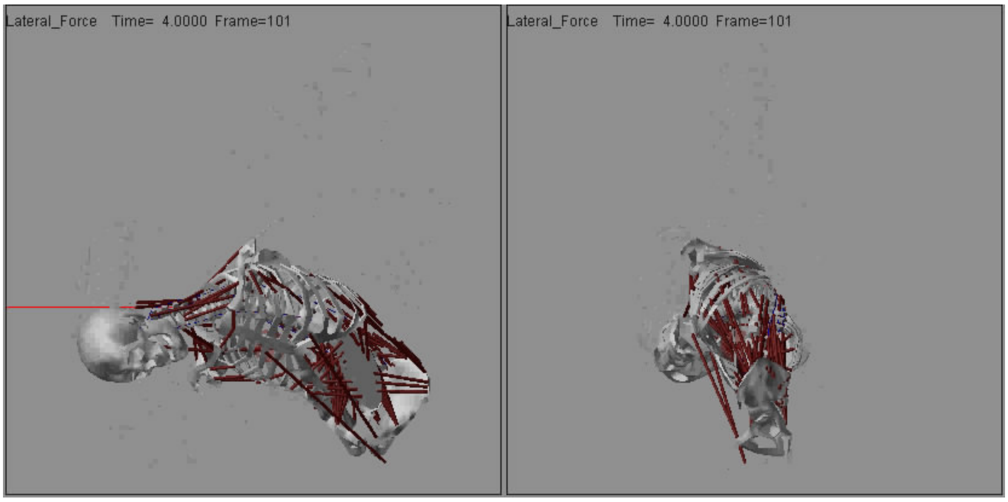

Figure 3.21 Some lumbar muscles injured under lateral forces

3.3.5. Adding intra-abdominal pressure

Since LifeMOD and ADAMS provide tools that only generate concentrated or distributed forces, it is not possible to implement directly intra-abdominal pressure into the spine model. To overcome this difficulty, a new approach to intra-abdominal pressure modeling is proposed and described thoroughly in this study. Initially, an equivalent spring structure able to mimic all mechanical properties of intra-abdominal pressure such as tension/compression, anterior/posterior shear, lateral shear, flexion/extension, lateral bending and torsion is created. After that, the translational and torsional stiffnesses of the string structure are determined. Finally, since adding this spring structure into the spine model is quite difficult, a bushing element that can specify all stiffness properties of the structure is used instead. In general, the process of modeling intra-abdominal pressure (IAP) includes the following steps: building a spring structure; finding abdominal volume and mean section area; computing stiffness values of the spring structure; and using an equivalent bushing element.

3.3.5.1. Building a spring structure

Since the spine is normally symmetric about the sagittal plane, the spring structure also needs to be symmetric. Figure 3.22 shows the spring structure used in this research. To be convenient for calculating parameters of the structure in subsequent steps, some assumptions are made: (a) springs in each direction have equal stiffness values; (b) the lengths of the structure in x and z directions are identical.

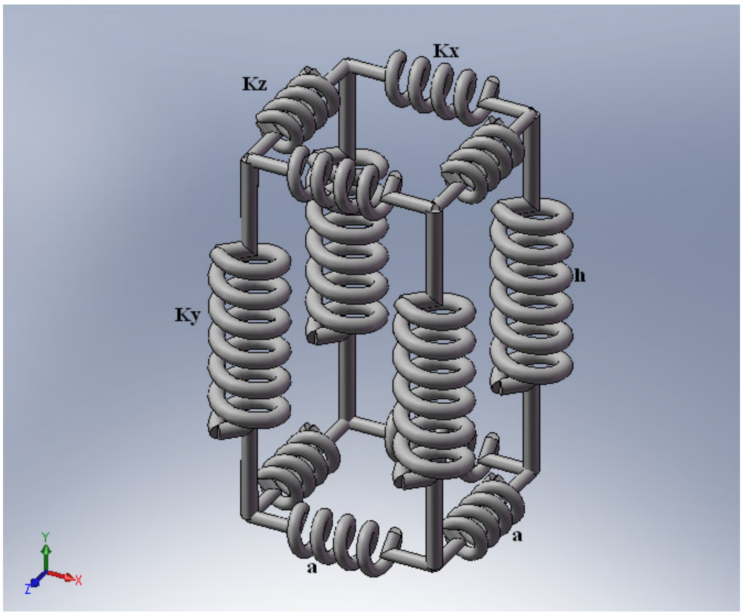

Figure 3.22 The spring structure used in this current research

3.3.5.2. Finding abdominal volume and mean section area

Abdominal volume obtained in this study is approximate value. This value is calculated based on the geometry of the ribcage and the lumbar spine. Five closed circuits symmetric about sagittal plane are drawn to measure perimeters of abdomen at different heights as shown in Figure 3.23. Each circuit will pass through the middle region of the body part of each lumbar vertebra and the rectus sheath. Then, the volume V_{L1L5} occupying from L1 to L5 can be determined using SolidWorks as shown in Figure 3.24. Similarly, surface area of each circuit S_i is also easily found in Figure 3.25.

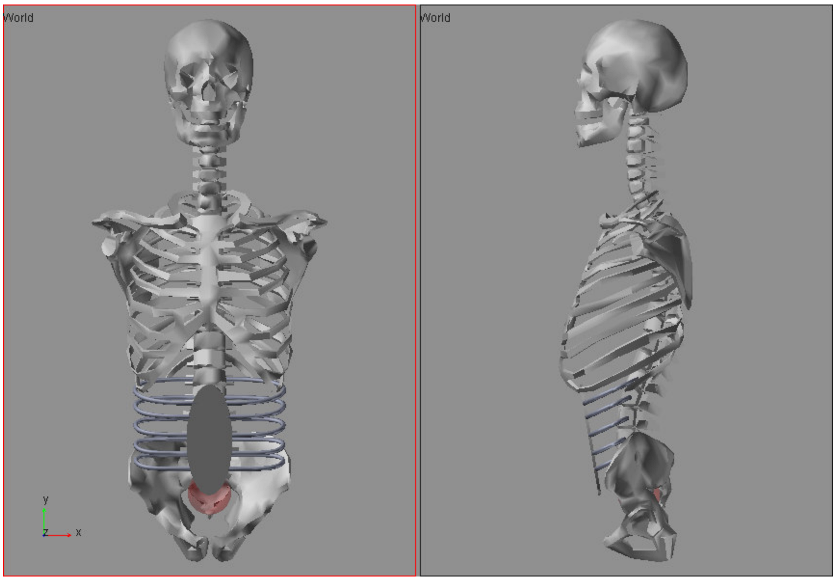

Figure 3.23 Approximate perimeters of abdomen at different heights

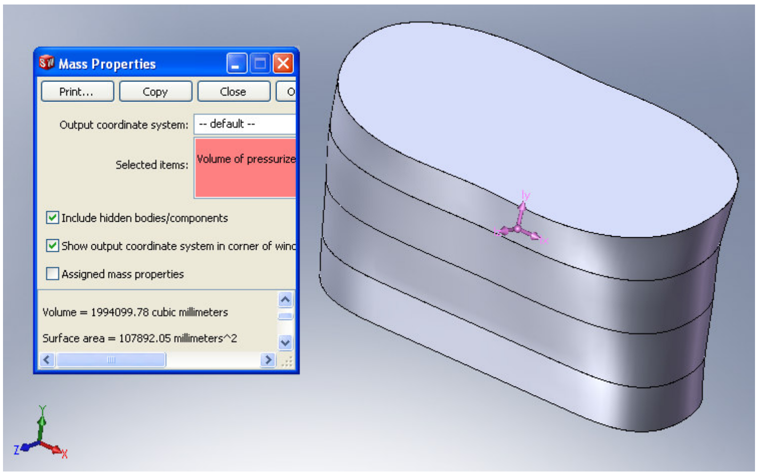

Output coordinate system: -- default --

Selected items: Volume of pressurize

☑ Include hidden bodies/components

☑ Show output coordinate system in corner of winc

☐ Assigned mass properties

Volume = 1994099.78 cubic millimeters

Surface area = 107892.05 millimeters^2

Figure 3.24 Approximate volume of the abdomen computed in SolidWorks

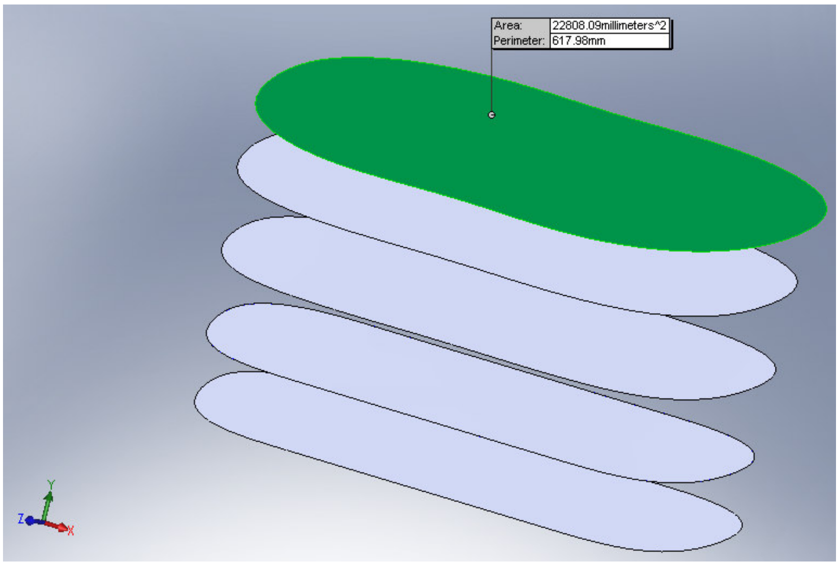

Area: 22808.09millimeters^2
Perimeter: 617.98mm

Figure 3.25 Surface area of each circuit determined in SolidWorks

Therefore, mean surface area S_{mean} can be obtained as follow:

$$S_{mean} = \frac{\sum_{n} S_i}{n} \tag{3.1}$$

where n is number of closed circuits.

3.3.5.3. Computing stiffness values of the spring structure

The height of lumbar spine region h_{L1L5} is computed by the equation below:

$$h_{L1L5} = \frac{V_{L1L5}}{S_{mean}} \tag{3.2}$$

Since IAP is generated in the abdomen connecting the ribcage, the lumbar spine region and the pelvis together, the volumes occupying from L1 to the ribcage and from L5 to the pelvis need to be taken into account. Since the volumes at different heights in z direction of the spring structure are assumed to be equal, the height of the abdomen h is calculated as follow:

$$h = \frac{3}{2} h_{L1L5} \tag{3.3}$$

The length of the spring structure a is determined as:

$$a = \sqrt{S_{mean}} \tag{3.4}$$

To compute the translational stiffnesses of the spring structure K_x, K_y, K_z, the minimum potential energy principle is used. This principle states that for a system to be in a stable equilibrium, its potential energy must be at a relative minimum. In the spring structure mentioned above, the potential energy V is taken to be the elastic energy stored in translational springs $V_{springs}$ minus the work generated by the IAP W_{IAP} and is given as:

$$V = V_{springs} - W_{IAP} \tag{3.5}$$

When the system is in equilibrium state, the potential energy V is zero and the Equation (3.5) can be expressed as:

$$V_{springs} = W_{IAP} \tag{3.6}$$

To calculate translational stiffnesses of the springs in y direction K_y, a certain surface perpendicular to these springs is chosen to be fixed. In other words, the lower surface connecting to the pelvis is static as shown in Figure 3.26.

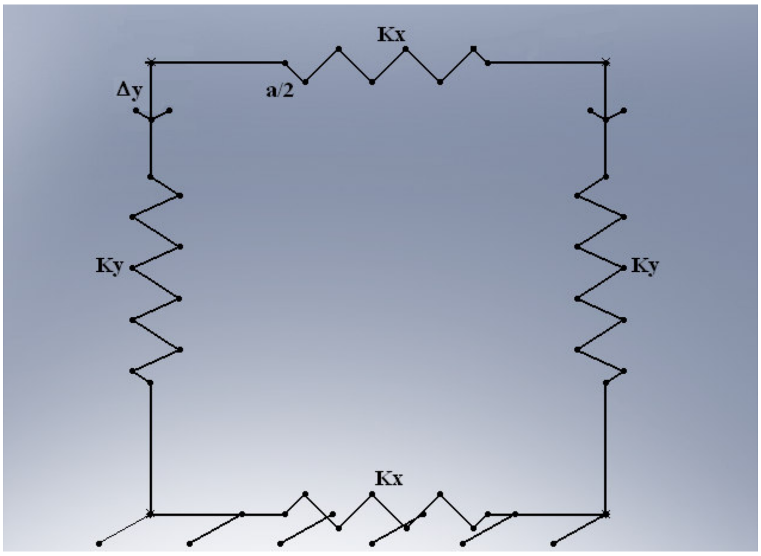

Figure 3.26 Front view of the spring structure under compression

Given a small translation Δy, Equation (3.6) is rewritten as:

$$\frac{1}{2}4k_y\Delta y^2 = Pa^2\Delta y \tag{3.7}$$

where P is normal intra-abdominal pressure of healthy adults.

Equation (3.7) can be simplified as:

$$k_y\Delta y = \frac{1}{2}Pa^2 \tag{3.8}$$

To make the spring structure act like the abdomen where IAP is always created, the value of Δy is chosen to be 1mm. This means that the spring structure will immediately generate the same resultant force as IAP does under such small displacement. In addition, normal intra-abdominal pressure of healthy adults can be easily found in the literature (Cobb et al., 2005). Hence, the translational stiffness K_y is computed as:

$$k_y = \frac{1}{2} P a^2 \tag{3.9}$$

Using the similar procedure, the translational stiffnesses K_x and K_z can be determined by the following equation:

$$k_x = k_z = \frac{1}{2} P a h \tag{3.10}$$

To calculate torsional stiffnesses of the spring structure, a small rotational angle of 1 degree about a specific axis is given. Figure 3.27 shows the frontal plane of the spring structure under counterclockwise moment M_z.

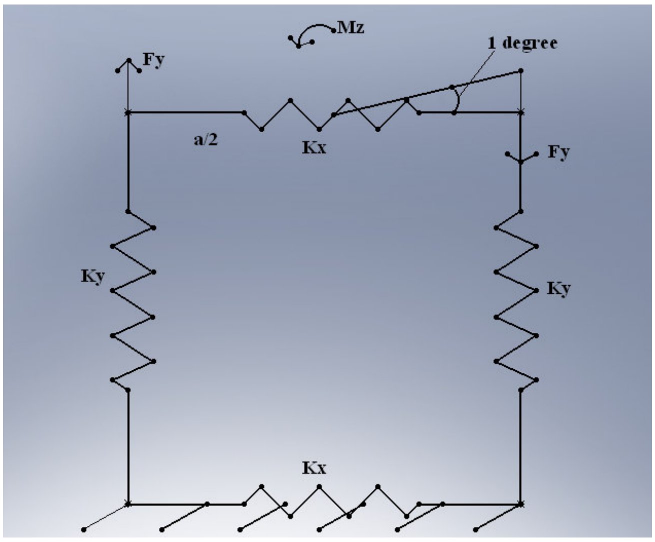

Figure 3.27 The spring structure under moment Mz

In this case, the lower surface attaching to the pelvis is fixed. Hence, the relative translation in y direction Δy is expressed as follow:

$$\Delta y = \frac{\pi a}{360} \tag{3.11}$$

And the moment M_z is given as:

$$M_z = 2\left(F_y \frac{a}{2} + F_y \frac{a}{2} \right) = 2 F_y a$$

Or: $M_z = 2k_y \Delta y a = 2k_y \frac{\pi a}{360} a = k_y \frac{\pi}{180} a^2$ (3.12)

Since the lengths in x and z directions are equal, we have:

$$M_x = M_z = k_y \frac{\pi}{180} a^2 \tag{3.13}$$

Similarly, the torsional stiffness M_y is determined as follow:

$$M_y = k_x \frac{\pi}{180} a^2 = k_z \frac{\pi}{180} a^2 \tag{3.14}$$

3.3.5.4. Using an equivalent bushing element

Although the spring structure is successfully built, inserting it into the spine model is really tedious. The reason is that locating coplanar attachment points of the spring structure on the ribs and on the pelvis is quite complicated. Instead, a bushing element is used in this case. Bushing element is a six-degrees-of-freedom joint that allows translational and rotational motions. Figure 3.28 shows adding the bushing element which replaces the spring structure into the spine model.

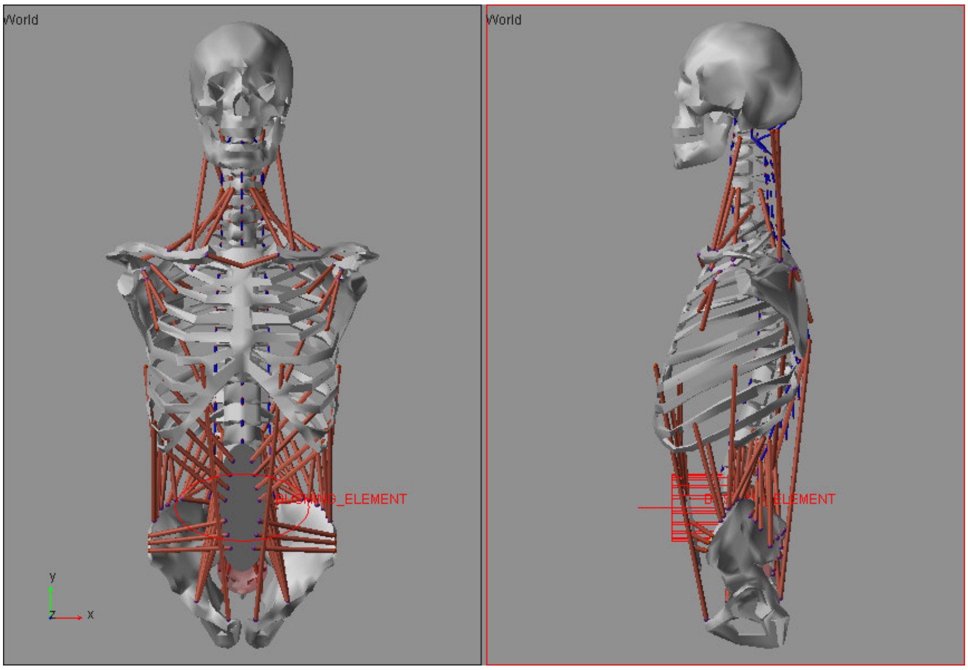

Figure 3.28 An equivalent bushing element replacing the spring structure

The translational and rotational stiffnesses of the bushing element are specified in the following expressions:

$$k_x' = k_z' = 4k_x = 4k_z \tag{3.15}$$

$$k_y' = 4k_y \tag{3.16}$$

$$M_x' = M_z' = k_y \frac{\pi}{180} a^2 \tag{3.17}$$

$$M_y' = k_x \frac{\pi}{180} a^2 = k_z \frac{\pi}{180} a^2 \tag{3.18}$$

For more detail information on computing translational and rotational stiffnesses mentioned above, please refer to Appendix C. After IAP was implemented into the spine model in this fifth stage, simulations were conducted to observe the effect of IAP on the stability performance of the spine when lateral forces with different magnitudes were applied onto the same vertebra. Figure 3.29 displays two simulation cases of the spine model under lateral forces of 800 N and 600 N.

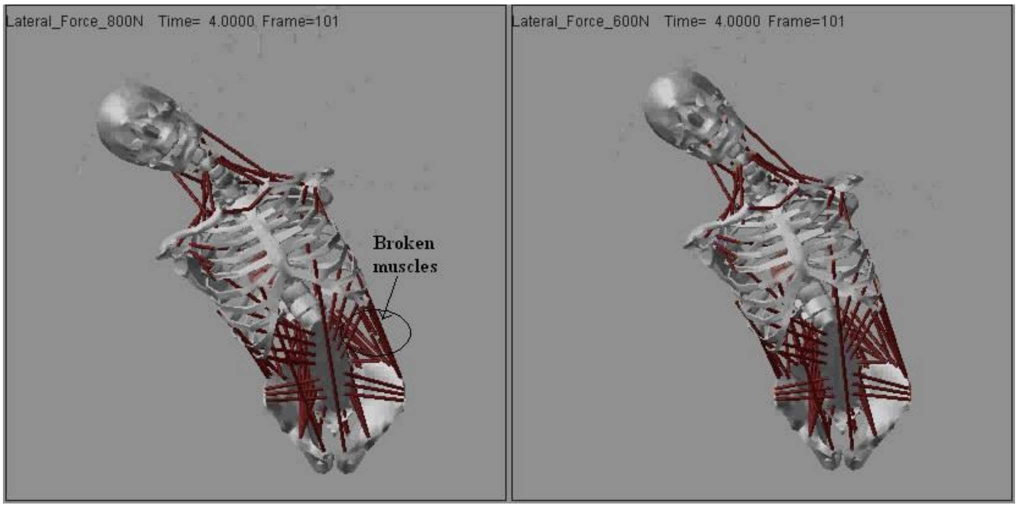

Figure 3.29 The spine model under lateral forces of 800N and 600N

As can be seen in Figure 3.29, with the presence of IAP, the spine in both cases achieves a stable state. However, compared to the latter case, some muscles in the former are still broken, resulting in injury in the lumbar region of human body. This is because the applied lateral force in the former is quite large and exceeds the force limit that muscles can sustain. Hence, maximum external forces applied on a certain vertebra of the spine in this research are limited to 600 N.

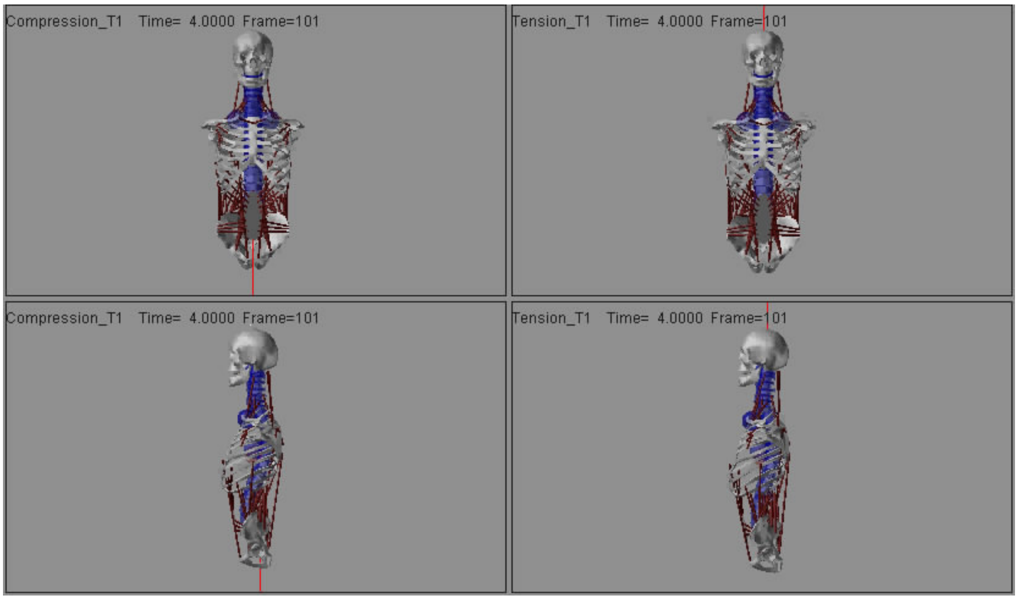

Figure 3.30 The spine model under compression and tension on vertebra T1

Besides lateral forces, external forces in y directions were also applied on some certain vertebrae to check the equilibrium state of the spine model. Figure 3.30 shows two cases of compressive and tensile forces acting on the same vertebra T1. In both cases, the spine model immediately obtains balance state and its movement is very small. Similar results are achieved when these forces are applied on other vertebrae. This implies that compressive or tensile forces mainly influence the stress, strain of vertebrae and intervertebral discs but not on the locomotion of the spine. Furthermore, Figure 3.31 displays the simulation of the spine model under external moment about the y axis. As can be seen in Figure 3.31, the spine model quickly stabilizes although the applied moment is large.

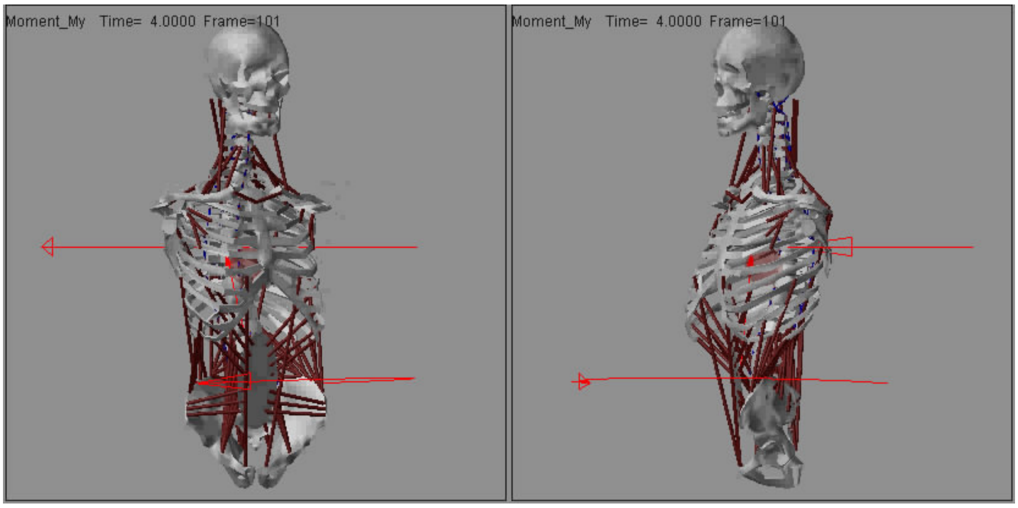

Figure 3.31 The spine model under moment My

Based on all simulations in the five developing stages presented above, it is concluded that a fully discretized musculo-skeletal multi-body spine model was successfully built. Under external forces and moments in different directions, this detailed spine model can finally achieve equilibrium state. However, it is important to validate the spine model before coming into use. In the next section, this validation will be described in detail.

3.4. Validation of the Detailed Spine Model

To validate the detailed spine model in this research, two approaches are used and presented as follows:

- With the same extension moment generated in upright position, axial and shear forces in the L5-S1 disc calculated in the model are compared to those obtained from Zee's model (2007) and experimental data (McGill and Norman, 1987).
- While a subject holds a crate of beer weighing 19.8 kg, the axial force of the L4-L5 disc is computed and compared with in-vivo intradiscal pressure measurements (Wilke et al., 2001).

In the first approach, a gradually increasing horizontal force was applied onto the vertebra T7 of the spine model from posterior to anterior in the sagittal plane as shown in Figure 3.32. From this force, axial and shear forces as well as the moment about the L5-S1 disc were calculated.

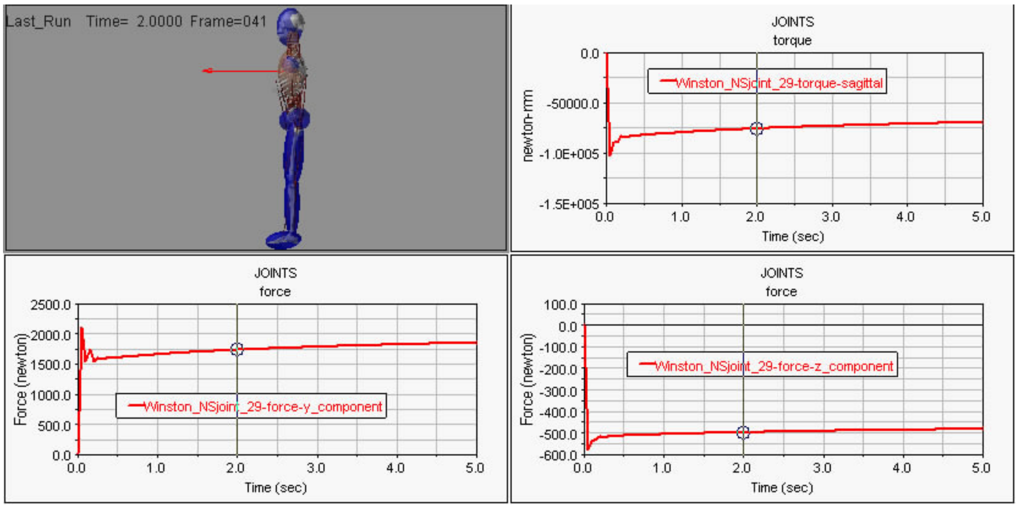

Figure 3.32 Self balance of the spine model under external force applied on T7

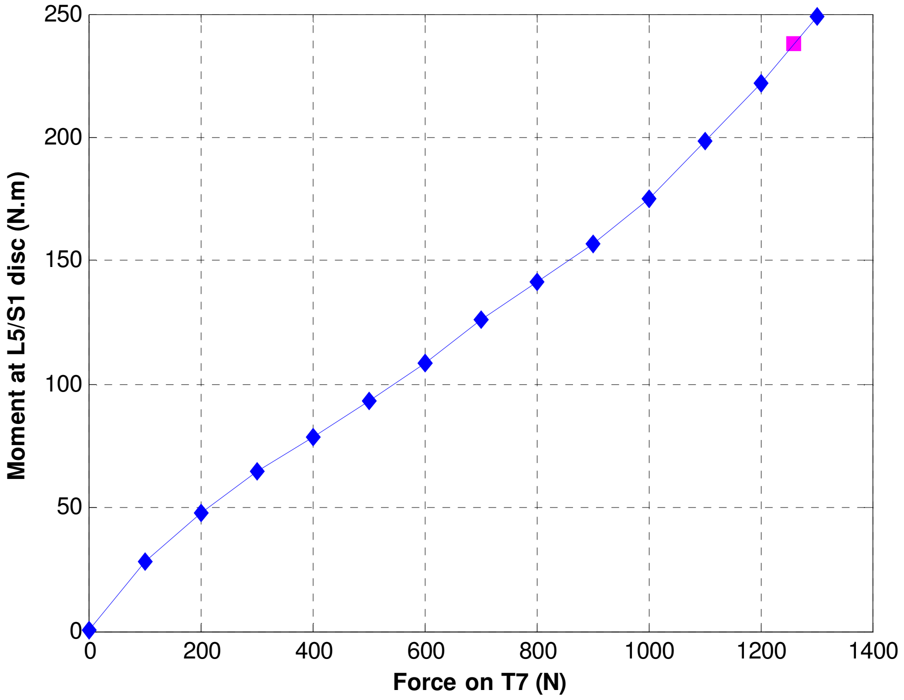

Figure 3.33 Sagittal moment at L5/S1 disc versus external forces on T7

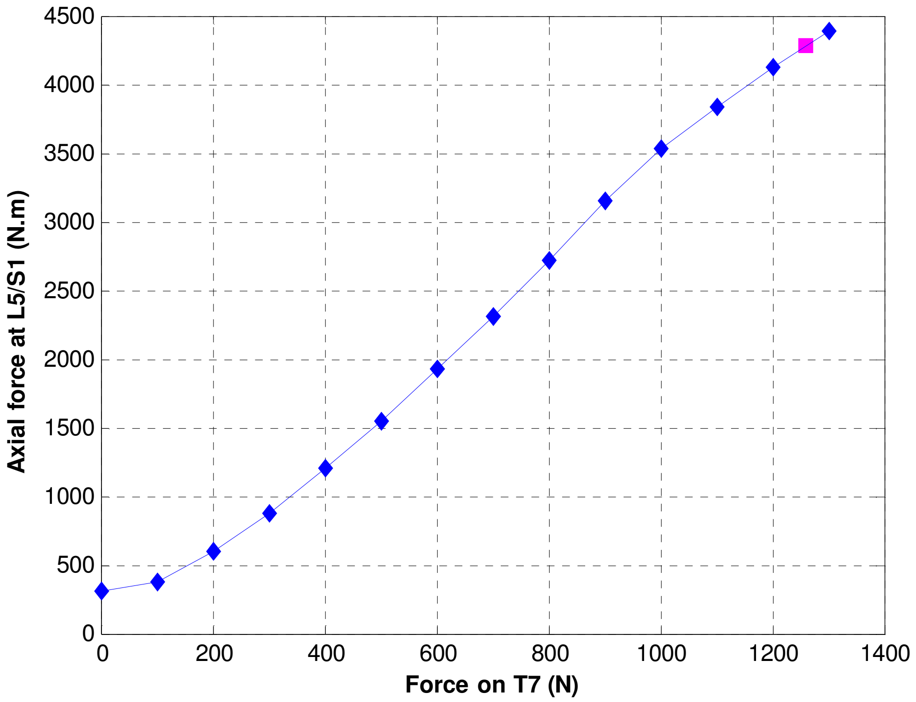

Figure 3.34 Axial force Fy versus external forces on T7

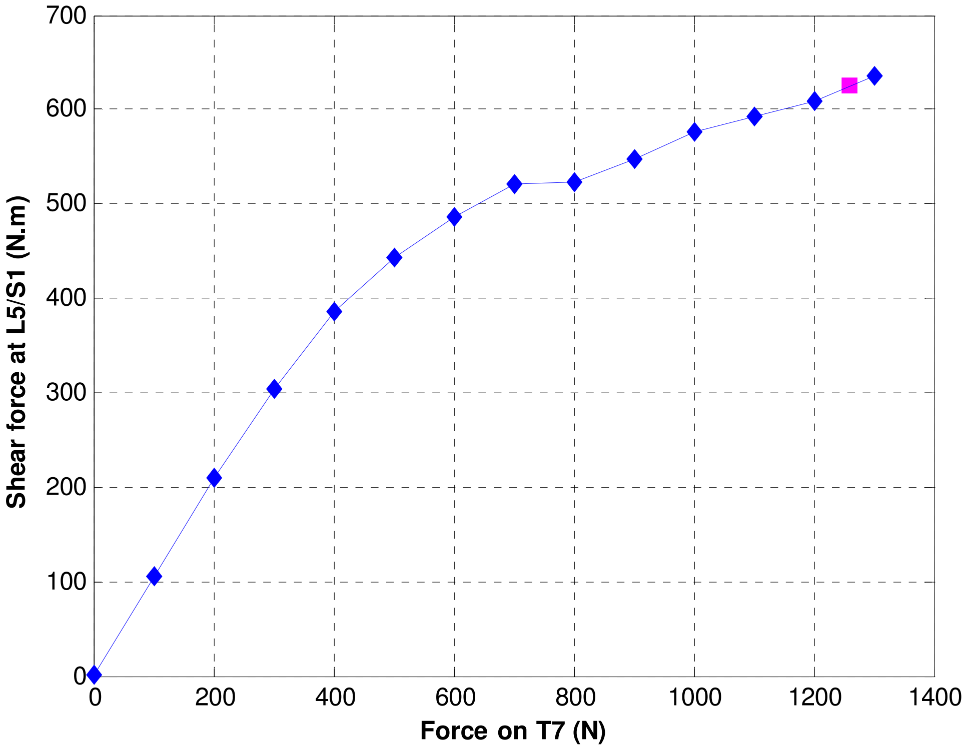

Figure 3.35 Shear force Fz versus external forces on T7

Zee’s model estimated an axial force of 4520 N and shear force of 639 N in the L5-S1 disc at a maximum extension moment of 238 Nm. Meanwhile, to obtain the same extension moment, the external force that needs to be applied in the present model is 1260 N as shown in Figure 3.33. Corresponding with this force, axial and shear forces obtained in the model were 4582 N and 625 N, respectively (Figure 3.34 and Figure 3.35). This is in accordance with the results presented by McGill et al. (1987) who found axial forces in the range of 3929–4688 N and shear forces up to 650 N.

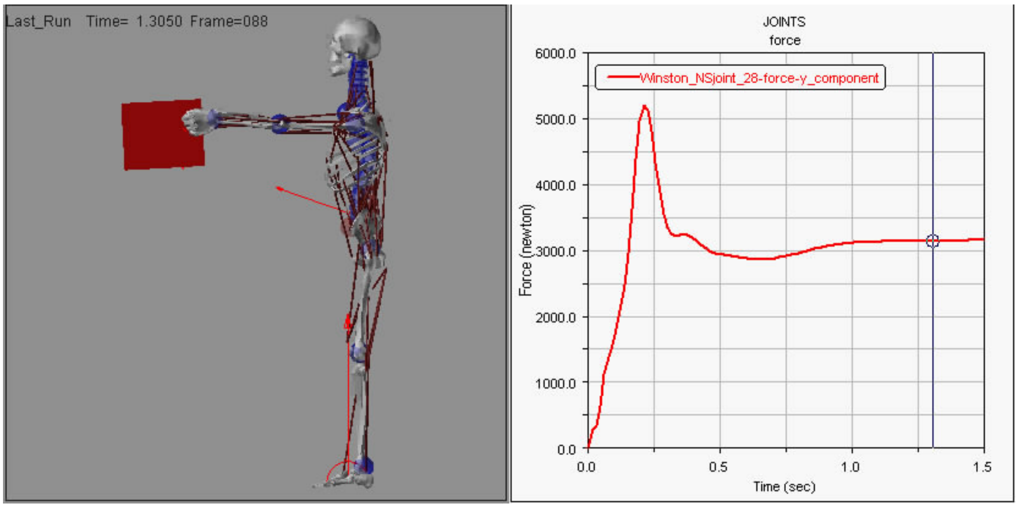

Figure 3.36 The model holding a crate of beer in equilibrium state

In the second approach, a comparison was made with *in-vivo* intradiscal pressure measurements of the L4–L5 disc as reported by Wilke et al. (2001). They measured a pressure of 1.8 MPa in the L4–L5 disc while the subject (body mass: 70 kg; body height: 1.74 m) was holding a full crate of beer (19.8 kg) 60 cm away from the chest. The disc area was 18 cm^2 and based on this the axial force was calculated to be 3240 N. The same situation was simulated using the spine model in this research. The estimated axial force was 3161.6 N as can be seen in Figure 3.36. This is a good match considering the fact that no attempt was made to scale the model to the subject in this study. Body mass and body height of the subject in this study are quite similar to the body mass and height used in the model.

Following the validation of this spine model, dynamic behaviour of the whole spine can be thoroughly investigated by applying external forces in three different directions onto the vertebrae. This investigation will be clearly presented in the subsequent section.

3.5. Dynamic Behaviour Simulation and Analysis of the Detailed Spine Model

The purpose in this stage is to analyze and describe the locomotion of the whole detailed spine model under varying external forces applied onto a certain vertebra in an arbitrary direction. Since the movement of the spine is complex and different when the applied external forces change from vertebra to vertebra, it is difficult to depict this movement. To overcome this difficulty, it is found that determining the relation between the spine motion and the external forces is critical. Since the arbitrary external forces can be divided into three component forces in x, y and z directions, the motion of the spine is a combination of its three types of motions corresponding to these three component forces. Moreover, it is noted that the motion of the whole spine is constituted by the concurrent connection of all vertebrae’s motions. Thus, it is important to define motion functions of all vertebrae under the external forces in x, y and z directions.

To do that, some constraints are imposed on the spine model. The pelvis is fixed in 3D space. Then, constant forces are applied on each specific vertebra in the thoracic region in each axis-aligned direction during simulation. The force magnitude is gradually increased with an equal increment in subsequent simulations. Corresponding to each value of force, dynamic characteristics of all vertebrae (e.g. translation, rotation) can be automatically obtained using the plots in LifeMOD as a reference. The dynamic properties are recorded after the spine model is stabilized. Based on these recorded dynamic properties, displacement-force relationships can be interpolated using the least-squares method and expressed in terms of polynomial functions.

3.5.1. Dynamic properties of the spine model under external forces in axis-aligned directions

Since external forces in y-axis direction nearly have no affect on the movement of the spine as presented in subsection 3.3.5, dynamic properties of the spine model are now dependent on external forces in z and x-axis directions. Initially, the locomotion of the spine in the sagittal plane is carefully examined when external forces in the z-axis direction are applied. Figure 3.37 shows forward force in sagittal plane acting on thoracic vertebra T1 in this research.

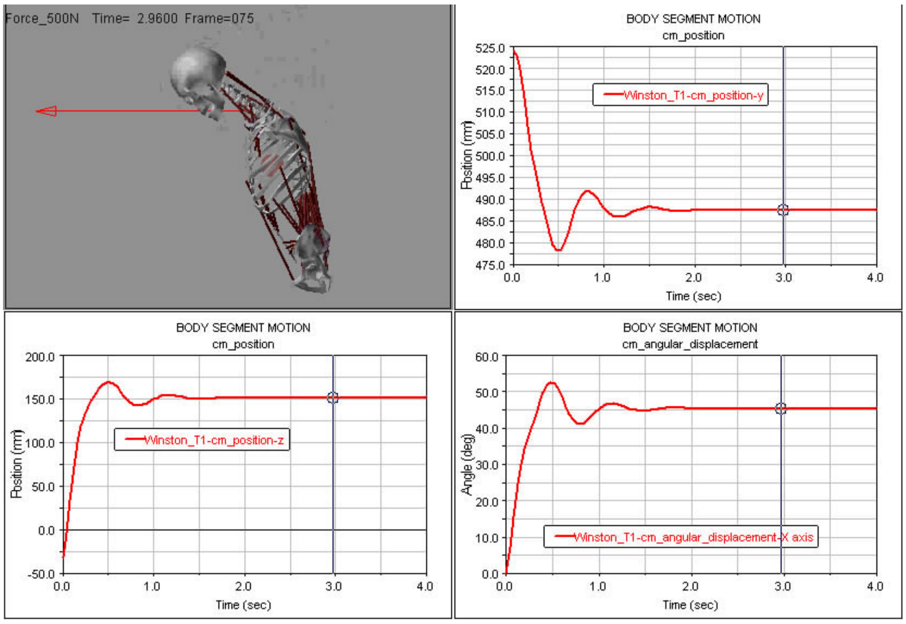

Figure 3.37 Three main dynamic properties obtained under forward force

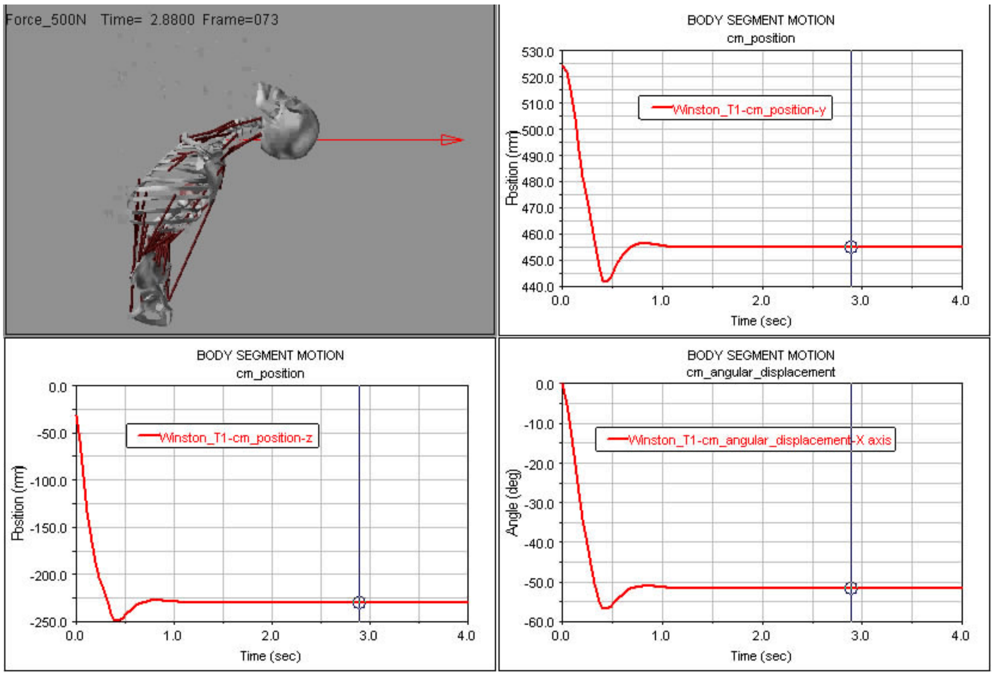

Figure 3.38 Three main dynamic properties obtained under backward force

As can be seen in Figure 3.37, three main dynamic properties obtained in the simulation are translations in y and z directions and rotation angle about x axis. This is because the spine achieves symmetric equilibrium about the sagittal plane after stabilizing. The same can be said with the case of backward forces (Figure 3.38).

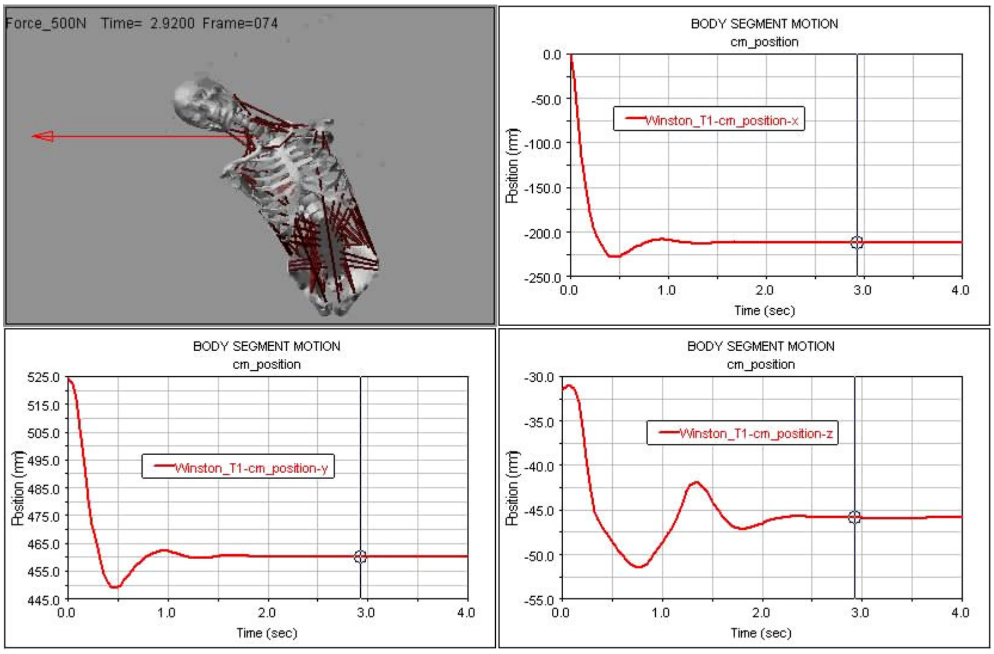

Figure 3.39 Three translational displacements obtained under lateral force

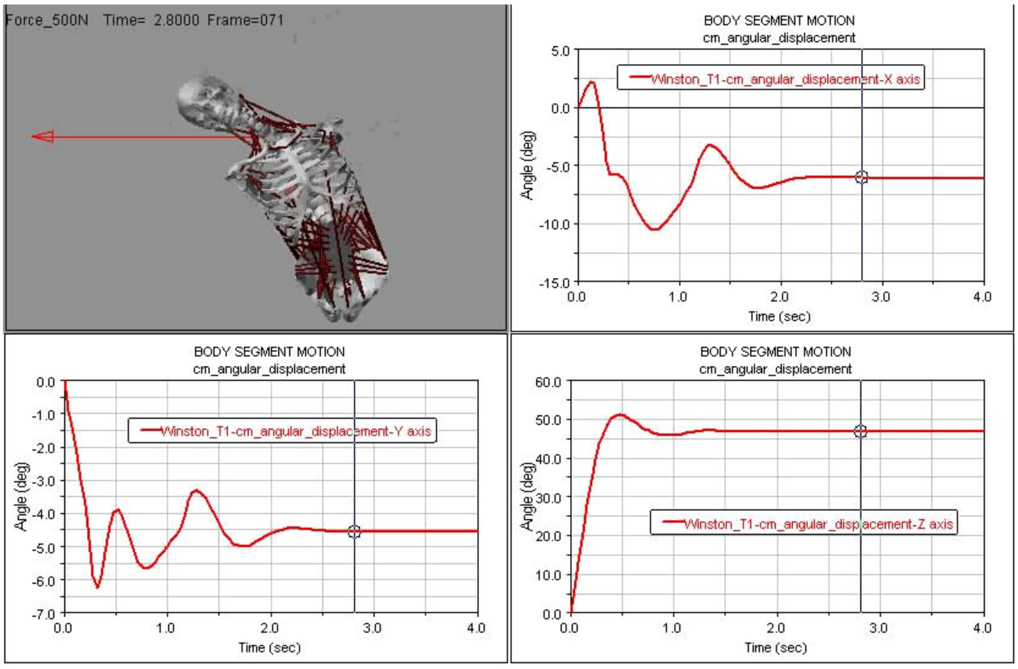

Figure 3.40 Three rotational displacements obtained under lateral force

Different from forces in z-axis direction, when a specific vertebra of the spine model is under external forces in x-axis direction, there are six dynamic properties such as three translations and three rotations obtained in this case as shown in Figure 3.39 and Figure 3.40. Since the spine model is symmetric about the sagittal plane, with the same vertebra under the same external forces but in opposite directions, spine configuration will be symmetric with that seen in Figure 3.39 and Figure 3.40.

3.5.2. Displacement-force relationship interpolation

After necessary dynamic properties of all vertebrae under external forces in z-and x-axis directions were obtained, the displacement-force relationships of the vertebrae can be interpolated. The force increment used in this research was 50 N. To ensure no injury happens to human body, maximum external forces in all directions were limited to 600 N as mentioned in subsection 3.3.5. Figure 3.41, Figure 3.42 and Figure 3.43 show the graphs of three dynamic properties of vertebra T1 versus forward forces in sagittal plane. Meanwhile, the graphs of six dynamic properties of vertebra T1 under lateral forces in the x-axis negative direction are shown Figure 3.44 to Figure 3.49. In these figures, each series of markers presents each dynamic property of one vertebra obtained in the simulations and the continuous line closely fit to that series is the corresponding interpolated line. This interpolated line is expressed in term of a polynomial function as seen in these figures.

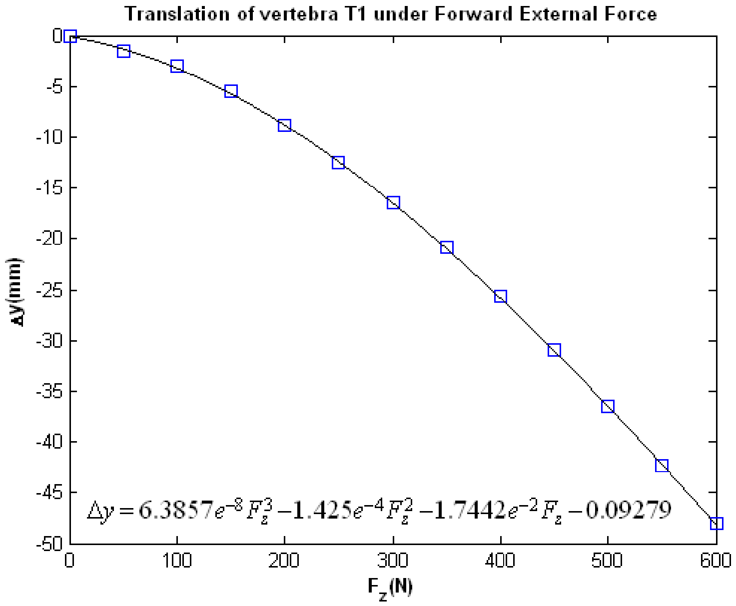

Figure 3.41 Relative translation Δy of T1 versus forward force

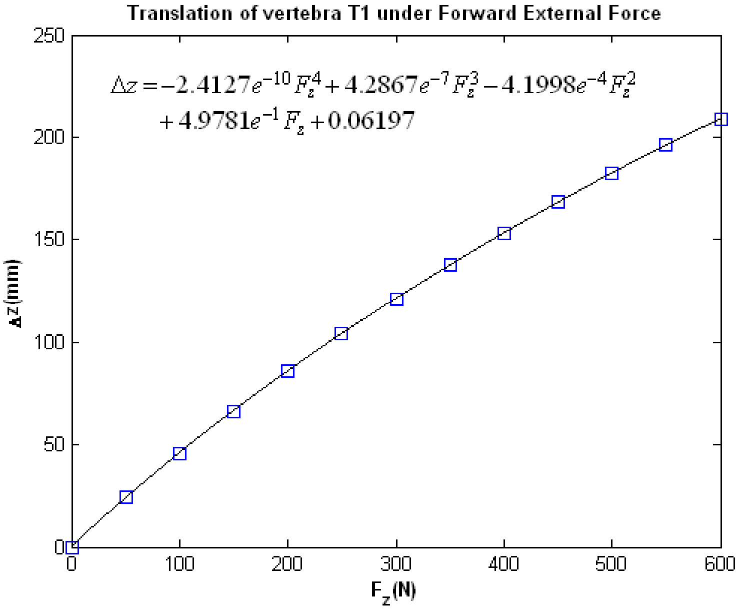

Figure 3.42 Relative translation Δz of T1 versus forward force

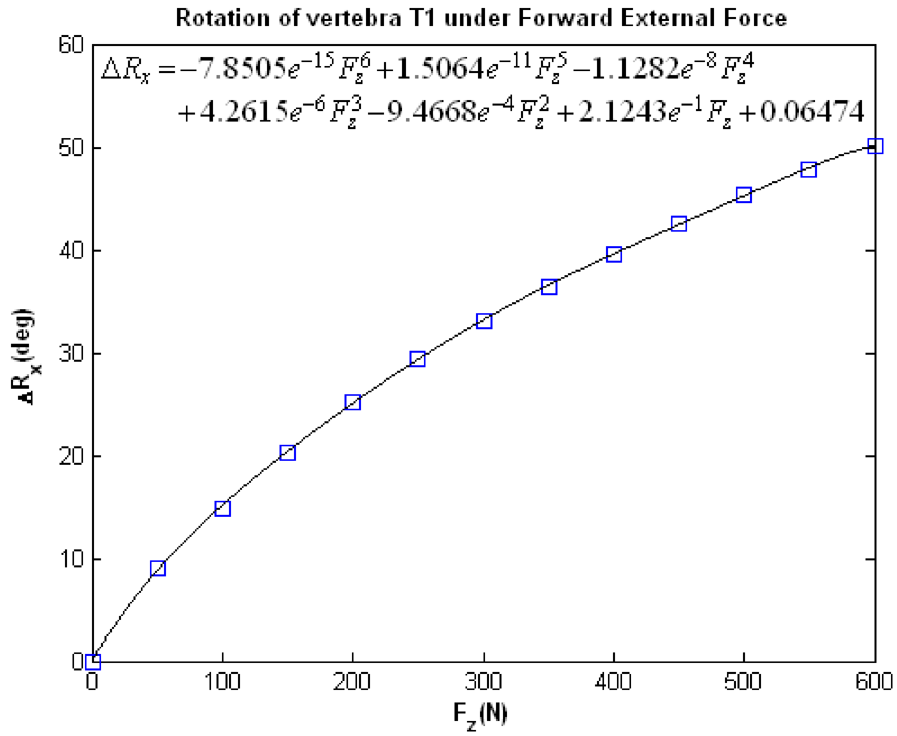

Figure 3.43 Relative rotation ΔR_x of T1 versus forward force

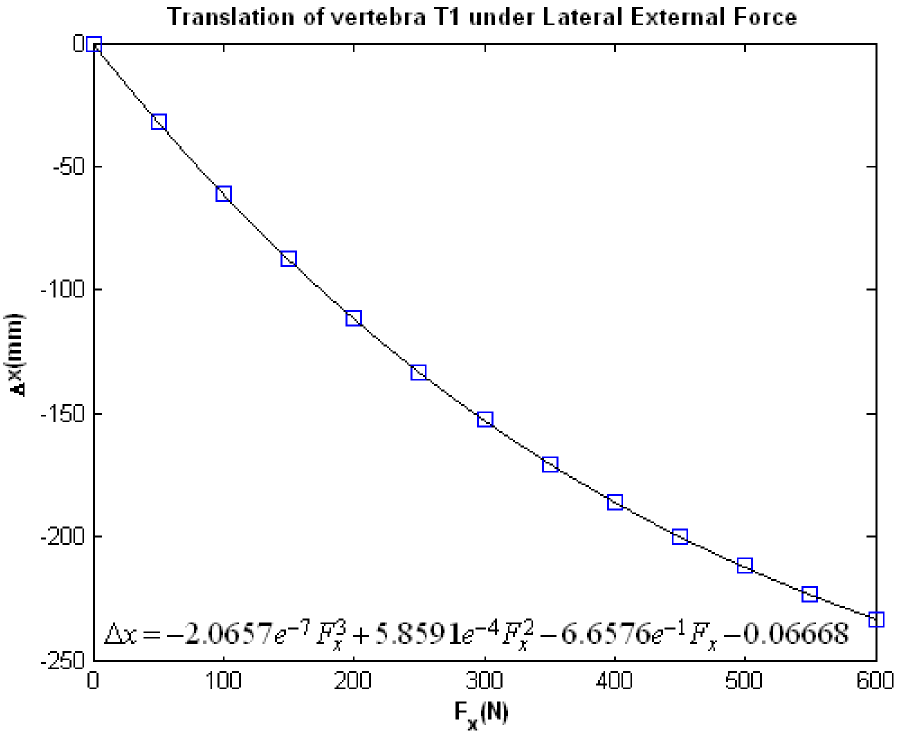

Figure 3.44 Relative translation Δx of T1 under lateral force

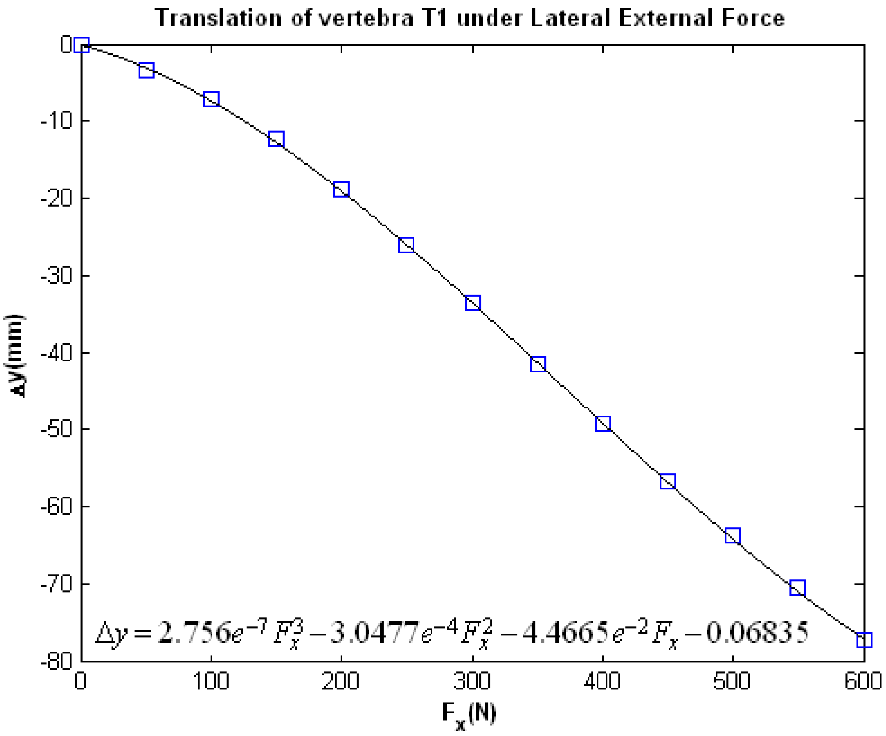

Figure 3.45 Relative translation Δy of T1 under lateral force

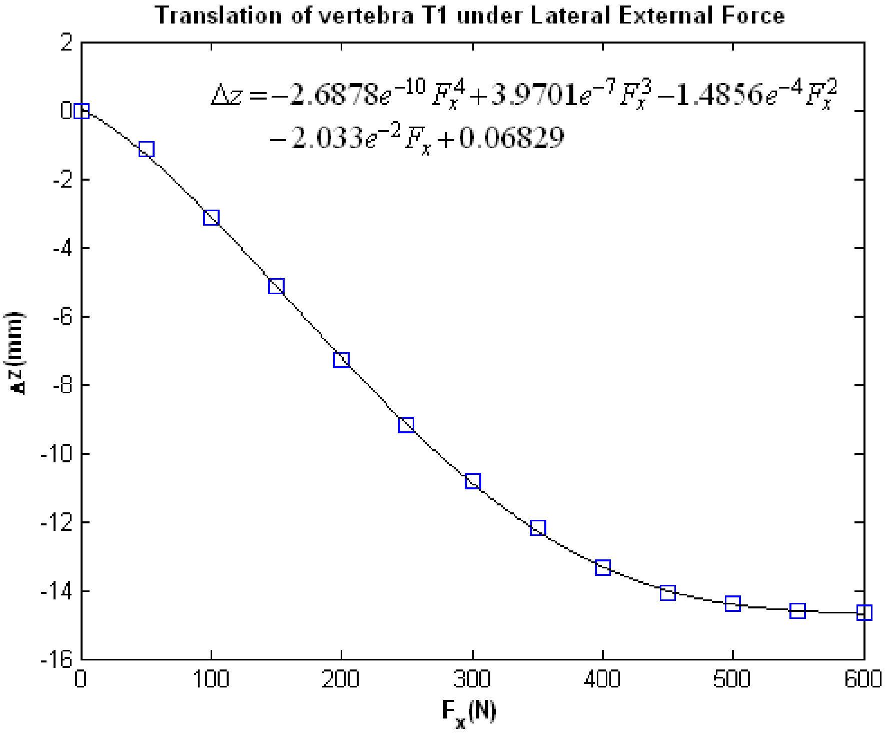

Figure 3.46 Relative translation Δz of T1 under lateral force

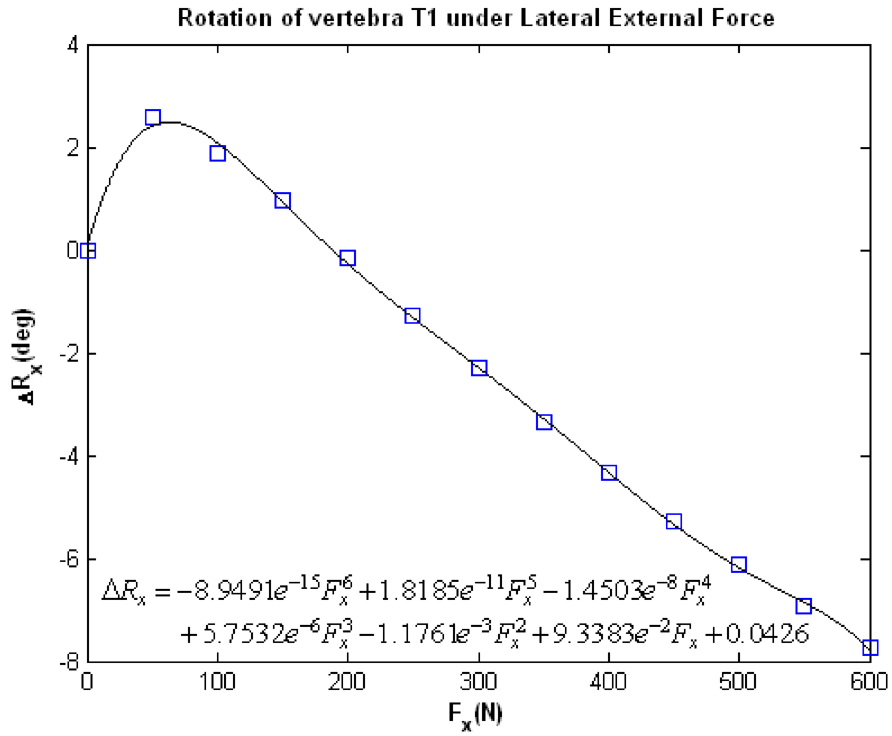

Figure 3.47 Relative rotation ΔR_x of T1 under lateral force

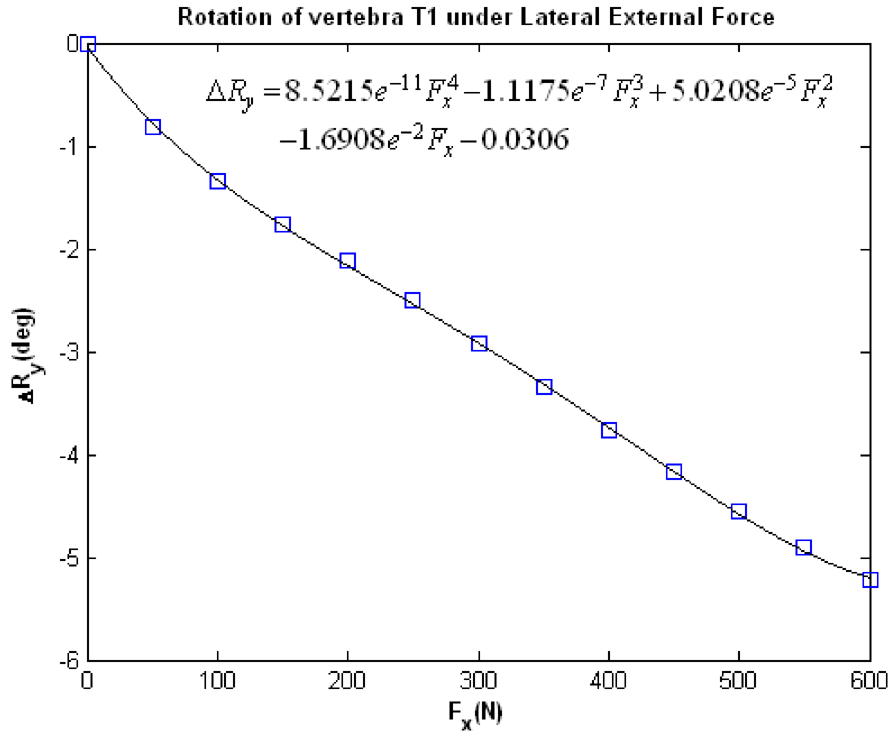

Figure 3.48 Relative rotation ΔR_y of T1 under lateral force

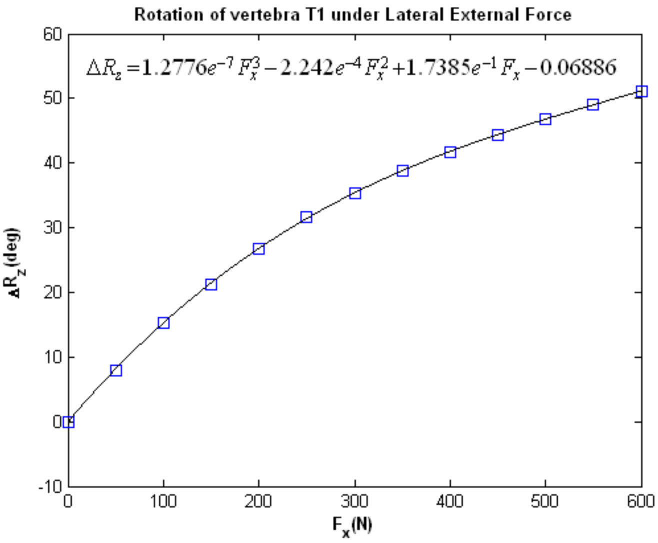

Figure 3.49 Relative rotation ΔR_z of T1 under lateral force

For each case of external forces acting on a specific vertebra in all directions, there are twelve sets of dynamic properties are determined. Each set of a dynamic property includes seventeen interpolated functions of all vertebrae from T1 to L5. Figure 3.50 to Figure 3.53 show two sets of dynamic properties under external forces applied from posterior to anterior onto vertebra T1. For further information on the graphs of all dynamic properties corresponding to cases of external forces acting on other vertebrae in all directions, please refer to Appendix D.

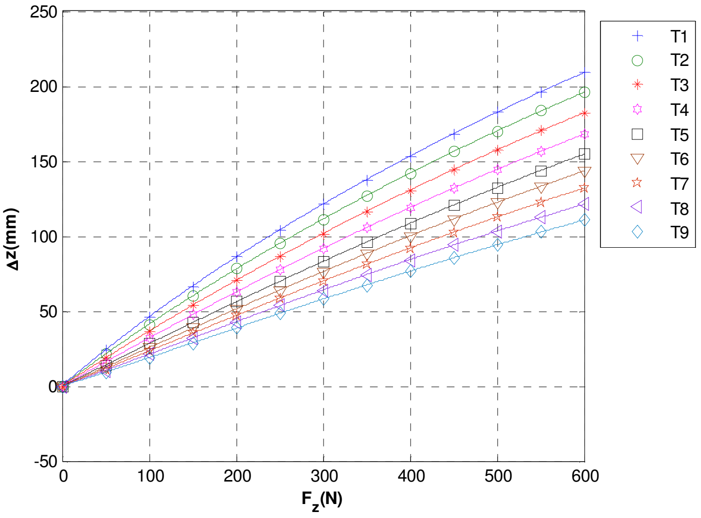

Figure 3.50 Translation Δz of vertebrae T1-T9 under forward force on T1

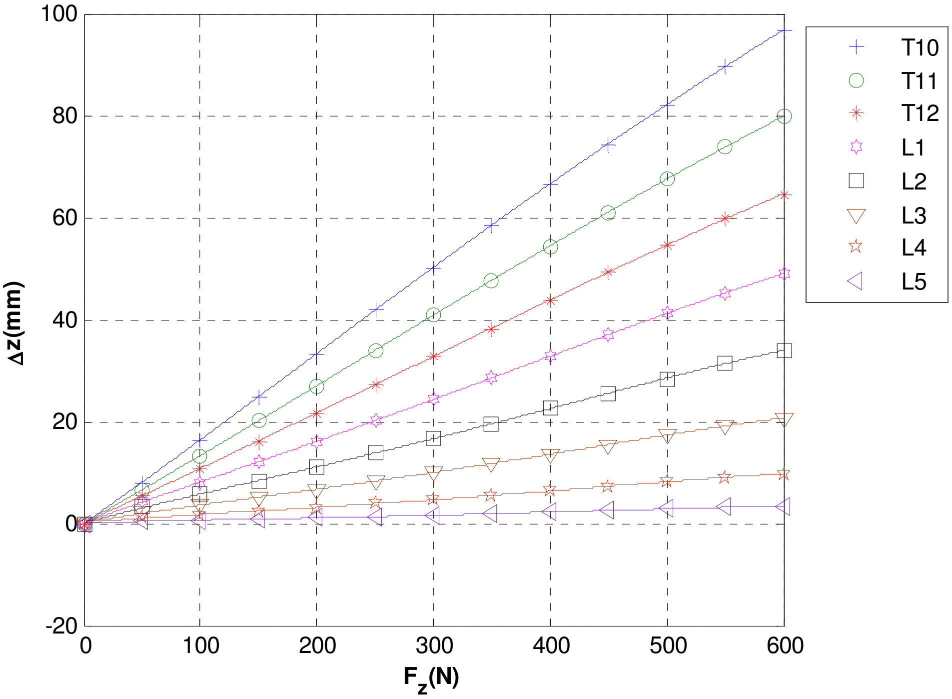

Figure 3.51 Translation Δz of vertebrae T10-L5 under forward force on T1

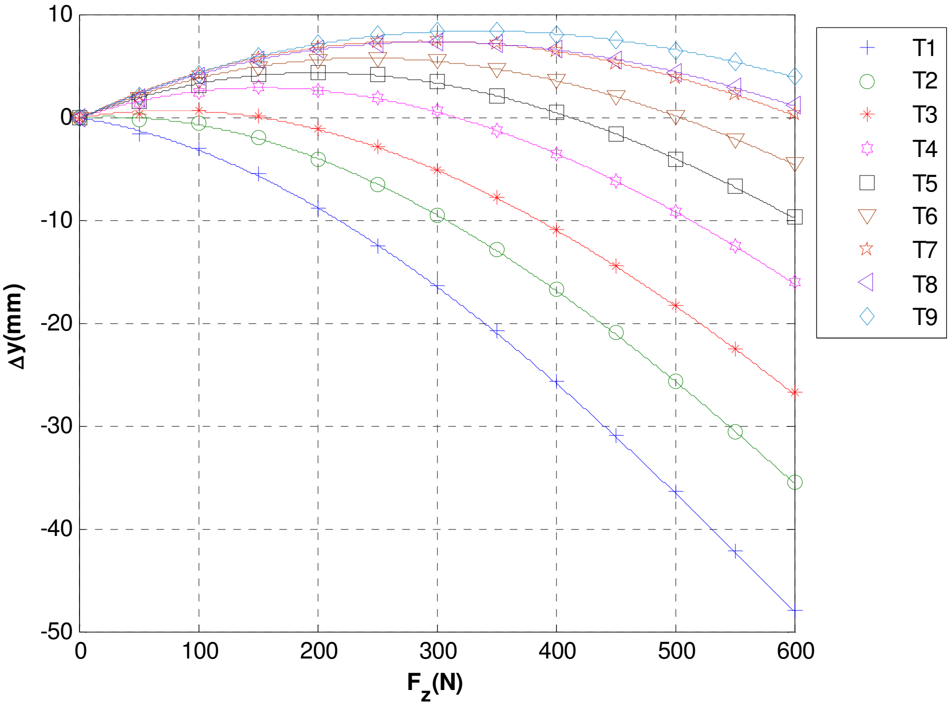

Figure 3.52 Translation Δy of vertebrae T1-T9 under forward force on T1

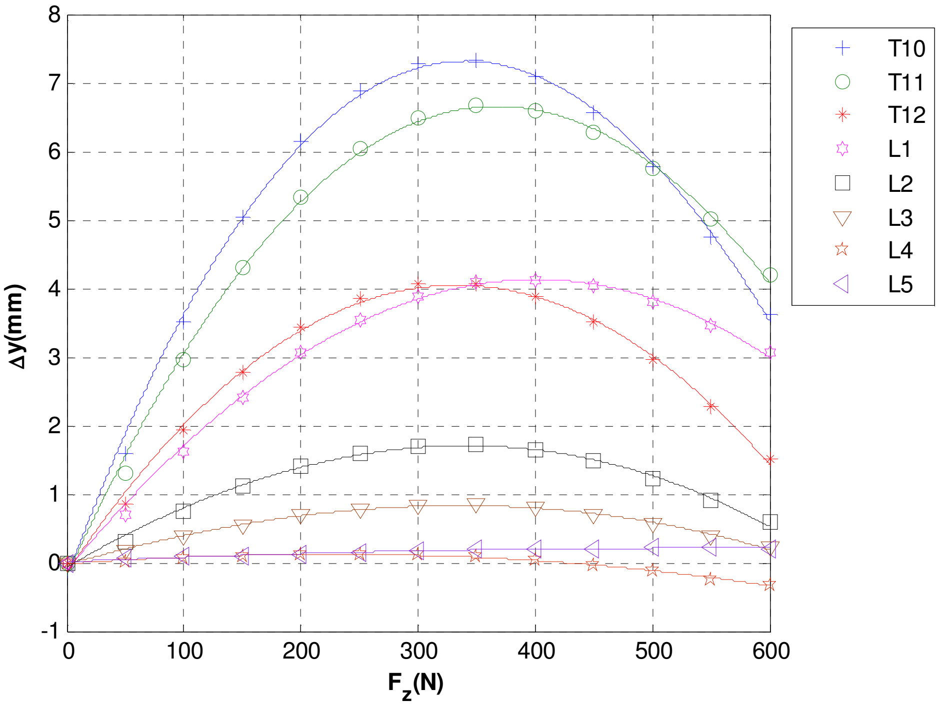

Figure 3.53 Translation Δy of vertebrae T10-L5 under forward force on T1

3.6. Summary

This chapter firstly introduced an overview of LifeMOD which helps users sufficiently understand basic functional principles, modeling methods and necessary skills to build a certain desire human body model in accordance with their own purposes. Secondly, the development process of an entirely discretized musculo-skeletal multi-body spine model in five stages was thoroughly presented. The ligaments, lumbar muscles and intra-abdominal pressure implemented into the spine model in each stage played an important role in stabilizing the spine under external forces in different axis-aligned directions. Thirdly, the validation of the detailed spine model was carefully conducted. As aforementioned, axial and shear forces of L5-S1 disc were in good agreement with those obtained from another spine model in the literature and experimental data. Moreover, axial force of L4-L5 disc estimated when the human model was holding a full crate of beer closely fit with *in-vivo* measurements. Lastly, under external forces acting on each vertebra in x-, y- and z-axis directions, dynamic properties of the spine model such as translation, rotation were simulated and analyzed. Based on these obtained dynamic properties, displacement-force relationships of all vertebrae were interpolated and expressed in term of polynomial functions. These polynomial functions are very useful for the real time simulation of spine models in a haptically integrated graphic interface which will be presented in next chapter.

CHAPTER 4

A HAPTICALLY INTEGRATED GRAPHIC INTERFACE FOR STUDYING BIO-DYNAMICS OF SPINE MODELS

4.1. Introduction

Biodynamic investigations of human spine are important since they are useful to provide surgeons additional information in finding treatments for spinal diseases. Furthermore, dynamic simulation of the human spine with haptic interface may offer better realism compared to those with only a visual interface. Hence, this chapter is focused on thoroughly describing a haptically integrated graphic interface system which can simulate dynamic behaviour of spine models. The architecture of this system can be seen in Figure 4.1.

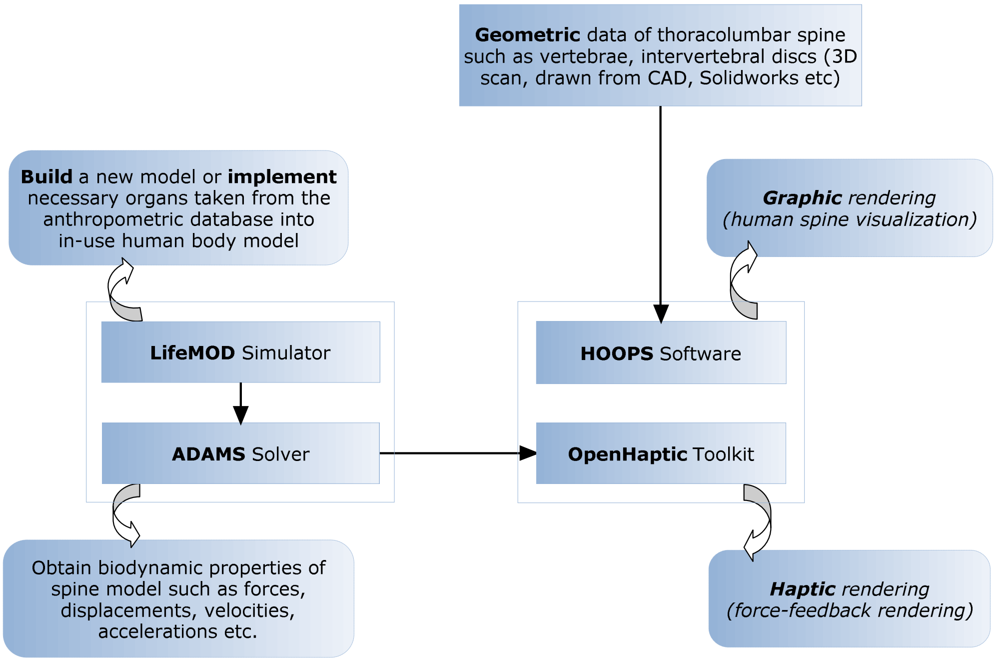

Figure 4.1 The architecture of the proposed system

Initially, an overview of the HOOPS graphic interface is briefly introduced. Next, a thoracolumbar spine model with complex geometry, which is digitized from a resin spine prototype, will be utilized in this graphic interface. Afterwards, some general backgrounds of haptic technique will be introduced since this novel technique has just investigated in last two decades. Then, an available haptic rendering method is presented in detail so that the interaction between virtual objects becomes more realistic. The surgeons can manipulate the haptic cursor represented by a certain tool to directly touch, grasp and apply external forces onto any vertebra of the spine model. Subsequently, connecting polynominal functions of displacement-force relationships of all vertebrae to a real-time haptic simulation is clearly mentioned. By using these functions, the surgeons can observe and conveniently investigate the locomotion and dynamic properties of the spine.

4.2. Computer Graphics

4.2.1. Basic concepts of HOOPS

HOOPS is a set of software libraries designed to aid developers of 2D and 3D industrial graphics applications reduce development time, effort and cost and achieve faster time to market.

HOOPS is officially described as HOOPS/3dAF which stands for the HOOPS 3D Application Framework. ‘Application Framework’ references the fact that HOOPS is not simply a scenegraph system. The HOOPS package comprises high-level application libraries that map Graphic User Interface (GUI) events directly onto interactions within HOOPS, integrations with common GUI frameworks such as .NET, WPF and Qt, and bridges to commonly used third party libraries such as the Siemens Parasolid modelling kernel or the Autodesk RealDWG libraries. HOOPS consists of many libraries. However, the two popularly used and important libraries can be mentioned as below:

- The HOOPS 3D Graphics System (HOOPS/3dGS) is a high performance 3D graphics toolkit for developers building applications for the Windows and UNIX operating systems and the Internet. HOOPS/3dGS' highly optimized data structures and algorithms dramatically simplify the development of 2D and 3D, interactive, vector and raster graphics-based CAD/CAM/CAE, Scientific Visualization, and Geographical Information System (GIS) applications. HOOPS/3dGS contains a subroutine library that provides for the creation, management, querying and editing of an application's graphical information and is linked with an application's object code. The libraries can be dynamically or statically linked. In addition, it also gives a large suite of supporting demonstration and integration code to assist developers in learning about HOOPS/3dGS and incorporating it into their application.
- The HOOPS Model View Operator (HOOPS/MVO) is a set of platform-independent C++ objects that implement much of the common functionality found in CAD/CAM/CAE applications, such as viewing and model creation and manipulation. The classes are implemented with the HOOPS 3D Graphic System. The HOOPS/MVO objects can be directly incorporated into an application or custom object or they can be used as a foundation for building custom objects. To facilitate the extension of these objects, clear source code is also provided in readable form.

Figure 4.2 shows the main interface of HOOPS. Full information of HOOPS can be found online (HOOPS)

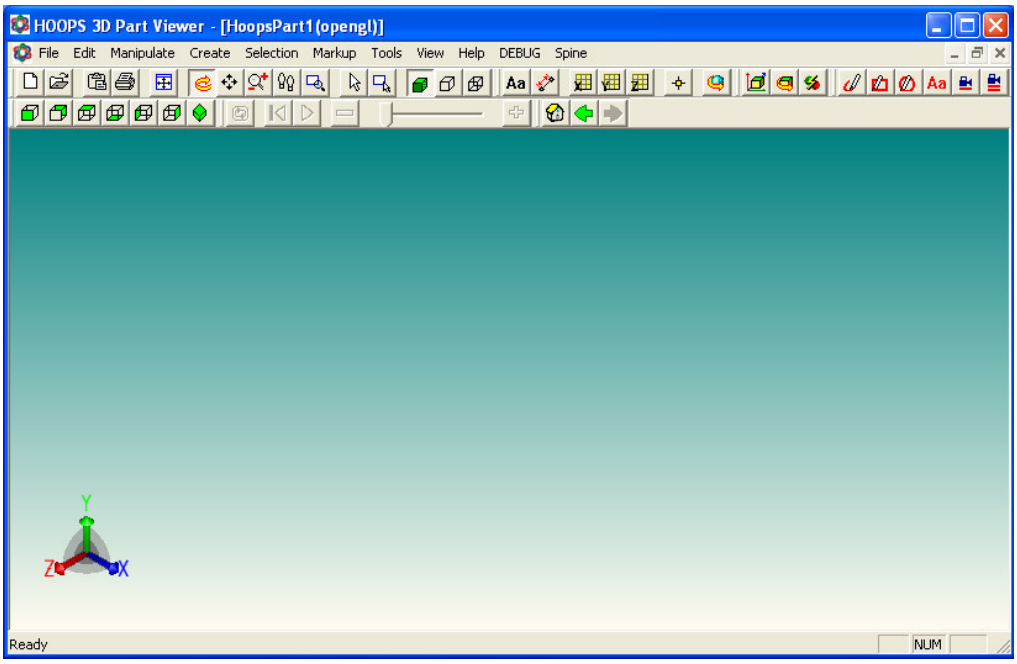

Figure 4.2 The main interface of HOOPS

4.2.2. Thoracolumbar spine modeling in HOOPS

Since importing the geometry of the spine model in LifeMOD into HOOPS is very difficult, a thoracolumbar spine model with complex geometry of vertebrae was used in this case to observe better the locomotion of the spine. This spine model was generated by obtaining detailed polygonal mesh models of the vertebrae which were digitized from a resin spine prototype of a Chinese-Singaporean cadaver (Budget Vertebral Column CH-59X Life Size 29" Tall) through 3D laser scanning. Figure 4.3 shows different views of the thoracolumbar spine model in HOOPS. After this stage, in the next subsection, haptic technique will be presented in detail to integrate into the graphic interface HOOPS.

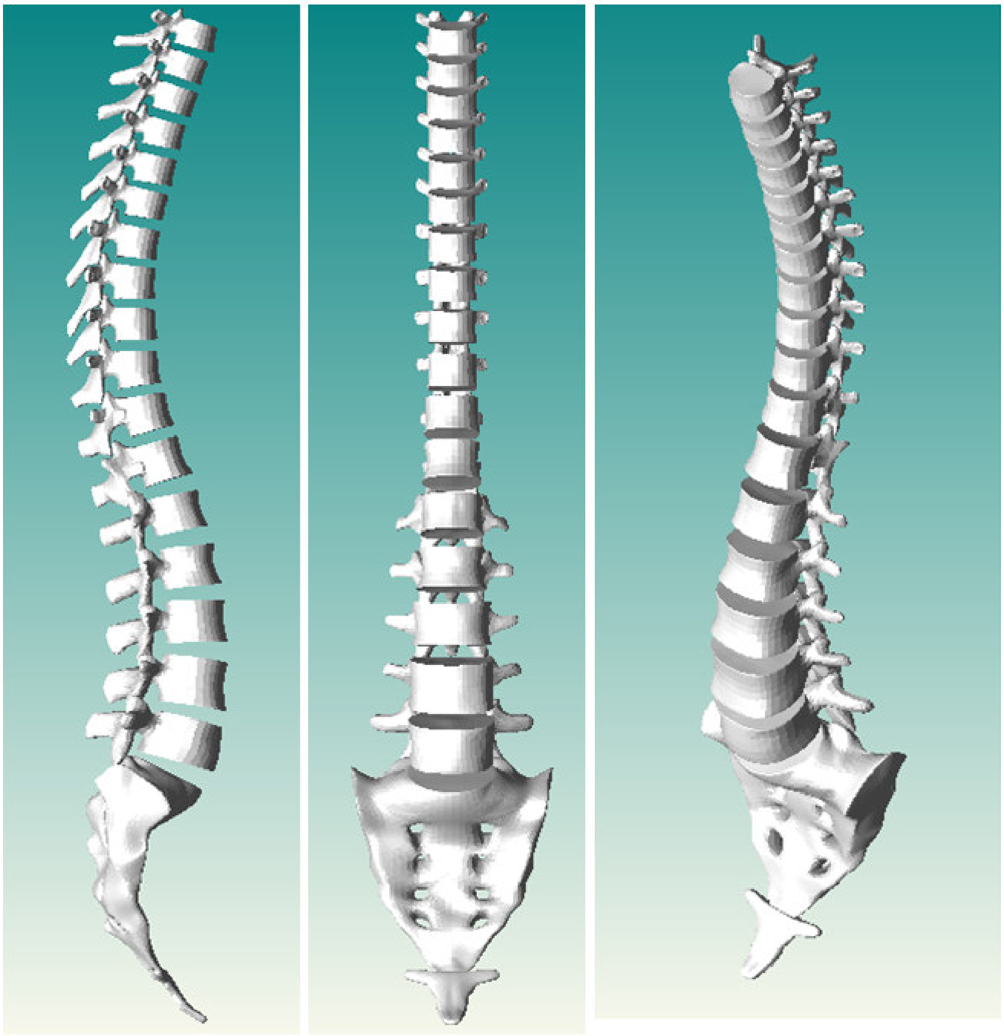

Figure 4.3 Different views of thoracolumbar spine model in HOOPS

4.3. Computer Haptics

In the early 20th century, psychophysicists introduced the word haptics (from the Greek haptikos, meaning to touch) to describe the research field that addresses human touch-based perception and manipulation (Salisbury et al., 2004). In the early 1990s, the word *haptics* started to have new meanings. The synergy of psychology, biology, robotics and computer graphics made *computer haptics* possible. Much like computer graphics is concerned with synthesizing and rendering visual images, computer haptics is the art and science of synthesizing computer generated forces to the user for perception and manipulation of virtual objects through the sense of touch (Salisbury et al., 2004). Haptic interfaces output mechanical signals that stimulate human touch channels (Hayward et al., 2004). Researchers in this area are concerned with the development and testing of haptic feedback hardware and software that enable users to feel and manipulate 3D virtual objects. The field of computer haptics is also growing rapidly. Applications of haptics are very rich and can be divided into the following areas (Srinivasan and Basdogan, 1997):

- Medicine: surgical simulators for medical training; manipulating micro robots for minimally invasive surgery; aids for the disabled such as haptic interfaces for the blind.
- Entertainment: video games and simulators that enable the user to feel and manipulate virtual tools and avatars.
- Education: giving students the feel of phenomena at nano, macro, or astronomical scales; ‘what if’ scenarios for non-terrestrial physics.
- Industry: integration of haptics into CAD systems such that a designer can model, modify and manipulate the mechanical components of an assembly in an immersive environment.
- Arts: virtual art exhibits and museums in which the user can touch and feel the haptic attributes of the displays remotely.

4.3.1. Fundamentals of haptics

There are two categories of haptic senses: tactile and kinesthetic. Tactile sensations include pressure, texture, puncture, thermal properties, softness, wetness, friction-induced phenomena such as slip and adhesion, as well as local features of objects such as shape, edges and embossing (Hayward et al., 2004). Kinesthetic perception refers to the awareness of one's body state, such as position, velocity and forces supplied by the muscles through a variety of receptors located in the skin, joints, skeletal muscles, and tendons. Both kinesthetic and tactile sensations are fundamental to manipulation and locomotion.

To understand how the human interacts with the virtual objects through the haptic interfaces, the subsystems and information flow underlying interactions between human users and force-reflecting haptic interfaces are shown in Figure 4.4 (Srinivasan and Basdogan, 1997).

- Human sensorimotor loop: when a human user touches a real or virtual object, forces are imposed on the skin. The associated sensory information is conveyed to the brain and leads to perception. The motor commands issued by the brain activate the muscles and result in hand and arm motion.
- Machine sensorimotor loop: when the human user manipulates the end-effector of the haptic interface device, the position sensors on the device convey its tip position to the computer. The computer calculate the force commands to the actuators on the haptic interface in real-time, so that appropriate reaction forces are applied on the user, leading to tactual perception of virtual objects.

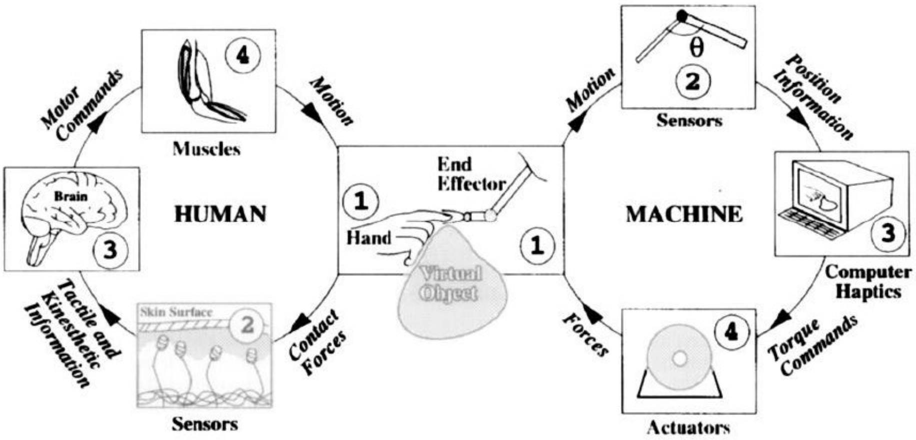

Figure 4.4 Haptic interaction between humans and machines

4.3.2. Haptic interface devices

In general, haptic interface devices can be viewed as having two basic functions: (1) to measure the positions and contact forces (and time derivatives) of the user's hand (or other body parts) and (2) to apply contact forces and positions (or their spatial and temporal distributions) to the user.

Salisbury et al. (2004) summarizes two methods to classify haptic interface devices: (1) grounding locations and (2) intrinsic mechanic behavior.

The first way to distinguish between haptic interface devices is by their grounding locations. The ground based haptic interface devices have a fixed reference frame. The DELTA device from ForceDimension is an example of ground based style desktop devices (Figure 4.5). The PHANToM device from the Sensable Technology is another example (Figure 4.6).

Figure 4.5 DELTA haptic device (ForceDimension 2004)

Figure 4.6 PHANToM device (SenAble)

Another category is exoskeleton mechanisms or body-based haptic interfaces, which a person wears on his arm or body. The exoskeleton devices can present more complex multiple DOFs haptic feedback to the user. The word exoskeleton means a mechanical system that is attached to the body of users and looks like a skeleton. Users wear the exoskeleton haptic device on their body or on their hands. The CyberGrasp from Immersion is an exoskeleton device that fits over user's hands (Figure 4.7). This device does not have independent position sensors and it has to be used together with a data glove called CyberGlove. Users first put on CyberGlove data glove, then put on CyberGrasp on the top of CyberGlove data glove. The data glove measures the position and gesture of the user and the CyberGrasp haptic device then sends force according to the position information from the data glove. The CyberGrasp device adds resistive force feedback to each finger. With the CyberGrasp force feedback system, users are able to feel the size and shape of computer-generated 3D objects in the virtual environment. Because the exoskeleton devices are worn on the user's body, their reference frames are not fixed but movable. As a result, the force feedback from exoskeleton devices can prevent the user from crushing a virtual object in their hand, but it cannot prevent them pushing through a wall. In this research, the available PHANToM device (SensAble) as shown in Figure 4.6 is used.

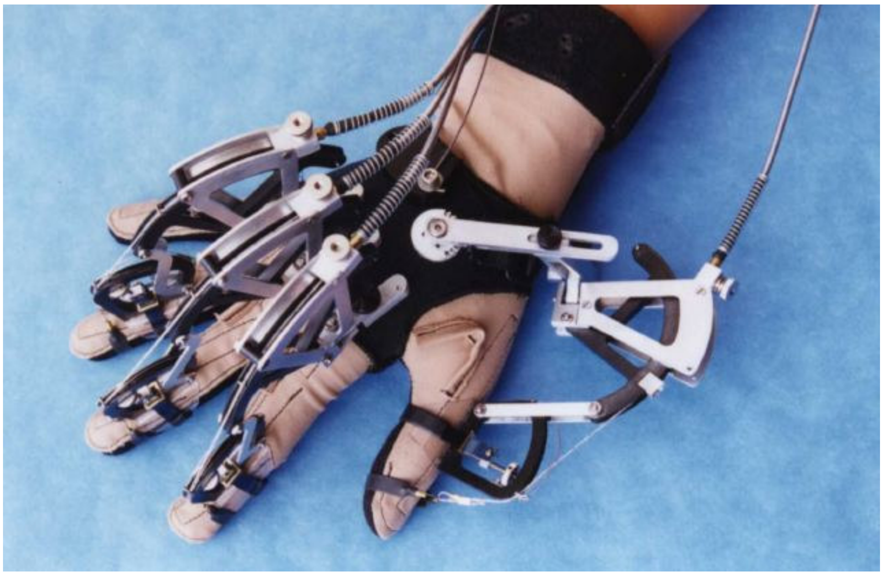

Figure 4.7 CyberGrasp from Immersion (Immersion 2004)

4.3.3. Haptic rendering

Haptic rendering is the process of applying forces to give the operators a sense of touch and interaction with physical objects. Typically, a haptic rendering algorithm consists of two parts: collision detection and collision response. Figure 4.8 illustrates in detail the procedure of haptic rendering. Note the update rate of haptic rendering has to be maintained at around 1000 Hz for stable and smooth haptic interaction. Otherwise, virtual surfaces feel softer. Even worse, the haptic device vibrates.

Although the basic principle of haptic rendering seems easy and straightforward, rendering of complex 3D objects requires more sophisticated algorithms. Despite of the difficulties, several haptic rendering techniques have been developed recently to simulate complex touch interactions in virtual environments.

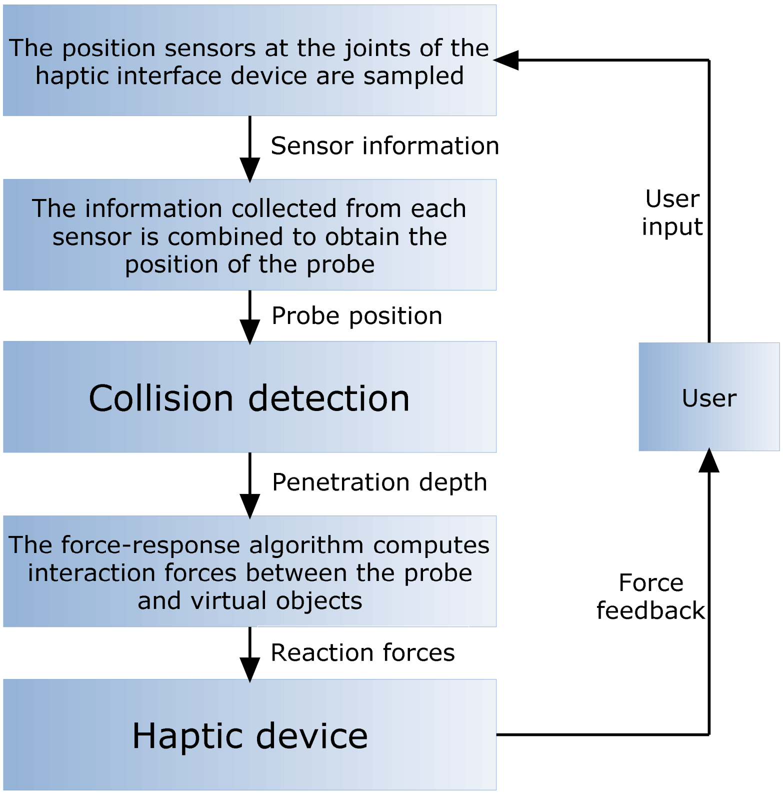

Figure 4.8 Procedure of haptic rendering

The existing techniques for haptic rendering can be categorized according to the way the probing object is modeled: (1) a point, (2) a line (or a ray) segment, or (3) a 3D object made of groups of points, line segments and polygons (Basdogan et al., 1998).

The point-object haptic rendering paradigm assumes that we interact with the virtual world with a point probe, therefore only the three interaction force components at the probe's tip need to be computed. This feature greatly simplifies the haptic device design and facilitates collision detection and force computation (Salisbury et al., 2004). Although the point-object paradigm is a seemingly simple technique, it could provide the users with similar force feedback as what they would feel when exploring the objects in real environments with the tip of a stick. Also, it provides us very rich interaction possibilities.

Various point-object style approaches for haptically rendering triangular mesh virtual objects have been developed. The simplest algorithm of point-object style haptic rendering is based on the virtual wall model. In this model, the magnitude of force is proportional to the penetrating depth and the direction of reaction force is determined by the normal of the contacted surface.

Although the virtual wall point-object method often works well, it does not record past probe positions. Therefore, this method often has difficulty with determining the reaction force's direction when virtual objects are small or thin or have complex shapes. To solve this problem, Zilles and Salisbury (1995) and Ruspini et al. (1997) independently introduced the *god-object* and proxy algorithms. Both algorithms are based on the same principle: use additional variables to track a physically realistic contact point on the object's surface. The contact point is called the god object or proxy. Then, a spring is placed between the point probe and god object or proxy to create a realistic force feedback to the user. If no collision happens, the haptic interface point probe and the god object/proxy are collocated and thus no force is applied to the user.

Morgenbesser and Srinivasan (1996) introduced *force shading* to obtain smooth-changing forces when interacting with polygonal mesh surface. Just like the Phong shading technique in graphical rendering of polygonal meshes, the force shading method interpolates normals of neighboring polygonal patches to obtain more smooth-feeling force feedback.

Besides triangular meshes, point-object haptic interaction paradigm is extended to render other geometric representations, such as implicit surface, NURBS surface and voxel-based model. Salisbury and Tarr (1997) introduced an algorithm for virtual objects based on implicit surfaces with an analytical representation. For implicit surfaces, collision detection is much faster and convenient. Kim et al. (2002) introduced a haptic algorithm which is mainly for a non-analytical implicit surface representation which represents the surface with potential values in a 3D regular grid. Thompson et al. (1997) introduced a tracing algorithm and an algorithm for surface proximity testing to provide haptic rendering for sculptured models in NURBS representation. Avila and Sobierajski (1996) developed a direct haptic rendering method for volumetric models.

Although the point-object interaction metaphor has proven to be convincingly useful and efficient, it has limitations of being unable to simulate torques and hence is not capable of simulating more general tool-object interactions. To improve on this situation, some approaches use probes that can exert both forces and torques to virtual objects.

Basdogan et al. (1997) implemented a ray-based haptic rendering method which can provide 5-DOF interaction between a line segment probe and virtual objects. In their method, the probe is modeled as a finite-length line segment and can be considered as an approximation of a long tool. Also, a more complex 3D geometric model of the probe object can be simplified to a set of connected line segments so that ray-based rendering technique can be used and will be faster than simulation of full 3D object interactions (Basdogan and Srinivasan, 2002). However, if the geometry shape of the probe object is too complex to be easily represented with a set of line segments, object-object style haptic interactions has to be considered.

The object-object haptic interface can introduce a much more complex haptic cursor into the haptic simulation, thus improving the degree of realism and hence is desirable for many applications. However, this kind of haptic rendering simulation is computationally expensive. Gregory et al. (2000) presented an algorithm for haptic display of moderately complex polygonal models with a polygonal haptic cursor by making use of incremental algorithms for contact determination between convex primitives. McNeely et al. (1999) put forward a simple, fast, and approximate voxel-based approach. This approach enables the manipulation of a modestly complex haptic cursor within an arbitrarily complex environment of static rigid objects. Nelson et al. (1999) derived a novel velocity formulation for use in a parametric surface-surface tracing paradigm and integrated it into a three step tracking process to compute reaction force between two NURBS surfaces. More detail information on haptic rendering methods can be found in the literature review of Laycock and Day (2007).

Since our research is focused on investigating dynamic behavior of spine models, an available and suitable haptic rendering is selected and clearly presented in subsequent subsection.

4.4. Haptic Rendering Method of the Thoracolumbar Spine Model

In real-time haptic simulation, users can only interact with the thoracolumbar spine model by manipulating a rigid virtual object considered as a probe on the computer screen. At present, a simple probe such as a sphere is used in this study. Since this interaction carries out at a high update rate of 1 kHz, the chosen haptic rendering method needs to be reasonable and effectively computational. As mentioned in section 4.3, a haptic rendering method includes two stages: collision detection and collision response. For the collision detection, the simple algorithm proposed by James Arvo (1990) is utilized to check intersection between the probe and the spine model. For collision response, the algorithm developed by Gao and Gibson (2006) is mentioned to determine force feedback. In the following parts, these two stages are clearly presented.

4.4.1. Collision detection

The problems of interference detection between two or more geometric models in static and dynamic environments are fundamental in computer graphics. There are a multitude of various algorithms extensively studied in the literature to provide a fast way to determine exact collision detection between complex models and speed up the performance of real-time simulations for interactive applications, especially for haptically integrated applications (Jiménez et al., 2001). These algorithms are based on using bounding volumes and spatial decomposition techniques in a hierarchical manner. Further information on these two techniques can be found in the book of Ericson (2005).

In this study, axis-aligned bounding box algorithm is selected because the algorithm is not only faster to build and test collision detection but also uses less storage compared to others for rigid models. The axis-aligned bouding box (AABB) is a rectangular six-sided box in 3D (four-sided in 2D) categorized by having its faces oriented in such a way that its face normals are at all times parallel with the axes of the given coordinate system. By using this algorithm, an AABB tree including bounding boxes of all vertebrae of the spine model is built and examined in the subsequent part.

4.4.1.1. Building AABB tree

The AABB tree for each vertebra of the spine model in this study is a binary tree and constructed top-down, by recursive subdivision. At each recursion step, the smallest AABB of the set of primitives is computed, and the set is split by ordering the primitives with respect to a well-chosen partitioning plane. This process continues until each subset contains one element. Thus, an AABB tree for a set of n primitives has n leaves and $n - 1$ internal nodes.

At each step, the partitioning plane orthogonal to the longest axis of the AABB is specified by choosing δ, the coordinate on the longest axis where the partitioning plane intersects the axis. In general, the best performance is achieved by simply choosing δ to be the median point on the longest axis of the AABB, thus splitting the box in two equal halves. The set of primitives is then split into a negative and positive subset corresponding to the respective halfspaces of the plane. A primitive is classified as positive if the midpoint of its projection onto the axis is greater than δ, and negative otherwise. Figure 4.9 shows a primitive that straddles the partitioning plane depicted by a dashed line. This primitive is classified as positive. It can be seen that by using this subdivision method, the degree of overlap between the AABBs of the two subsets is kept small. Based on the procedure mentioned above, Figure 4.10 illustrates an AABB tree of a vertebra.

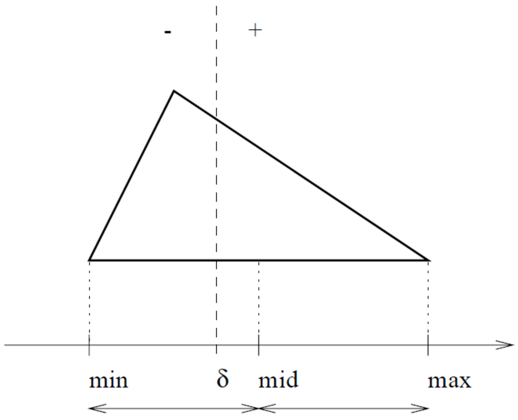

Figure 4.9 An example of classifying a primitive based on partitioning plane

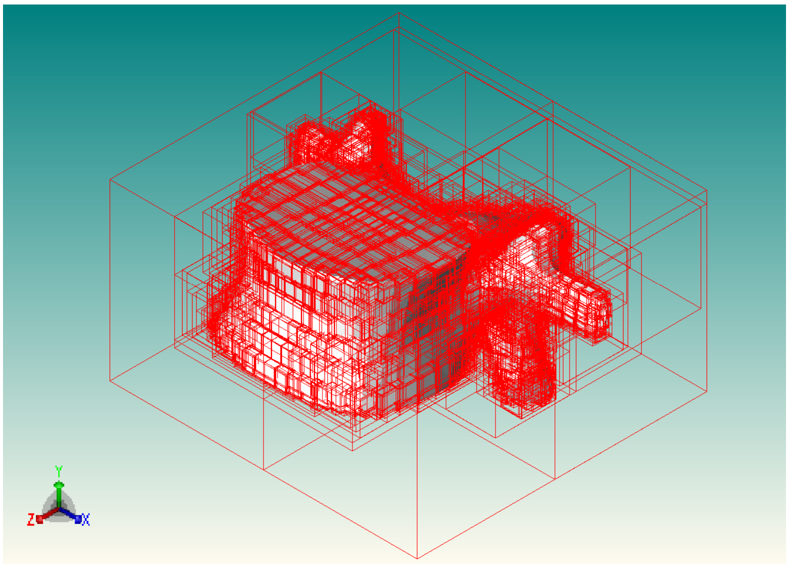

Figure 4.10 An AABB tree of a vertebra

4.4.1.2. Sphere-AABB intersection

After AABB trees of the spine model are constructed, haptic simulation is executed and collision between the spherical probe and the spine during interaction process will happen. This collision detection can be determined by using a simple method developed by Arvo (1990) to check sphere-AABB intersection. The method states that testing whether a sphere intersects an axis-aligned bounding box is based on comparing the distance between the sphere center and the AABB with the sphere radius. If the distance is less than the radius, the sphere and the AABB must be intersecting. Figure 4.11 and Figure

4.12 show some 2D nonintersecting and intersecting cases between the sphere and the AABB, respectively.

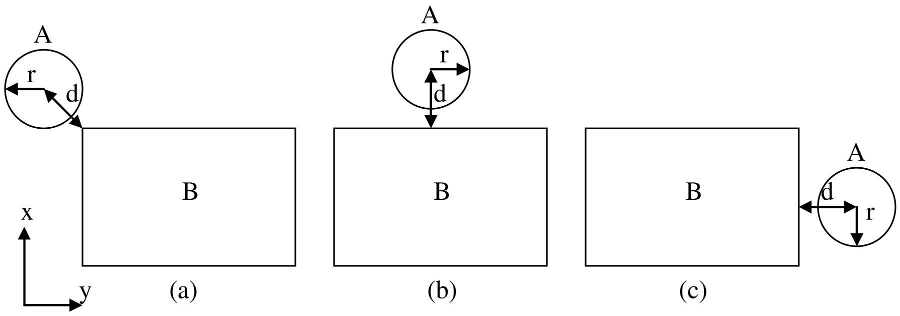

Figure 4.11 Nonintersecting cases between a sphere A and a box B

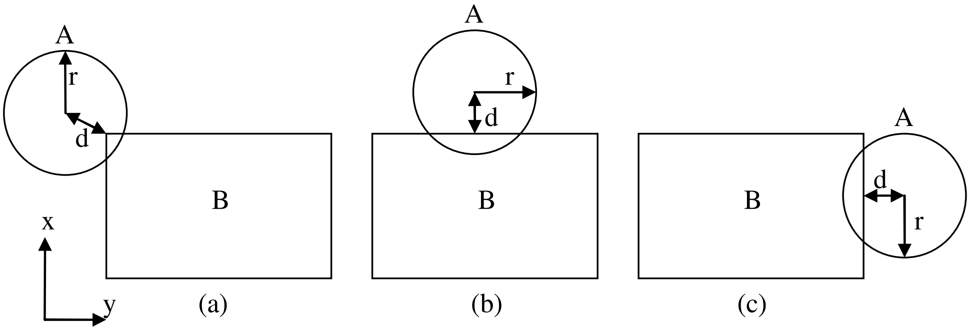

Figure 4.12 Intersecting cases between a sphere A and a box B

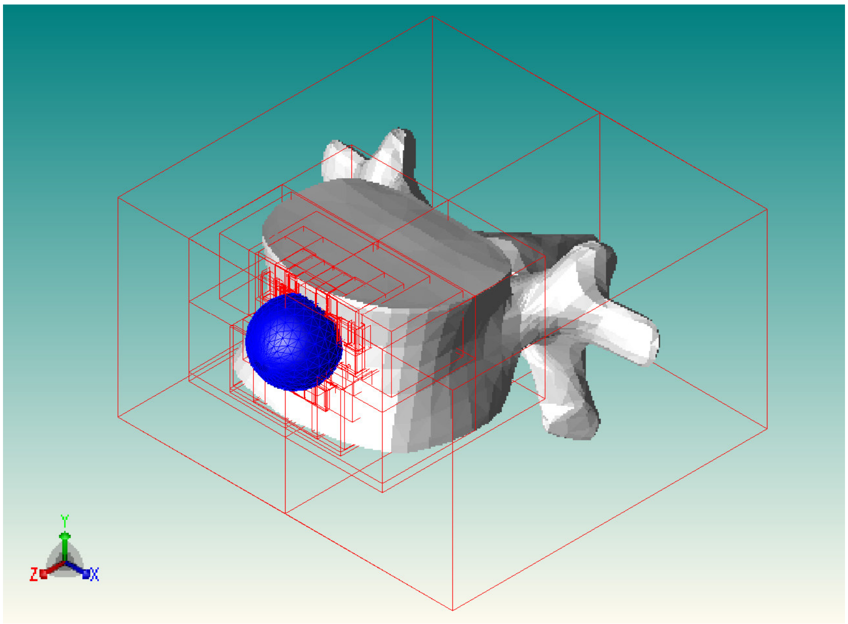

Figure 4.13 Collision between the sphere and AABBs of the vertebra

Using this simple algorithm, collision detection between the spherical probe and the spine model is quickly found. Figure 4.13 shows all AABBs of a vertebra intersecting with the spherical probe. It should be noted that the purpose of this stage is to determine all primitives (triangles in this case) included in AABBs which are intersecting with the spherical probe. These primitives will be processed during collision response stage which is thoroughly presented in next subsection to compute the force feedback.

4.4.2. Collision response

To calculate the reaction force generated from a specific vertebra of the spine model which users can feel through the PHANToM device, the method proposed by Gao (2006) is utilized in this study. An important prerequisite of this method is that intersecting points with the spherical probe have to be specified. Since all triangles (primitives) included in AABBs intersecting with the probe are found during collision detection, the next step in this stage is to determine the points of those triangles that are intersecting with the probe.

4.4.2.1. Determining intersecting points with the spherical probe

The geometry of the sphere and other simple objects can be displayed in the form of mathematical equations which are either in implicit or in explicit representations. The implicit representation of the surface S is described by the following implicit equation:

$$S = \{(x, y, z) \in R3 \mid f(x, y, z) = 0\} \tag{4.1}$$

where $f(x, y, z)$ is the implicit function, $R3$ is the 3D space and (x, y, z) is the coordinate of a point in 3D space.

Here $f(x, y, z)$ could be polynomials, discrete grids of points or some black box functions. When $f(x, y, z)$ is a polynomial, it yields an implicit algebraic surface. When $f(x, y, z)$ is linear, it describes a plane. When $f(x, y, z)$

is quadratic, it describes a quadric surface, such as an ellipsoid, a sphere or a cylinder. If the potential value of *f(x, y, z)* is 0, then the point *f(x, y, z)* is on the surface. The set of points for which the potential value is 0 defines the implicit surface. If the potential value is positive, then the point *f(x, y, z)* is outside the surface. If *f(x, y, z)* is negative, the point *f(x, y, z)* is inside. Homogeneous representation of quadric surfaces is expressed in the following equation:

$$\begin{aligned} f(x) = {} & Ax^2 + 2Bxy + 2Cxz + 2Dxw + \\ & Ey^2 + 2Fyz + 2Gyw + Hz^2 + 2Izw + Jw^2 \end{aligned} \tag{4.2}$$

Equation (4.2) can be converted to matrix form in Equation (4.3) as follow for computation convenience:

$$f(x) = \begin{bmatrix} x & y & z & w \end{bmatrix} \begin{bmatrix} A & B & C & D \\ B & E & F & G \\ C & F & H & I \\ D & G & I & J \end{bmatrix} \begin{bmatrix} x \\ y \\ z \\ w \end{bmatrix} \tag{4.3}$$

Let *Q* be the 4×4 symmetric matrix above, therefore Equation (4.3) can be written as:

$$f(x, y, z, w) = \begin{bmatrix} x & y & z & w \end{bmatrix} Q \begin{bmatrix} x \\ y \\ z \\ w \end{bmatrix} \tag{4.4}$$

Matrix *Q* defines the algebraic property, shape and size of the quadratic surface. The normal vector of implicit surface can be computed by calculating the gradient of the definition function. Thus the normal is:

$$N = \begin{bmatrix} \dfrac{\partial f}{\partial x} & \dfrac{\partial f}{\partial y} & \dfrac{\partial f}{\partial z} \end{bmatrix} \tag{4.5}$$

To transform a quadratic surface, the property matrix *Q* of the quadratic surface needs to be transformed to yield a new matrix that represents the transformed surface. Given a 4×4 homogeneous transformation matrix T, the transformation of a quadric surface takes the form as below:

$$Q' = T^{*}QT^{*T} \tag{4.6}$$

where T^{*} is the adjoint of T and T^{*T} is the transposed matrix of T^{*}.

By using Equations (4.4) and (4.6), the intersecting points on specific vertebrae of the spine model are quickly determined. Figure 4.14 shows intersecting points during colliding process between the probe and a vertebra. After these intersecting points are found, the final step in this stage is to calculate the reaction forces generated from the vertebrae of the spine model.

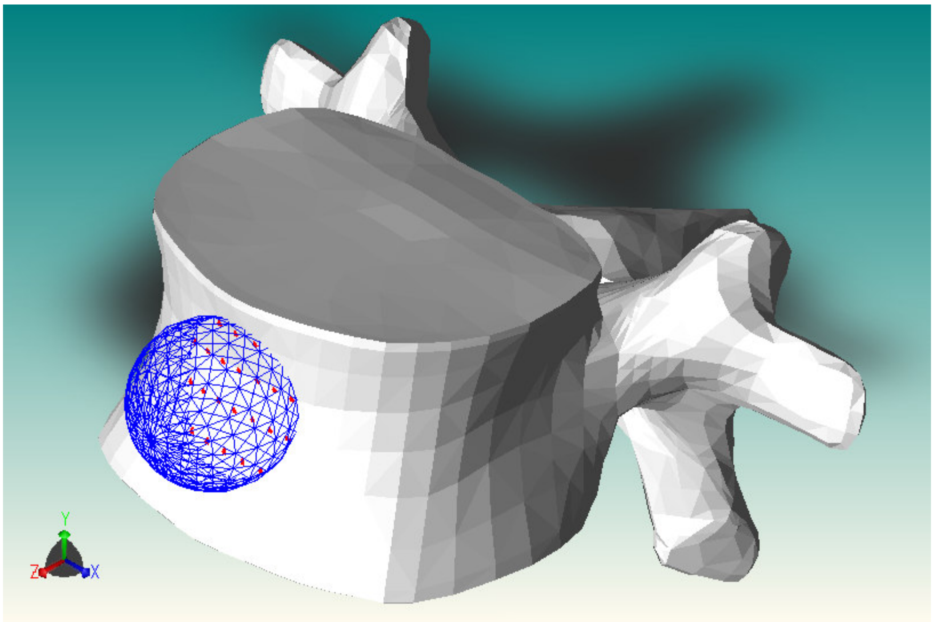

Figure 4.14 Intersecting points between the probe and the vertebra

4.4.2.2. Computing the reaction forces of the vertebrae

Computing the reaction forces of the vertebrae is concerned with finding force magnitudes which the probe applied to the intersecting points on the contact surface areas of the vertebrae and force directions at those points. And the force calculated here is also the force which users can feel through the sense of touch.

(a) Force magnitude

According to classical mechanics, the probe should be viewed as a rigid body instead of a single mass point, therefore forces applied on the surface of the probe not only form a force vector but also a torque. However, the PHANToM device provides only 3-DOF force feedback but no torque output. To simplify the problem, only the force is considered at this stage. However, note that the probe is a rigid body in nature, so it would be quite easy to adapt the algorithm to 6-DOF haptic rendering later. Penalty and constraint haptic rendering methods determine force magnitude by Hooke's law:

$$F = k * s \tag{4.7}$$

where k is spring constant, s is the displacement of mass point connected to the spring.

To make the system more stable, a damping force is added. Hence the equation becomes:

$$F = k * s - d * \dot{s} \tag{4.8}$$

where d is the damping factor and $\dot{s}$ is the velocity of the point.

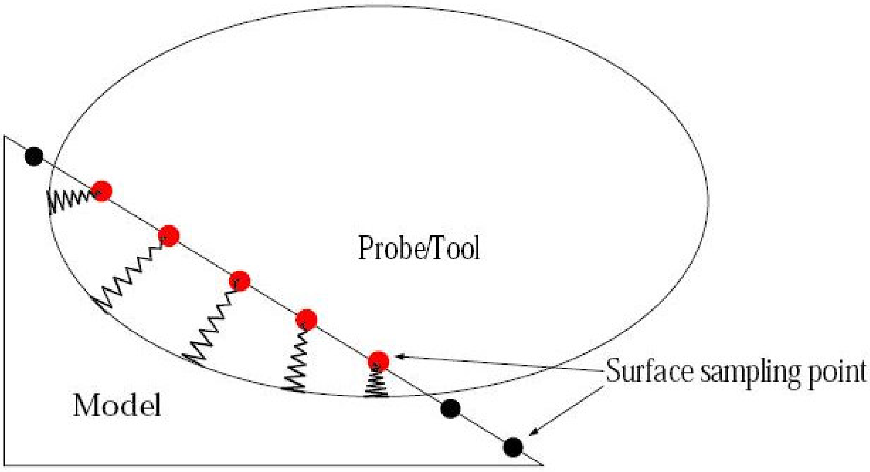

Figure 4.15 Distributed springs of the probe

Figure 4.15 shows a probe penetrating a planar surface of a model. Red dots denote the surface sampling points inside the probe and black ones are sampling points outside. The depths of colliding sampling points are the distances between those sampling points to the correspondingly closest points on the implicit surface.

Note the potential value from *f(x, y, z)* is not Euclidean distance from a point to the implicit surface of probe. Although Lagrange multiplier method can be used to find the minimum distance to the algebraic surface, it requires several iterations to find the numerical roots for the equation. The approximate solution is found by shooting a normal vector from the sampling point P_o and finding out the intersection between the vector and the implicit surface of probe. The distance between P_o and the intersection point is the depth. The normal vector of point $P_o(X_o, Y_o, Z_o)$ can be found as $N_o(N_x, N_y, N_z)$. Since the sampling point is inside the implicit surface instead of on the surface, the normal vector N_o can be viewed as a normal vector of a smaller surface offset from the original one. If the implicit function is quadratic, in this case an ellipsoid, an analytic solution for the intersection points can be found easily. The magnitude of force is defined as:

$$|F| = \sum_{i=0}^{n} \left(k * s_i - d * \dot{s}_i \right) \tag{4.9}$$

Figure 4.16 shows what happens when a spherical probe, with a diameter of 800, passes through a plane with continuous force magnitude. The output force reaches the maximum when the intrusion depth is 400. At that moment the center of probe touches the plane so that the probe has the largest contact area with a surface. After the peak the force magnitude decreases.

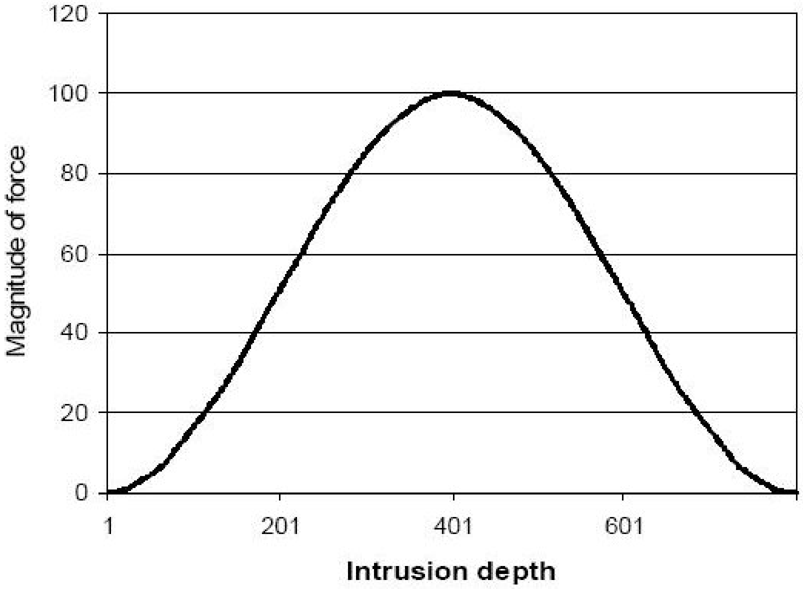

Figure 4.16 Intrusion depth and force magnitude

According to Equation (4.9), force magnitude is proportional to the number of points colliding with a probe. Therefore, even at the same intrusion depth, a bigger probe generates a bigger force because it has more points in collision with the model than a smaller probe has. Figure 4.17 shows two spherical probes, one bigger one smaller, at the same depth, the bigger probe has more sampling points in collision.

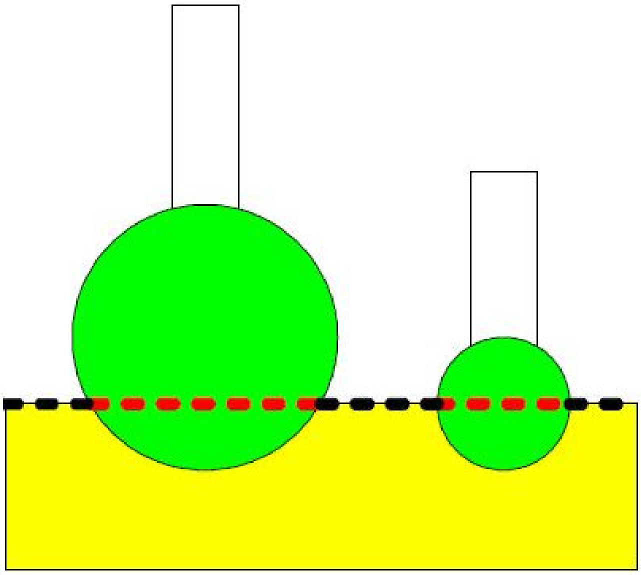

Figure 4.17 Two probes of different size generate different force feedbacks

Figure 4.18 shows force magnitudes recorded when two spherical probes pass through a planar surface. When the smaller probe reaches the force peak at depth 200, the force magnitude is less than 20 units, while the force feedback of the larger probe is over 40 units at the same depth. This is an undesirable effect which makes the haptic interaction unstable and changeable. In practice, when the user increases the size of probe/tool, he may find the force feedback increases drastically and the surface of model becomes increasingly harder. The force feedback level may even exceed the safe threshold of PHANToM device and result in a hardware error.

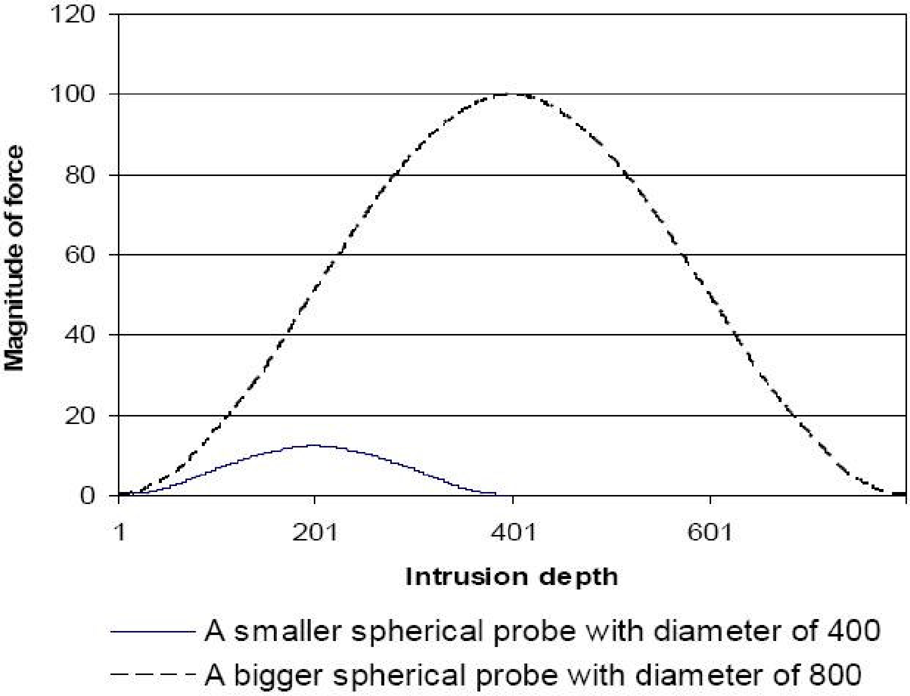

Figure 4.18 Intrusion depth and force of two probes of different sizes

To resolve this effect, Equation (4.9) has to be modified to make the force output not related to the size of probe/tool. Since the intrusion depth and force magnitude is not linearly related, to totally eliminate the impact of size is not realistic. A simple way to modify the equation is as follow:

$$|F| = \frac{\sum_{i=0}^{n} \left(k * s_i - d * \dot{s}_i \right)}{S_{MaxSec}} \tag{4.10}$$

where S_{MaxSec} is the maximum sectional area of the probe.

Figure 4.19 shows nearly the same situation of experiment of Figure 4.18 except Equation (4.10) used in this example. At the force output peak of the smaller probe, the levels of force of both probes are nearly the same. Before the depth of 200 units, the smaller probe generates a larger force than the bigger probe does. According to Gao's test, the difference is nearly indiscernible.

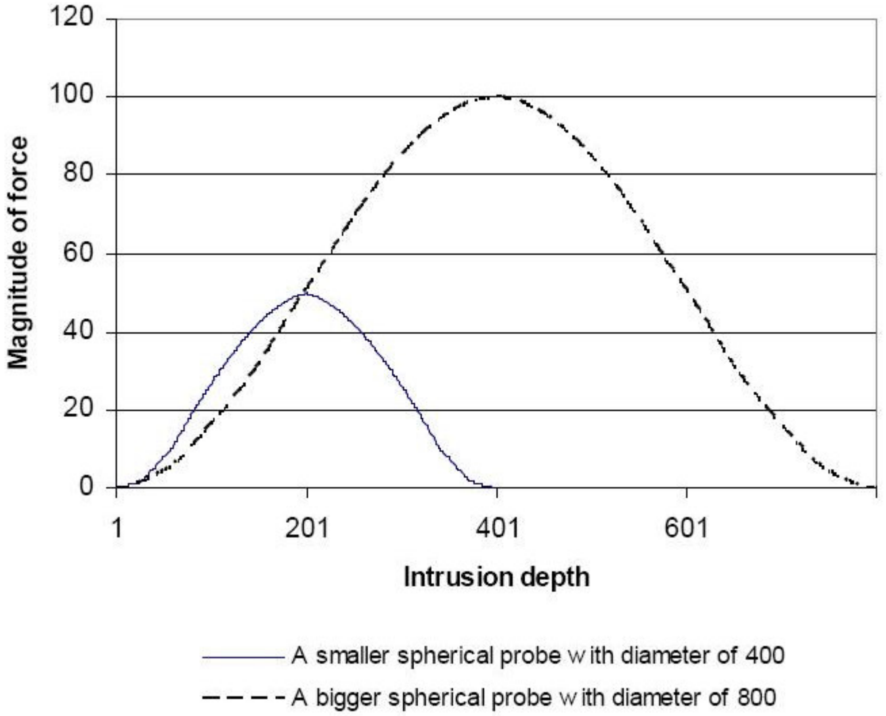

Figure 4.19 Force magnitude with improved method

(b) Force direction

Penalty-based approaches and constraint-based approaches generally compute force vectors according to the normal vector of contacted surface. In Gao's paper (Gao and Gibson, 2006), he developed a method called probe normal method, where a force vector is not derived from the surface of the model but from the implicit surface of the probe instead. If there is no friction between the probe and model surface, the pressing force and reaction force are normal to the surface of contact area. Therefore, if the approximate normal vectors of contact area on the implicit surface of the probe can be obtained, the reaction force direction will be determined by the summation of those normal vectors. Therefore, the direction of force is formulated as:

$$\vec{F} = \frac{\sum_{i=0}^{n} \vec{N}_i * s_i}{n} \tag{4.11}$$

where n is the number of surface sampling points inside probe, N_i as the normal vector of surface sampling point and s_i as the depth. The direction of force feedback is an average of the normal vectors weighted by the depth. This makes sense because the point having bigger depth plays a bigger role in determining the direction of force.

By using Equations (4.10) and (4.11), the magnitude and direction of the reaction force generated from the vertebrae colliding with the spherical probe can be determined and the users can feel this reaction force though the sense of touch. One important point should be emphasized after this collision response stage is that the users can only manipulate the spherical probe to interact with the static spine model. Under various external forces applied by the users though the PHANToM device, the spine model behaves differently. These dynamic behaviors will be presented in detail in next section.

4.5. Connection Displacement-Force Functions to Real-Time Haptic Simulation

To observe the locomotion and study dynamic properties of the spine model, the users can control the probe to apply external forces in an arbitrary direction onto any vertebra by pressing the PHANToM stylus button. In essence, the haptic rendering process in this research has two stages: the rigid stage and the compliant stage. Without pressing the stylus button, the users can touch and explore the whole spine model since it is considered to be rigid throughout. The haptic rendering algorithm used in this rigid stage is clearly presented in the above section.

After the users locate a specific vertebra where he/she wishes to apply force, they can then press the PHANToM stylus button and push or drag the vertebra to make the whole spine model deform. Once the stylus button is pressed, the system switches to another haptic rendering algorithm that uses the stretched-spring model. A virtual spring is set up connecting the vertebra and the haptic probe. The spring has two hook points: one is on the vertebra and the other is on the haptic probe. Both of the hook points displace during spine deformation. The force magnitude is determined by the length of the virtual spring and its stiffness while the force direction depends on the vector of the virtual spring. To conveniently compute the movement of the spine model, the displacement-force functions mentioned in subsection 3.5.2 are utilized here. Based on the magnitude of the external forces applied by the users, dynamic properties of all vertebrae can be easily calculated via these functions and the locomotion of the whole spine model will be rapidly observed. Some real-time haptic simulation cases of the thoracolumbar spine model under various external forces are illustrated in subsection 6.3.

In short, the step-by-step procedure of the real time haptic simulation of the spine model in this study can be shown in Figure 4.20 below.

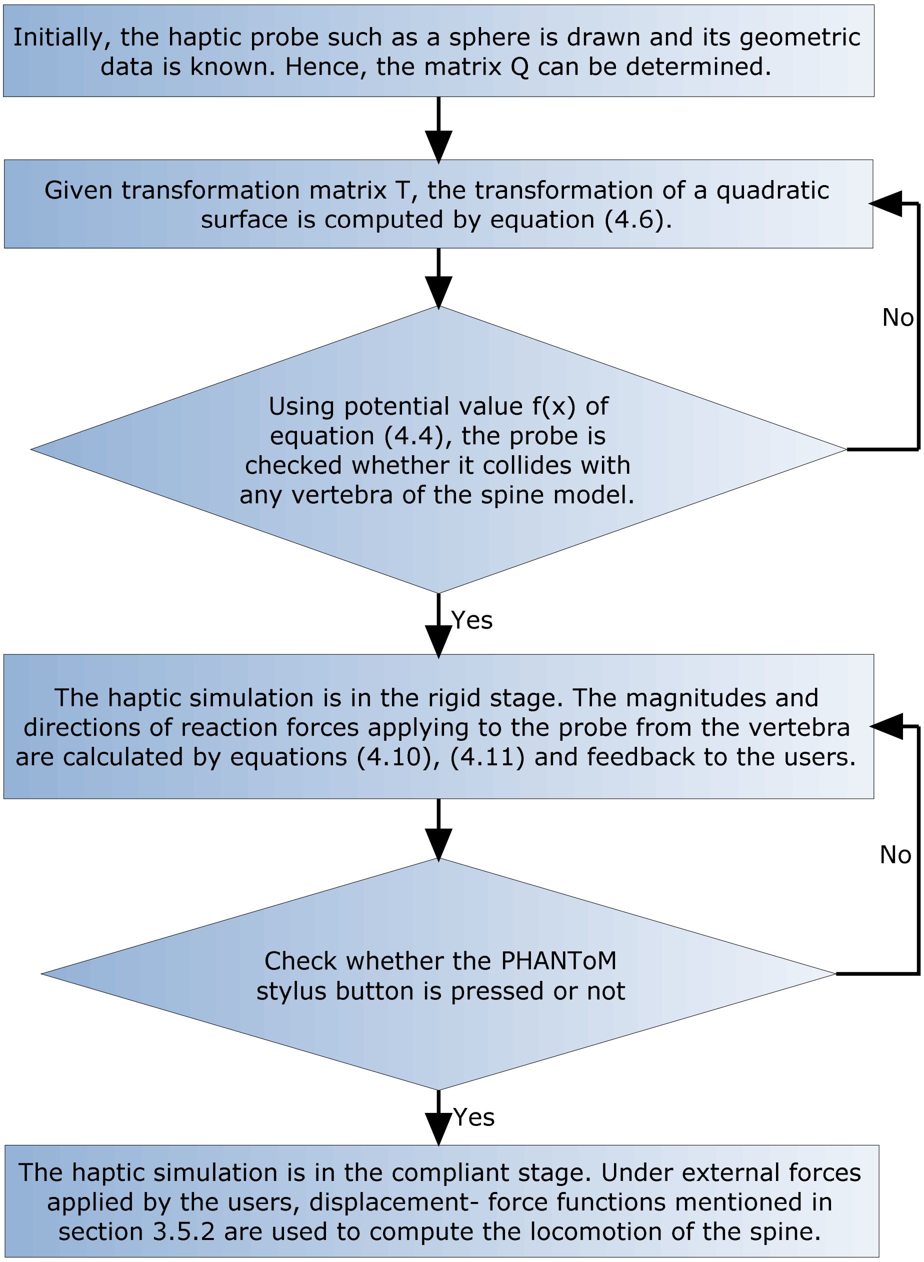

Figure 4.20 Step-by-step haptic simulation process of the spine model

4.6. Summary

This chapter addressed the development of a haptically integrated graphic interface which can simulate dynamic behaviour of spine models. A popular and powerful graphic application software named HOOPS was used as the main interface for real-time simulation in this study. Then, some background information of computer haptics was provided to help users get familiar with this novel technique. Afterwards, an effective haptic rendering method was described. Using this method, the interaction between the spherical probe manipulated by the users with the spine model becomes much more realistic. The users can directly explore the spine model by touching, grasping and even applying forces in any arbitrary direction onto any vertebra. To observe the locomotion of the spine model under external forces, displacement-force polynomial functions of all vertebrae determined in subsection 3.5.2 was utilized during real-time haptic simulation. Via these functions, the users can quickly and conveniently investigate the motion and dynamic properties of the spine model. Since the geometry of spine model includes only vertebrae, it is not possible to observe deformation behaviour of all intervertebral discs during spine movement. Thus, in the next section, a new tetrahedral mass-spring system model of intervertebral disc is presented in detail. Based on this model, intervertebral discs are generated and interposed between vertebrae, and offline simulations following after real-time haptic simulations can be executed to achieve deformation responses of these intervertebral discs.

CHAPTER 5

A NEW TETRAHEDRAL MASS-SPRING SYSTEM MODEL OF INTERVERTEBRAL DISC

This chapter is mainly focused on developing a new deformable model of intervertebral disc which can be inserted between vertebrae to investigate deformation behavior of intervertebral discs when the spine model is under external forces in an arbitrary direction. Initially, some necessary techniques of deformable object modeling are briefly introduced. Then, a novel tetrahedral mass-spring system model of intervertebral disc is proposed and presented in detail. After that, deformation behavior of this intervertebral disc model is tested to examine how well the model performs under loading. Subsequently, a combination of the tetrahedral mass-spring system model of intervertebral disc and the thoracolumbar spine model is thoroughly described. This hybrid model can be used to study biodynamic behavior of the spine as well as deformation response of intervertebral discs either in real-time haptic simulations or in offline simulations.

5.1. Techniques of Deformable Object Modeling

Deformable object modeling has been studied in computer graphics for more than two decades, across a range of applications. In computer-aided design and computer drawing applications, deformable models are used to create and edit complex curves, surfaces, and solids. Computer aided apparel design uses deformable models to simulate fabric draping and folding (Gibson and Mirtich, 1997). In image analysis, deformable models have been used to segment images and to fit curved surfaces to noisy image data (McInerny and Terzopoulos, 1996). Moreover, deformable models have been used in animation and computer graphics, particularly for the animation of clothing, facial expression, and human or animal characters (Ng and Grimsdale, 1996, Platt and Badler, 1981). Finally, surgical simulation and training systems also demand both real-time and physically realistic modeling of complex, non-linear, deformable tissues.

Approaches for modeling object deformation range from non-physical methods such as B-spline or NURBS surface and Free Form Deformation where individual or groups of control points or shape parameters are manually adjusted for shape editing and design-to physically based methods such as Mass Spring System and Finite Element Method-which account for the effects of material properties, external forces, and environmental constrains on object deformation. For non-physical methods, modeling deformation is limited by the expertise and patience of the user (Gibson and Mirtich, 1997). Deformations must be explicitly specified by the designer. Using nonphysical tools alone, modeling a complex object is a difficult task. Compared to non-physical methods, physics-based modeling approaches are becoming more and more attractive for curve or surface design. Physics-based methods use physical principles and computational power for realistic simulation of complex physical processes (Celniker and Gossard, 1991). Users interact with the model by exerting virtual forces, which produce physics-meaningful and intuitive shape alteration. This allows the user to interactively manipulate the object shape not only through the traditional indirect fashion, such as adjusting control points and setting weights, but also through direct physical manipulation, such as exerting virtual force and applying shape constraints. Generally, the physics-based modeling methods are realistic and intuitive. The main drawback of the physics-based modeling methods is the long computational time involved.

Mass spring systems are one physically based technique that has been used widely and effectively for modeling deformable objects (Gibson and Mirtich, 1997). In a mass spring system, an object is modeled as a collection of point masses connected by springs in a lattice structure. Newton's Second Law governs the motion of each single mass point in the lattice. Mass spring system is a simple physical model and easy to construct. The updating rate of mass spring system is much higher than that of some continuum methods such as finite element method. Interactive simulation of mass spring systems is possible with today's desktop systems. However, mass spring systems have some drawbacks (Baraff and Witkin, 1992). The discrete model is an approximation of continuous objects. The lattice is tuned through its spring constants, and proper values for these constants are not always easy to derive from measured material properties. In addition, mass spring systems sometimes exhibit poor stability, requiring the numerical integrator to take small time-steps and thus resulting in a slow simulation.

Finite element method provides more precise simulation by treating deformable objects as continuum solid bodies. In finite element method, the model and the method used to solve it are separated. Models can be discrete or continuous whilst the numerical methods used for solving the models are discrete. Similar to mass spring system, finite element method also needs numerical integration techniques to approximate the system at discrete time steps. Furthermore, even a continuum model must be parameterized by a finite state vector. However, unlike the discrete mass spring models, continuum models are derived from equations of continuum mechanics. The use of finite element method in computer graphics has been limited because of the computational requirements. In particular, it has proven difficult to apply finite element method in real-time systems. Because the force vectors and the mass and stiffness matrices are computed by integrating over the object, they must, in theory, be re-evaluated as the object deforms. This reevaluation is very costly and therefore is frequently avoided by assuming that objects undergo only small deformations.

Based on two types of techniques mentioned above, it is found that mass spring system is the more suitable choice in this study since the updating rate of mass spring system is much faster than that of finite element method, resulting in being able to integrate with real-time systems such as haptic interfaces which require high update rates of around 1000 Hz. In the next section, this selected technique will be applied to model intervertebral discs.

5.2. Physically Based Modeling of Intervertebral Disc

5.2.1. Classification of mass-spring systems

Mass spring system can be divided into two categories: 2D mass spring systems such as quadrilateral mesh (Figure 5.1) and triangular mesh (Figure 5.2); 3D mass spring systems such as layer based mesh (Figure 5.3), tetrahedral mesh (Figure 5.4) and hexahedral mesh (Figure 5.5). 2D mass spring systems can be used for surfaces or surface represented objects while 3D mass spring systems are applied to volumetric objects.

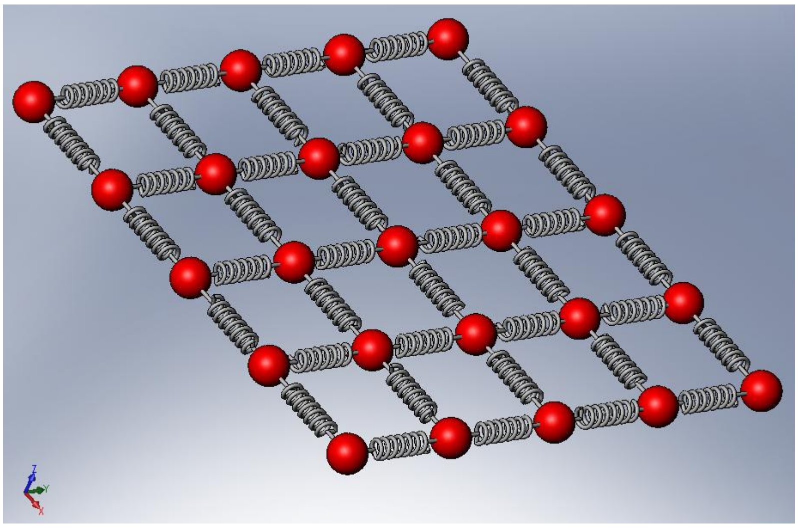

Figure 5.1 Quadrilateral mesh

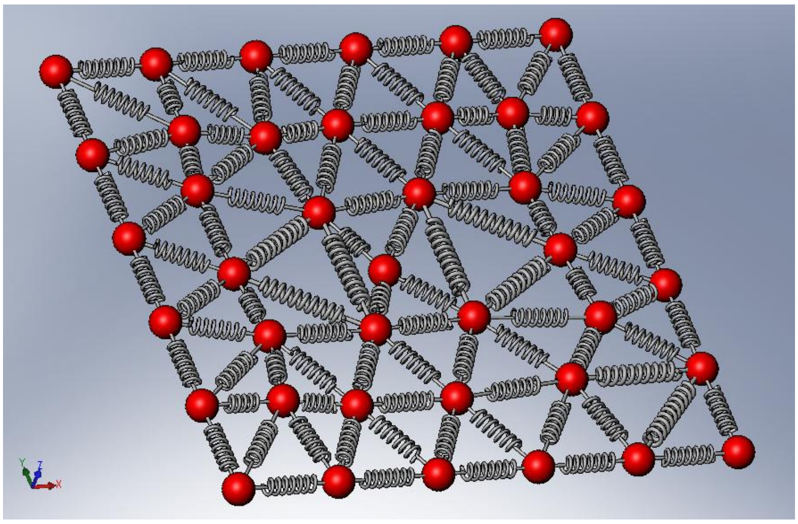

Figure 5.2 Triangle mesh

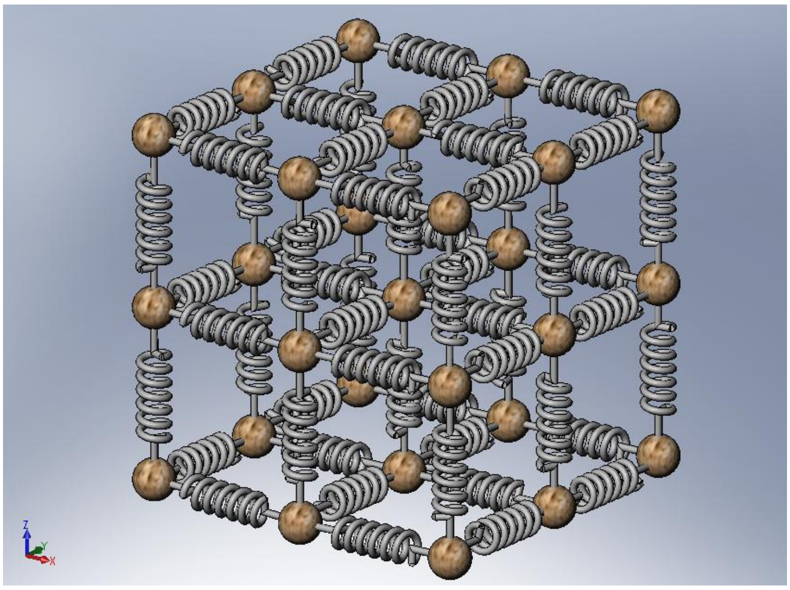

Figure 5.3 Layer based mesh

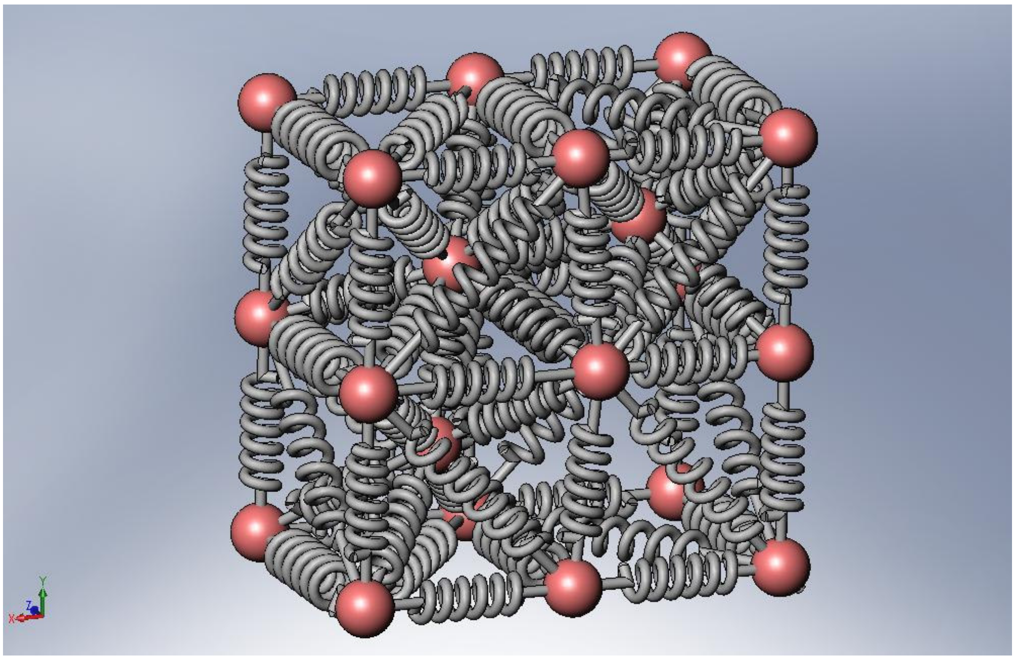

Figure 5.4 Tetrahedral mesh

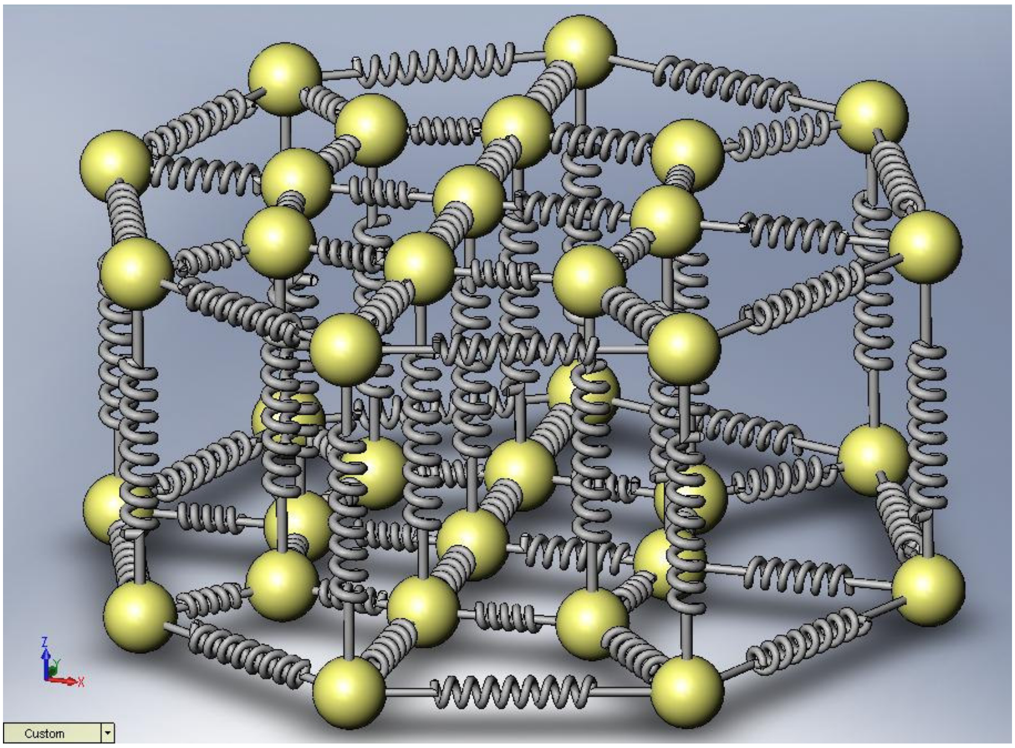

Figure 5.5 Hexahedral mesh

Compared to layer based meshes, tetrahedral and hexahedral meshes are able to represent complicated objects better. Hence, these two types of mass spring systems are widely used for modeling deformable objects. However, of these two mass spring systems, tetrahedral meshes are more commonly utilized than hexahedral ones since the geometries that hexahedral meshes can define are more limited. Thus, tetrahedral mass spring system (MSS) is selected in this study to model intervertebral discs (IVDs) which are clearly mentioned in next subsections.

5.2.2. Geometric modeling of intervertebral discs

Based on the geometry of vertebrae used as a template, the IVDs can be drawn using SolidWorks (Figure 5.6(a)). Solid models of the discs are then imported to ABAQUS software to automatically generate tetrahedral meshes as can be seen in Figure 5.6(b). Mechanical properties of the discs are assumed to be homogeneous and linear elastic. Then, the physically-based models of the IVDs can be achieved by assigning mass spring systems to the tetrahedral meshes of the discs.

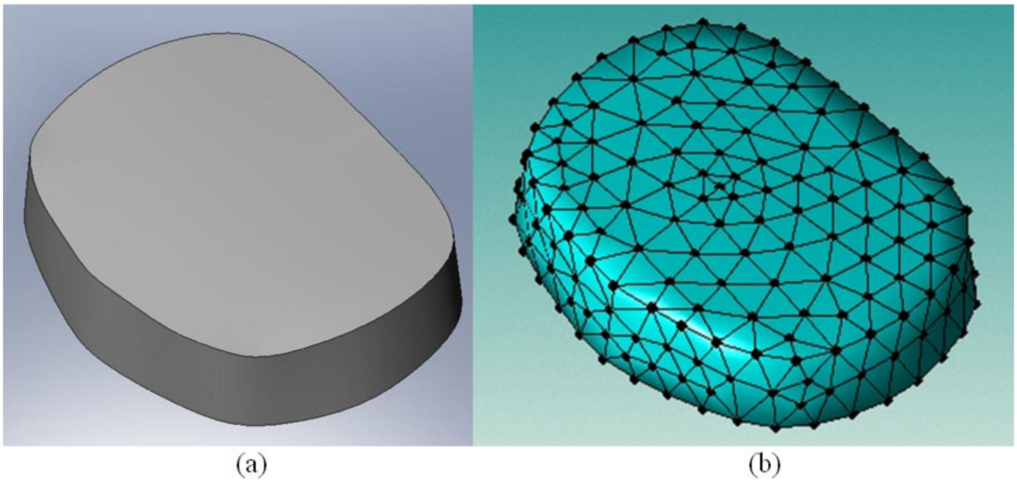
(a) (b)

Figure 5.6 Drawing and generating tetrahedral mesh of an intervertebral disc

5.2.3. Tetrahedral mass-spring system generation

Based on given nodes and elements of the disc model, masses are assigned to all nodes and springs will be attached to two ends of each pair of nodes. So, the tetrahedral mass spring system of the disc model is created. To calculate the masses of nodes in the disc model, methods based on Voronoi zones can be used (Deussen et al., 1995). However, to speed up the program, Mollemans et al. (2003) simplified this method by presuming the mass of a tetrahedron is equally divided among its vertices. The mass m_i of node *i* is thus estimated as:

$$m_i = \sum_{\forall j \in \Omega_i} \frac{1}{4} \rho_j V_j \tag{5.1}$$

where Ω_j is the union of all tetrahedra containing point *i*; ρ_j is the local density of the material in tetrahedron *j*; V_j is the volume of tetrahedron *j*.

Gelder et al. (1998) suggested a formula to compute spring stiffness for a 3D mesh that is closest to an elastic continuous representation. Let E_i be the local material elastic modulus, the spring constant of spring *i* is given by:

$$k_i = \frac{E_i * \sum_{\forall j \in \Omega_i} V_j}{l_{0i}^2} \tag{5.2}$$

where Ω_j is the collection of all tetrahedra containing spring *i*; l_{0i} is the rest length of spring *i*.

5.2.4. Adding radial springs for volume conservation

Animating constant volume deformations with mass spring systems is not straightforward. For these systems, forces are only applied along the edges of each volume element, while maintaining a constant volume basically requires adding radial forces or displacements (Promayon et al., 1996). In each tetrahedron, linear radial springs are added between the barycenter point and each vertex to simply ensure volume preservation (Bourguignon and Cani, 2000, Lee et al., 1995). Figure 5.7 shows an illustration of barycenter point and radial springs.

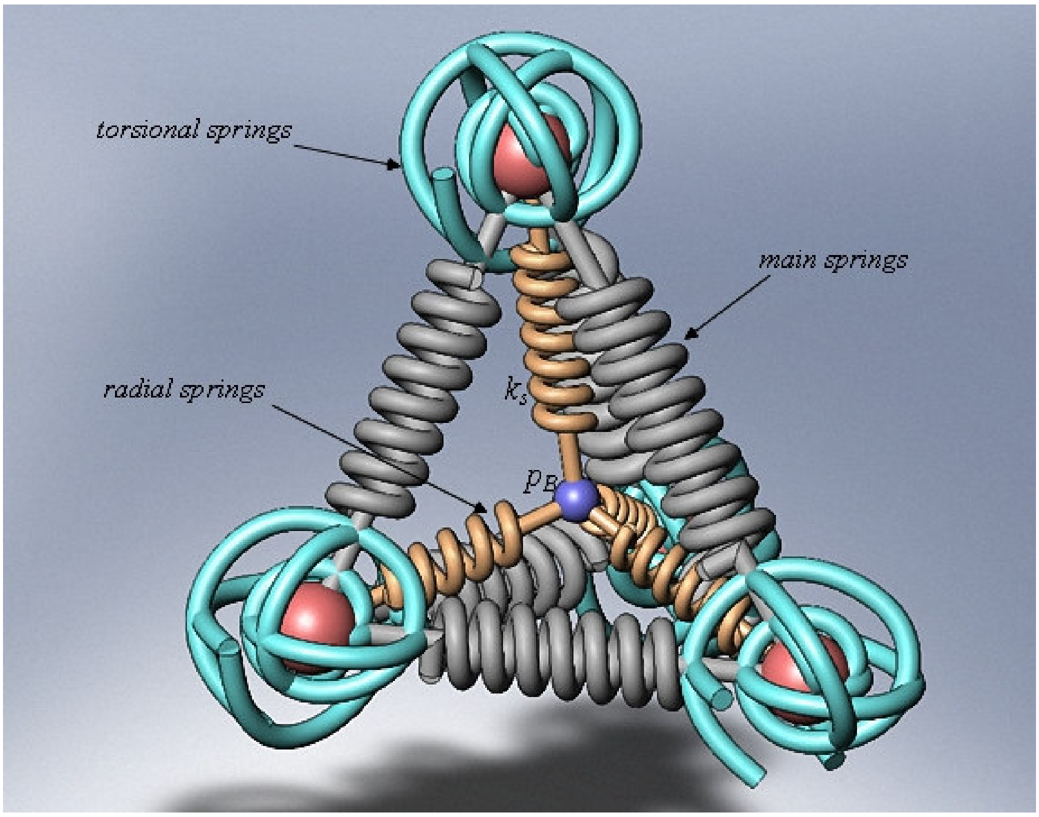

Figure 5.7 Barycenter point and radial springs in a tetrahedron

Barycenter position p_B in a tetrahedral element is defined as:

$$p_B = \frac{1}{4}\sum_{i=0}^{3} p_i \tag{5.3}$$

where p_i is the position of the ith vertex.

Then, "volume force" applying on the ith vertex in the jth tetrahedron is computed as follows:

$$f_{ij}^{vol} = k_s\left[\sum_{j=0}^{3}\left|p_j - p_B\right| - \sum_{j=0}^{3}\left|p_j - p_B\right|_{t=0}\right]\frac{p_B - p_i}{\left|p_B - p_i\right|} \tag{5.4}$$

where k_s is the stiffness of radial springs; $\sum\left|p_j - p_B\right|_{t=0}$ is the summation of the rest lengths of radial springs.

Hence, the total volume force acting on point i is:

$$f_i^{vol} = \sum_{\forall j\in\Omega_i} f_{ij}^{vol} \tag{5.5}$$

where Ω_i is the list of tetrahedra containing point i.

5.2.5. Torsional springs

To support the disc model in resisting torsion and bending, torsional springs are attached at each node in the tetrahedral MSS (Figure 5.7). In each tetrahedral element, there will be three torsional springs added at each vertex. These torsional springs lie in the planes created by the vertex they are attached to and two of the other vertices. If two tetrahedral elements have three vertices in common, they will share three torsional springs created by those three vertices. The stiffness coefficients of all torsional springs in the MSS are assumed to be equal. By using an equivalent cylinder intervertebral disc model, these coefficients can be found by the following equations:

$$D_m = \frac{D_u + D_l}{2} \tag{5.6}$$

$$L_m = \frac{4V}{\pi D_m^2} \tag{5.7}$$

$$k_t = \frac{G\pi D_m^4}{32 L_m n_t} \tag{5.8}$$

where D_m, L_m are mean diameter and length of a cylinder disc model, respectively; D_u, D_l are diameters of upper and lower surfaces of used disc model, respectively; V, n_t are volume and total number of torsional springs of used disc model, respectively; G is shear modulus of utilized material.

Based on Equations (5.1), (5.2), (5.6)-(5.8), different material properties of the tetrahedral MSS of the intervertebral disc can be specified with the given modulus and density. Since annulus and nucleus regions have different moduli, the approximate elastic and shear moduli for the entire disc are used in this study. Volume percentages of annulus and nucleus regions can be estimated by computing their cross-sectional area percentages. The ratio of the cross-sectional area of the nucleus to the total disc cross-sectional area is assumed to be 40% (Krismer et al., 1996). Material properties of the disc such as modulus, density, and Poisson's ratio can be found in literature (Qiu et al., 2006, Zhang et al., 2008).

5.2.6. Physical-based deformation of mass-spring system

Total force F_i applied on a mass point i of MSS includes external forces and internal forces, which can be expressed as below:

$$F_i = f_i^{ext} + f_i^{\text{int}} \tag{5.9}$$

where f_i^{ext} and f_i^{int} are external forces and internal forces acting on the ith point, respectively.

The internal forces f_i^{int} are defined as:

$$f_i^{\text{int}} = f_i^{main} + f_i^{vol} + f_i^{tor} + f_i^{damp} \tag{5.10}$$

where f_i^{main}, f_i^{vol}, f_i^{tor} and f_i^{damp} are forces of main springs, radial springs, torsional springs and damping factor acting on the ith point, respectively.

The damping force f_i^{damp} is given by:

$$f_i^{damp} = -K_d v_i \tag{5.11}$$

where K_d is damping constant of ambient environment; v_i is the velocity of the ith point.

The force of main springs f_i^{main} is computed as:

$$f_i^{main} = \sum_{\forall j \in \Omega_i} k_{ij} \frac{l_{ij}}{\left|l_{ij}\right|}\left(\left|l_{ij}\right| - r_{ij}\right) \tag{5.12}$$

where Ω_i is the collection of all springs connected to point i; l_{ij} is the vector from point i to point j; k_{ij} and r_{ij} are stiffness constant and rest length of the spring connected from point i to point j, respectively.

Equation for torsional forces f_i^{tor} is:

$$f_i^{tor} = -\sum_j \frac{Axis\, x\, l_{ij}}{\left|Axis\, x\, l_{ij}\right|}\left(\frac{k_t\left(\theta_r - \theta\right)}{\left|l_{ij}\right|}\right) \tag{5.13}$$

where *Axis* is vector of cross product of two connecting l_{ij}; θ is angle between two connecting l_{ij}; θ_r is corresponding rest angle of torsional spring.

Under external forces, the position, velocity and acceleration of each mass point in the mass spring system can be computed using Newton's second law. Let t denote the time variable, the mass spring system can be described as a system of differential equations

$$\begin{bmatrix} \frac{dx_1}{dt} \\ \frac{dx_2}{dt} \\ \vdots \\ \frac{dx_n}{dt} \end{bmatrix} = \begin{bmatrix} v_1 \\ v_2 \\ \vdots \\ v_n \end{bmatrix} \tag{5.14}$$

And

$$\begin{bmatrix} \frac{dv_1}{dt} \\ \frac{dv_2}{dt} \\ \vdots \\ \frac{dv_n}{dt} \end{bmatrix} = \begin{bmatrix} F_1/m_1 \\ F_2/m_2 \\ \vdots \\ F_n/m_n \end{bmatrix} \tag{5.15}$$

Define

$$X(t) = \begin{bmatrix} x_1 \\ x_2 \\ \vdots \\ x_n \end{bmatrix}, V(t) = \begin{bmatrix} v_1 \\ v_2 \\ \vdots \\ v_n \end{bmatrix} \tag{5.16}$$

And

$$a(t) = \begin{bmatrix} F_1/m_1 \\ F_2/m_2 \\ \vdots \\ F_n/m_n \end{bmatrix} \tag{5.17}$$

Equations (5.14) and (5.15) become:

$$\frac{dX(t)}{dt} = V(t) \tag{5.18}$$

$$\frac{dV(t)}{dt} = a(t) \tag{5.19}$$

Since Equations (5.18) and (5.19) show that this is a first order differential equation system, numerical methods can be used to solve these equations. To find out the new position and velocity of the mass points, the most straightforward approach is Euler integration. At each finite time step Δt of the integration, the velocity $\Delta \vec{X}(t)/\Delta t$ of the mass point is updated according to the applied forces as well as the material parameters such as mass, damping, and stiffness. The mass points are moved to a new position $\vec{X}(t_{i+1})$ which is calculated as follows:

$$\frac{d}{dt}\vec{X}(t_{i+1}) = \frac{d}{dt}\vec{X}(t_i) + \frac{d^2}{dt^2}\vec{X}(t_i) * \Delta t \tag{5.20}$$

$$\vec{X}(t_{i+1}) = \vec{X}(t_i) + \frac{d}{dt}\vec{X}(t_i) * \Delta t \tag{5.21}$$

Since Euler integration for mass spring system deformation requires small time steps to maintain stability, it can run at 1 kHz. The initial value of positions, velocities, and external forces are preset before the program executes. The initial internal force is zero everywhere in the beginning. Then, the total force of every mass point is computed and the new position and velocity are determined according to Equations (5.20) and (5.21). After the tetrahedral MSS model of intervertebral discs are generated, it is necessary to test the functional performance of this model which will be presented in the subsequent section.

5.3. Testing the Functional Performance of Tetrahedral Mass-Spring System Model of IVDs

The purpose of this section is to examine how well the tetrahedral MSS model of intervertebral discs performs under loading before combining it into the thoracolumbar spine model. Initially, to verify if the tetrahedral MSS model of an intervertebral disc consistently deforms and its volume is preserved under external forces, a spherical rigid probe is used for interacting with the disc. The users can control the probe by manipulating the haptic PHANToM device to apply forces on the disc model. These forces are considered as external forces for calculating the deformation of the disc as presented in subsection 5.2.6. Figure 5.8 shows the volume preservation of an intervertebral disc under continuous deformation.

As can be seen in Figure 5.8, the users can manipulate the rigid probe to explore and perceive the mechanical properties of the disc such as rigidity and compliance through the force feedback of the PHANToM device. For the materials of high Young’s modulus, the user can touch and feel the exact shape of the disc. Since the stiffness constants of all springs in the tetrahedral MSS are large, the disc acts as a rigid object. Conversely, for the materials of low Young’s modulus or small stiffness constants, the disc becomes a soft object and the users can easily deform the disc with the probe. Besides, the anisotropic property of the disc can be observed during the deformation process. With equal applying forces, the deformation at each region in the disc is different. This is because the masses of all nodes and the stiffness constants of all springs in the MSS are defined differently. During deformation, the volume of the disc is constant. This property is clearly seen in Figure 5.8. In the first three figures (Figure 5.8(a), (b) and (c)), the probe is controlled to apply external force to the disc surface. In a short period of time, the deformation process occurs quickly and the disc is deformed. Then, the probe is pulled out and deforms at another region of the disc (Figure 5.8(d), (e) and (f)). Meanwhile, the previously deformed region starts to restore its shape gradually. In the last three figures (Figure 5.8(g), (h) and (i)), the disc is largely deformed and finally returns to the original shape.

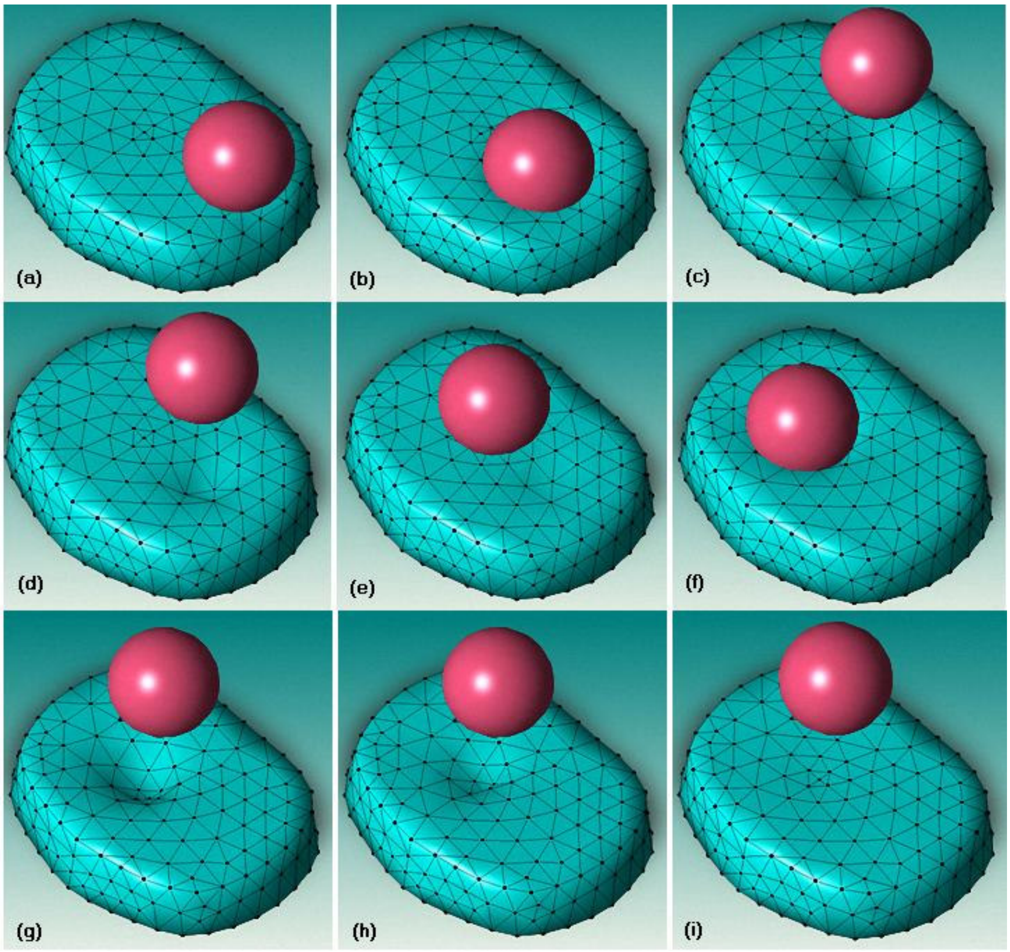

Figure 5.8 Volume preservation under continuous deformation

After the first test above, the disc is interposed between two vertebrae such as L2-L3 in this study and a second test can be conducted. In the second test, the users can manipulate the vertebrae instead of the probe to interact with the disc. The upper and lower surfaces of the disc are rigidly attached to the lower and upper surfaces of the superior and inferior vertebrae respectively. The inferior vertebra L3 is fixed in 3D space. When the users control superior vertebra L2 to apply forces to the disc, the disc regions adjacent to the upper surface are deformed. After that, the deformation of the adjacent regions will propagate through the entire intervertebral disc via the tetrahedral MSS model. As a result, the ultimate deformation of the disc can be obtained.

To test the influence of different materials on the deformation performance of the intervertebral disc, some selected materials such as rubber and low-density polyethylene are used in this study. Table 5.1 below lists the properties of these materials.

Table 5.1 Properties of some selected materials

Materials	Density (kg/mm^3)	Young modulus (MPa)	Shear modulus (MPa)
Rubber	1.522×10^{-6}	30	0.6
Polyethylene	0.91×10^{-6}	200	117
Real disc	1.038×10^{-6}	3.22	1.106

Figure 5.9 shows the disc compression performance of these two materials compared to an approximation of the actual material of the disc. In Figure 5.9, disc compression responses in the first three figures (Figure 5.9(a), (b) and (c)) are of actual material of the disc, the next three (Figure 5.9(d), (e) and (f)) are of rubber and the last three (Figure 5.9(g), (h) and (i)) are of polyethylene. As can be seen in Figure 5.9, the disc is compressed most with

actual material and least with polyethylene material. This is because the Young's modulus of polyethylene material is highest, leading to the stiffness coefficients being largest.

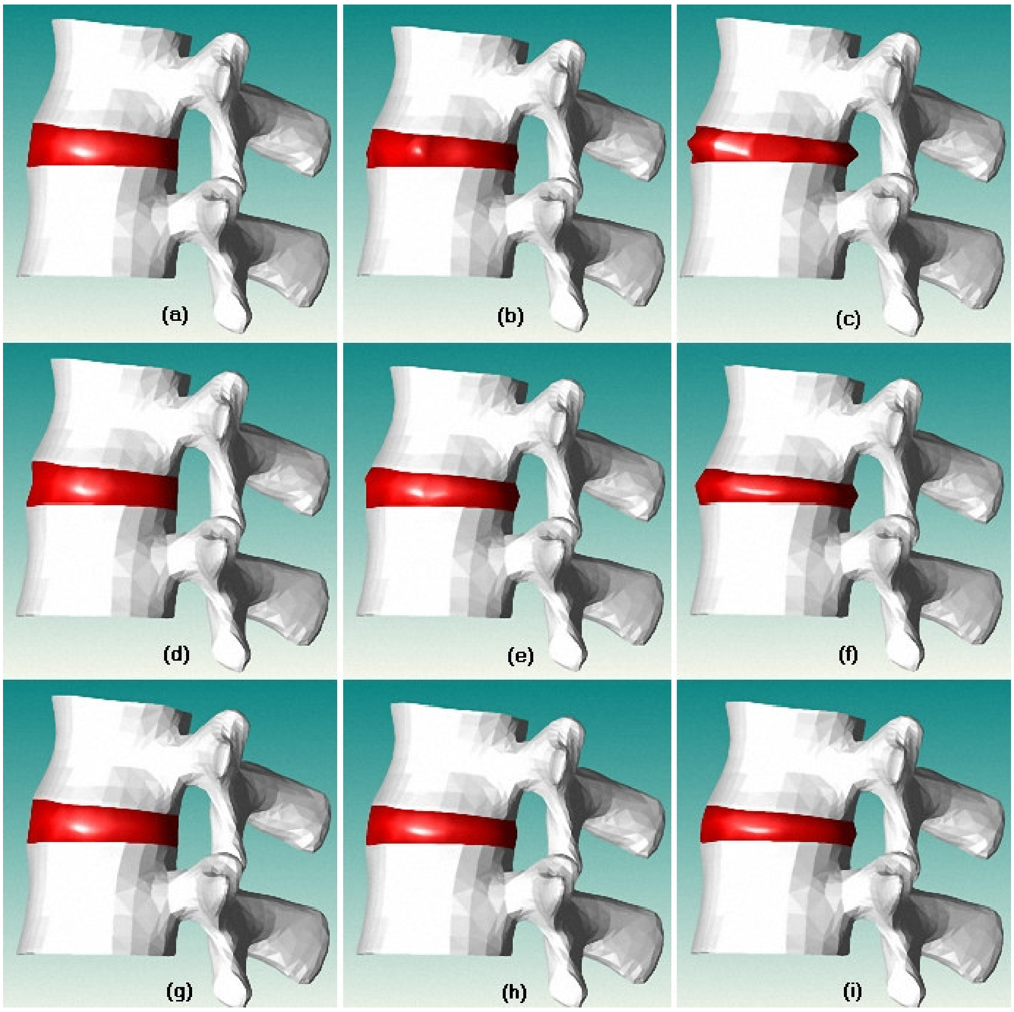

Figure 5.9 Disc compression with different materials

Based on the two tests mentioned above, it is obviously concluded that the tetrahedral MSS model of the intervertebral discs can preserve their volumes under continuous loading and consistently deform with different assigned materials. After these tests, connection between this tetrahedral MSS model of the intervertebral discs and the thoracolumbar spine model will be clearly described in the next section.

5.4. Combination between the Tetrahedral Mass-Spring System Model of Intervertebral Discs and the Thoracolumbar Spine Model

The purpose of combining the tetrahedral MSS model of IVDs with the thoracolumbar spine model is to create a hybrid model which can be used to conveniently study biodynamic behavior of the spine in real-time haptic simulations as well as deformation response of all IVDs in offline simulations. As presented in section 5.2, after tetrahedral MSS models of all IVDs are generated, these IVDs will be interposed between vertebrae of the thoracolumbar spine model. The upper and lower surfaces of each IVD are rigidly attached to the lower and upper surfaces of the superior and inferior vertebrae respectively. Figure 5.10(a) shows all tetrahedral MSS models of IVDs. Figure 5.10(b) and (c) show IVDs before and after assembling into the thoracolumbar spine model.

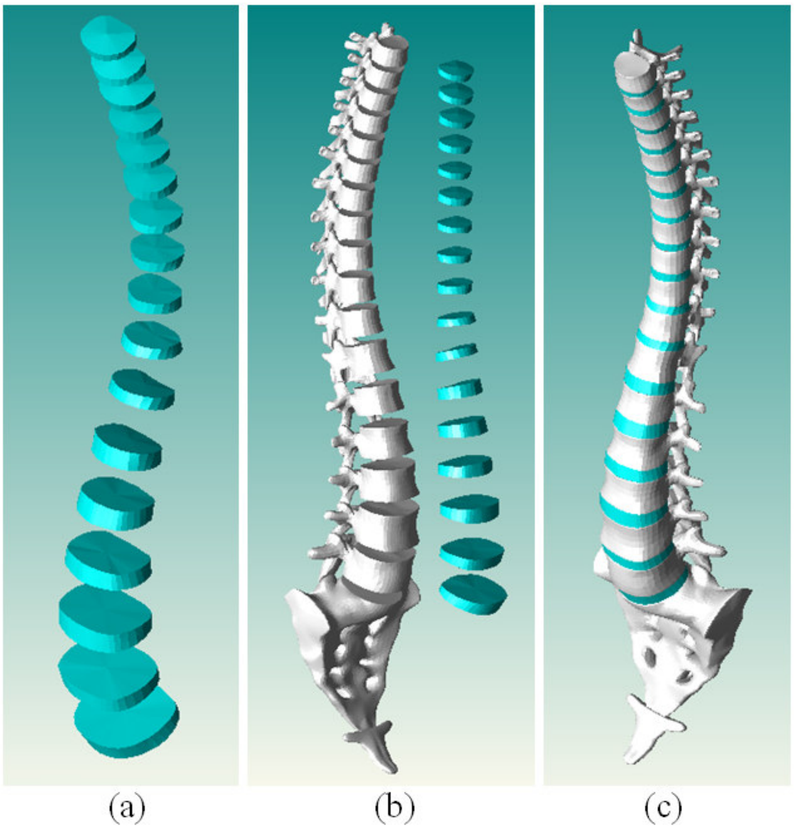

Figure 5.10 Combination between tetrahedral MSS models of IVDs and the thoracolumbar spine model

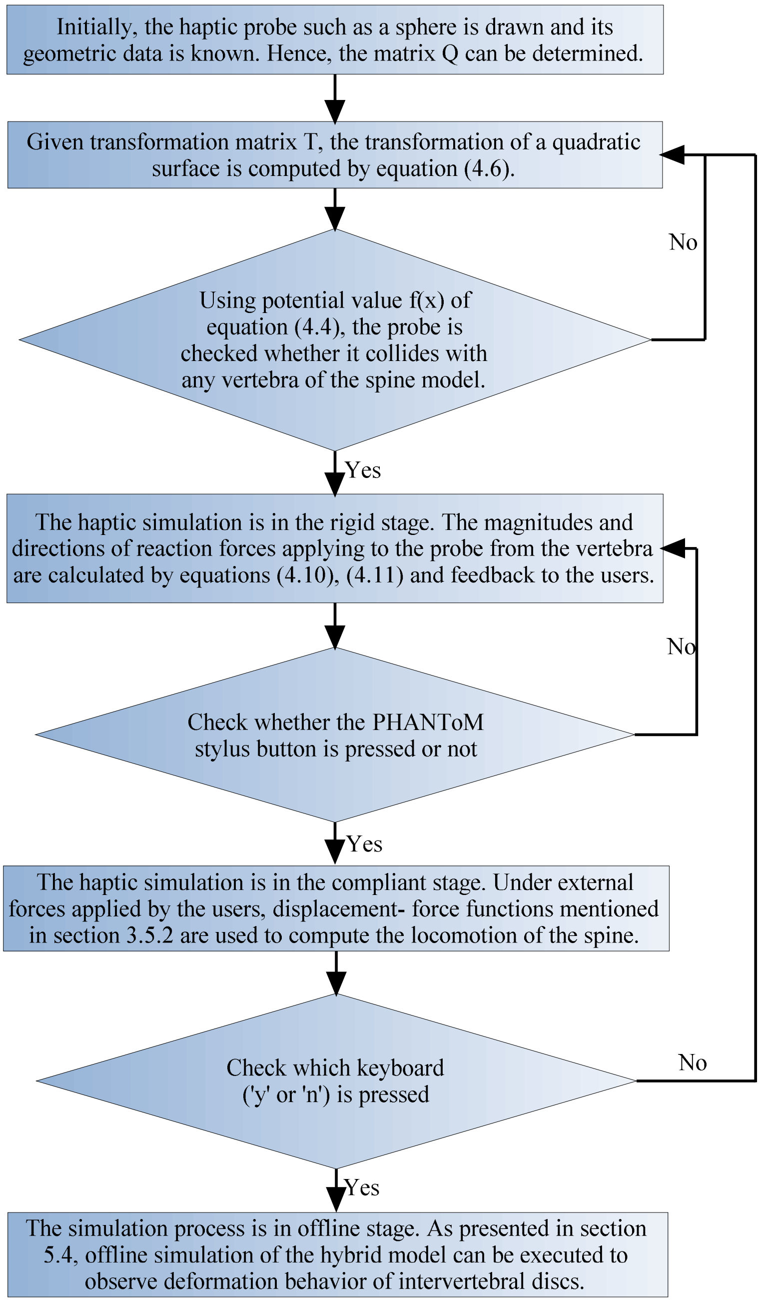

Figure 5.11 Complete simulation process of the spine model in this research

In this research, the complete simulation process consists of two stages in order: real-time haptic simulation of the spine and offline simulation of IVDs (Figure 5.11). The thoracolumbar spine model including vertebrae only is used in the real-time haptic simulation whereas in the offline simulation of IVDs is the hybrid one. To combine with offline simulation of IVDs, the haptic real-time simulation of the spine model is required first to record the

)

information of displacements, rotations and orientations of all vertebrae. The recording process is started when the users presses the PHANToM stylus button to apply external forces onto a certain vertebra where he/she wishes to explore. This process is continued and ended when the users release the stylus button to remove the external forces. Next, based on recorded information of displacements, rotations and orientations of all vertebrae, deformation behavior of all IVDs is calculated using tetrahedral MSS. Then, the whole thoracolumbar spine model including all IVDs is graphically rendered in the offline simulation. The users can start another new haptic real-time simulation by pressing the stylus button again and a new offline simulation of all IVDs will be executed when the stylus button is released. Some simulation cases of this hybrid model are illustrated in sections 6.3 and 6.4 of chapter 6.

5.5. Summary

This chapter mainly focused on developing a novel tetrahedral mass-spring system model of intervertebral discs to study offline deformation behavior of the spine model including intervertebral discs under external forces applying onto any vertebra in any arbitrary direction. At first, some basic techniques of deformable object modeling such as finite element and mass-spring system methods were briefly introduced. Compared to finite element method, mass-spring system one was chosen in this study because it is able to integrate with haptic interfaces better. After that, several common mass-spring systems were mentioned and tetrahedral mass-spring system is chosen as the most suitable choice since it can represent more complicated geometries than other approaches. Then, a new physically-based model of intervertebral discs using this tetrahedral mass-spring system was presented in detail. Afterwards, some tests on functional performance of this tetrahedral mass-spring system model of intervertebral discs were conducted before coming into use. The tests proved that the tetrahedral mass-spring system model of intervertebral discs can maintain volume conservation under loading and consistently deform with different assigned materials. Subsequently, the tetrahedral mass-spring system model of intervertebral discs was combined with the thoracolumbar spine model to generate a hybrid model which can be useful for quickly and conveniently studying biodynamic behavior of the spine in real-time haptic simulations as well as deformation response of all IVDs in offline simulations. These simulations will be clearly illustrated in the next chapter.

CHAPTER 6

APPLICATIONS OF THE SPINE MODEL

After the discretized musculo-skeletal multi-body spine model was completely developed in LifeMOD and a haptically integrated graphic interface was successfully built in previous chapters, some important and useful applications of the spine model to the medical field such as clinical treatment and surgical training are thoroughly presented here.

6.1. Studying and comparing biodynamic behaviour of spinal fusion with normal spine models

Spinal fusion became a popular surgical procedure for chronic disabling back pain during the past 20 years but is widely considered to be a last resort as long-term complications can often arise due to the nature of the procedure. Although surgical procedures involving vertebral fusion produce a relatively good short-term clinical result in relieving pain, they alter the biomechanics of the spine. For example, they will immobilize the spine unit and reduce the spine’s range of motion. In addition, they can lead to further degeneration of the discs at adjacent levels.

These problems can be verified by using the detailed spine model presented above. In the present spine model, spinal fusion can be made at either L3-L4 or L4-L5 level by applying fixed joints between vertebrae. In severely degenerated cases, these two levels are fused together. Then, external forces are imposed on a certain vertebra and comparison between spinal fusion and a normal spine model can be achieved. Figure 6.1 to Figure 6.3 show three cases of locomotion comparisons between the normal spine model and fusion at L3-L4 level, fusion at L3-L4 and at L4-L5 levels, fusion at L3-L4 and at L3-L4-L5 levels respectively.

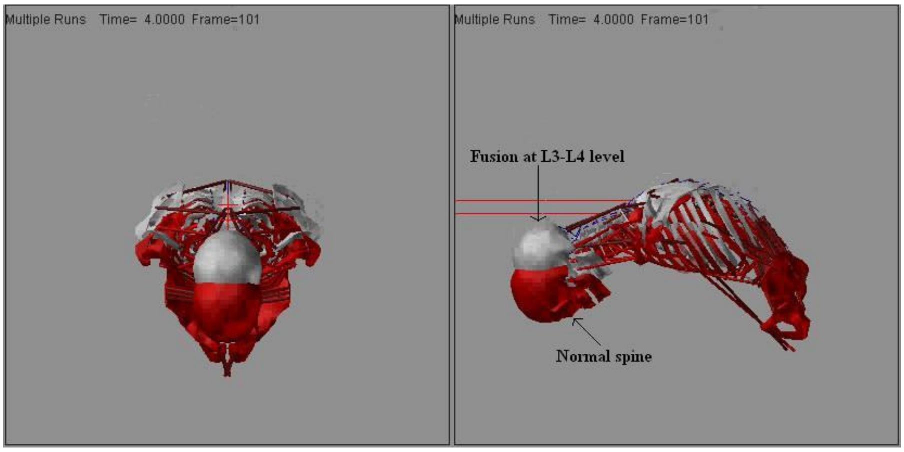

Figure 6.1 Locomotion comparison between normal spine and spinal fusion at L3-L4 level

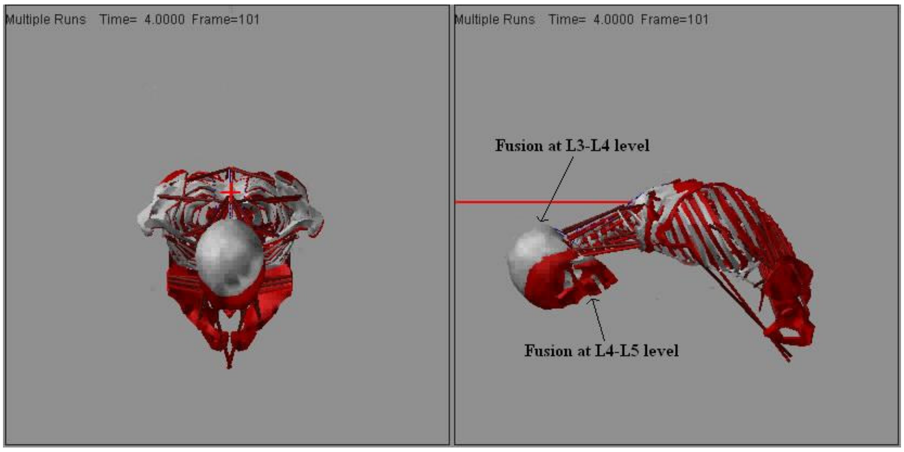

Figure 6.2 Locomotion comparison between spinal fusion at L3-L4 level and at L4-L5 level

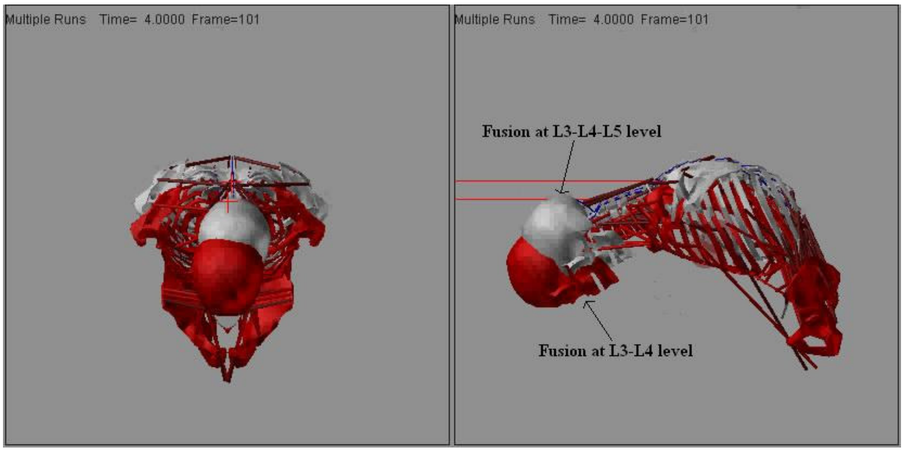

Figure 6.3 Locomotion comparison between spinal fusion at L3-L4 level and at L3-L4-L5 level

In the first case, as can be seen in Figure 6.1, under identical external forces on the same vertebra, the locomotion of the normal spine model is more flexible than that of spinal fusion at L3-L4 level. This is because each intervertebral disc interposing between two vertebrae allows them to have relative movement to each other in the normal spine whereas this movement does not exist in fusion at L3-L4 level. Meanwhile, in the second case, Figure 6.2 displays that the displacement of spinal fusion at L4-L5 level is a little bit more flexible comparing to spinal fusion at L3-L4 level. In the third case, it is easily observed that the locomotion of spinal fusion at L3-L4-L5 levels is much less flexible than that of spinal fusion at L3-L4 level (Figure 6.3). Through these three cases, it can be consistently concluded that spinal fusion made at L3-L4-L5 levels will restrict the range of motion of the whole spine the most and spinal fusion at L3-L4 level will reduce the range of motion more than at L4-L5 level. The same results are achieved when applying equal backward and lateral forces on the same vertebra of the spine model.

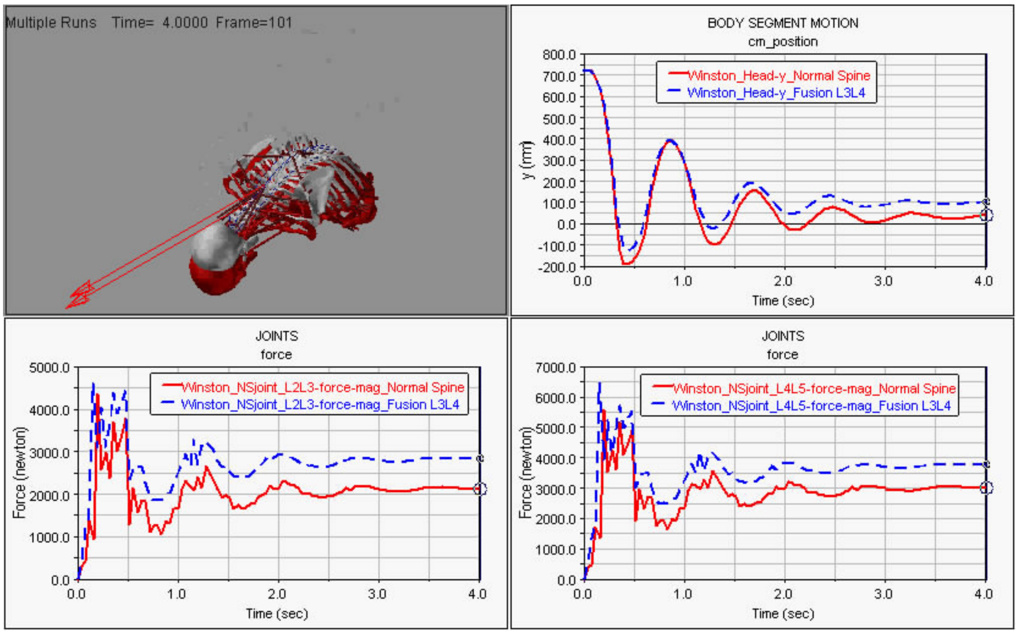

Figure 6.4 Comparing forces acting on intervertebral joints between normal spine and fusion at L3-L4 level

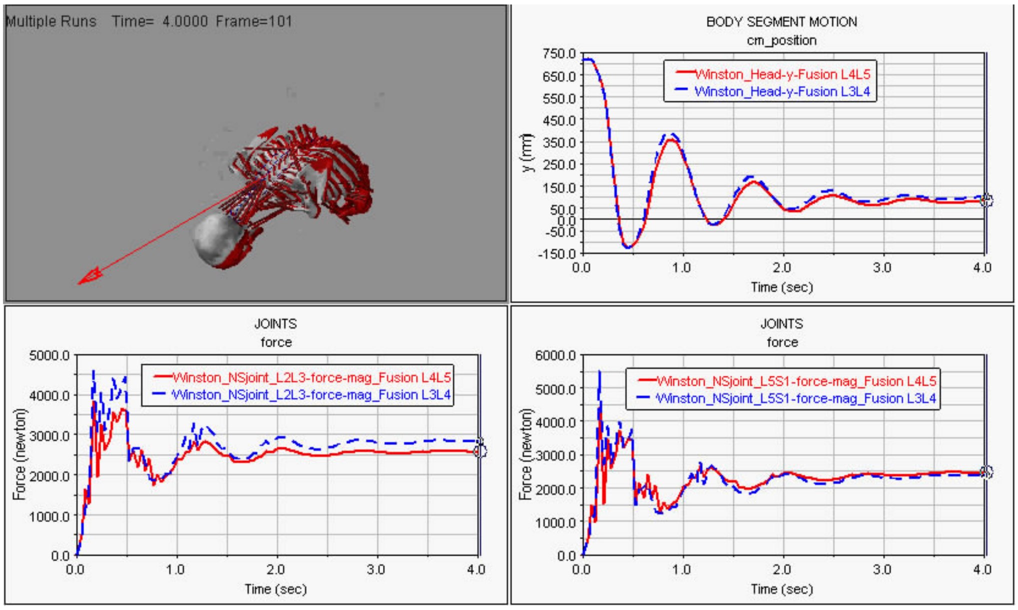

Figure 6.5 Comparing forces acting on intervertebral joints between fusion at L3-L4 and at L4-L5 levels

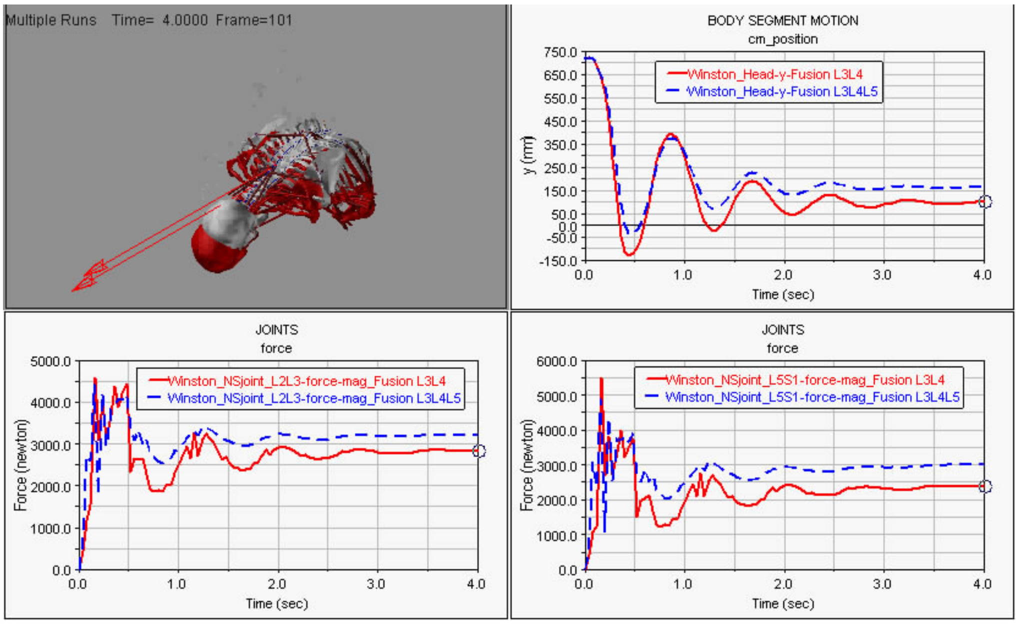

Figure 6.6 Comparing forces acting on intervertebral joints between fusion at L3-L4 and at L3-L4-L5 levels

In addition to the locomotion comparisons, comparing dynamic properties (such as forces acting on intervertebral joints) between the normal spine model and spinal fusions corresponding to three cases above are also conducted in this study. Figure 6.4 to Figure 6.6 display translation in the y-axis direction of the head and forces on joints upper and lower the fusion level, which corresponds to the three cases aforementioned.

In the first case, as can be seen in Figure 6.4, although the locomotion of spinal fusion at L3-L4 level is much less than that of the normal spine under identical forward forces on the same vertebra, internal forces generated on intervertebral joints adjacent to the fusion level are much larger than those of the normal spine. This result implies that spinal fusion will lead to further degeneration of the adjacent levels in the long term. In the second case, Figure 6.5 shows that internal forces on the L5-S1 joint corresponding to spinal fusion made either at L3-L4 or at L4-L5 level are more or less equal whereas the force on L2-L3 joint of fusion at L3-L4 level is larger than that of fusion at L4-L5 level. In the third case, it is obviously observed that forces either on L2-L3 or on L5-S1 joint of spinal fusion at L3-L4-L5 levels are much larger than those of spinal fusion at L3-L4 level (Figure 6.6). In general, some consistent findings can be drawn from these three cases. Firstly, since internal forces generated on L2-L3 and L5-S1 joints corresponding to the spinal fusion at L3-L4-L5 levels are largest, further degeneration of these adjacent levels will occur most rapidly compared to the other cases. Secondly, fusion at L3-L4 level will make the L2-L3 level degenerate more than that at fusion at L4-L5 level. However, degeneration rate at L5-S1 level in both types of fusion is almost the same due to nearly equal forces generated on this L5-S1 joint. In other words, degeneration may happen least with fusion at L4-L5 level. These key findings are greatly valuable for surgeons to gain insight into the biomechanical difference between spinal fusions and the normal spine as well as degeneration process of the adjacent vertebra segments and to find suitable solutions for the spinal fusions. It should be noted that these findings obtained here are rough results for a specific human anatomy and can vary in accordance with different personal anatomies.

6.2. Step-by-step developing a human-wheelchair interface to provide means of designing effective seating solutions

As presented earlier, the prolonged sitting in a chair was reported to be linked with lower back problems. Hence, a feasible application of the detailed spine model briefly introduced in this section is that developing a design system which can simulate the kinematic behavior of musculoskeletal forms, and generating a human-wheelchair interface to provide an accurate means of designing effective seating solutions for wheelchair users and preventing long-term spinal deformities. This virtual simulation platform can help clinicians in their analysis to ensure a higher degree of accuracy and consistency in their prescriptions.

Initially, a CAD model of a wheelchair design was imported into the LifeMOD environment. Then, a detailed spine model as presented in previous chapters was generated to interact with the chair model during simulation. The spine model can provide useful information (such as contact forces between each vertebrae and wheelchair model, load acting on the intervertebral disc joints, relative angles between vertebrae in the seated position, and tension in the spine muscles) for clinicians to deeply understand the complex spine biomechanics and do clinically important analysis. Figure 6.7 illustrates human-chair interactive simulation and the obtained contact force between lower torso and the chair model. Figure 6.8 shows force and torque of the L5-S1 disc in x, y, z directions. These results can aid the clinicians to propose simple seating solutions like placing conventional pillows, towels at appropriate positions of improved back supports for developing special seating solutions for wheelchair-bound patients.

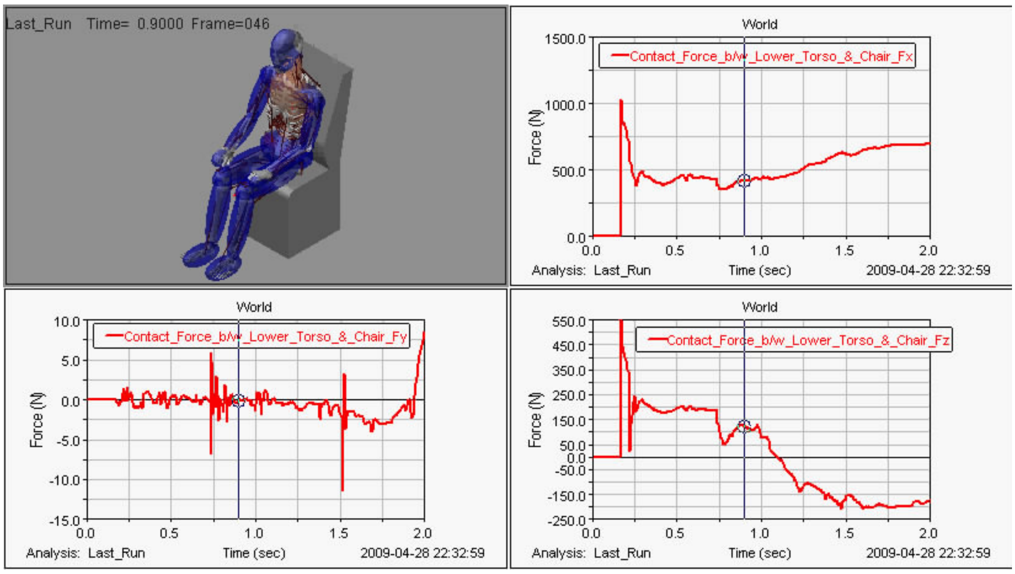

Figure 6.7 Contact force between lower torso and chair model

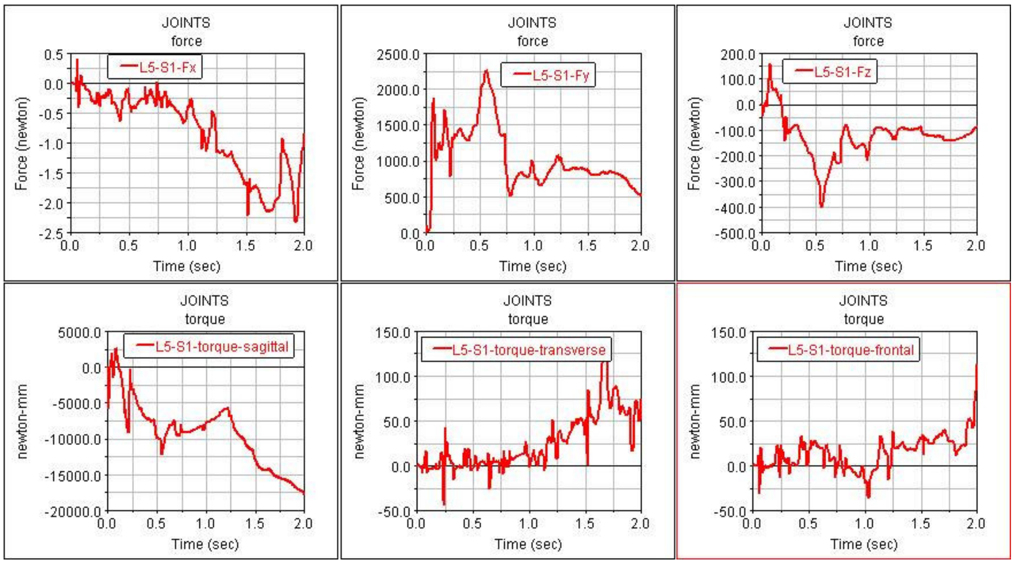

Figure 6.8 Force and torque of the L5-S1 disc in x, y, z directions

6.3. Real-time haptic simulation of a thoracolumbar spine model under external haptic forces

After the haptically integrated graphic interface was successfully built as presented in Chapter 4, some real-time haptic simulations of the spine model under external forces acting on a certain vertebra in axis-aligned or in arbitrary directions are conducted. Figure 6.9 to Figure 6.11 illustrate three real-time haptic simulation cases of spine locomotion when applying force on vertebra T1 in x-axis, z-axis and arbitrary directions respectively. Figure 6.12 to Figure 6.17 and Figure 6.18 to Figure 6.25 show relative translation of each pair of vertebrae corresponding to the first and second cases above.

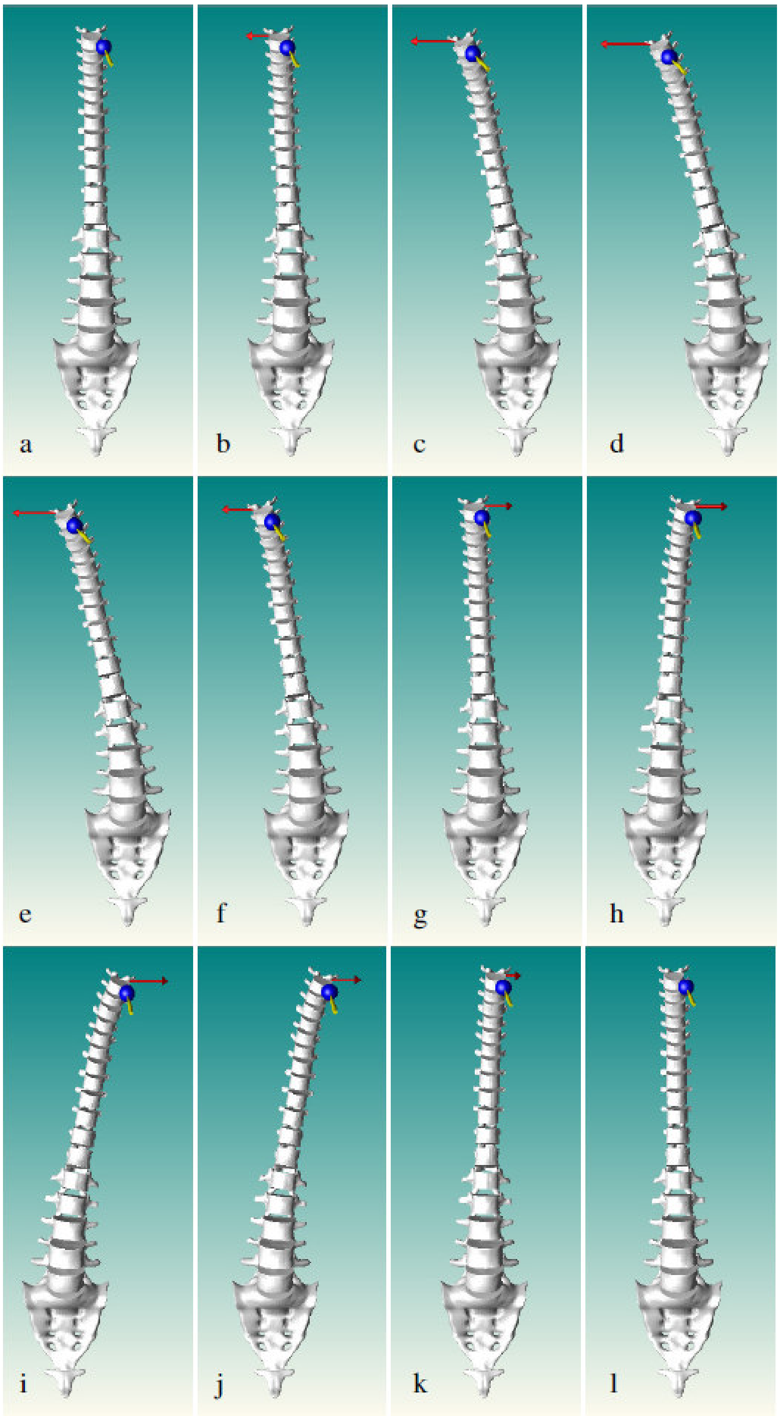

Figure 6.9 Haptic simulation of the spine under lateral force on T1

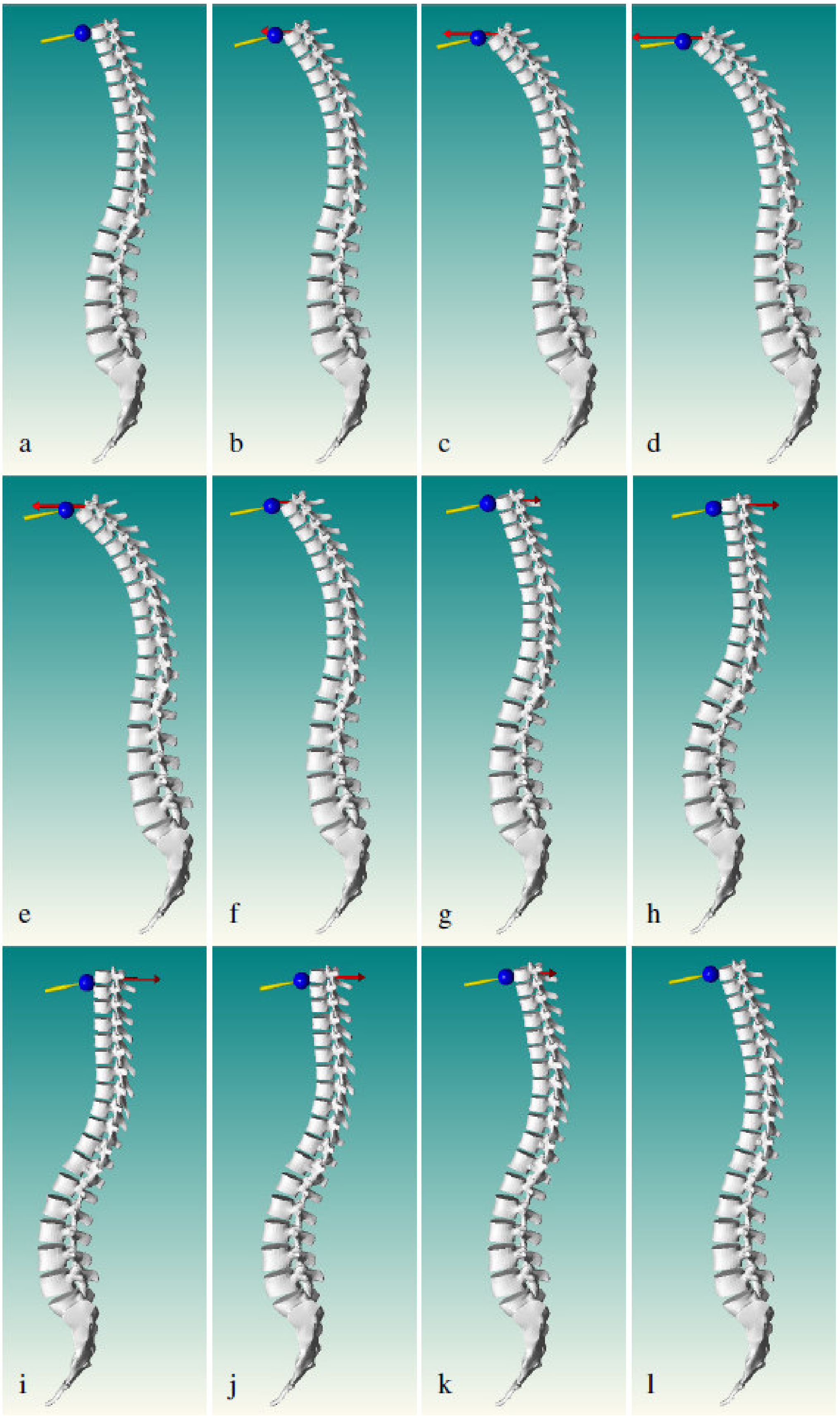

Figure 6.10 Haptic simulation of the spine under sagittal force on T1

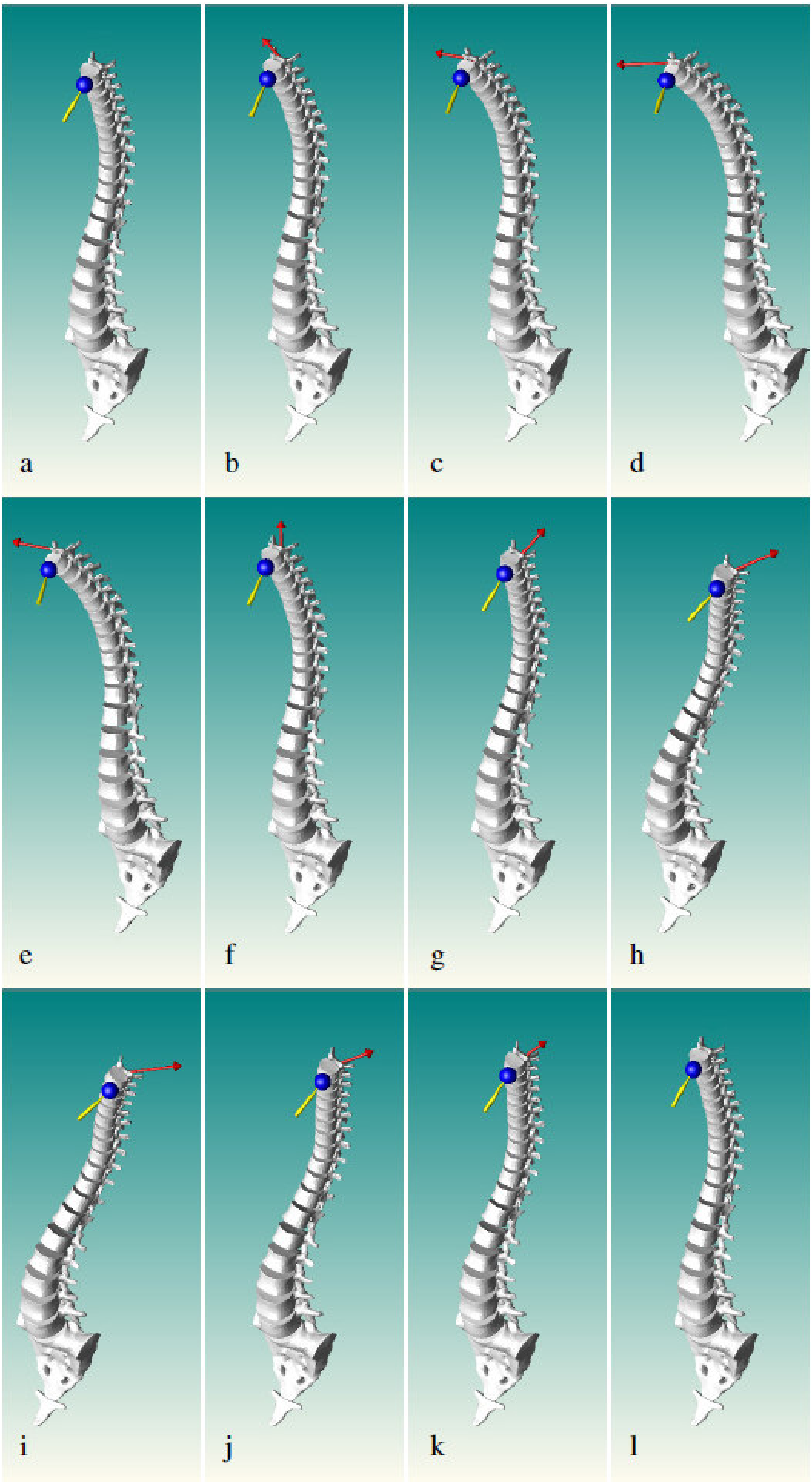

Figure 6.11 Haptic simulation of the spine under arbitrary force on T1

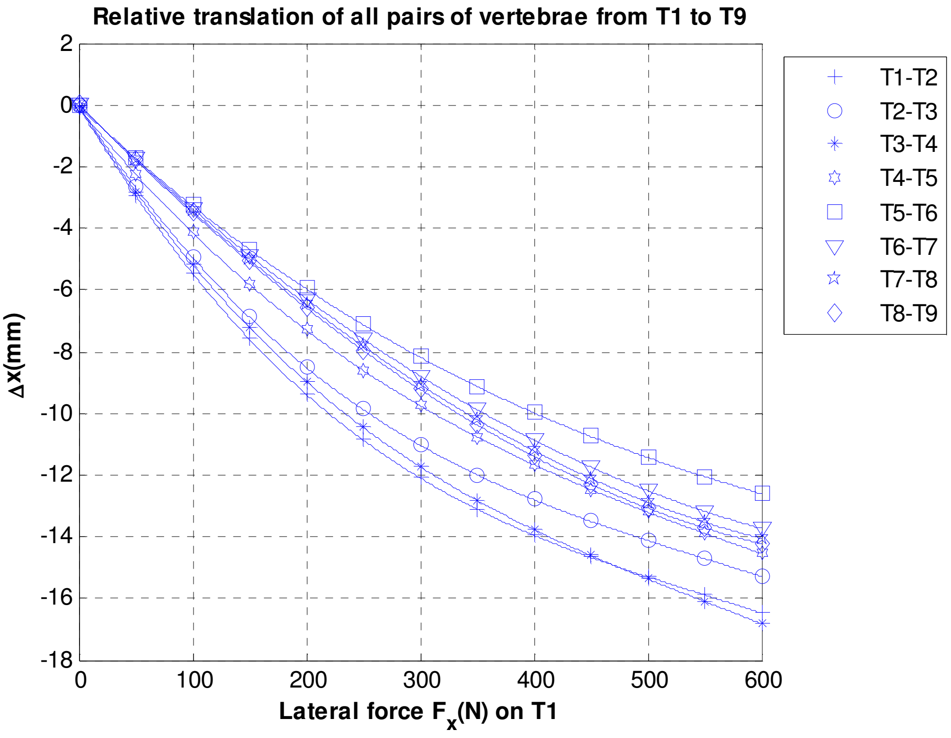

Figure 6.12 X-axis relative translation of all pairs of vertebrae from T1 to T9 under lateral force on T1

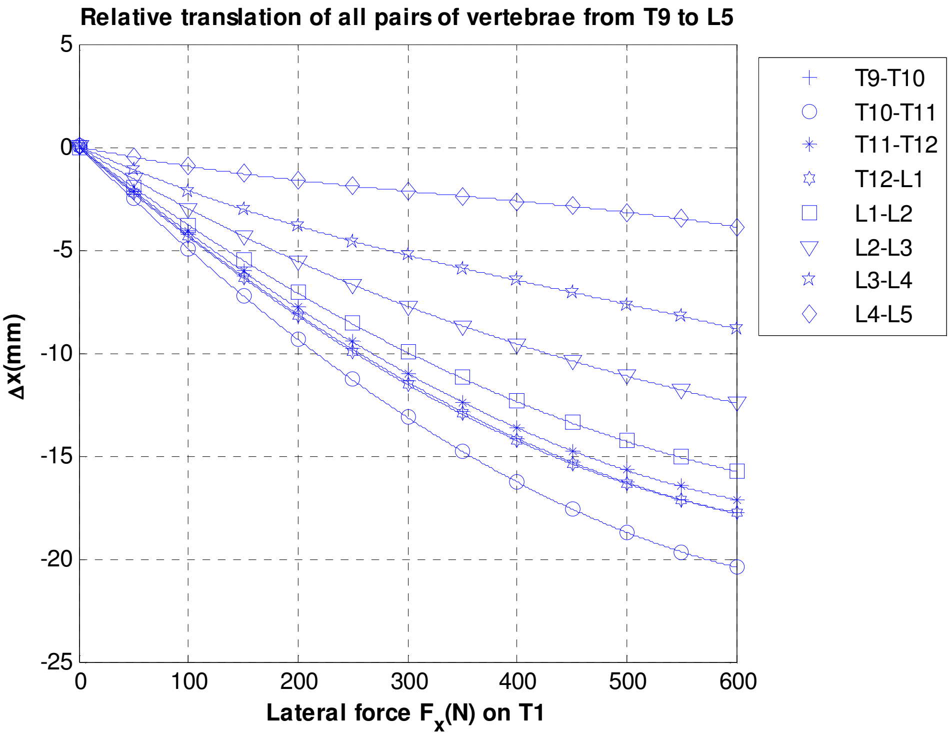

Figure 6.13 X-axis relative translation of all pairs of vertebrae from T9 to L5 under lateral force on T1

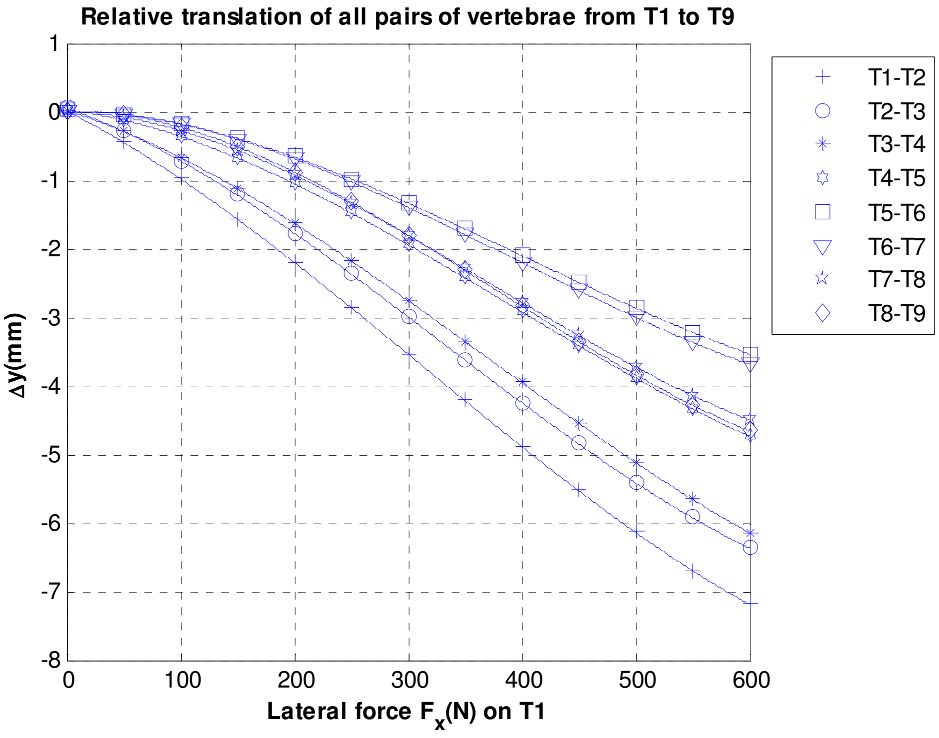

Figure 6.14 Y-axis relative translation of all pairs of vertebrae from T1 to T9 under lateral force on T1

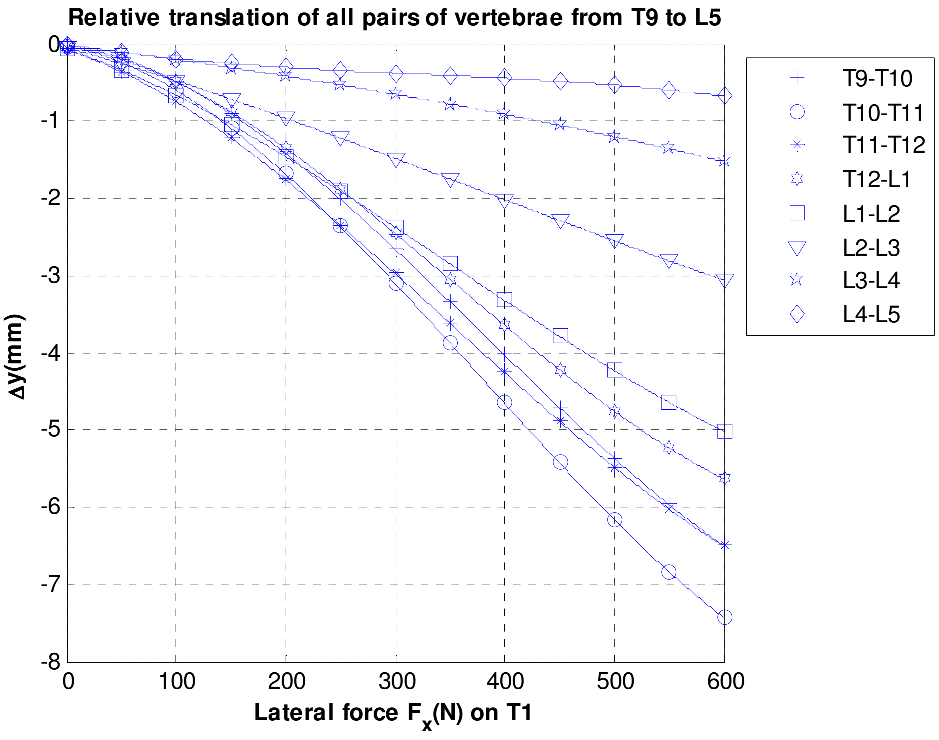

Figure 6.15 Y-axis relative translation of all pairs of vertebrae from T9 to L5 under lateral force on T1

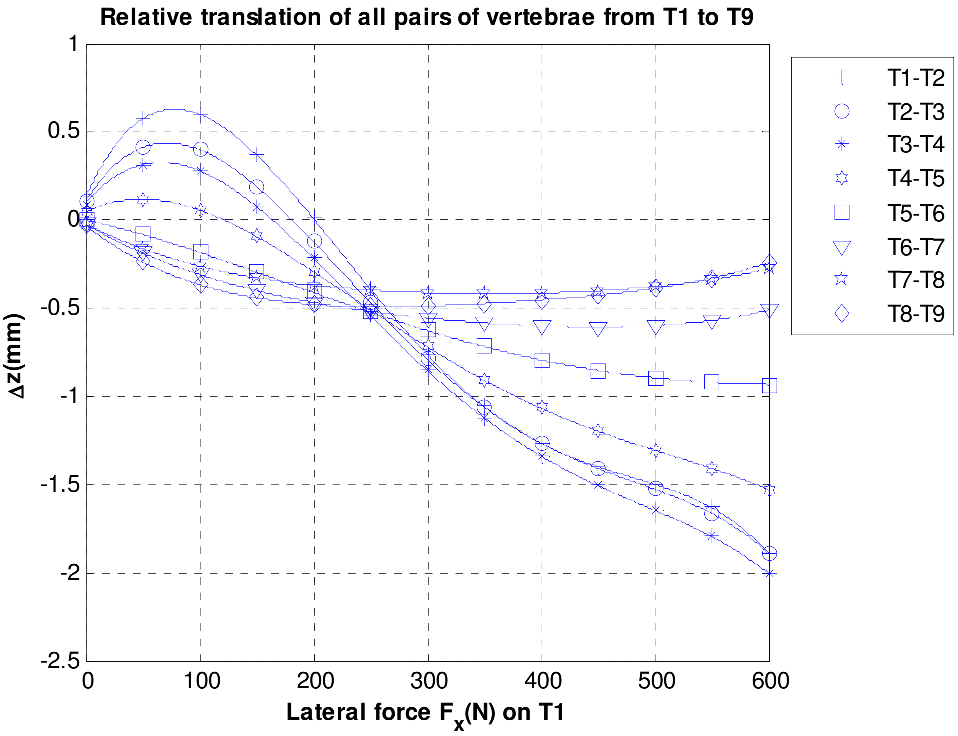

Figure 6.16 Z-axis relative translation of all pairs of vertebrae from T1 to T9 under lateral force on T1

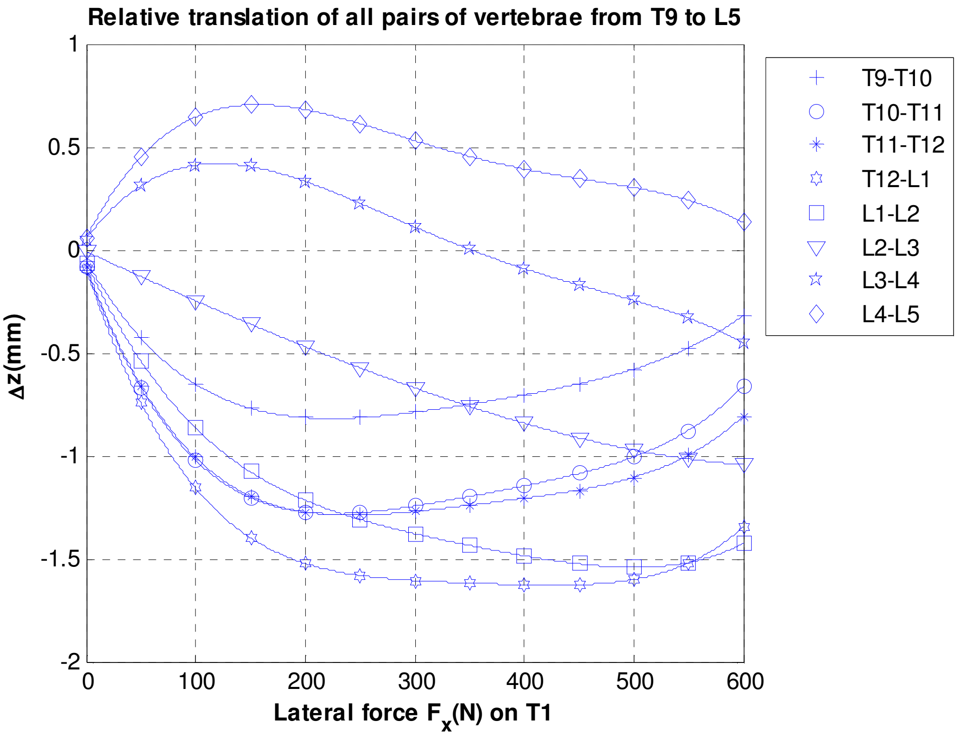

Figure 6.17 Z-axis relative translation of all pairs of vertebrae from T9 to L5 under lateral force on T1

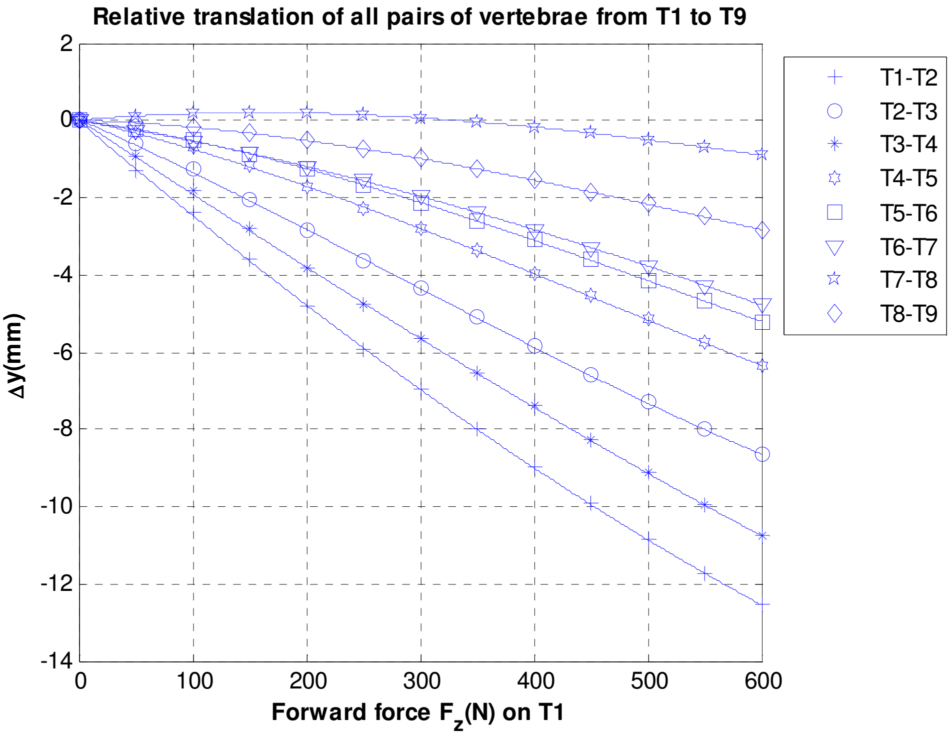

Figure 6.18 Y-axis relative translation of all pairs of vertebrae from T1 to T9 under forward force on T1

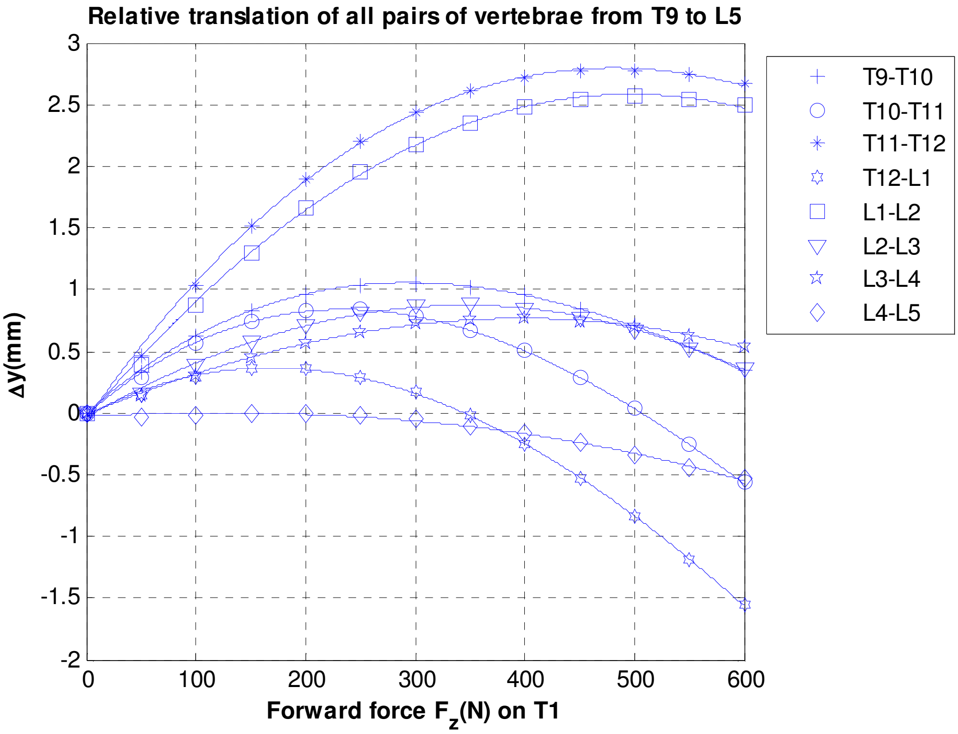

Figure 6.19 Y-axis relative translation of all pairs of vertebrae from T9 to L5 under forward force on T1

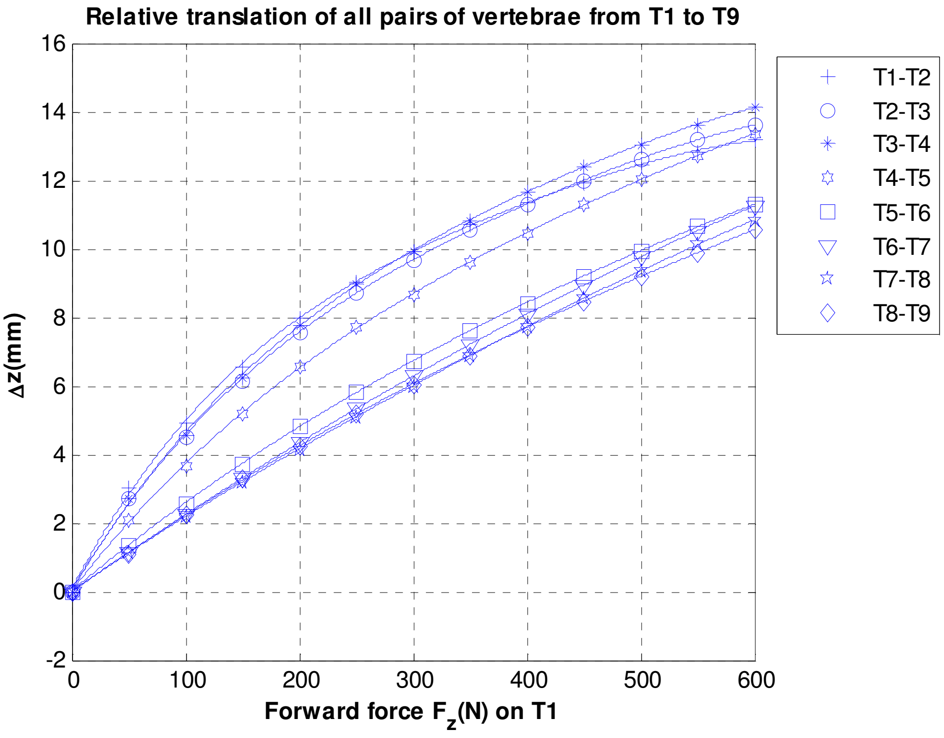

Figure 6.20 Z-axis relative translation of all pairs of vertebrae from T1 to T9 under forward force on T1

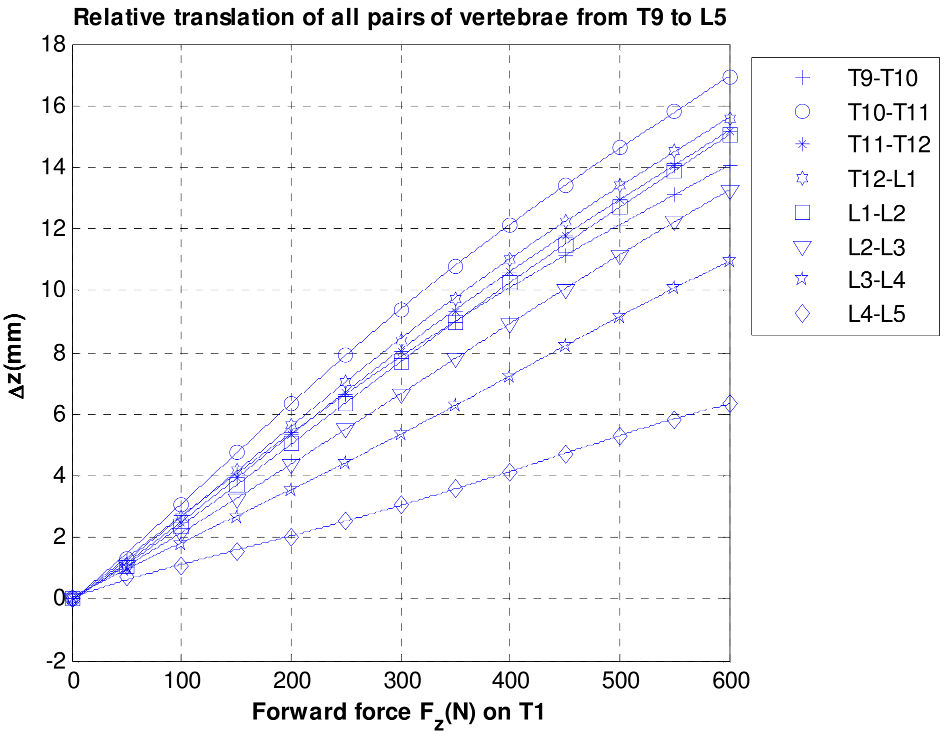

Figure 6.21 Z-axis relative translation of all pairs of vertebrae from T9 to L5 under forward force on T1

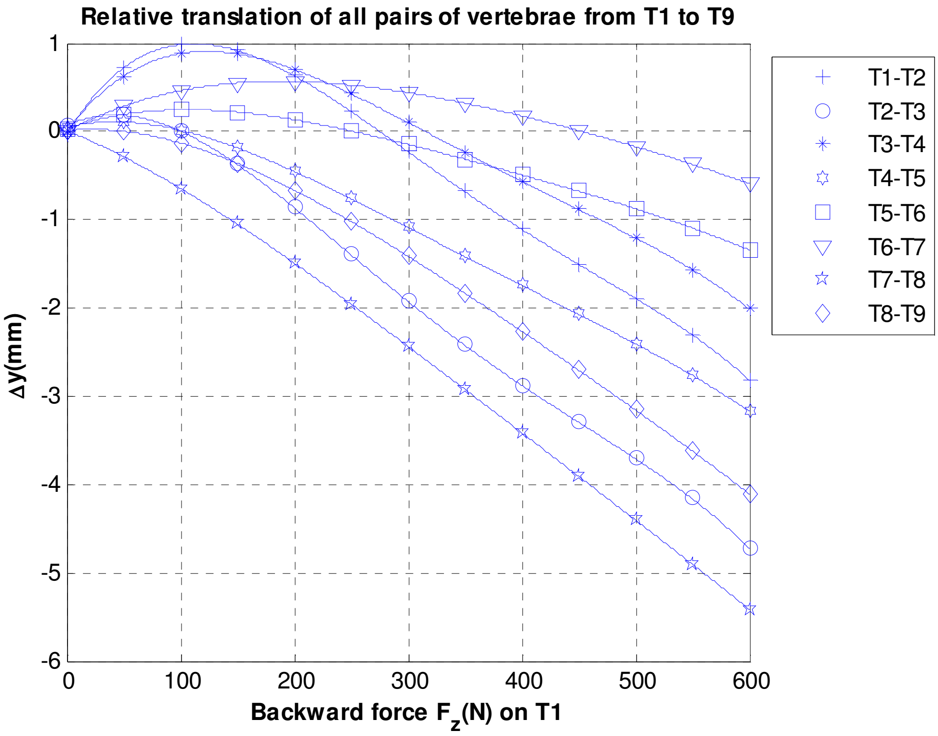

Figure 6.22 Y-axis relative translation of all pairs of vertebrae from T1 to T9 under backward force on T1

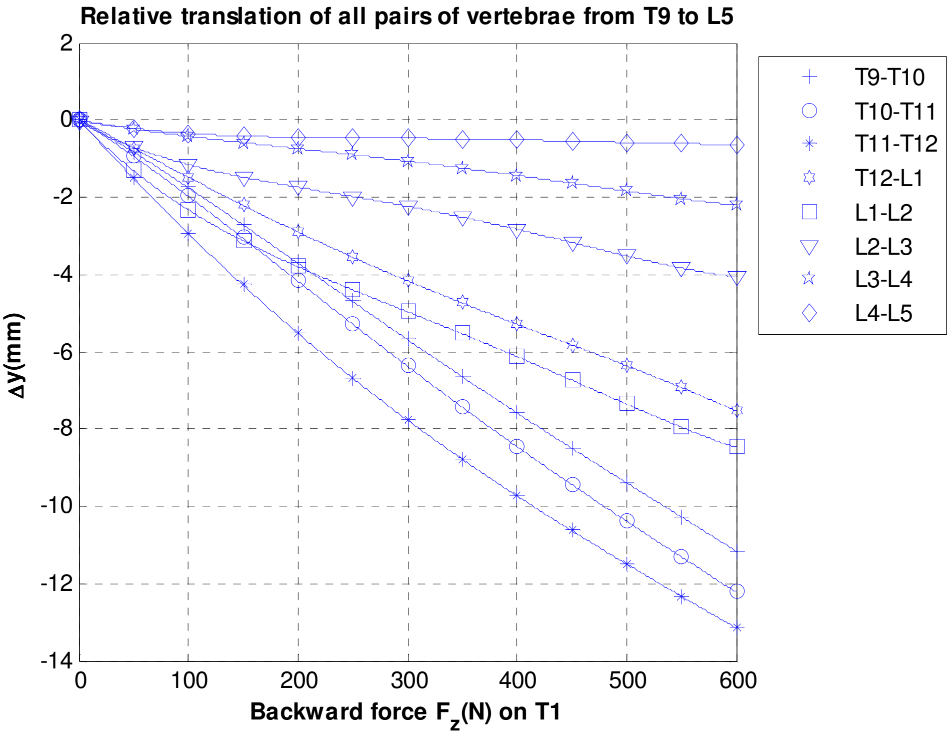

Figure 6.23 Y-axis relative translation of all pairs of vertebrae from T9 to L5 under backward force on T1

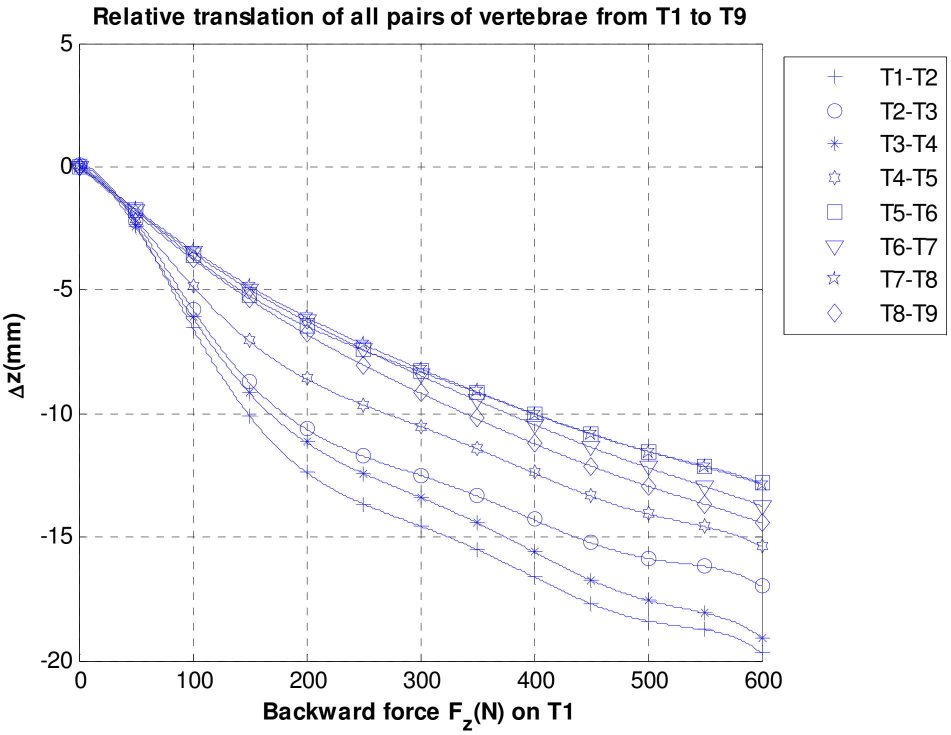

Figure 6.24 Z-axis relative translation of all pairs of vertebrae from T1 to T9 under backward force on T1

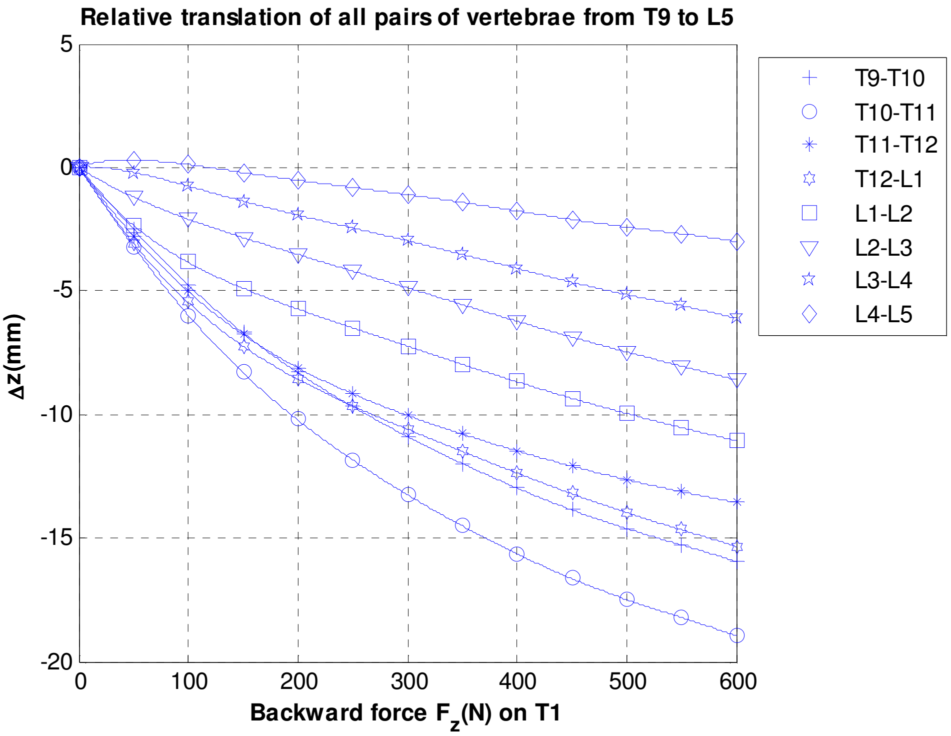

Figure 6.25 Z-axis relative translation of all pairs of vertebrae from T9 to L5 under backward force on T1

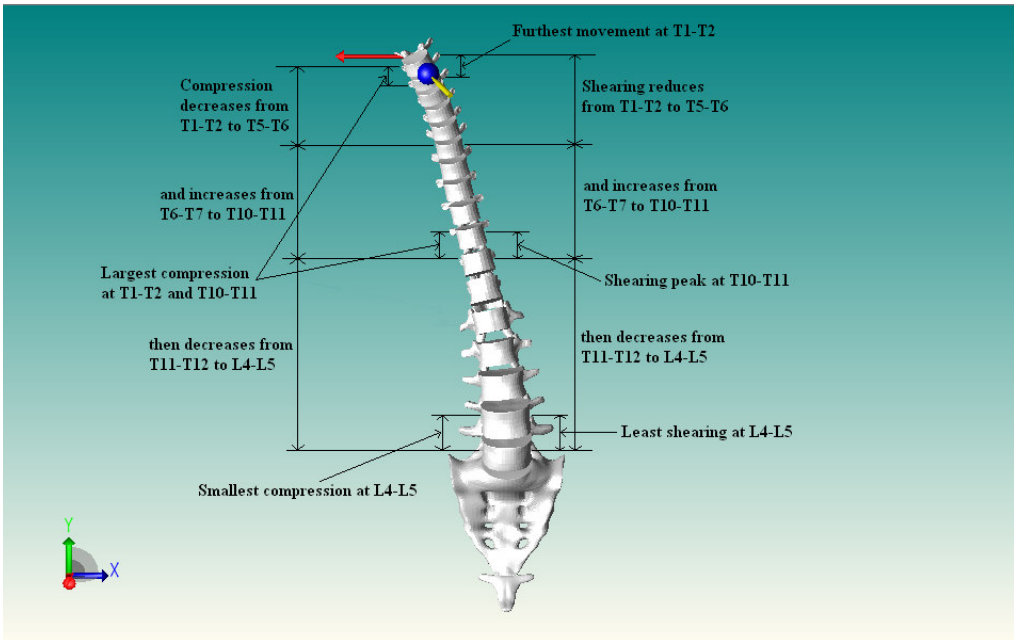

Figure 6.26 Analyzing translational properties of the spine model under lateral force acting on T1

Under lateral force on T1, as can be seen in Figure 6.12 and Figure 6.13, it is found that the upper vertebra moves faster than the lower one for all pairs of vertebrae. This leads to the whole spine becoming under lateral shearing. The shearing tends to reduce from T1-T2 to T5-T6, and increase from T6-T7 to T10-T11, then start to decrease again to L4-L5. An interesting point here is that although level T1-T2 moves furtherest, shearing peak is located at level T10-T11 and level L4-L5 has the least shearing. This is because the level T10-T11 has furthest relative translation between two vertebrae compared to the other levels, resulting in maximum shearing at this level. Meanwhile, it is also found that the whole spine is under compression at all levels of vertebrae as seen in Figure 6.14 and Figure 6.15. The dynamic trend of the whole spine in this direction is quite similar to that in x-axis direction. This means the compression decreases from T1-T2 to T5-T6, then increases from T6-T7 to T10-T11, and begins to reduce again to L4-L5. Moreover, it is shown in these two figures that smallest compression occurs at L4-L5 and largest compression lies at both T10-T11 and T1-T2 since relative translations of these two levels are more or less equal. For relative translation in z-axis direction, Figure 6.16 and Figure 6.17 indicate that the movement of the whole spine in this direction is very small in general. This implies that the shearing occurring in the spine is negligible. All dynamic properties analyzed above are clearly shown in Figure 6.26.

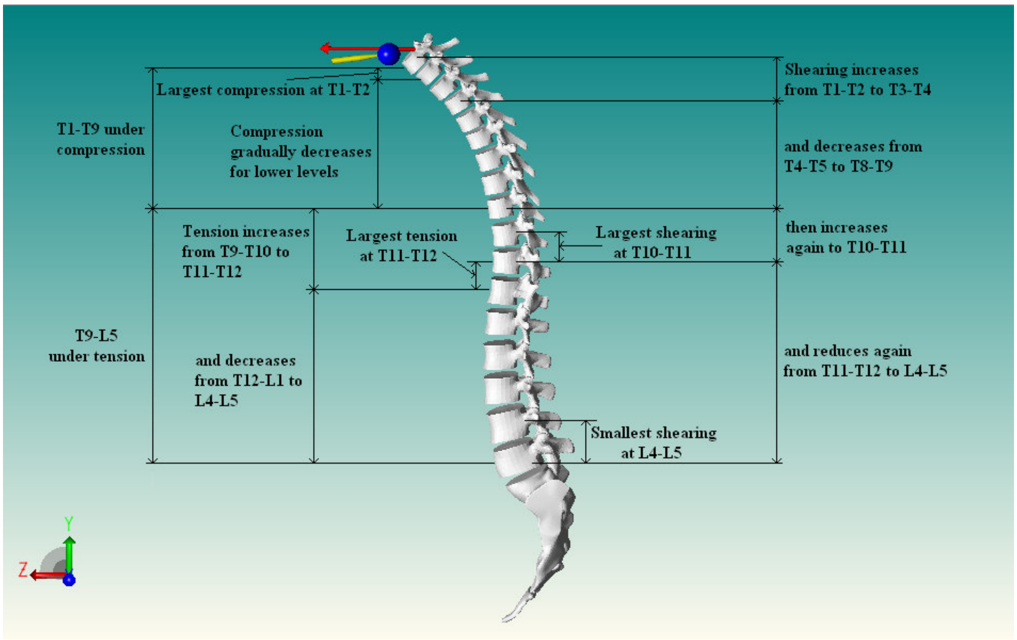

Figure 6.27 Analyzing translational properties of the spine model under forward force acting on T1

In the sagittal plane of the spine, when forward force is applied on T1, as can be seen in Figure 6.18 and Figure 6.19, it is found that the spine region from T1-T9 is under compression while tension happens in the region from T9-L5. In the former region, largest compression occurs in first level T1-T2 and starts to gradually decrease for lower levels. In the latter region, it is clear that maximum tension lies at level T11-T12 and corresponds to a force magnitude of 500N. In almost levels in this region, tension initially increases up to the peak at level T11-T12 and then turns to decrease when applying force is large. Meanwhile, Figure 6.20 and Figure 6.21 show that the whole spine is under antero-posterior shearing for all levels of vertebrae. At the beginning, the shearing increases from T1-T2 to T3-T4, and then decreases from T4-T5 to T8-T9. The shearing then increases again to T10-T11 and turns to reduce again to L4-L5. Under forward force, the largest and smallest shearing levels are located at T10-T11 and L4-L5 respectively. The dynamic properties examined in this case are illustrated in Figure 6.27.

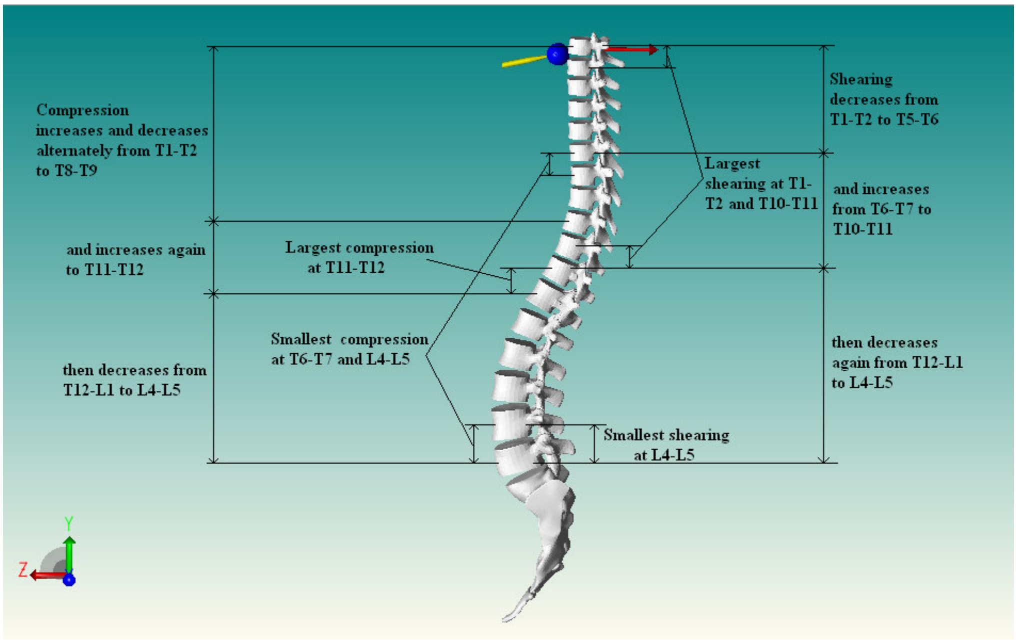

Figure 6.28 Analyzing translational properties of the spine model under backward force acting on T1

When backward force is acting on T1, Figure 6.22 and Figure 6.23 indicate that the whole spine is under compression at all levels of vertebrae. The maximum compression found is at T11-T12 and the minimum lies at both T6-T7 and L4-L5. From first level T1-T2 to level T8-T9, the dynamic trend varies in such a way that increasing and decreasing compression happen alternately. Then, compression increases again to level T11-T12 and then gradually reduces to level L4-L5. Meanwhile, similar to the case under the forward force, Figure 6.24 and Figure 6.25 show that the whole spine is under postero-anterior shearing for all levels of vertebrae. It is obvious that the largest shearing exists in both level T1-T2 and level T10-T11 and smallest shearing is at level L4-L5. Under the backward force, the shearing initially decreases from T1-T2 to T5-T6, and turns to increase from T6-T7 to T10-T11, and then reduces again to L4-L5. All dynamic properties analyzed above are displayed in Figure 6.28. In this section, dynamic analysis of the spine model is done with the case in which external forces are applied on vertebra T1. For further detail on the graphs of relative translations of all pairs of vertebrae in other cases, please refer to Appendix E.

6.4. Offline deformation response simulation of intervertebral discs

As presented in Chapter 5, offline simulation of IVDs can run only when the real-time haptic simulation of the thoracolumbar spine model is executed first. Figure 6.29 to Figure 6.31 display offline simulations of the hybrid spine model corresponding to the three cases discussed in section 6.3. Figure 6.32 to Figure 6.37 illustrate close-up offline simulations of lumbar and thoracic regions corresponding to the three cases mentioned above. And Figure 6.38 to Figure 6.43 and Figure 6.44 to Figure 6.47 show relative rotation angles of each pairs of vertebrae corresponding to the first and the second cases above.

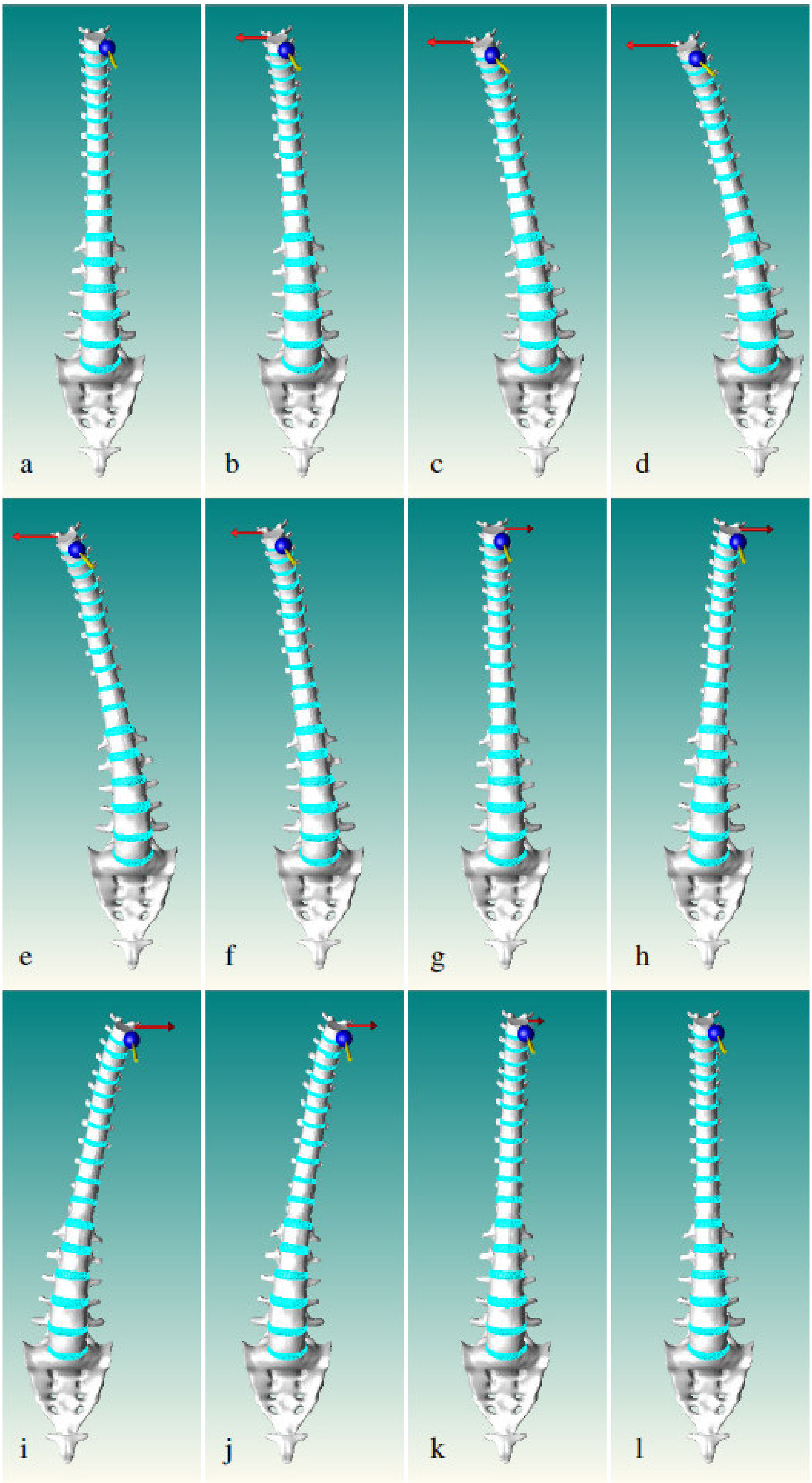

Figure 6.29 Offline simulation of the spine under lateral force on T1

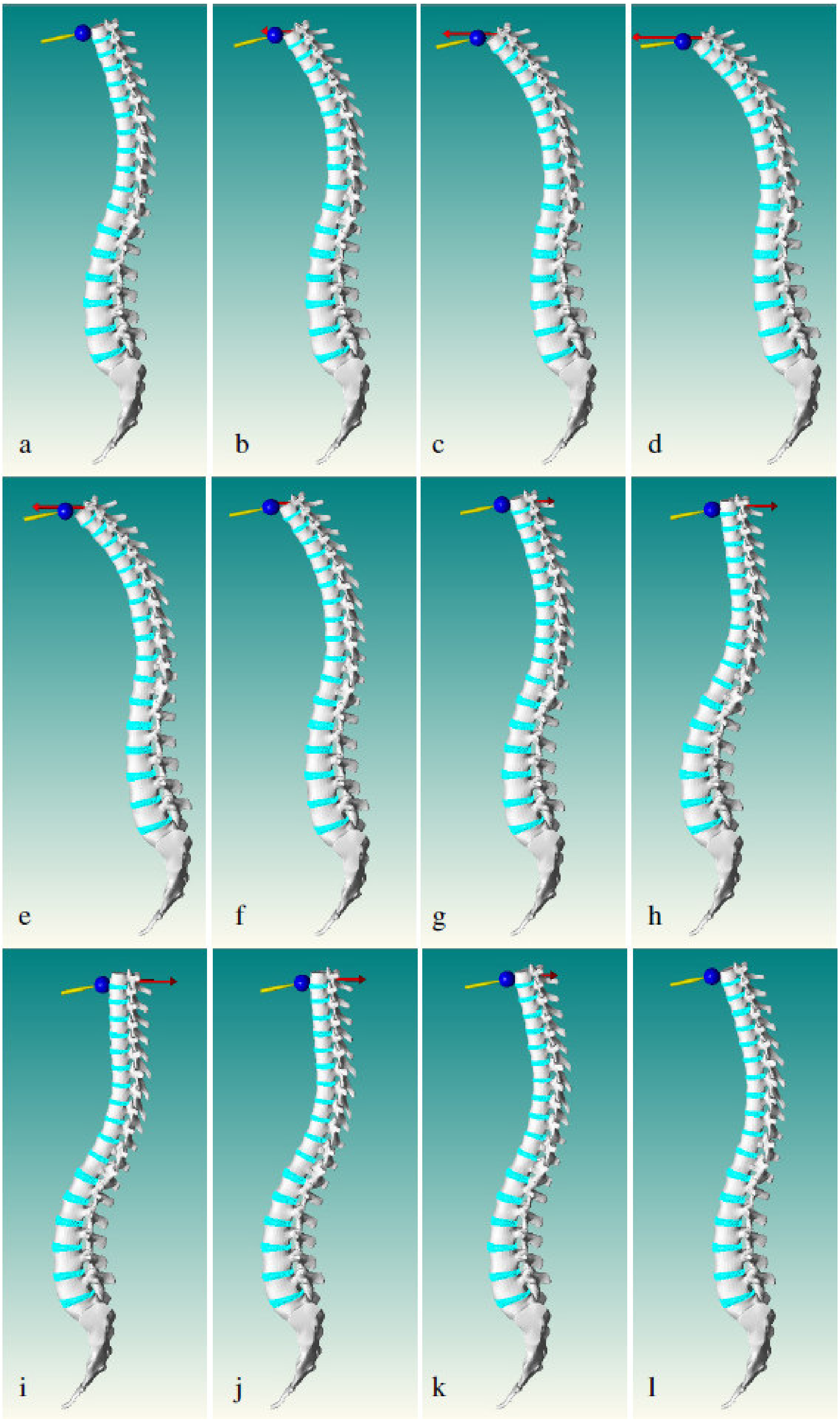

Figure 6.30 Offline simulation of the spine under sagittal force on T1

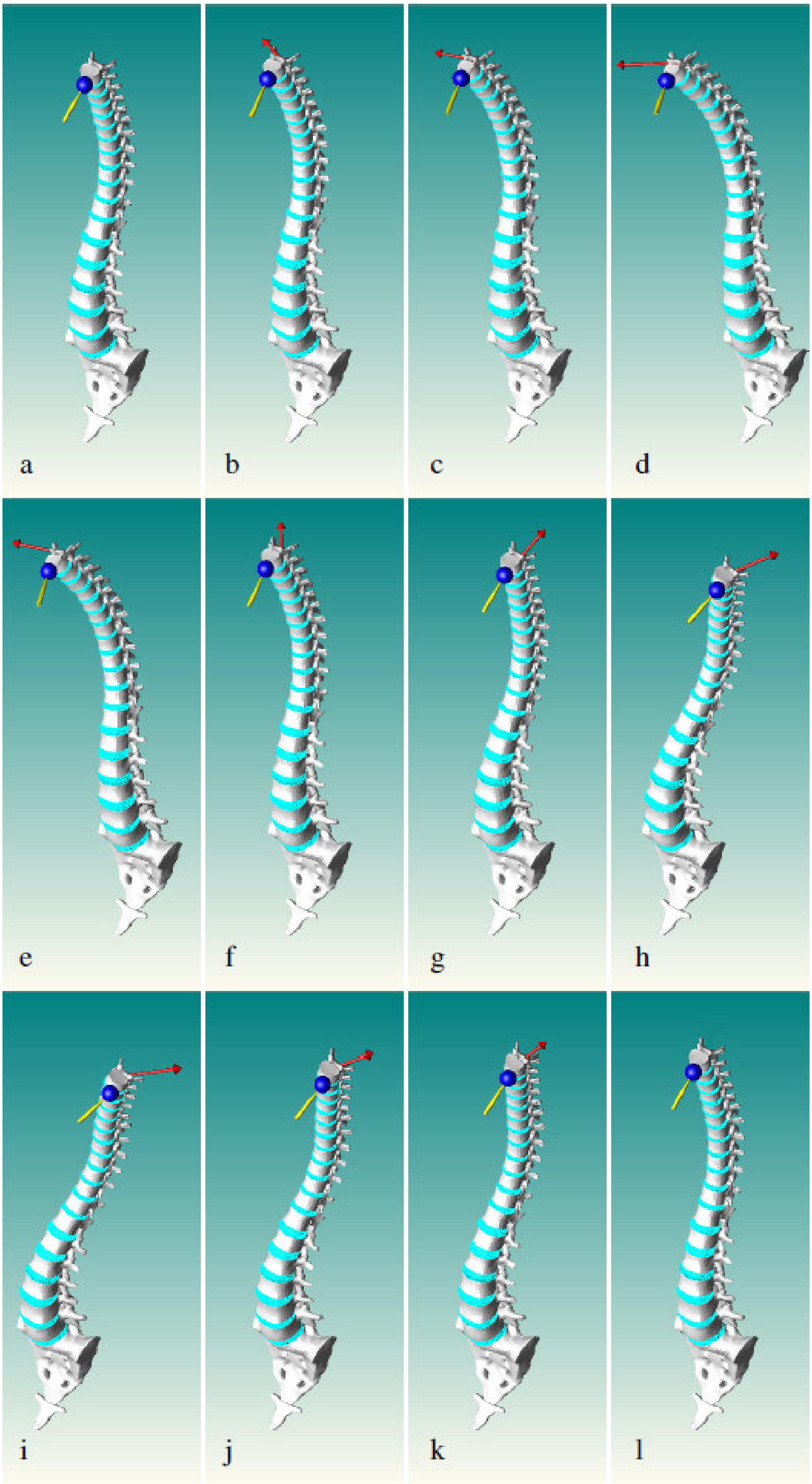

Figure 6.31 Offline simulation of the spine under arbitrary force on T1

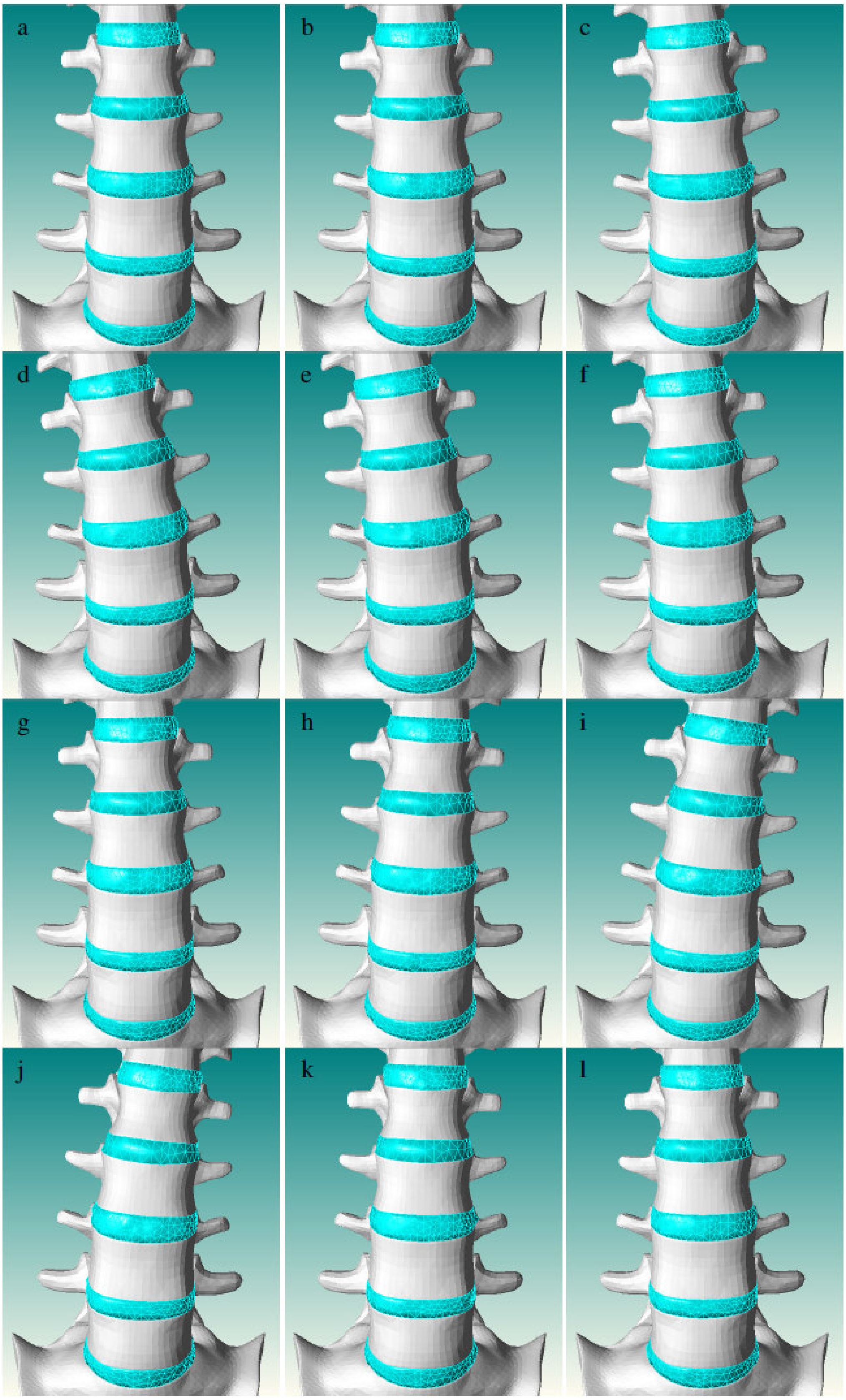

Figure 6.32 Offline simulation of lumbar region under lateral force on T1

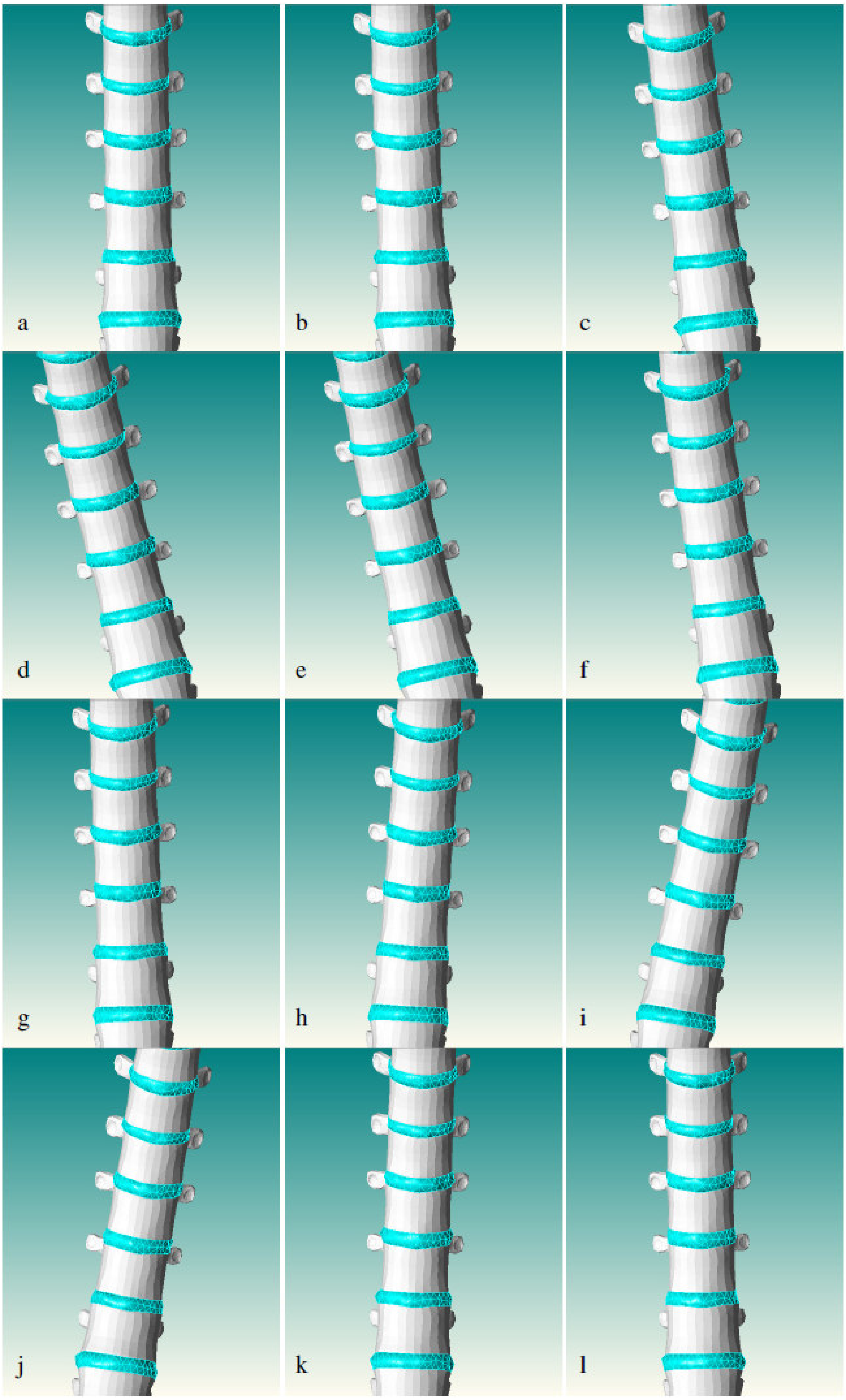

Figure 6.33 Offline simulation of thoracic region under lateral force on T1

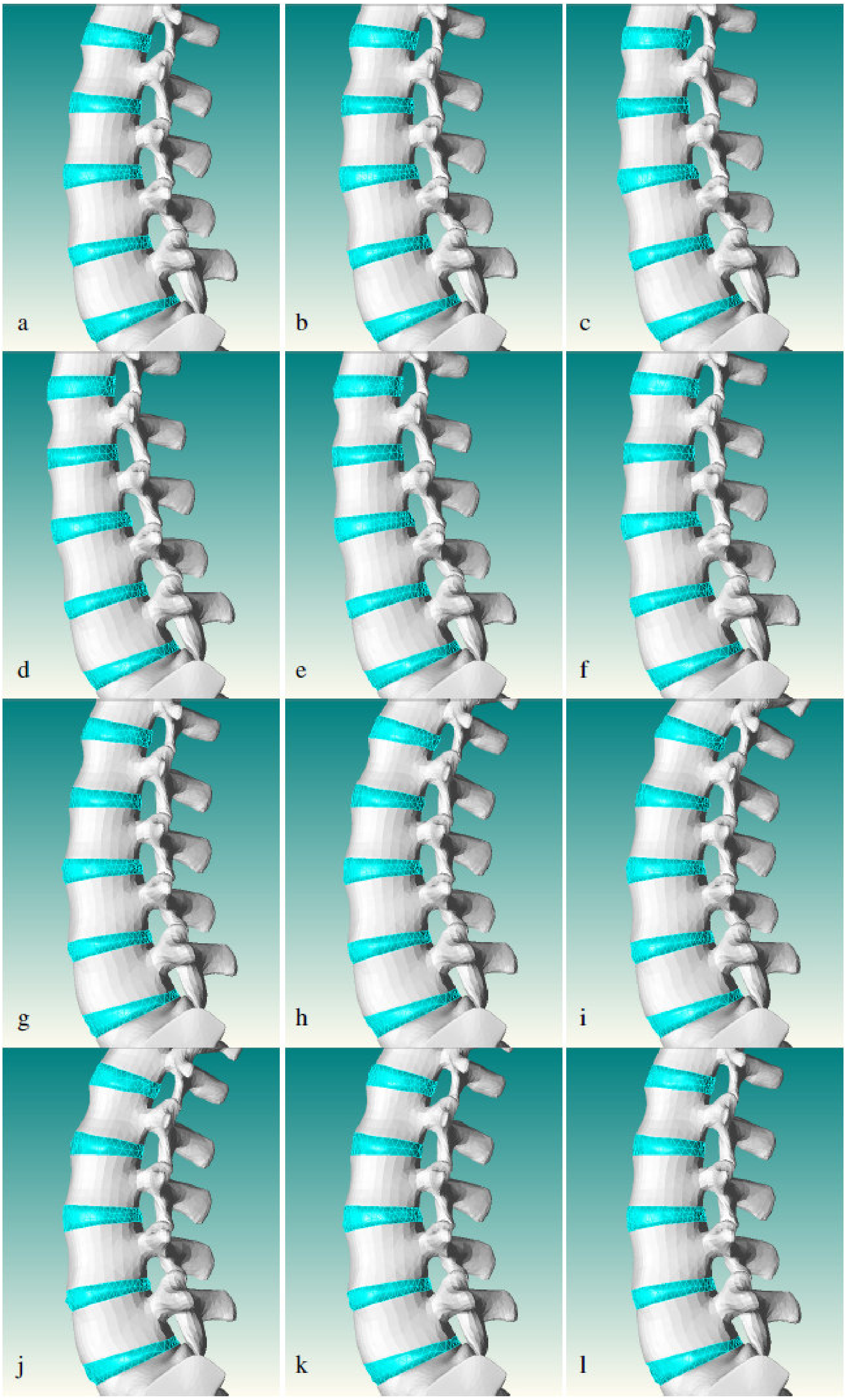

Figure 6.34 Offline simulation of lumbar region under sagittal force on T1

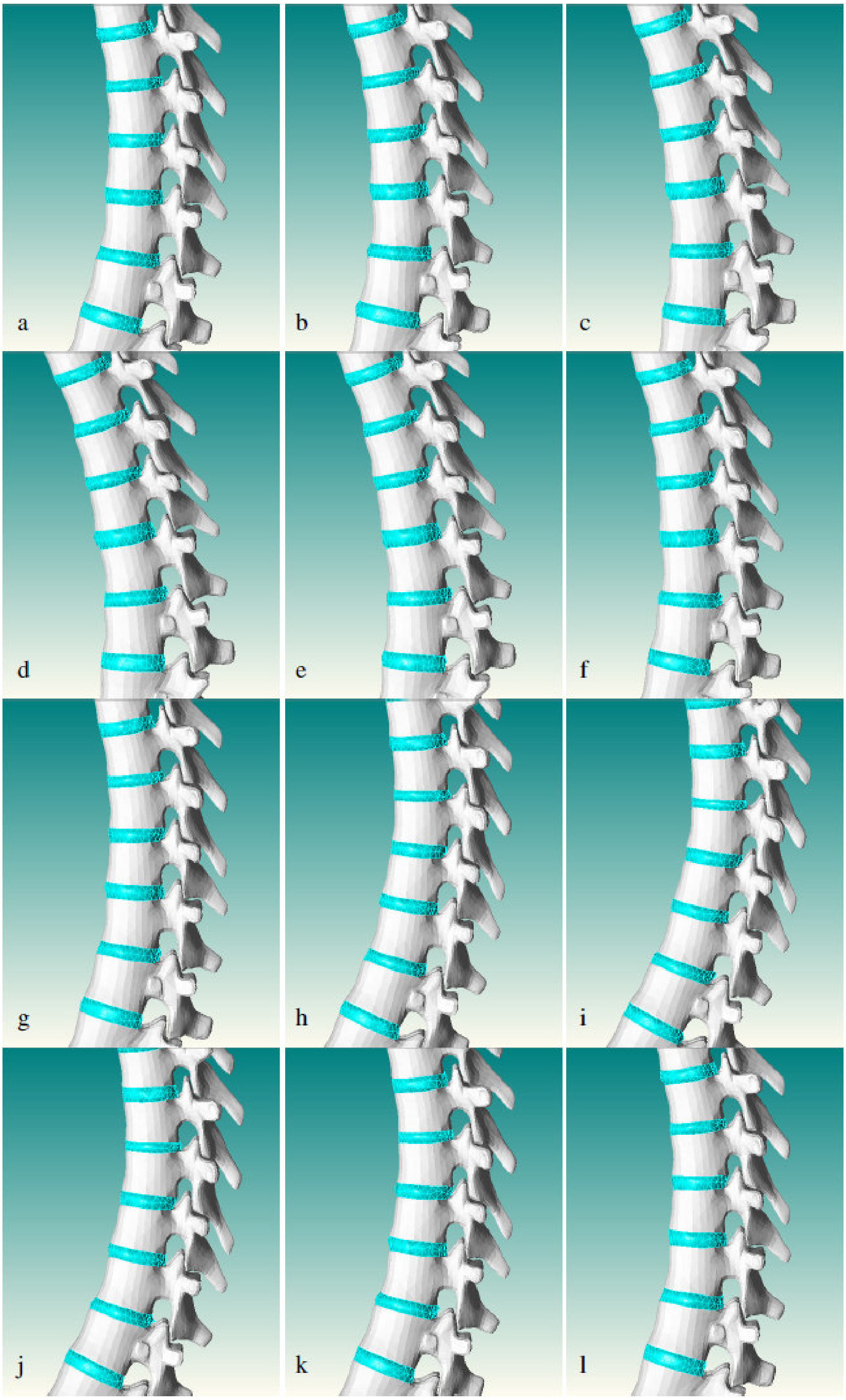

Figure 6.35 Offline simulation of lumbar region under sagittal force on T1

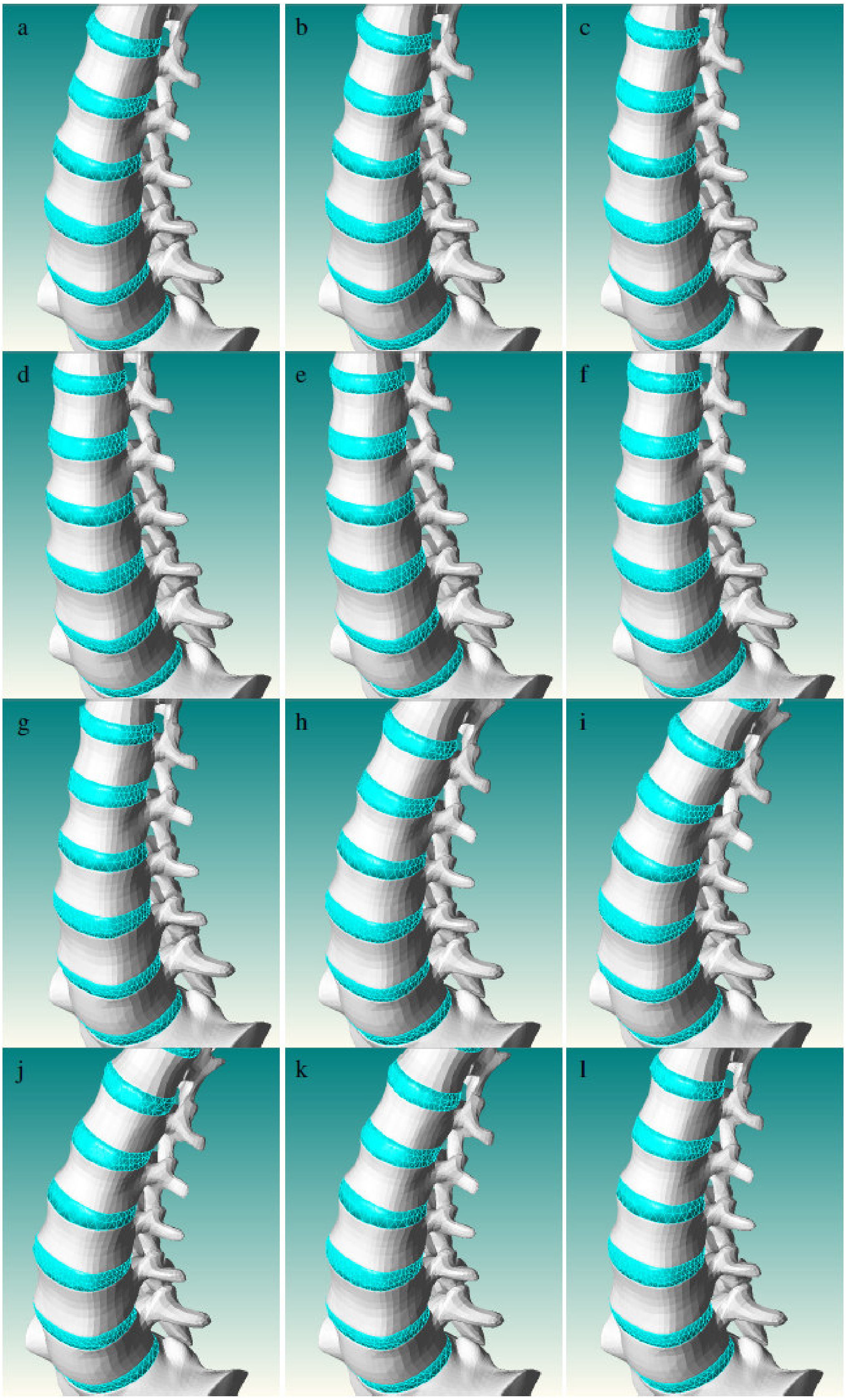

Figure 6.36 Offline simulation of lumbar region under arbitrary force on T1

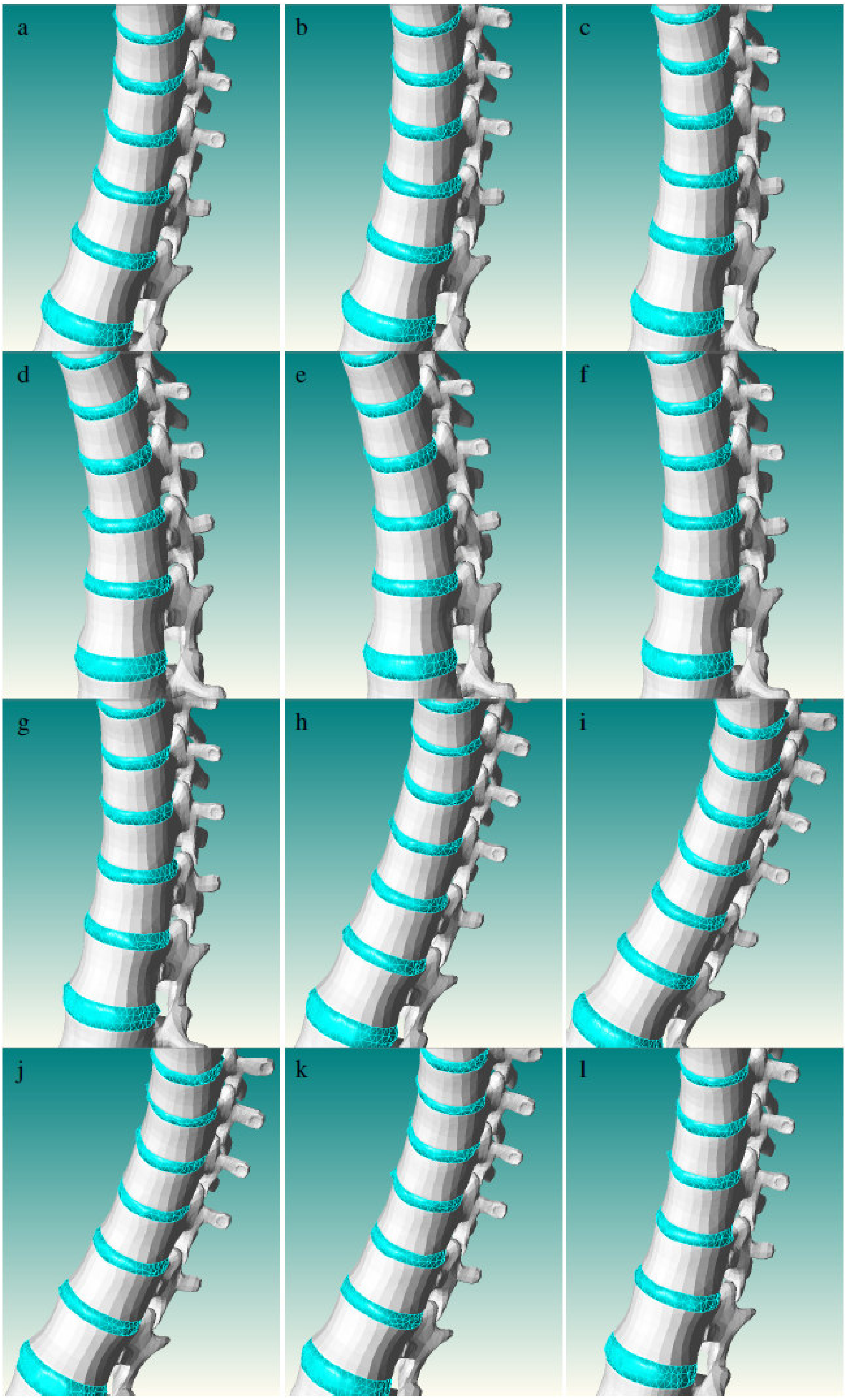

Figure 6.37 Offline simulation of lumbar region under arbitrary force on T1

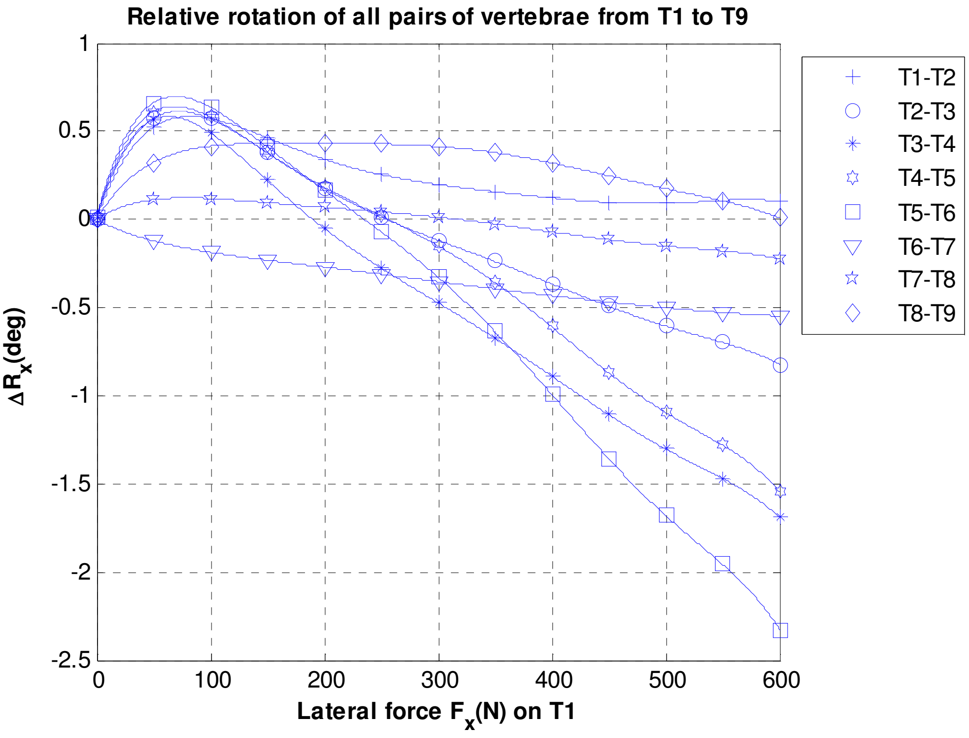

Figure 6.38 Relative rotation about x axis of all pairs of vertebrae from T1 to T9 under lateral force on T1

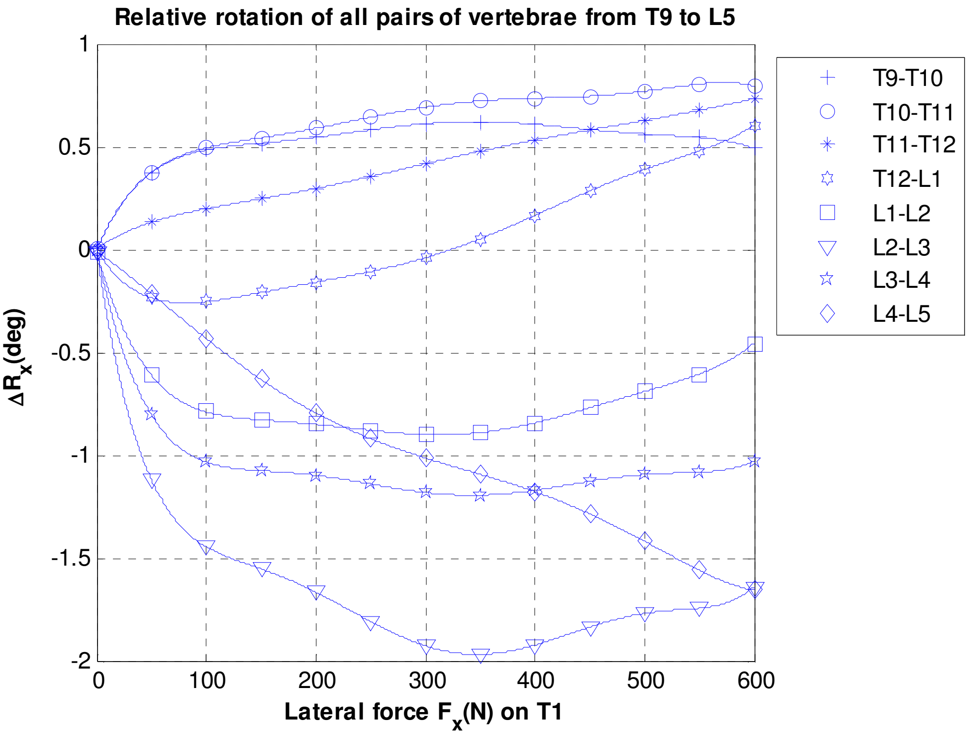

Figure 6.39 Relative rotation about x axis of all pairs of vertebrae from T9 to L5 under lateral force on T1

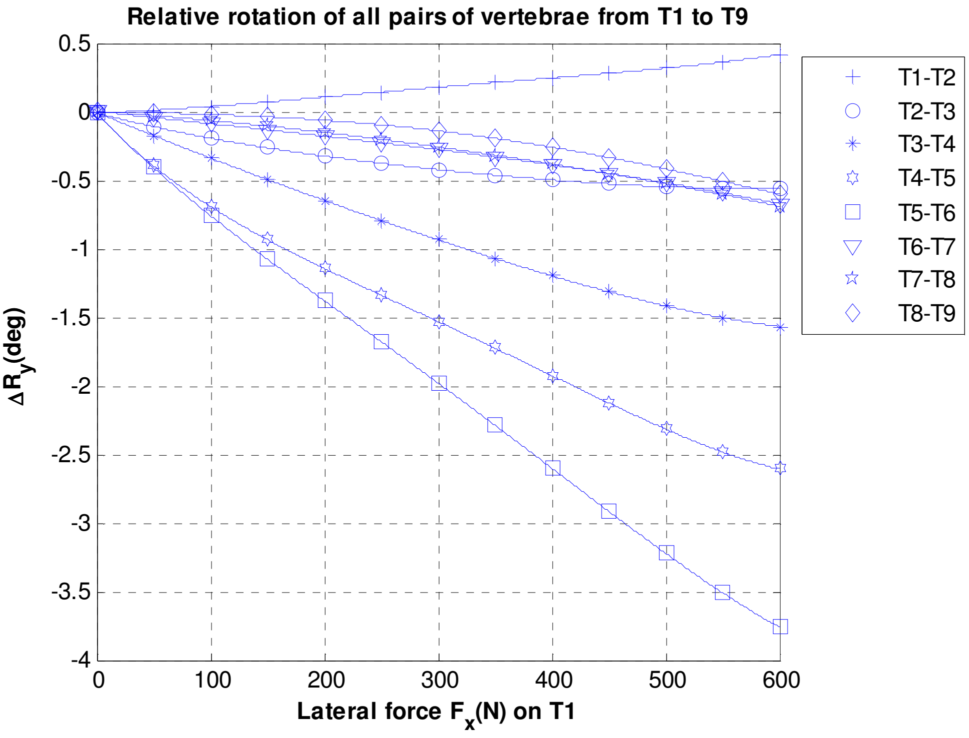

Figure 6.40 Relative rotation about y axis of all pairs of vertebrae from T1 to T9 under lateral force on T1

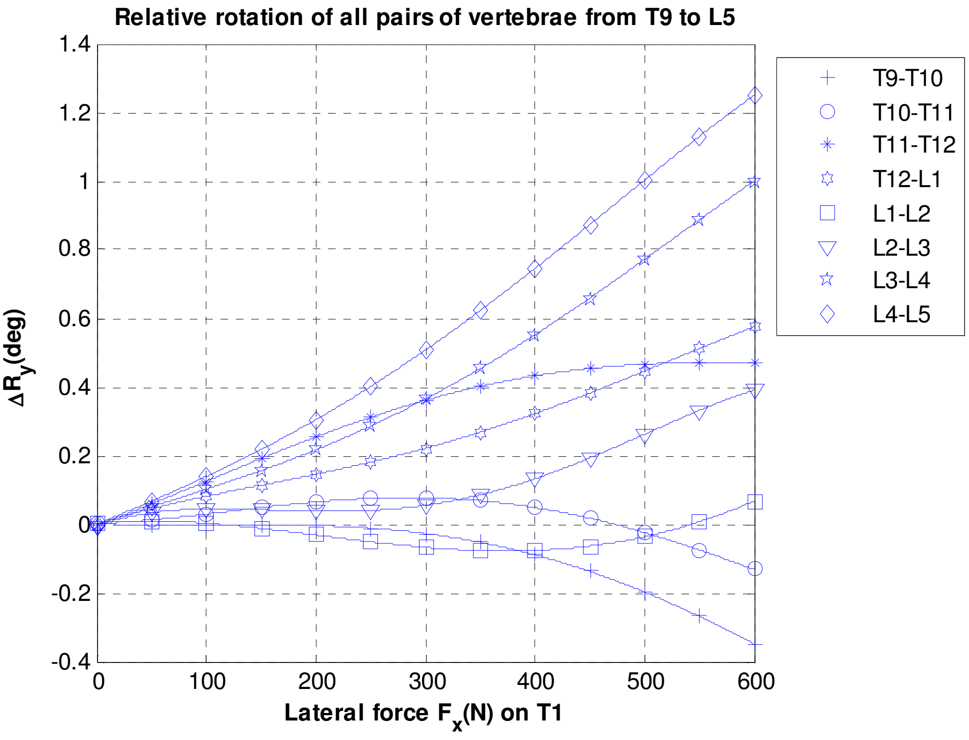

Figure 6.41 Relative rotation about y axis of all pairs of vertebrae from T9 to L5 under lateral force on T1

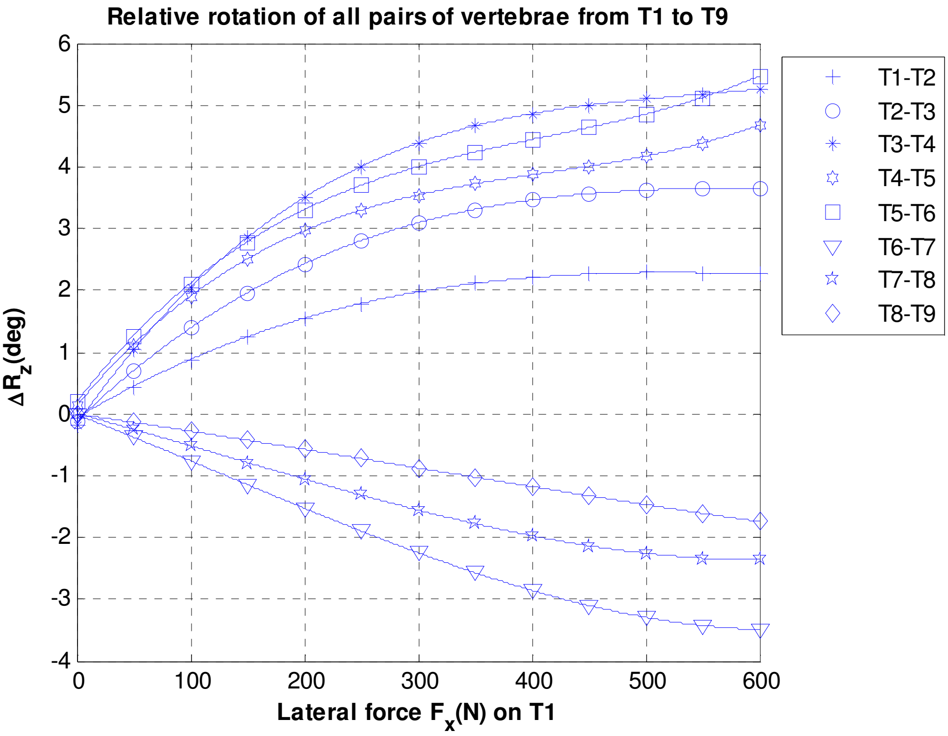

Figure 6.42 Relative rotation about z axis of all pairs of vertebrae from T1 to T9 under lateral force on T1

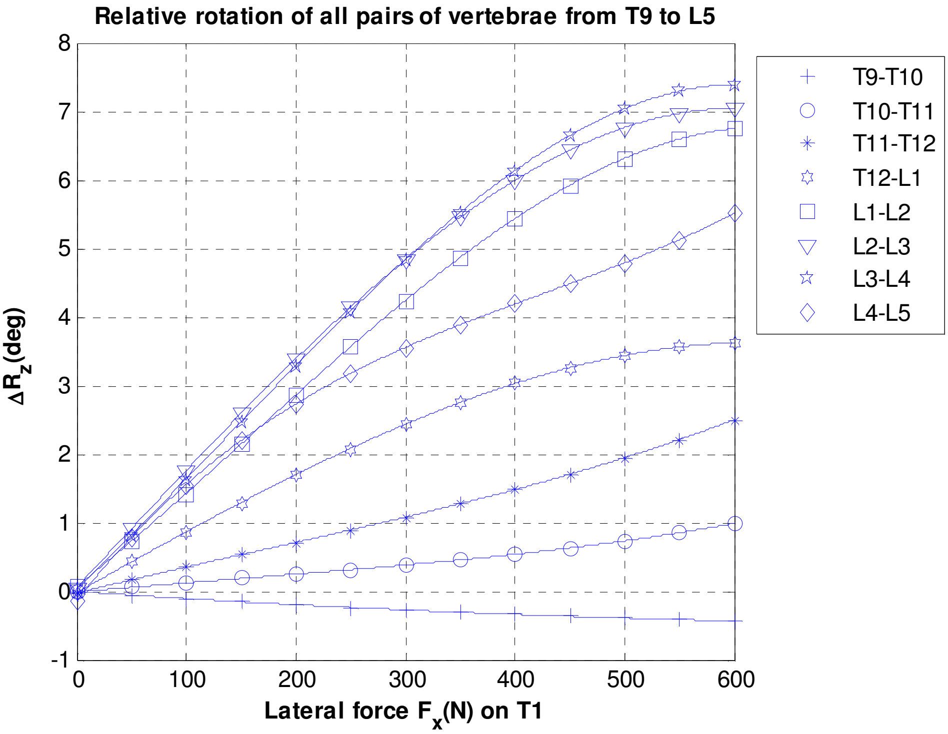

Figure 6.43 Relative rotation about z axis of all pairs of vertebrae from T9 to L5 under lateral force on T1

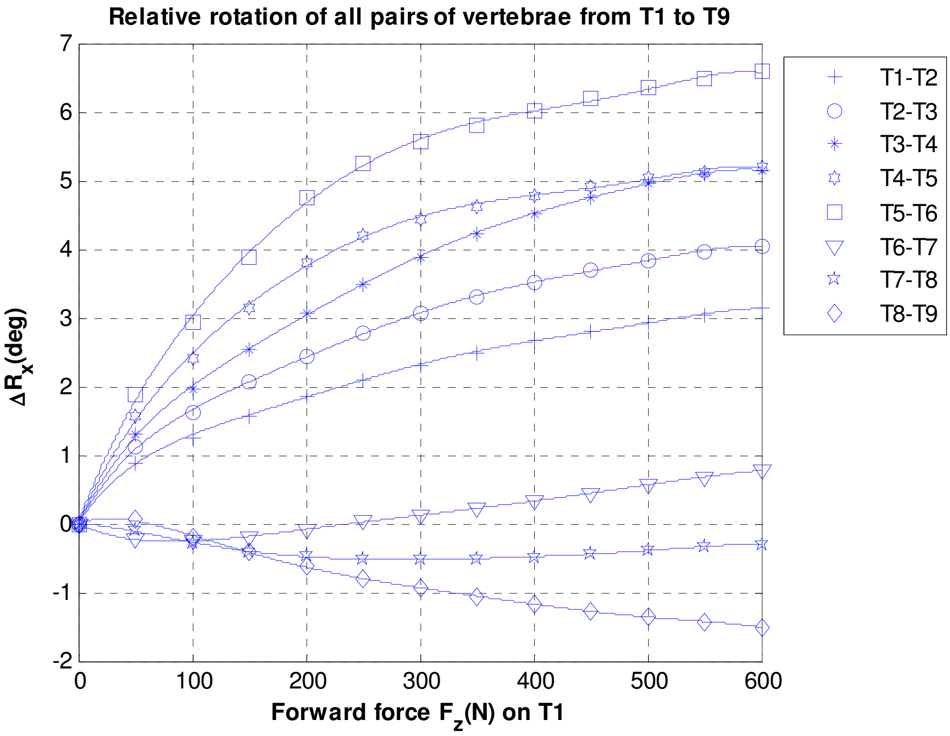

Figure 6.44 Relative rotation about x axis of all pairs of vertebrae from T1 to T9 under forward force on T1

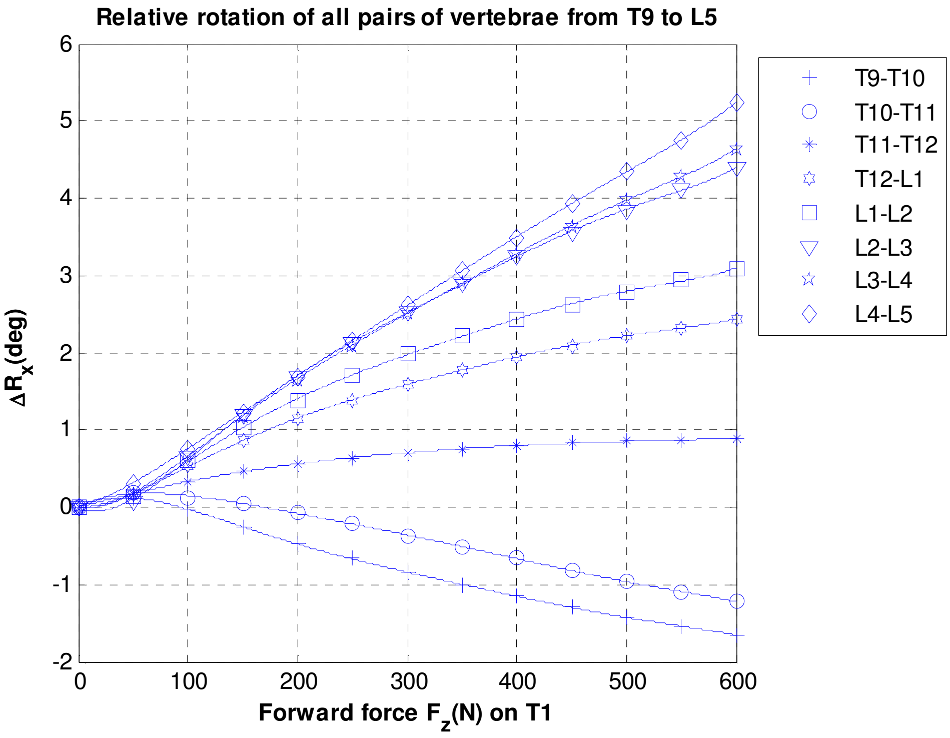

Figure 6.45 Relative rotation about x axis of all pairs of vertebrae from T9 to L5 under forward force on T1

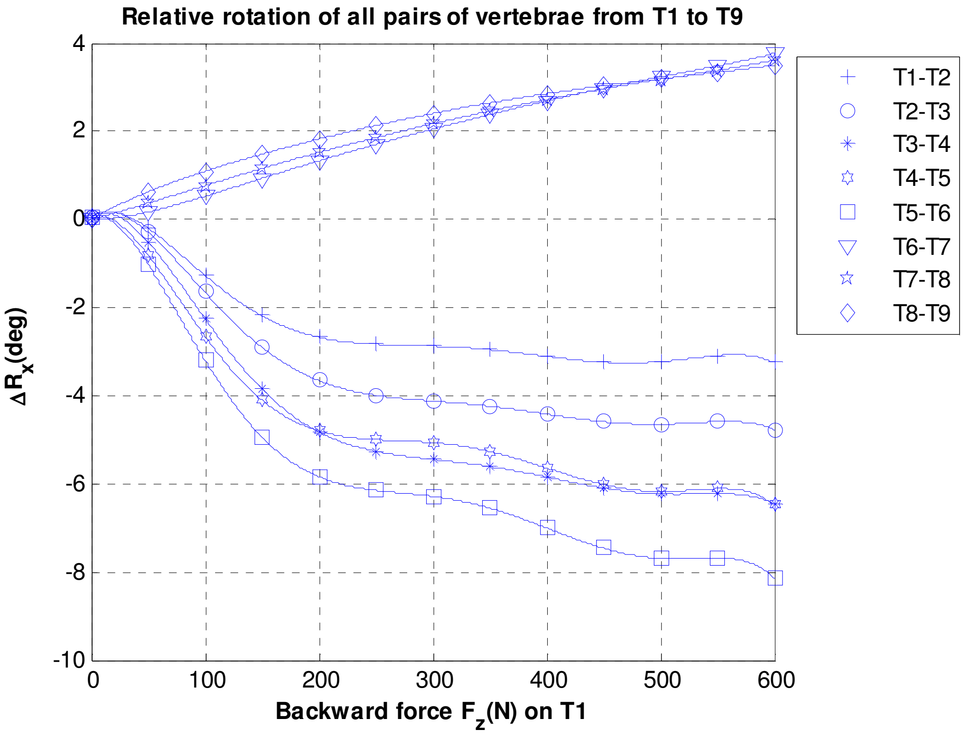

Figure 6.46 Relative rotation about x axis of all pairs of vertebrae from T1 to T9 under backward force on T1

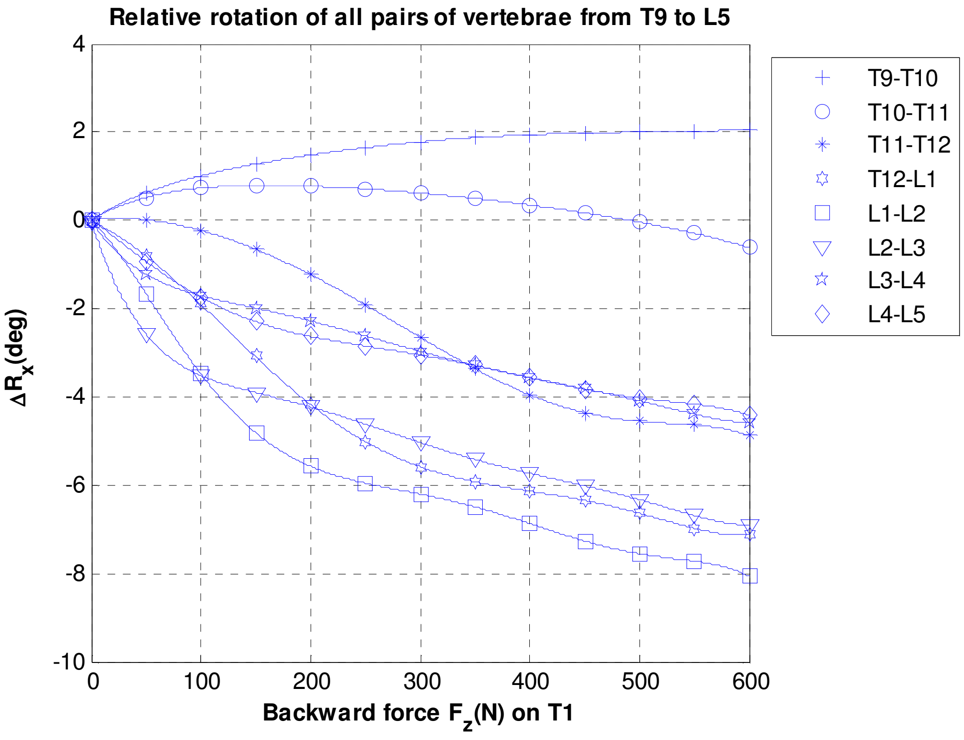

Figure 6.47 Relative rotation about x axis of all pairs of vertebrae from T9 to L5 under backward force on T1

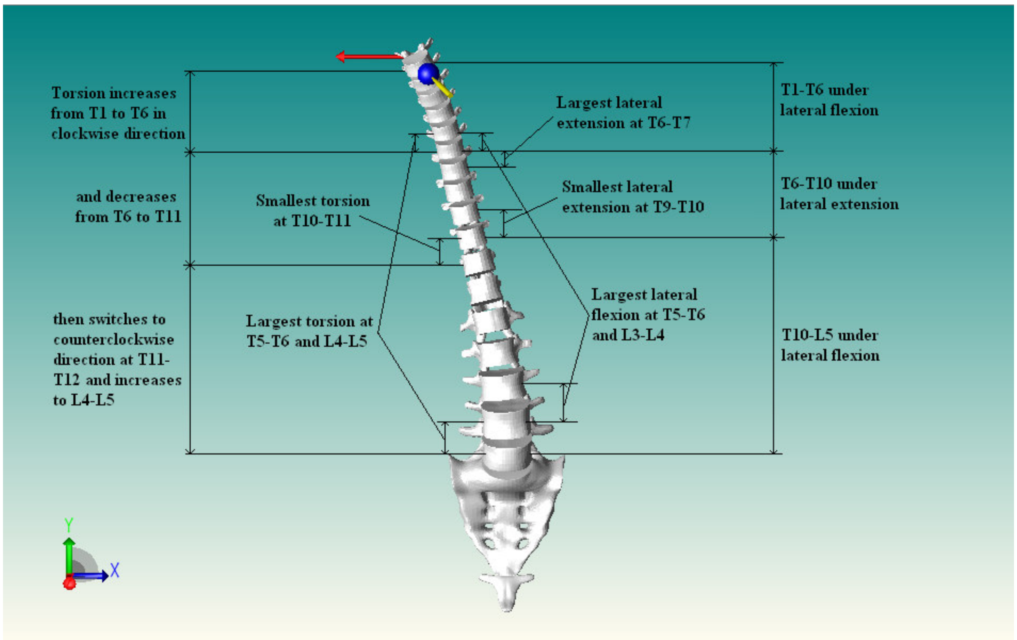

Figure 6.48 Analyzing rotational properties of the spine model under lateral force acting on T1

Under lateral force on T1, as can be seen in Figure 6.38 and Figure 6.39, it is found that relative rotational angles of all pairs of vertebrae are very small in general. This can be deduced that flexion or extension of the whole spine is negligible. Meanwhile, Figure 6.40 and Figure 6.41 indicate that the whole spine is under very small torsion generally. The smallest torsion lies at level T10-T11 and the largest torsion is found at level T5-T6 and L4-L5. At the beginning, torsion increases from T1-T2 to T5-T6 in clockwise direction, and decreases from T6-T7 to T10-T11. Then, torsion switches to counterclockwise direction from level T11-T12 and increases to level L4-L5. For relative rotation angles about z axis of all pairs of vertebrae, Figure 6.43 shows that while the spine region from T10-L5 is under lateral flexion, there are two opposite states occurring in the region T1-T10 as can be seen in Figure 6.42. The levels from T1-T6 are under lateral flexion whereas the levels from T6-T10 are under lateral extension. The largest lateral flexion corresponding to two spine regions T1-T10 and T10-L5 lies at level T5-T6 and L3-L4, respectively. The smallest extension is found at level T9-T10 and the largest is located at level T6-T7. All dynamic properties analyzed above are clearly shown in Figure 6.48.

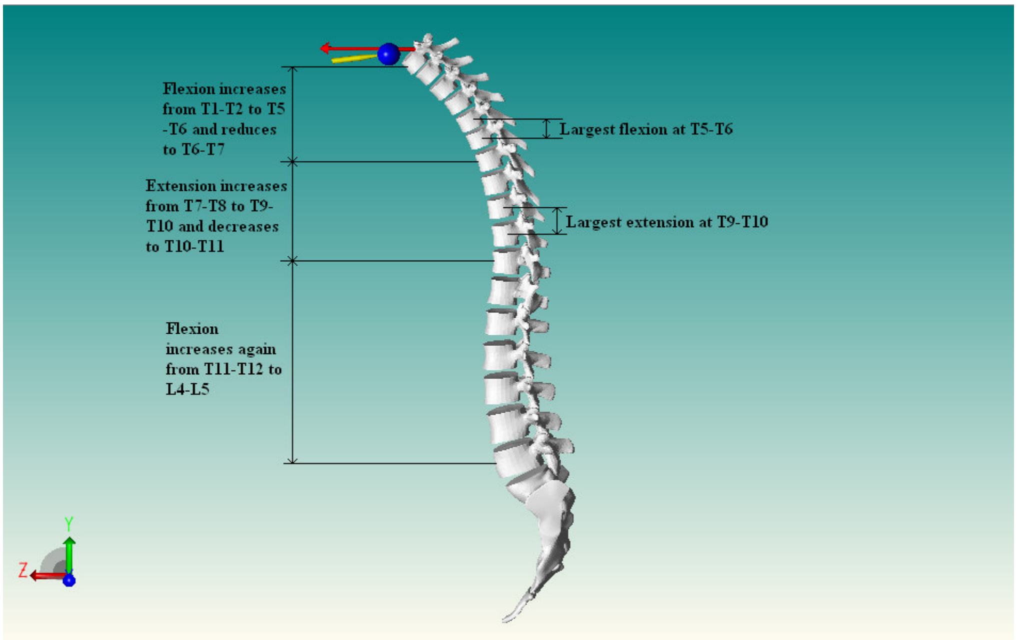

Figure 6.49 Analyzing rotational properties of the spine model under forward force acting on T1

In sagittal plane of the spine, when forward force is applied on T1, as can be seen in Figure 6.44 and Figure 6.45, it is found that the spine is under flexion in the region at T1-T7 and T11-L5 while extension happens in the region T7-T11. The maximum flexion and extension are located at level T5-T6 and T9-T10 respectively. Initially, flexion increases from T1-T2 to T5-T6 and reduces to level T6-T7. At this level, the spine switches to be under extension. This extension increases from T7-T8 to T9-T10, and decreases to level T10-T11. Then, the spine starts to be flexed again and the flexion increases to level L4-L5. The dynamic properties examined here are illustrated in Figure 6.49. When backward force is acting on T1, Figure 6.46 and Figure 6.47 indicate that extension happens in the region T1-T6 and T10-L5 while flexion occurs in the region T6-T10. The largest extension lies at both level

T5-T6 and L1-L2 while the largest flexion is at level T6-T7. Initially, the extension increases from T1-T2 to T5-T6, then rapidly decreases and switches to be flexed at level T6-T7. At this level, the flexion gradually reduces to level T9-T10. Once again, the spine is under extension here. The extension starts to increase to L1-L2 and reduces to L4-L5. The dynamic properties analyzed in this case are displayed in Figure 6.50. It should be noted that dynamic behavior of the whole spine analyzed in this section only corresponds the case in which external forces are applied on vertebra T1. For more detail on the graphs of relative rotations of all pairs of vertebrae in other cases, please refer to Appendix E. Although the real-time haptic simulation of the thoracolumbar spine model and offline simulation of IVDs work well as shown in the figures above, there are still some limitations remaining in this study which will be discussed in next chapter.

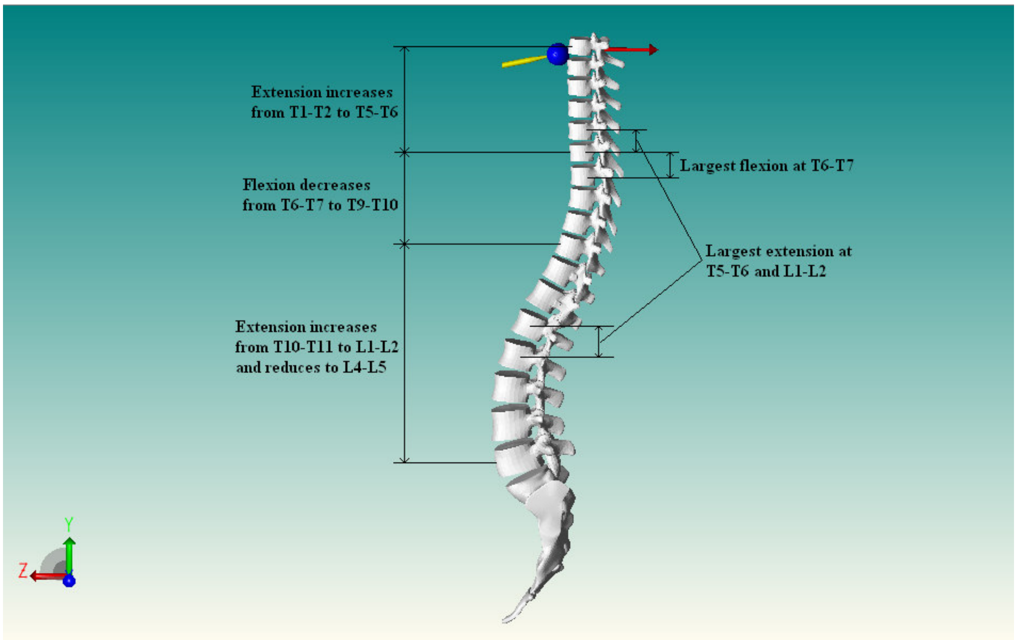

Figure 6.50 Analyzing rotational properties of the spine model under backward force acting on T1

CHAPTER 7

CONCLUSIONS AND FUTURE WORKS

7.1. Conclusions

This thesis achieved several main objectives as follows: developing an entirely discretized multi-body spine model in LifeMOD; validation of the detailed spine model; analyzing dynamic characteristics of the spine model under external forces; developing a haptically integrated graphic interface; and proposing a new tetrahedral MSS model of intervertebral disc.

The first objective of this thesis was to develop a completely discretized musculo-skeletal muti-body spine model using LifeMOD Biomechanics Modeler. The full development process of the spine model was conducted in five stages. It was found that the ligaments, lumbar muscles and intra-abdominal pressure implemented into the spine model in each stage play an important role in stabilizing the spine under external forces in different axis-aligned directions. The simulation stages indicated that ligaments generate resultant forces to restrict excessive movement of the spine when forward forces in sagittal plane are applied onto a specific vertebra. Meanwhile, under external forces in opposite direction, lumbar muscles are the key component in maintaining equilibrium state of the spine. Moreover, lumbar muscles also partly strengthen the spine in resisting flexion or extension motions. In addition to ligaments and muscles, intra-abdominal pressure is considered a crucial factor in stabilizing the spine under lateral forces applied in the frontal plane. It was also found that with the presence of intra-abdominal pressure the spine quickly and consistently obtains ultimate balance state in case external forces in other directions as well as moments such as torques are acted on it. Based on these five development stages, the detailed spine model is successfully built and it is obvious that this model is considerably useful for surgeons to investigate biodynamic behavior of the whole spine under external forces applied onto any vertebra in any arbitrary direction.

Followed by the development process, the validation of the detailed spine model was thoroughly conducted in this research by comparing simulation results with those obtained from another spine model in the literature, experimental data as well as in-vivo measurements. The results demonstrated that axial and shear forces of L5-S1 disc are in good agreement with those of the spine model developed by Zee et al. (2007) in the literature and experimental data reported by McGill et al. (1987). Furthermore, it was proven that axial force of L4-L5 disc estimated when the human model was holding a full crate of beer closely fits with in-vivo intradiscal pressure measurements mentioned by Wilke et al. (2001). This is a good match considering the fact that no attempt was made to scale the model to the subject in the experiment. These findings are of significantly importance since they verify the accuracy of the spine model presented in the thesis and show that biodynamic behavior of the spine attained in the simulation process is reliable.

After the spine model is validated, dynamic characteristics of the whole spine were simulated and investigated in detail to describe the locomotion of the spine under varying external forces applied onto a certain vertebra in an arbitrary direction. It was found that determining relation between the spine motion and the external forces is critical since the movement of the spine is complex and different when the applied external forces change from vertebra to vertebra. As the arbitrary external forces can be divided into three component forces in x, y and z directions, the motion of the spine is a combination of its three types of motions corresponding to these three component forces. In addition, it is noted that the motion of the whole spine is constituted by the concurrent connection of all vertebrae's motions. Therefore, to precisely depict the movement of the spine, it is important to define motion functions of all vertebrae versus external forces in x, y and z directions. Under the forces acting on each vertebra in these three directions, dynamic properties of the spine model such as translation, rotation were achieved. Based on these obtained dynamic properties, displacement-force relationships of all vertebrae were interpolated and expressed in terms of polynomial functions. The key benefit of these polynomial functions is that they remarkably reduce computation cost in real time simulations and quickly help surgeons observe the locomotion of the spine model.

To enhance realism level during the interaction between the surgeons and the spine model, a novel haptic technique was successfully integrated into the HOOPS graphic environment. One major advantage of this technique is that dynamic simulation of the spine with a haptic interface offers better realism compared to those with only a visual interface. To achieve this realism, an available, reasonable and effective computational haptic rendering method was selected and presented in the thesis. Based on this method, the exploration process of the surgeons for the spine model becomes much more realistic. The surgeons can control the haptic cursor represented by a certain tool to directly touch, grasp and feel geometric shape as well as rigidity of the spine through the force feedback of the PHANToM device. Moreover, they can even apply external forces in any arbitrary direction onto any vertebra of the spine model. In this case, they can push or drag the vertebra to make the whole spine model deform. To observe the movement of the spine under external forces, displacement-force polynomial functions of all vertebrae as aforementioned was used in the haptically integrated graphic environment. By simulating in such versatile interface, the surgeons should be able to quickly and more realistically investigate the locomotion and dynamic properties of the spine model.

Since the geometry of spine model includes only vertebrae, it is not possible to observe deformation behaviour of all intervertebral discs during spine movement. Hence, a novel tetrahedral mass-spring system model of intervertebral disc was proposed and presented in detail in this thesis. Some tests on the functional performance of this tetrahedral MSS model of intervertebral discs were conducted before coming into use. The tests proved that the tetrahedral MSS model of intervertebral discs can preserve their volume under continuous loading and consistently deform with different assigned materials. After these tests, a combination of the tetrahedral MSS model of intervertebral disc and the thoracolumbar spine model was thoroughly described in this research. All models of IVDs are generated and interposed in position between vertebrae of the thoracolumbar spine model. Then, the upper and lower surfaces of each IVD are rigidly attached to the lower and upper surfaces of the superior and inferior vertebrae respectively. This combination of these two models creates a hybrid spine model which rapidly and conveniently provides deeper and more complete insight of biodynamic behavior of the spine in real-time simulations as well as deformation response of all IVDs in offline simulations.

7.2. Future works

Although the entirely discretized musculo-skeletal multi-body spine model is thoroughly developed in this thesis, there are still several limitations which can be considered interesting recommendations for future research.

Firstly, the modeling of the thoracic spine region during the stage of discretizing the default spine segments was still defective. For the thoracic spine region, the twelve pairs of ribs articulate posteriorly with the spine at the costovertebral joints. However, in this thesis, it is not possible to create the 12 pairs of costovertebral joints between the ribcage and the corresponding thoracic vertebrae. The reason is that the objects in LifeMOD are modeled as completely rigid bodies and therefore the deformation properties cannot be assigned to them. Simultaneously connecting the ribcage segment to multiple vertebra segments can result in software errors in the simulation process since the ribcage will deform during locomotion. To avoid these errors, the ribcage segment was linked to the thoracic spine region only at the 6th thoracic vertebra. Further study is needed to improve the modeling of this region. A possible solution is that the ribcage and sternum in LifeMOD can be discretized into smaller separate parts using a new software called 3-Matic (Materialise). Being able to solve this problem indicates that spinal deformities can be created in LifeMOD. In addition, as default spine models in LifeMOD are fully parameterized where input parameters (such as height, weight, gender) are easily varied, highly versatile models can be obtained and conveniently tuned to suit various individual spines. In other words, different types of scoliotic spine models can be generated and utilized for conducting in-depth studies on the motion of these spines subjected to dynamic forces.

Secondly, during the stage of implementing lumbar muscles, the intertransversarii and the interspinalis muscles were not included in the spine model. These muscles lie laterally to the axis of lateral flexion and behind the axis of sagittal rotation. Since they lie very close to these axes and are very small muscles, the forces they generate are considered negligible. Furthermore, it was suggested that their main function is to act as large, proprioceptive transducers (Bogduk, 1997). In a model based on inverse dynamics as presented in this thesis, it is therefore acceptable to exclude these muscles. However, it will be interesting to implement these two types of muscles into the spine model in future to make it more complete and accurate.

Thirdly, external forces applied onto each vertebra of the spine model in thee axis-aligned directions in LifeMOD were restricted to constant forces. Moreover, external moments about x, y and z axes were not explored in the thesis. Hence, further research should attempt to take these issues into account. For the former one, another direct extension of the work would be replacing the constant forces with varying forces. This can be achieved by assigning time-dependent force functions to the spine model via programming. For the latter one, although external moments such as torsion, flexion/extension and lateral bending can be applied onto each vertebra of the spine model, it is not possible to integrate these moments into the PHANToM device used in this research. Since the available PHANToM device in this research only provides force output in x, y and z directions, it is unable to make surgeons feel moment feedback in this case. To solve the problem, a possible solution is that a more advanced haptic device which gives 6-DOF output (i.e. forces and moments) can be utilized in future instead.

Fourthly, although the deformation of IVDs constructed by tetrahedral MSS model looks quite reasonable, further works in the future are required to validate this MSS model with an offline FEM model. To achieve this, geometries of two vertebrae and one IVD can be imported into ABAQUS. Then, the tetrahedral FEM of the IVD can be automatically generated. Comparing deformation of this tetrahedral FEM (e.g. displacement of nodes) obtained after simulation with that of the tetrahedral MSS will provide consistent data to estimate the accuracy of the tetrahedral MSS model. In addition, since mechanical properties of the tetrahedral MSS model of IVDs were assumed to be homogeneous and linear elastic, another possible avenue of future work is that this model can be extended into a heterogeneous and nonlinear one to more correctly depict the properties of the IVDs. As a result, deformation behavior of the IVDs when the spine model is under external forces will become more precise and reliable.

REFERENCES

Ahmed AM, Shirazi-Adl A, and Shrivastava SC, "A finite element study of a lumbar motion segment subjected to pure sagittal plane moments", *Journal of Biomechanics*, Vol. 19, No. 4, pp. 331-350, 1986.

Andersson E, Oddsson L, Grundstrom H, and Thorstensson A, "The role of the psoas and iliacus muscles for stability and movement of the lumbar spine, pelvis and hip", *Scandinavian Journal of Medicine and Science in Sports*, Vol. 5, No. 1, pp. 10-16, 1995.

Argoubi M and Shirazi-Adl A, "Poroelastic creep response analysis of a lumbar motion segment in compression", *Journal of Biomechanical Engineering*, Vol. 29, No. 10, pp. 1331-1339, 1996.

Arjmand N and Shirazi-Adl A, "Role of intra-abdominal pressure in the unloading and stabilization of the human spine during static lifting tasks", *European Spine Journal*, Vol. 15, No. 8, pp. 1265-1275, 2006.

Arvo J, "A simple method for box-sphere intersection testing", *Graphics Gems*, pp. 335-339, 1990.

Aubin CE, "Scoliosis study using finite element models", *Studies in Health Technology and Informatics*, Vol. 91, pp. 309-313, 2002.

Avila RS and Sobierajski LM. *A haptic interaction method for volume visualization*. in *Proceedings of IEEE Visualization*. 1996.

Baraff D and Witkin A, "Dynamic simulation of non-penetrating flexible bodies", *In Proceedings of SIGGRAPH*, pp. 303-308, 1992.

Basdogan C, Ho CH, and Srinivasan MA. *A ray-based haptic rendering technique for displaying shape and texture of 3D objects in virtual enviroments*. in *Proceedings of ASME Dynamic Systems and Control Division*. 1997.

Basdogan C, Ho CH, Srinivasan MA, Small SD, and Dawson SL, "Force interaction in laparoscopic simulations: haptic rendering of soft tissues." *Stud. Health Technol. Inform.*, Vol. 50, pp. 385-391, 1998.

Basdogan C and Srinivasan MA. *Haptic rendering in virtual environments*. in *Handbook of Virtual Environments: Design, Implementation, and Applications*. 2002.

Belytschko T and Privitzer E, "Refinement and validation of a three-dimensional head-spine model", 1978.

Belytschko TB, Andriacchi TP, Schultz AB, and Galante JO, "Analog studies of forces in the human spine: computational techiniques", *Journal of Biomechanics*, Vol. 6, No. 4, pp. 361-371, 1973.

Berkson MH, "Mechanical properties of human lumbar spine motion segments-part 2: response in compression and shear; influence of gross morphology", *Journal of Biomechanical Engineering*, Vol. 101, pp. 53-57, 1979.

Bogduk N, Macintosh JE, and Pearcy MJ, "A universal model of the lumbar back muscles in the upright position", *Spine*, Vol. 17, No. 8, pp. 897-913, 1992a.

Bogduk N, Pearcy MJ, and Hadfield G, "Anatomy and biomechanics of psoas major", *Clinical Biomechanics*, Vol. 7, No. 2, pp. 109-119, 1992b.

Bogduk N, *Clinical anatomy of the lumbar spine and sacrum*. 1997, Edinburgh: Churchill Livingstone.

Bos WVD, Duersen DLV, and Kingma I, "Non-linear behavior of the intervertebral disc, a finite element approach", 2002.

Bourguignon D and Cani MP. *Controlling anisotropy in mass spring systems*. in *Proceedings of the Eleventh Eurographics Workshop on Computer Animation and Simulation*. 2000.

Bozic KJ, Keyak JH, Skinner HB, Bueff HU, and Bradford DS, "Three-dimensional finite element modeling of a cervical vertebra: an investigation of burst fracture mechanism", *Journal of Spinal Disorders*, Vol. 7, No. 2, pp. 102-110, 1994.

Buck B and Woelfel HP, "Dynamic three-dimensional finite element model of a sitting man with a detailed representation of the lumbar spine and muscles", pp. 379-386, 1998.

Celniker G and Gossard D, "Deformable curve and surface finite elements for free form shape design", *Computer & Graphics*, Vol. 25, No. 4, pp. 257-266, 1991.

Cheung JTM, Zhang M, and Chow DHK, "Biomechanical responses of the intervertebral joints to static and vibrational loading: a finite element study", *Clinical Biomechanics*, Vol. 18, No. 9, pp. 790-799, 2003.

Cholewicki J, Juluru K, and McGill SM, "Intra-abdominal pressure mechanism for stabilizing the lumbar spine", *Journal of Biomechanics*, Vol. 32, No. 1, pp. 13-17, 1999.

Cobb WS, Burns JM, Kercher KW, Matthews BD, James NH, and Todd HB, "Normal intraabdominal pressure in healthy adults", *Journal of Surgical Research*, Vol. 129, No. 2, pp. 231-235, 2005.

Deng YC and Goldsmith W, "Response of a human head/neck/upper torso replica to dynamic loading. Part 1: physical model", *Journal of Biomechanics*, Vol. 20, pp. 471-486, 1987a.

Deng YC and Goldsmith W, "Response of a human head/neck/upper torso replica to dynamic loading. Part 2: analytical/numerical model", *Journal of Biomechanics*, Vol. 20, No. 487-497, 1987b.

Deussen O, Kobbelt L, and Tucke P, "Using simulated annealing to obtain good nodal approximations of deformable objects", pp. 1-14, 1995.

Ericson C, *Real-time collision detection*. 2005, San Francisco: Morgan Kaufmann.

Esat V and Acar M, "A multi-body model of the whole human spine for whiplash investigations", 2007.

Fritz M, "Estimation of spine forces under whole-body vibration by means of a biomechanical model and transfer functions", *Aviat. Space Environ. Med.*, Vol. 68, No. 6, pp. 512-519, 1997.

Fritz M, "Three-dimensional biomechanical model for simulating the response of the human body to vibration stress", *Journal of Medical & Biological Engineering & Computing*, Vol. 36, No. 6, pp. 686-692, 1998.

Fritz M, "Simulating the response of a standing operator to vibration stress by means of a biomechanical model", *Journal of Biomechanics*, Vol. 33, No. 7, pp. 795-802, 2000.

Gao Z and Gibson I, "Haptic sculpting of multi-resolution B-spline surfaces with shaped tools", *Computer Aided Design*, Vol. 38, No. 6, pp. 661-676, 2006.

Garcia T and Ravani B, "A biomechanical evaluation of whiplash using a multi-body dynamic model", *Journal of Biomechanical Engineering*, Vol. 125, No. 2, pp. 254-265, 2003.

Gelder AV, "Approximate simulation of elastic membranes by triangulated spring meshes", *Journal of Graphics Tools*, Vol. 3, No. 2, pp. 21-41, 1998.

Gibson SFF and Mirtich B, "A survey of deformable modeling in computer graphics", *MERL*, pp. 1-33, 1997.

Gignac D, Aubin CE, Dansereau J, and Labelle H, "Optimization method for 3D bracing correction of scoliosis using a finite element model", *European Spine Journal*, Vol. 9, No. 3, pp. 185-190, 2000.

Goel VK, Kim YE, Lim TH, and Weinsrein JN, "An analytical investigation of the mechanics of spinal instrumentation", *Spine*, Vol. 13, pp. 1003-1011, 1988.

Goel VK, Park H, and Kong WZ, "Investigation of vibration characteristics of the ligamentous lumbar spine using the finite element approach", *Journal of Biomechanical Engineering*, Vol. 116, No. 4, pp. 377-383, 1994.

Goel VK, Monroe BT, Gilbertson LG, Brinckmann P, and Nat R, "Interlaminar shear stresses and laminae separation in a disc : finite element analysis of the L3-L4 motion segment subjected to axial compressive loads", *Spine*, Vol. 20, No. 6, pp. 689-698, 1995.

Goel VK and Clausen JD, "Prediction of load sharing among spinal components of a C5-C6 motion segment using the finite element approach", *Spine*, Vol. 23, No. 6, pp. 684-691, 1998.

Gorman P, Krummel T, Webster R, Smith M, and Hutchens D, "A prototype haptic lumbar puncture simulator", *Studies in Health Technology and Informatics*, Vol. 70, 2000.

Greaves CY, Gadala MS, and Oxland TR, "A three-dimensional finite element model of the cervical spine with spinal cord: an investigation of three injury mechanisms", *Annals of Biomedical Engineering*, Vol. 36, No. 3, pp. 396-405, 2008.

Gregory A, Mascarenhas A, Ehmann S, Lin M, and Manocha D. *Six degree-of-freedom haptic display of polygonal models*. in *Proceedings of Visualization*. 2000.

Guo LX and Teo EC, "Predication of the modal characteristics of the human spine at resonant frequency using finite element models", *Journal of Engineering in Medicine*, Vol. 219, No. 4, pp. 277-284, 2005.

Guo LX and Teo EC, "Influence of injury and vibration on adjacent components of spine using finite element methods", *Journal of Spinal Disorders & Techniques*, Vol. 19, No. 2, pp. 118-124, 2006.

Guo LX, Zhang M, Wang ZW, Zhang YM, Wen BC, and Li JL, "Influence of anteroposterior shifting of trunck mass centroid on vibrational configuration of human spine", *Computers in Biology and Medicine*, Vol. 38, No. 1, pp. 146-151, 2008.

Hayward V, Astley OR, Hernandez MC, and Grant D, "Haptic interfaces and devices", *Sensor Review*, Vol. 24, No. 1, pp. 16-29, 2004.

Heiplatz P, Hartle SL, and Gentle CR, "A three-dimensional large deformation finite element analysis of a ligamentous C4-C7 spine unit", *Third International Symposium on Computer Methods in Biomechanics and Biomechanical Engineering*, pp. 387-394, 1998.

Heitplatz F, Hartle SL, and Gentle CR, "A 3-dimensional large deformation finite element analysis of a ligamentous C4-C7 spine unit", pp. 387-394, 1997.

Himmetoglu S, Acar M, Taylor AJ, and Marouf KB, "A multi-body head-and-neck model for simulation of rear impact in cars", *Journal of Automobile Engineering*, Vol. 221, No. 5, pp. 527-541, 2007.

Hinz B, Seidel H, Hofmann J, and Menzel G, "The significance of using anthropometric parameters and postures of European drivers as a database for finite-element models when calculating spinal forces during whole-body vibration exposure", *International Journal of Industrial Ergonomics*, Vol. 38, No. 9-10, pp. 816-843, 2007.

Hodges PW, Cresswell AG, Daggfeldt K, and Thorstensson A, "In vivo measurement of the effect of intra-abdominal pressure on the human spine", *Journal of Biomechanics*, Vol. 34, No. 3, pp. 347-353, 2001.

Hofmann J, Pankoke S, and Woelfel HP, "Individualised FE-model of seated humans and representation of motion segments of the lumbar spine as substructure to determine internal loads during vibration exposure", 2003.

HOOPS [cited; Available from: http://www.techsoft3d.com/].

Ishikawa Y, Shimada Y, Iwami T, Kamada K, Matsunaga T, Misawa A, et al., "Model simulation for restoration of trunk in complete paraplegia by functional electrical stimulation", 2005.

Jager M, "Assessing spinal load during mannual material handling via the compressive strength of cadaveric lumbar-spine elements", 1996.

Jager M, Sauren A, Thunnissen JGM, and Wismans JSHM, "A global and detailed mathematical model for head-neck dynamics", *SAE Tech. Pap. Ser.*, 1996.

Jiménez P, Thomas F, and Torras C, "3D collision detection: a survey", *Computer & Graphics*, Vol. 25, No. 2, pp. 269-285, 2001.

Jun Y, "A computational model of the human head and cervical spine for dynamic impact simulation", 2006.

Kang YB, Jung DY, Tanaka M, Yoshino N, Tsutsumi S, and Ikeuchi K, "Numerical analysis of three-dimensional cervical behaviors in posterior-oblique car collisions using 3-D human whole body finite element model", *JSME International Journal Series C*, Vol. 48, No. 4, pp. 598-606, 2005.

Kim L, Kyrikou A, Sukhatme GS, and Desbrun M. *An implicit-based haptic rendering technique*. in *Proceedings of IEEE IROS 2002*. 2002.

Kim SM, Yang IC, and Lee MP, "Cervical spine injury analysis regarding frontal and side impacts of wheelchair occupant in vehicle by LifeMOD", *IFMBE Proceedings*, Vol. 14, pp. 2521-2524, 2007.

Kim YE, Goel VK, Weinstein JN, and Lim TH, "Effect of disc degeneration at one level one the adjacent level in axial mode", *Spine*, Vol. 16, No. 3, pp. 331-335, 1991.

Kitazaki S and Griffin MJ, "Resonance behaviour of the seated human body and effects of posture", 1996.

Kitazaki S and Griffin MJ, "A model analysis of whole-body vertical vibration, using a finite element model of the human body", *Journal of Sound and Vibration*, Vol. 200, No. 1, pp. 83-103, 1997.

Kong WZ and Goel VK, "Ability of the finite element models to predict response of the human spine to sinusoidal vertical vibration", *Spine*, Vol. 28, No. 17, pp. 1961-1967, 2003.

Krismer M, Heid C, and Rabl W, "The contribution of annulus fibers to torque resistance", *Spine*, Vol. 21, No. 22, pp. 2551-2557, 1996.

Kroonenberg AVD, Thunnissen J, and Wismans J, "A human model for low-severity rear-impacts", *In Proceedings of the 1997 International IRCOBI Conference*, pp. 117-132, 1997.

Kulak RF, Belytschko T, and Schultz AB, "Nonlinear behavior of the human intervertebral disc under axial load", *Journal of Biomechanics*, Vol. 9, No. 6, pp. 377-386, 1976.

Kumaresan S, Yoganandan N, and Pintar FA, "Finite element analysis of the cervical spine: a material property sensitivity study", *Clinical Biomechanics*, Vol. 14, No. 1, pp. 41-53, 1999.

Kumaresan S, Yoganandan N, Pintar FA, and Maiman DJ, "Finite element modeling of the cervical spine: role of intervertebral disc under axial and eccentric loads", *Medical Engineering Physics*, Vol. 21, No. 10, pp. 689-700, 1999.

Kumaresan S, Yoganandan N, Pintar FA, Maiman DJ, and Goel VK, "Contribution of disc degeneration to osteophyte formation in the cervical spine: a biomechanical investigation", *Journal of Orthopedic Research*, Vol. 19, No. 5, pp. 977-984, 2001.

Kurowski P and Kubo A, "The relationship of degeneration of the intervertebral disc to mechanical loading conditions on lumbar vertebrae", *Spine*, Vol. 11, No. 7, pp. 726-731, 1986.

Kurtz SM and Edidin AA, *Spine technology handbook*. 2006, San Diego: Elsevier.

Kyureghyan NC and Marras W, "Prediction of intervertebral disc creep during flexion using a combined experimental and finite element approach", 2005.

Lafage V, Dubousset J, Lavaste F, and Skalli W, "3D finite element simulation of Cotrel-Dubousset correction", *Computer Aided Surgery*, Vol. 9, No. 1-2, pp. 17-25, 2004.

Laible JP, Pflaster DS, Krag MH, Simon BR, and Haugh LD, "A poroelastic-swelling finite element model with application to the intervertebral disc", *Spine*, Vol. 18, No. 5, pp. 659-670, 1993.

Laycock SD and Day AM, "A survey of haptic rendering techniques", *Computer Graphics Forum*, Vol. 26, No. 1, pp. 50-65, 2007.

Lee Y, Terzopoulos D, and Waters K. *Realistic face modeling for animation.* in *Proceedings of SIGGRAPH '95 Conference*. 1995.

Liebschner MAK, Kopperdahl DL, Rosenberg WS, and Keaveny TM, "Finite element modeling of the human thoracolumbar spine", *Spine*, Vol. 28, No. 6, pp. 559-565, 2003.

LifeMOD Biomechanics Modeler [cited; Available from: http://www.lifemodeler.com/].

LifeMOD Manual [cited; Available from: http://www.lifemodeler.com/LM_Manual/overview_quickstart.shtml].

Linder A, "A new mathematical neck model for a low-velocity rear-end impact dummy: evaluation of components influencing head kinematics", *Accident Analysis and Prevention*, Vol. 32, No. 2, pp. 261-269, 2000.

Lopik DWV and Acar M, "A computational model of the human head and neck system for the analysis of whiplash motion", *International Journal of Crashworthiness*, Vol. 9, No. 5, pp. 465-473, 2004.

Lopik DWV and Acar M, "Development of a multi-body computational model of human head and neck", *Proceedings of the Institution of Mechanical Engineers, Part K: Journal of Multi-body Dynamics*, Vol. 221, No. 2, pp. 175-197, 2007.

Luan F, Yang KH, Deng B, Begeman PC, Tashman S, and King AI, "Qualitative analysis of neck kinematics during low-speed rear-end impact", *Clinical Biomechanics*, Vol. 15, No. 9, pp. 649-657, 2000.

Luo ZP and Goldsmith W, "Reaction of a human head-neck-torso system to shock", *Journal of Biomechanics*, Vol. 24, No. 7, pp. 499-510, 1991.

Luoma K, Riihimaki H, Luukkonen R, Raininko R, Viikari-Juntura E, and Lamminen A, "Low back pain in relation to lumbar disc degeneration", *Spine*, Vol. 25, No. 4, pp. 487-492, 2000.

Macintosh JE and Bogduk N, "The morphology of the human lumbar multifidus", *Clinical Biomechanics*, Vol. 1, No. 4, pp. 196-204, 1986.

Macintosh JE and Bogduk N, "1987 Volvo award in basic science: the morphology of the lumbar erector spinae", *Spine*, Vol. 12, No. 7, pp. 658-668, 1987.

Macintosh JE and Bogduk N, "The attachments of the lumbar erector spinae", *Spine*, Vol. 16, No. 7, pp. 783-792, 1991.

Martinez JB, Oloyede VO, and Broom ND, "Biomechanics of load-bearing of the intervertebral disc: an experimental and finite element model", *Medical Engineering Physics*, Vol. 19, No. 2, pp. 145-156, 1996.

3-Matic [cited; Available from: http://www.materialise.com/3-matic].

Maurel N, Lavaste F, and Skalli W, "A three-dimensional parameterized finite element model of the lower cervical spine: study of the influence of the posterior articular facets", *Journal of Biomechanics*, Vol. 30, No. 9, pp. 921-931, 1997.

McGill SM and Norman RW, "Effects of an anatomically detailed erector spinae model on L4/L5 disc compression and shear", *Journal of Biomechanics*, Vol. 20, No. 6, pp. 591-600, 1987.

McInerny T and Terzopoulos D, "Deformable models in medical image analysis: a survey", *Medical Image Analysis*, Vol. 1, No. 2, pp. 91-108, 1996.

McNeely W, Puterbaugh K, and Troy J. *Six degree-of-freedom haptic rendering using voxel sampling*. in *Proc. of ACM SIGGRAPH*. 1999.

Mollemans W, Schutyser F, Cleynenbreugel JV, and Suetens P, "Tetrahedral Mass Spring Model for Fast Soft Tissue Deformation ", Vol. 2673, pp. 145-154, 2003.

Morgenbesser HB and Srinivasan MA. *Force shading for haptic perception*. in *Proceedings of ASME Dynamic Systems and Control Division*. 1996.

Moroney SP, Schultz AB, Miller JAA, and Anderson GBJ, "Load-displacement properties of lower cervical spine motion segment", *Journal of Biomechanics*, Vol. 21, pp. 767-779, 1988.

Nabhani F and Wake M, "Computer modelling and stress analysis of the lumbar spine", *Journal of Materials Processing Technology*, Vol. 127, No. 1, pp. 40-47, 2002.

Natarajan RN, Ke JH, and Andersson GB, "A model to study the disc degeneration process", *Spine*, Vol. 19, No. 3, pp. 259-265, 1994.

Natarajan RN, Williams JR, Lavender SA, and Andersson GBJ, "Poro-elastic finite element model to predict the failure progression in a lumbar disc due to cyclic loading", *Computers & Structures*, Vol. 85, No. 11-14, pp. 1142-1151, 2007.

Nelson DD, Johnson DE, and Cohen E. *Haptic rendering of surface-to-surface sculpted model interaction*. in *Proceedings of 8th Annual Symp. Haptic Interfaces for Virtual Environment and Teleoperator Systems*. 1999.

Ng H and Grimsdale R, "Computer graphics techniques for modeling cloth", *IEEE Computer Graphics and Applications*, Vol. 16, No. 5, pp. 28-41, 1996.

Ng HW and Teo EC, "Development and validation of a C0-C7 FE complex for biomechanical study", *Journal of Biomechanics*, Vol. 127, No. 5, pp. 729-735, 2005.

Ono K, Kaneoka K, Wittek A, and Kajzer J, "Cervical injury mechanism based on the analysis of human cervical vertebral motion and head-neck-torso kinematics during low speed rear impacts", *SAE Tech. Pap. Ser.*, 1997.

Pang TY, "Transmission of vibration at the lower lumbar spine due to whole-body vibration", 2006.

Panjabi MM, Brand RA, and White AA, "Mechanical properties of the human thoracic spine as shown by three-dimensional load-displacement curves", *Journal of Bone and Joint Surgery*, Vol. 58, No. 5, pp. 642-652, 1976.

Panjabi MM, Dvorak J, Duranceau J, Yamamoto I, Geber M, Rausching W, et al., "Three-dimensional movements of the upper cervical spine", *Spine*, Vol. 13, pp. 726-730, 1988.

Panjabi MM, Crisco JJ, Lydon C, and Dvorak J, "The mechanical properties of human alar and transverse ligaments at slow and fast extension rates", *Clinical Biomechanics*, Vol. 13, No. 2, pp. 112-120, 1998.

Panjabi MM, Crisco JJ, Vasavada A, Oda T, Cholewicki J, Nibu K, et al., "Mechanical properties of the human cervical spine as shown by three-dimensional load-displacement curves", *Spine*, Vol. 26, No. 24, pp. 2692-2700, 2001.

Pankoke S, Buck B, and Woelfel HP, "Dynamic FE model of sitting man adjustable to body height, body mass and posture used for calculating internal forces in the lumbar vertebral disks", *Journal of Sound and Vibration*, Vol. 215, No. 4, pp. 827-839, 1998.

Pankoke S, Hofmann J, and Woelfel HP, "Determination of vibration-related spinal loads by numerical simulation", *Clinical Biomechanics*, Vol. 16, No. 1, pp. S45-S56, 2001.

Pelker RR, Duranceau J, and Panjabi MM, "Cervical spine stabilization: a three-dimensional biomechanical evaluation of rotational stability, strength and failure mechanism", *Spine*, Vol. 16, No. 2, pp. 117-122, 1991.

Penning L, "Psoas muscle and lumbar spine stability: a concept uniting existing controversies. Critical review and hypothesis", *European Spine Journal*, Vol. 9, No. 6, pp. 577-585, 2000.

Pintar FA, Yoganandan N, Myers T, Elhagediab A, and Sances AJ, "Biomechanical properties of human lumbar spine ligaments", *Journal of Biomechanics*, Vol. 25, No. 11, pp. 1351-1356, 1992.

Pitzen T, Geisler F, Matthis D, Storz HM, Barbier D, Steudel WI, et al., "A finite element model for predicting the biomechanical behaviour of the human lumbar spine", *Control Engineering Practice*, Vol. 10, No. 1, pp. 83-90, 2002.

Platt S and Badler N, "Animating facial expressions", *Computer & Graphics*, Vol. 15, No. 3, pp. 245-252, 1981.

Pope MH, Broman H, and Hansson T, "Factors affecting the dynamic of the seated subject", *Journal of Spinal Disorders*, Vol. 3, pp. 135-142, 1990.

Poulin F, Aubin CE, Stokes IA, Gardner-Morse M, and Labelle H, "Biomechanical modeling of instrumentation for the scoliotic spine using flexible elements: a feasibility study", *Annales De Chirurgie*, Vol. 52, No. 8, pp. 761-767, 1998.

Promayon E, Baconnier P, and Puech C, "Physically-based deformations constrained in displacements and volume." *Proceedings of Eurographics '96*, Vol. 15, No. 3, pp. 155-164, 1996.

Qiu TX, Tan KW, Lee VS, and Teo EC, "Investigation of thoracolumbar T12–L1 burst fracture mechanism using finite element method", *Medical Engineering Physics*, Vol. 28, No. 7, pp. 656-664, 2006.

Qiu TX, Teo EC, and Zhang QH, "Effect of bilateral facetectomy of thoracolumbar spine T11–L1 on spinal stability", *Medical and Biological Engineering and Computing*, Vol. 44, No. 5, pp. 363-370, 2006.

Qiu TX, Teo EC, and Zhang QH, "Effect of bilateral facetectomy of thoracolumbar spine T11-L1 on spinal stability." *Medical & Biological Engineering & Computing*, Vol. 44, No. 5, pp. 363-370, 2006.

Qiu TX, Zhang QH, and Teo EC, "Finite element analysis of head-neck kinematics under rear-end impact conditions", pp. 206-209, 2006.

Robert L. Williams I, Srivastava M, Howell JN, Robert R. Conatser J, Eland DC, Burns JM, et al. *The virtual haptic back for palpatory training*. in *Proceedings of the 6th international conference on multimodal interfaces*. 2004.

Rohlmann A, Zander T, Schmidt H, Wilke HJ, and Bergmann G, "Analysis of the influence of disc degeneration on the mechanical behaviour of a lumbar motion segment using the finite element method", *Journal of Biomechanics*, Vol. 39, No. 13, pp. 2484-2490, 2006.

Ruspini DC, Kolarov K, and Khatib O. *The haptic display of complex graphical environments*. in *Proceedings of ACM SIGGRAPH*. 1997.

Salisbury JK and Tarr C. *Haptic rendering of surfaces defined by implicit functions*. in *Proceedings of ASME Dynamic Systems and Control Division*. 1997.

Salisbury K, Conti F, and Barbagli F, "Haptic rendering: introductory concepts", *IEEE Computer Graphics and Applications*, Vol. 24, No. 2, pp. 24-32, 2004.

Schmidt H, Kettler A, Rohlmann A, Claes L, and Wilke HJ, "The risk of disc prolapses with complex loading in different degrees of disc degeneration – a finite element analysis", *Clinical Biomechanics*, Vol. 22, No. 9, pp. 988-998, 2007.

Schmidt H, Heuer F, Claes L, and Wilke HJ, "The relation between the instantaneous center of rotation and facet joint forces – A finite element analysis", *Clinical Biomechanics*, Vol. 23, No. 3, pp. 270-278, 2008.

Schroeder Y, Wilson W, Huyghe JM, and Baaijens FPT, "Osmoviscoelastic finite element model of the intervertebral disc", *European Spine Journal*, Vol. 15, No. 3, pp. 361-371, 2006.

Schultz AB, Belytschko TB, Andriacchi TP, and Galante JO, "Analog studies of forces in the human spine: mechanical properties and motion segment behavior", *Journal of Biomechanics*, Vol. 6, No. 4, pp. 373-383, 1973.

Schultz AB and Hirsch C, "Mechanical analysis of Harrington rod correction of idiopathic scoliosis", *The Journal of Bone and Joint Surgery. American Volume*, Vol. 55, No. 5, pp. 983-992, 1973.

Schultz AB and Hirsch C, "Mechanical analysis of techniques for improved correction of idiopathic scoliosis", *Clinical Orthopaedics and Related Research*, Vol. 100, pp. 66-73, 1974.

Schultz AB, "Mechanical properties of human lumbar spine motion segments-part 1: responses in flexion, extension, lateral bending and torsion", *Journal of Biomechanical Engineering*, Vol. 101, pp. 46-52, 1979.

Schultz AB, Warwick DN, Berkson MH, and Nachemson AL, "Mechanical properties of human lumbar spine motion segments-part 1: responses in flexion, extension, lateral bending and torsion", *Journal of Biomechanical Engineering*, Vol. 101, pp. 46-52, 1979.

Schultz AB and Ashton-Miller JA, *Biomechanics of the human spine*, in *Basic orthopaedic biomechanics*, V.C. Mow and W.C. Hayes, Editors. 1991, Raven Press: New York. p. 337-374.

Seidel H and Griffin MJ, "Modelling the response of the spine system to whole-body vibration and repeated shock", *Clinical Biomechanics*, Vol. 16, No. 1, pp. 3-7, 2001.

Seidel H, Hinz B, and Bluthner R, "Application of finite element models to predict forces acting on the lumbar spine during whole-body vibration", *Clinical Biomechanics*, Vol. 16, No. 1, pp. S57-S63, 2001.

SensAble PHANTOM [cited; Available from: http://www.sensable.com/].

Shea M, Edwards WT, White AA, and Hayes WC, "Variations of stiffness and strength along the human cervical spine", *Journal of Biomechanics*, Vol. 24, No. 2, pp. 95-107, 1991.

Shirado O, Kaneda K, Tadano S, Ishikawa H, McAfee PC, and Warden KE, "Influence of disc degeneration on mechanism of thoracolumbar burst fractures", *Spine*, Vol. 17, No. 3, pp. 286-292, 1992.

Shirazi-Adl A, "Nonlinear stress analysis of the whole lumbar spine in torsion—Mechanics of facet articulation", *Journal of Biomechanics*, Vol. 27, No. 3, pp. 289-299, 1994.

Shirazi-Adl SA, Shrivastava SC, and Ahmed AM, "Stress analysis of the lumbar disc-body unit in compression. A three-dimensional nonlinear finite element study", *Spine*, Vol. 9, No. 2, pp. 120-134, 1984.

Silva MJ, Keaveny TM, and Hayes WC, "Computed tomography-based finite element analysis predicts failure loads and fracture patterns for vertebral sections", *Journal of Orthopedic Research*, Vol. 16, No. 3, pp. 300-308, 1998.

Spilker RL, Daugirda DM, and Schultz AB, "Mechanical response of a simple finite element model of the intervertebral disc under complex loading", *Journal of Biomechanics*, Vol. 17, No. 2, pp. 103-112, 1984.

Spineuniverse [cited; Available from: http://www.spineuniverse.com/anatomy].

Srinivasan MA and Basdogan C, "Haptics in virtual environments: Taxonomy, research status, and challenges", *Computer & Graphics*, Vol. 21, No. 4, pp. 393-404, 1997.

Stemper BD, Yoganandan N, and Pintar FA, "Validation of a head-neck computer model for whiplash simulation", *Medical and Biological Engineering and Computing*, Vol. 42, No. 3, pp. 333-338, 2004.

Stokes IA and Laible JP, "Three-dimensional osseo-ligamentous model of the thorax representing initiation of scoliosis by asymmetric growth", *Journal of Biomechanics*, Vol. 23, No. 6, pp. 589-595, 1990.

Stokes IA and Gardner-Morse M, "Quantitative anatomy of the lumbar musculature", *Journal of Biomechanics*, Vol. 32, No. 3, pp. 311-316, 1999.

Teo EC and Ng HW, "Evaluation of the role of ligaments, facets and disc nucleus in lower cervical spine under compression and sagittal moments using finite element method", *Medical Engineering Physics*, Vol. 23, No. 3, pp. 155-164, 2001.

Teo EC and Ng HW, "First cervical vertebra (atlas) fracture mechanism studies using finite element method", *Journal of Biomechanics*, Vol. 34, No. 1, pp. 13-21, 2001.

The Wellington Hospital [cited; Available from: http://www.thewellingtonneurosurgeryunit.com/spine-anatomy-cord.asp].

Thompson TV, Johnson DE, and Cohen E. *Direct haptic rendering of sculptured models*. in *Proceedings of Symposium on Interactive 3D Graphics*. 1997.

Tyrrell A and Reilly T, "Circadian variation in stature and the effects of spinal loading", *Spine*, Vol. 10, No. 2, pp. 161-164, 1985.

Vallfors B, "Acute, subacute and chronic low back pain: clinical symptoms, absenteeism and working environment", *Scandinavian Journal of Rehabilitation Medicine. Supplement*, Vol. 11, pp. 1-98, 1985.

Van Der Horst MJ, "Human Head Neck Response in Frontal, Lateral and Rear End Impact Loading: Modeling and Validation", 2002.

Vanderby RJ, Daniele M, Patwardhan A, and Bunch W, "A method for the identification of in-vivo segmental stiffness properties of the spine", *Journal of Biomechanical Engineering*, Vol. 108, No. 4, pp. 312-316, 1986.

Verver MM, Hoof JV, Oomens CWJ, Wouw NVD, and Wismans JSHM, "Estimation of spinal loading in vertical vibrations by numerical simulation", *Clinical Biomechanics*, Vol. 18, No. 9, pp. 800-811, 2003.

Viviani GR, Ghista DN, Lozada PJ, Subbaraj K, and Barnes G, "Biomechanical analysis and simulation of scoliosis surgical correction", *Clinical Orthopaedics and Related Research*, No. 208, pp. 40-47, 1986.

Wilke HJ, Neef P, Hinz B, Seidel H, and Claes L, "Intradiscal pressure together with anthropometric data – a data set for the validation of models", *Clinical Biomechanics*, Vol. 16, No. 1, pp. S111-S126, 2001.

Yoganandan N, Kumaresan S, Voo L, Pintar FA, and Larson SJ, "Finite element modeling of the C4-C6 cervical spine unit", *Medical Engineering Physics*, Vol. 18, No. 7, pp. 569-574, 1996.

Yoganandan N, Kumaresan S, and Pintar FA, "Biomechanics of the cervical spine-Part 2: Cervical spine soft tissue responses and biomechanical modeling", *Clinical Biomechanics*, Vol. 16, No. 1, pp. 1-27, 2001.

Yoshimura T, Nakai K, and Tamaoki G, "Multi-body dynamics modelling of seated human body under exposure to whole-body vibration", Vol. 43, No. 3, pp. 441-447, 2005.

Zander T, Rohlmann A, Klockner C, and Bergmann G, "Comparison of the mechanical behavior of the lumbar spine following mono-and bisegmental stabilization", *Clinical Biomechanics*, Vol. 17, No. 6, pp. 439-445, 2002.

Zee MD, Hansen L, Wong C, Rasmussen J, and Simonsen E, "A generic detailed rigid-body lumbar spine model", *Journal of Biomechanics*, Vol. 40, No. 6, pp. 1219-1227, 2007.

Zhang QH, Teo EC, and Huang RC, "Finite element analysis of head-neck kinematics during motor vehicle accidents: analysis in multiple planes", *Medical Engineering Physics*, Vol. 29, No. 1, pp. 54-60, 2007.

Zhang QH, Li JZ, Serena Tan HN, and Teo EC, "A Finite Element Study of The Response of Thoracolumbar Junction to accidental mine blast scenario", Vol. 19, pp. 129-132, 2008.

Zhang QH, Li JZ, Serena Tan HN, and Teo EC, "A finite element study of the response of thoracolumbar junction to accidental mine blast scenario." *IFMBE Proceedings*, Vol. 19, No. 5, pp. 129-132, 2008.

Zilles C and Salisbury JK, "A constrain based god object method for haptic display." *International Conference of Intelligent Robots and Systems, Human Robot Interaction, and Cooperative Robots, IEEE CS Press*, 1995.

APPENDIX A

LIFEMOD PRACTICAL TUTORIALS

In this appendix, the LifeMOD interface is briefly introduced. Then, some tutorials are examined to help users become familiar with the LifeMOD environment and explore the features and capabilities of the software.

➢ LifeMOD control panels

LifeMOD provides a very intuitive and easy-to-use graphical interface with complete control panels for an end-user where the user is not required to know any programming language. These control panels enable the user complete functionality to generate, display, analyze, animate and plot data. Figure A. 1 displays the main modeling panel, the display toolbox and the automated tutorial control panel.

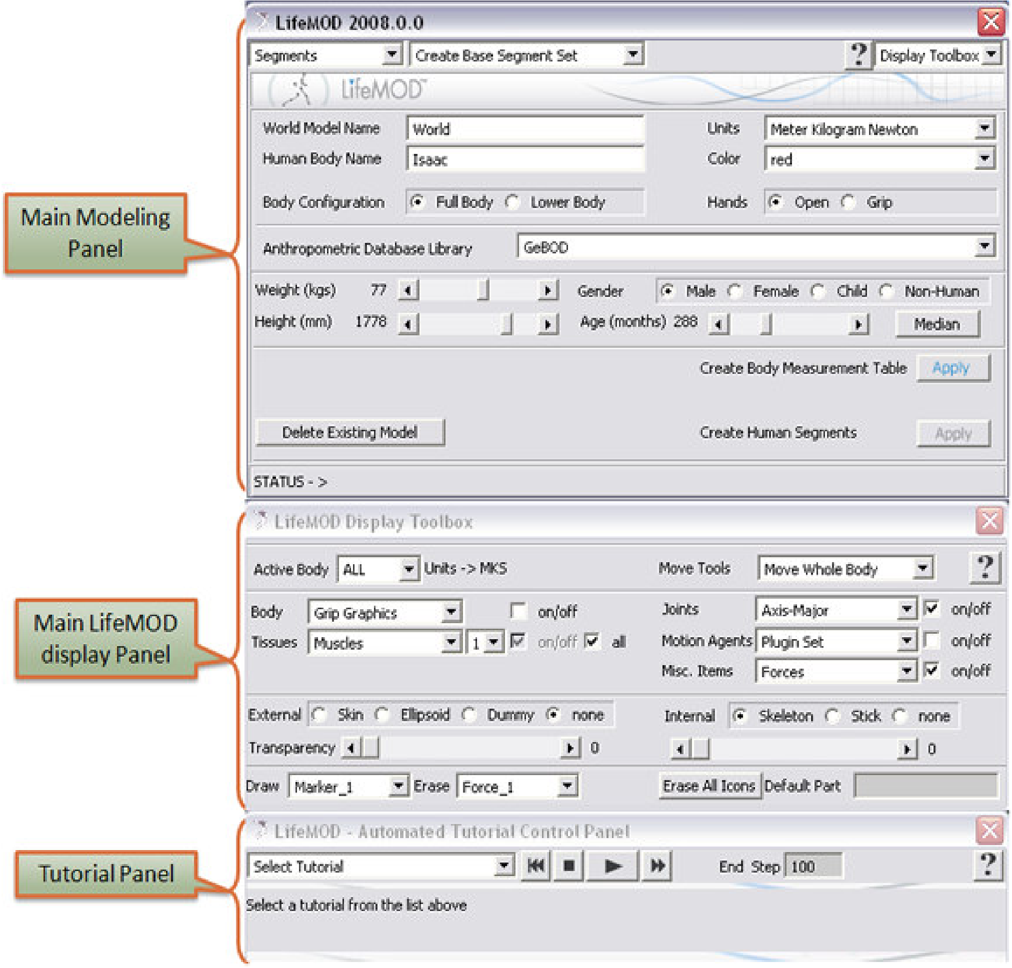

World Model Name: World
Human Body Name: Isaac
Units: Meter Kilogram Newton
Color: red
Body Configuration: ● Full Body ○ Lower Body
Hands: ● Open ○ Grip
Anthropometric Database Library: GeBOD
Weight (kgs): 77
Height (mm): 1778
Gender: ● Male ○ Female ○ Child ○ Non-Human
Age (months): 288
STATUS - >

Active Body: ALL
Units -> MKS
Move Tools: Move Whole Body
Body: Grip Graphics ☐ on/off
Tissues: Muscles 1 ☑ on/off ☑ all
Joints: Axis-Major ☑ on/off
Motion Agents: Plugin Set ☐ on/off
Misc. Items: Forces ☑ on/off
External: ○ Skin ○ Ellipsoid ○ Dummy ● none
Internal: ● Skeleton ○ Stick ○ none
Transparency: 0
Transparency: 0
Draw: Marker_1
Erase: Force_1

End Step: 100
Select a tutorial from the list above

Figure A. 1 LifeMOD control panels

The Main Modeling Panel of LifeMOD is the main model building command structure. Under each selection is a sub-menu which contains the actions for each main command. The toolboxes on the far right include the LifeMOD Display Toolbox, the Table Editor, the Automated Tutorial Panel, plus access to this manual and to the user's forums. This panel also contains a context sensitive help button which accesses the on-line manual section current for the selection in the main-menu and the sub-menu.

The Display Toolbox is used to manipulate the display of the model. The panel offers controls for body internal/external representation display functions. The user may vary the control of the external and internal transparencies using the sliders at the bottom of the panel. This is extremely useful especially during modeling process (e g. creating individual vertebrae segments) where the view is blocked by other body segments.

The Automated Tutorial Control Panel is used to guide users step-by-step through the human body modeling process in all available tutorials.

➢ LifeMOD tutorials

The tutorial resources available in LifeMOD present the features of LifeMOD to give user exposure to the modeling methods and procedures used to create model with a wide range of complexity and application. A few selected tutorials were investigated where the important features can be incorporated in the detailed spine modeling.

- *Golfing*

This is a forward dynamics simulation performed with the joints of the legs and upper body driving the motion. A human model which may interact with an external mechanical system such as flexible golf club is created. One of the key features exercised in this tutorial is creating foot-floor constraints where kinematics joints are used to represent the contact between the feet of the golfer and the playing surface (Figure A. 2). A bushing element was selected as the joint as it provides 6 degree of freedoms where the user can define the translational and rotational properties such as stiffness, damping and pre-load.

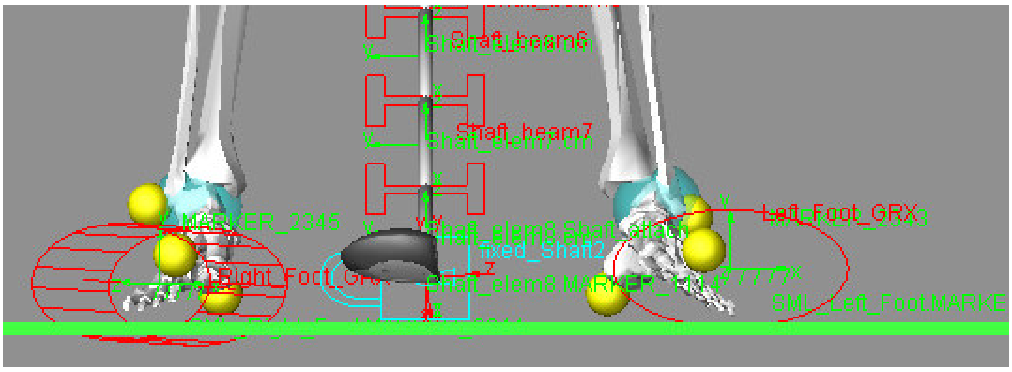

Figure A. 2 Golfing tutorial

- *Bed settling*

This tutorial simulates a human model (patient) for a bed settling analysis to determine the final resting configuration for models with two different sets of joint stiffness (Figure A. 3). The key feature exercised in this tutorial is creating contact forces between the human model and the environment such as chair or bed.

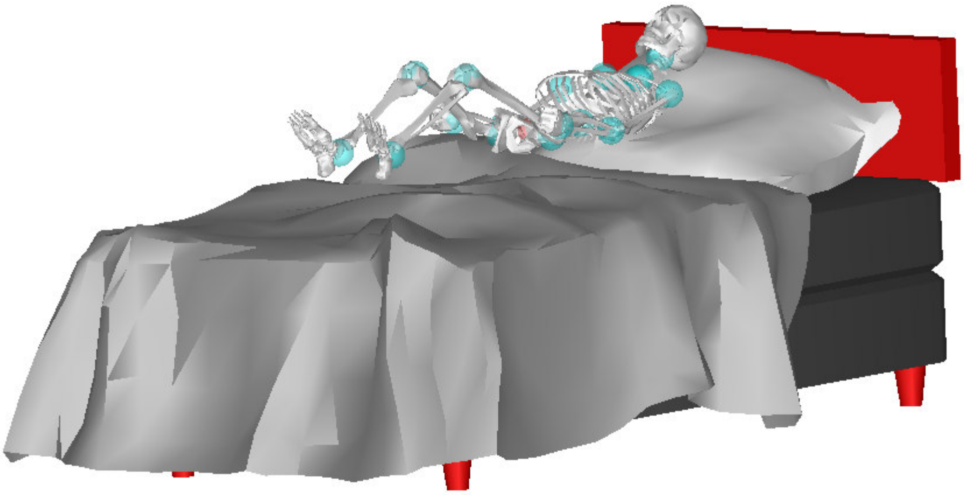

Figure A. 3 Bed settling tutorial

- *Car crash*

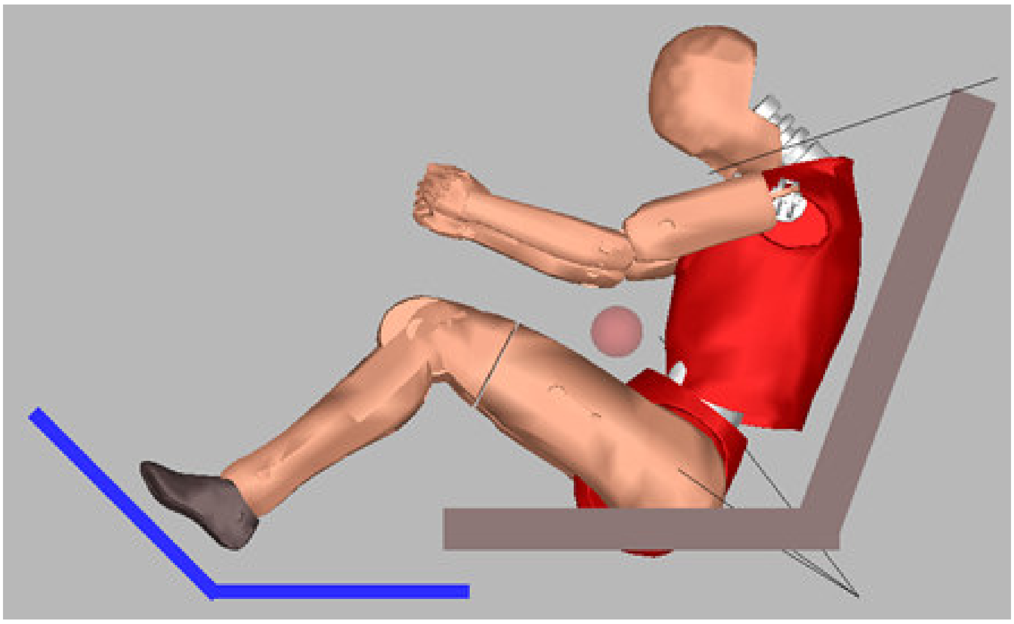

Figure A. 4 Car crash tutorial

This simulation uses a passive human model to evaluate the potential injuries sustained during vehicle crash (Figure A. 4). The human model will be combined with an ADAMS model of a car interior. The key features exercised in this tutorial include posture manipulation of the human model and most importantly creating an ADAMS environment in LifeMOD to interact with the human model. This allows the user to create a simple chair model in LifeMOD without importing a CAD model and run simple simulations.

- *Detailed spine*

This tutorial develops a detailed cervical spinal region in order to investigate the intervertebral compression loads when the neck is under flexion, extension and lateral bending (Figure A. 5). The key features exercised in this tutorial include refining a cervical spine segment into individual vertebrae, reassigning muscles, creating motion agents to control the model motion in inverse dynamics simulation and training the muscles for subsequent forward dynamics simulation.

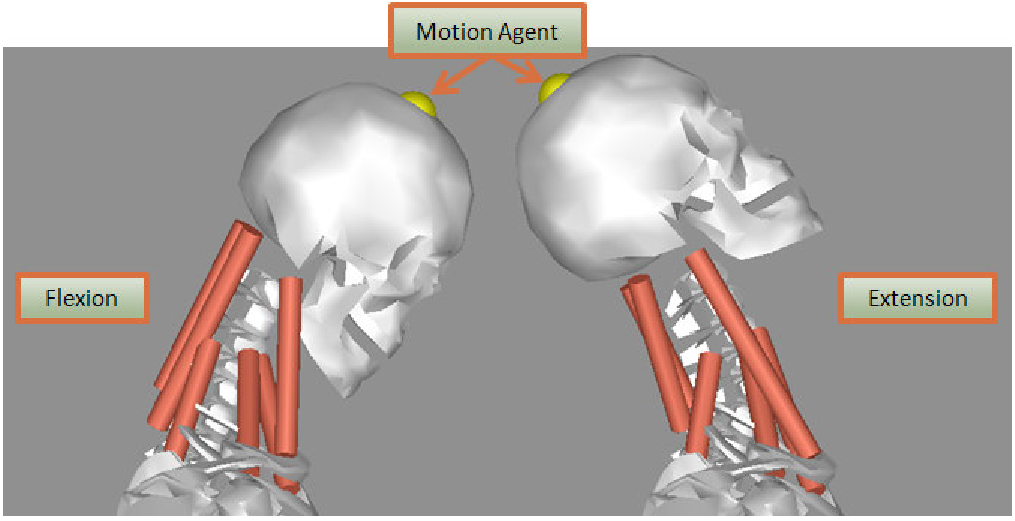

Figure A. 5 Detailed spine tutorial

APPENDIX B

STEP-BY-STEP GUIDELINE FOR DEVELOPING A DETAILED SPINE MODEL IN LIFEMOD

In this appendix, a step-by-step guideline for developing a fully discretized musculo-skeletal multi-body spine model will be shown in detail through 11 steps as below.

Step 1: Generating the body segments

The usual procedure of generating a human model is to create a complete set of body segments followed by redefining the fidelity of the individual segments. LifeMOD generates 19 body segments by default. Each segment may be further reduced to individual bones. The body segments of a complete standard skeletal model are first generated by LifeMOD depending on the user’s anthropometric input. The model used in this study was a median model created from the GeBod anthropometric database.

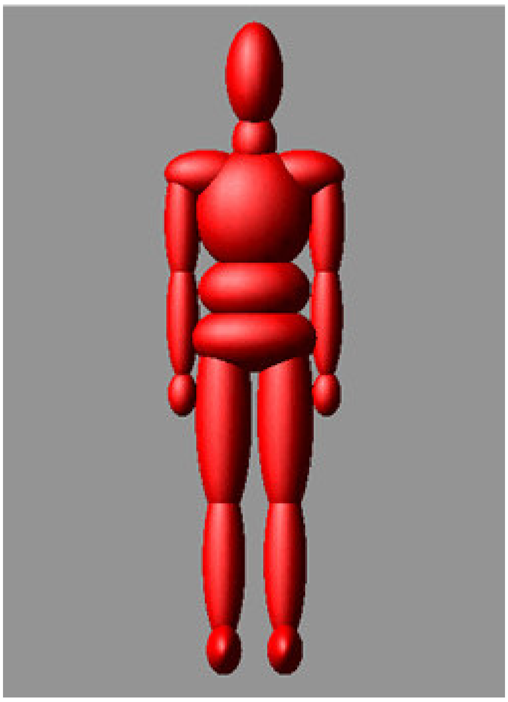

Figure B. 1 19-Segment human base model

Step 1.1: Bring up segments panel and set fields

Launch the LifeMOD™ software and select CREATE NEW MODEL to begin a new modeling session. Select SEGMENTS from the main-menu and CREATE BASE SEGMENT SET from the sub-menu.

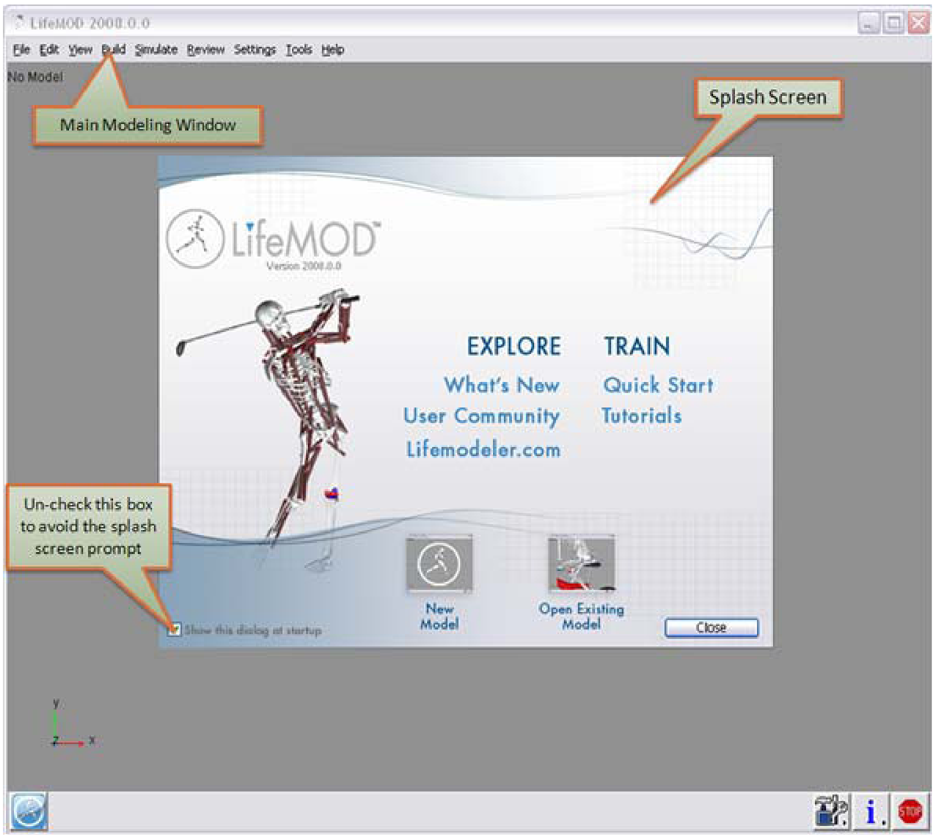

Main Modeling Window

Splash Screen

Un-check this box to avoid the splash screen prompt

Figure B. 2 Launching the LifeMOD software

Step 1.2: Create the body

Generate a full body model using the GeBod Database. Set human body name as “Winston’. Create a “Full Body” and set hands to ‘Grip’ and units as ‘Millimeter Kilogram Newton’. Set the model parameters as ‘Male’, weighing ‘70kg’ with height of ‘1778mm’ and age ‘288 months’ Select the “Apply” tab for the “Create Body Measurement Table” and then “Apply” for “Create Human Segments” to build the model.

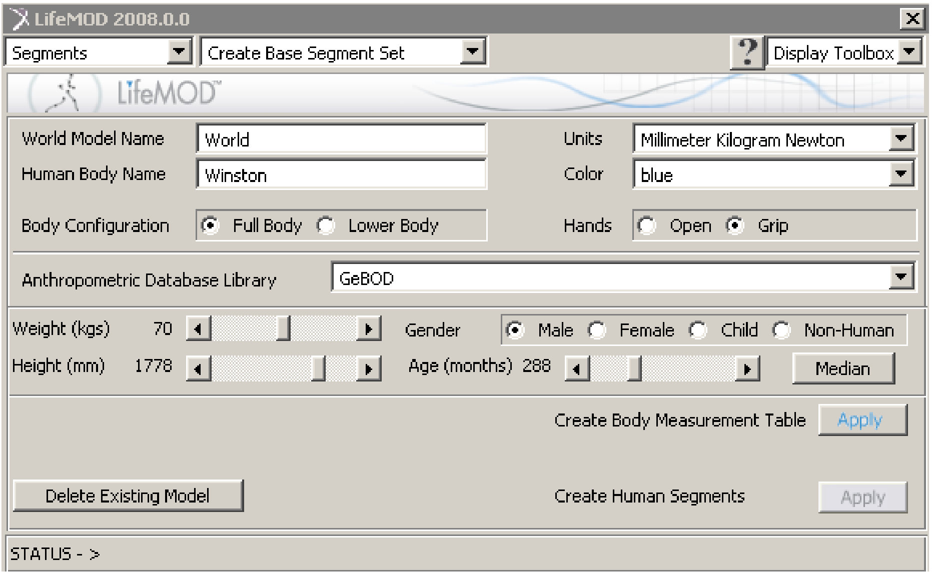

World Model Name: World

Human Body Name: Winston

Units: Millimeter Kilogram Newton

Color: blue

Body Configuration: ● Full Body ○ Lower Body

Hands: ○ Open ● Grip

Anthropometric Database Library: GeBOD

Weight (kgs): 70

Height (mm): 1778

Gender: ● Male ○ Female ○ Child ○ Non-Human

Age (months): 288

Create Body Measurement Table

Create Human Segments

STATUS - >

Figure B. 3 Panel settings to create body model

Note: “Create Body Measurement Table” allows the user to build and view the data used to construct the model. When this is selected a drop down menu will be displayed which allows the user to edit the body measurement table and/or the joint centre location table. In this way the user can refine segment parameters and body characteristics.

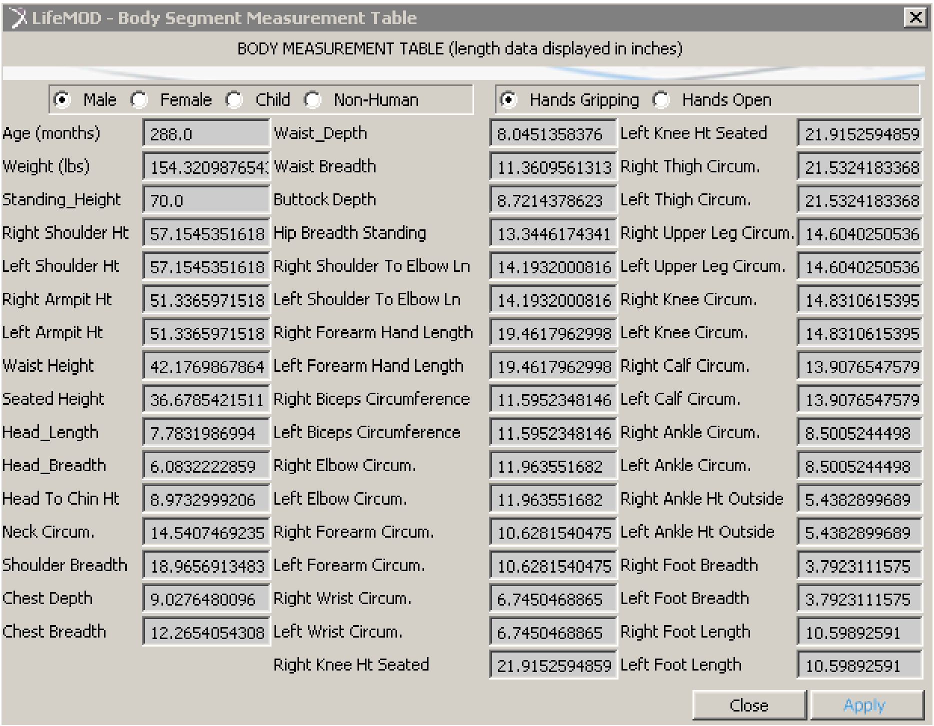

LifeMOD - Body Segment Measurement Table

BODY MEASUREMENT TABLE (length data displayed in inches)

● Male ○ Female ○ Child ○ Non-Human

● Hands Gripping ○ Hands Open

Age (months)	288.0	Waist_Depth	8.0451358376	Left Knee Ht Seated	21.9152594859
Weight (lbs)	154.320987654:	Waist Breadth	11.3609561313	Right Thigh Circum.	21.5324183368
Standing_Height	70.0	Buttock Depth	8.7214378623	Left Thigh Circum.	21.5324183368
Right Shoulder Ht	57.1545351618	Hip Breadth Standing	13.3446174341	Right Upper Leg Circum.	14.6040250536
Left Shoulder Ht	57.1545351618	Right Shoulder To Elbow Ln	14.1932000816	Left Upper Leg Circum.	14.6040250536
Right Armpit Ht	51.3365971518	Left Shoulder To Elbow Ln	14.1932000816	Right Knee Circum.	14.8310615395
Left Armpit Ht	51.3365971518	Right Forearm Hand Length	19.4617962998	Left Knee Circum.	14.8310615395
Waist Height	42.1769867864	Left Forearm Hand Length	19.4617962998	Right Calf Circum.	13.9076547579
Seated Height	36.6785421511	Right Biceps Circumference	11.5952348146	Left Calf Circum.	13.9076547579
Head_Length	7.7831986994	Left Biceps Circumference	11.5952348146	Right Ankle Circum.	8.5005244498
Head_Breadth	6.0832222859	Right Elbow Circum.	11.963551682	Left Ankle Circum.	8.5005244498
Head To Chin Ht	8.9732999206	Left Elbow Circum.	11.963551682	Right Ankle Ht Outside	5.4382899689
Neck Circum.	14.5407469235	Right Forearm Circum.	10.6281540475	Left Ankle Ht Outside	5.4382899689
Shoulder Breadth	18.9656913483	Left Forearm Circum.	10.6281540475	Right Foot Breadth	3.7923111575
Chest Depth	9.0276480096	Right Wrist Circum.	6.7450468865	Left Foot Breadth	3.7923111575
Chest Breadth	12.2654054308	Left Wrist Circum.	6.7450468865	Right Foot Length	10.59892591
		Right Knee Ht Seated	21.9152594859	Left Foot Length	10.59892591

Figure B. 4 Body measurement table

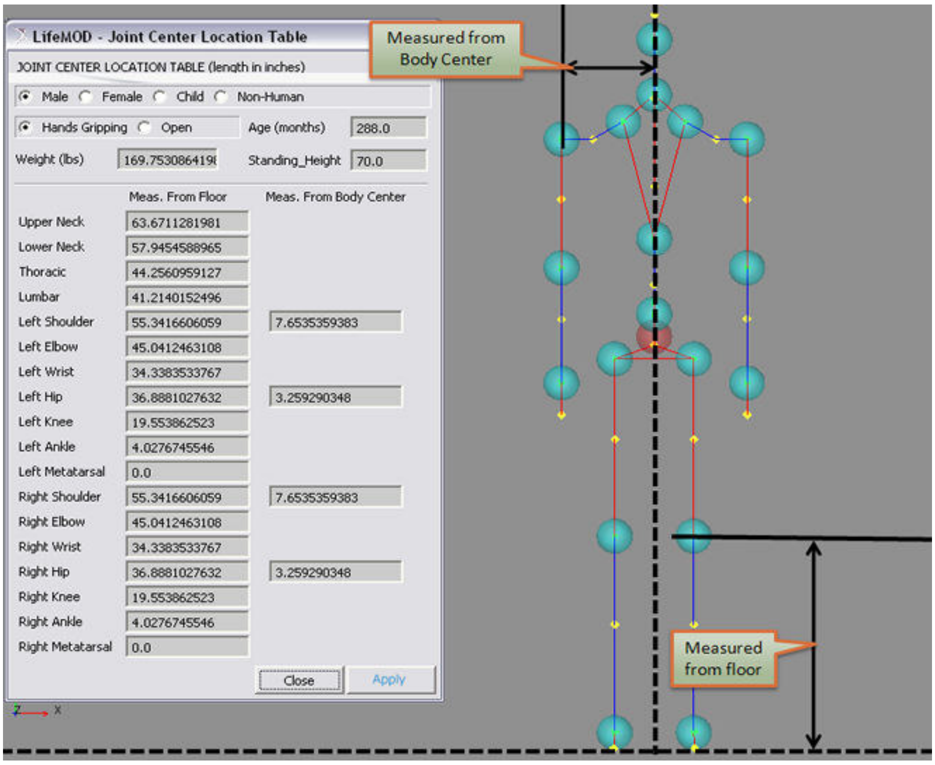

LifeMOD - Joint Center Location Table

JOINT CENTER LOCATION TABLE (length in inches)

● Male ○ Female ○ Child ○ Non-Human

● Hands Gripping ○ Open

Age (months): 288.0

Weight (lbs): 169.753086419(

Standing_Height: 70.0

	Meas. From Floor	Meas. From Body Center
Upper Neck	63.6711281981	
Lower Neck	57.9454588965	
Thoracic	44.2560959127	
Lumbar	41.2140152496	
Left Shoulder	55.3416606059	7.6535359383
Left Elbow	45.0412463108	
Left Wrist	34.3383533767	
Left Hip	36.8881027632	3.259290348
Left Knee	19.553862523	
Left Ankle	4.0276745546	
Left Metatarsal	0.0	
Right Shoulder	55.3416606059	7.6535359383
Right Elbow	45.0412463108	
Right Wrist	34.3383533767	
Right Hip	36.8881027632	3.259290348
Right Knee	19.553862523	
Right Ankle	4.0276745546	
Right Metatarsal	0.0	

Figure B. 5 Joint center location table

Step 2: Generating the base joints

Simple rotational joints are generated for the arms and legs except for the spine. The joint consists of a tri-axis hinge (sagittal, transvers and frontal) where the user can specify a separate function for each degree of freedom. In addition, the user is able to specify stiffness, damping, and angular limits and limit stiffness value for each joint.

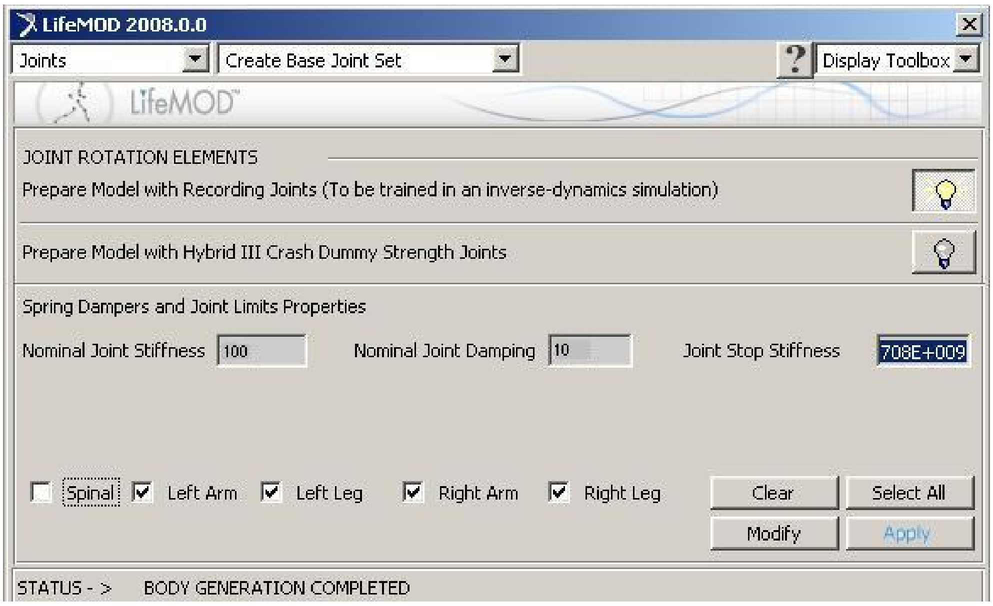

JOINT ROTATION ELEMENTS

Prepare Model with Recording Joints (To be trained in an inverse-dynamics simulation)

Prepare Model with Hybrid III Crash Dummy Strength Joints

Spring Dampers and Joint Limits Properties

Nominal Joint Stiffness 100
Nominal Joint Damping 10
Joint Stop Stiffness 708E+009

☐ Spinal ☑ Left Arm ☑ Left Leg ☑ Right Arm ☑ Right Leg

STATUS - > BODY GENERATION COMPLETED

Figure B. 6 Panel to create recording joints

Select JOINTS on the main-menu and CREATE BASE JOINT SET on the submenu. Select "Prepare Model with Recording Joints” (To be trained in an inverse-dynamics simulation) to bring up the sub-panel. Specify the nominal joint stiffness to be 100 and the damping to be 10. Deselect spinal joints and apply.

Step 3: Creating standard muscle sets

Standard muscle sets are generated from LifeMOD database of muscles. These muscles are to be trained in an inverse-dynamics simulation. The recording elements in the muscles record the contraction history of the muscle when the model is driven by the motion agents. They then serve as actuators for the forward-dynamics simulations. The muscle actuators are programmed not to exceed the physiological limits of the individual muscle.

Step 3.1: Bring up the tissue set create panel

Select SOFT TISSUES on the main-menu and CREATE BASE TISSUE SET on the sub-menu.

Step 3.2: Set the fields for the muscle generation

Select “Prepare Model with Recording Muscle Elements” (To be trained in an inverse-dynamics simulation) to bring up the panel displayed in Figure B. 7. Set the passive stiffness and damping to 0.444 and 1.75E-2 respectively and muscle resting load to 0, and set the muscle tone multiplier to 100%.

Step 3.3: Create the muscles

Check all (Head/Trunk, Left arm, Left Leg, Right arm, Right Leg) and select APPLY to create the muscles.

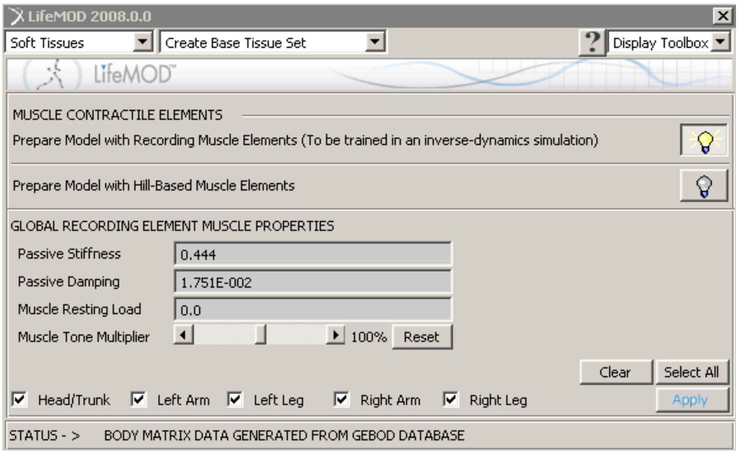

MUSCLE CONTRACTILE ELEMENTS

Prepare Model with Recording Muscle Elements (To be trained in an inverse-dynamics simulation)

Prepare Model with Hill-Based Muscle Elements

GLOBAL RECORDING ELEMENT MUSCLE PROPERTIES

Passive Stiffness	0.444
Passive Damping	1.751E-002
Muscle Resting Load	0.0
Muscle Tone Multiplier	100% Reset

☑ Head/Trunk ☑ Left Arm ☑ Left Leg ☑ Right Arm ☑ Right Leg

STATUS - > BODY MATRIX DATA GENERATED FROM GEBOD DATABASE

Figure B. 7 Panel to creating the muscles

Step 4: Discretizing vertebral bodies

Individual segments for the Neck (C1 – C7), Upper Torso (T1– T12) and Central Torso (L1 – L5), corresponding to the cervical, thoracic and lumbar regions are created. The centre of mass location of an individual segment is estimated and mass properties are determined via ellipsoid volume approximation and default human tissue density. The existing shell geometry is used for visualization. The Ribs and Sternum, which also belong to the default upper torso segment, are also re-created.

Step 4.1: Zooming into the spine segments

Change to wireframe model (Press Shift-S) and zoom into focus on the vertebrae (Press Z to zoom). Click on the Main Toolbox, (bottom right) to expand and use the view control tools to manipulate the model. Begin at the Cervical Region at the C1 vertebrae.

Step 4.2: Set up the working grid

From the Main Toolbar, go to Settings → Working Grid → Show Working Grid. Select Rectangular, set the size and spacing. Set Location to Global Origin and set Orientation to Global YZ. Select APPLY.

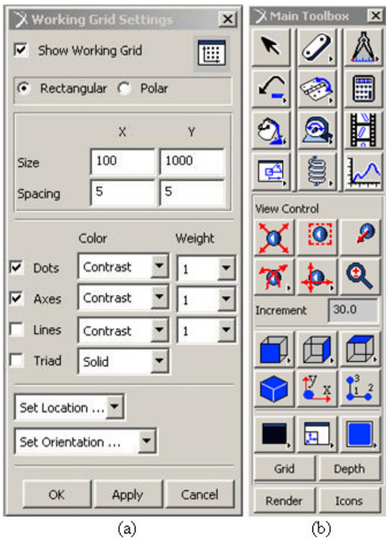

☑ Show Working Grid

● Rectangular ○ Polar

	X	Y
Size	100	1000
Spacing	5	5

	Color	Weight
☑ Dots	Contrast	1
☑ Axes	Contrast	1
☐ Lines	Contrast	1
☐ Triad	Solid	

Increment 30.0

Figure B. 8 Working Grid Panel and main toolbox

Step 4.3: Bring up the single segment creation panel

Select SEGMENTS on the main-menu and CREATE INDIVIDUAL SEGMENT on the sub-menu.

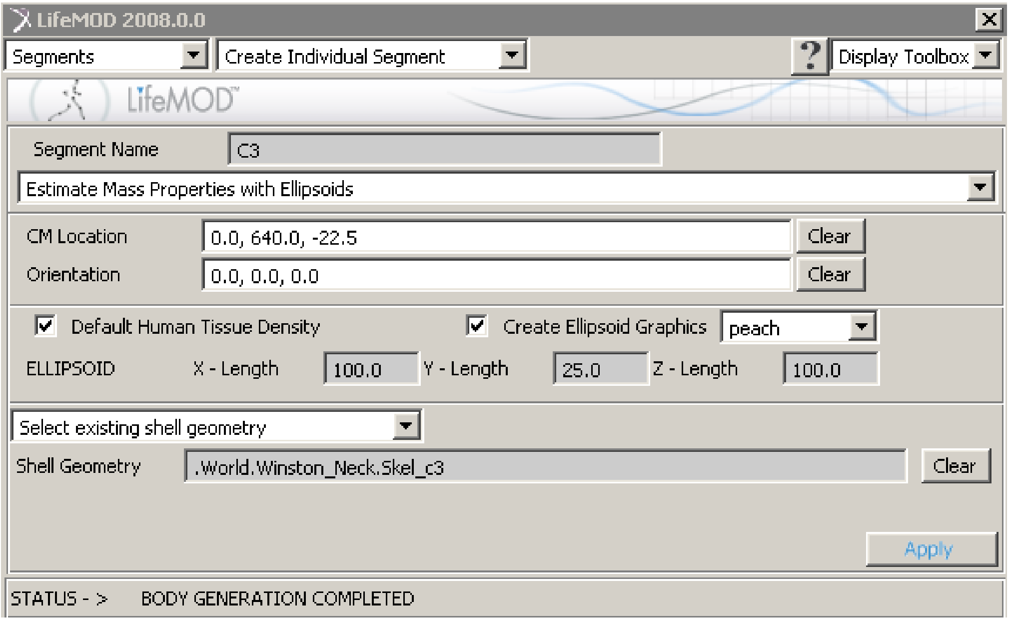

Segment Name: C3

Estimate Mass Properties with Ellipsoids

CM Location: 0.0, 640.0, -22.5

Orientation: 0.0, 0.0, 0.0

☑ Default Human Tissue Density

☑ Create Ellipsoid Graphics: peach

ELLIPSOID X - Length: 100.0 Y - Length: 25.0 Z - Length: 100.0

Select existing shell geometry

Shell Geometry: .World.Winston_Neck.Skel_c3

STATUS - > BODY GENERATION COMPLETED

Figure B. 9 Panel to creating individual segments

Step 4.4: Creating individual segments

Step 4.4.1: Defining the centre of mass location

Zoom to region under discretization. To select the CM in the CM Location field, right-click and select Pick Location. Next move the cursor to the model and pick the approximate CM location on that vertebra (If segment is C1, CM of atlas must be selected) the CM position will snap to the nearest grid coordinates on the working grid. The orientations of all vertebrae are set to (0, 0, 0).

Note: The data points used for CM location of each segment of the Winston model are given in Table F.1 in Appendix F. If a model with the same anthropometric parameters is created in future study, this data can be reused. This could save precious time as the data can be directly inserted and does not require working grid and manual selection of multiple points.

Step 4.4.2: Mass estimation

Select “Estimate Mass Properties with Ellipsoids” and check “Default Human Tissue Density” and bounding ellipsoid as bellow:

- Cervical: x-length = 100, y-length = 25, z- length = 100.
- Thoracic: x-length = 100, y-length = 40, z- length = 100.
- Lumbar: x-length = 100, y-length = 35, z- length = 100.

For the graphics, select existing geometry. (for C1 select .World.Winston_Neck.Skel_atlas, for T2 select .World.Winston_Upper_Torso.Skel_T2 etc.) Select Apply to create the individual vertebra segment.

Step 4.5: Discretizing the whole spine model

Repeat entire procedure under step 4.4 for vertebral bodies C1-C7, then T1-T12 and L1- L5.

Step 4.6: Create markers for joints in subsequent stage

Using Rectangular Working Grid, create marker using the Main Toolbox. (Bring up Main Toolbox from the Main Toolbar). Select Create Marker. Select the point between the inferior plane of segment A and superior plane of the segment B below it. Rename this marker as .World.Winston_[segment B name].[Marker ID]. Marker ID will range from 1-24. (E.g.: For first joint, a marker is placed between the inferior plane of the head and the superior plane of the C1 vertebrae. The marker is renamed .World.Winston_C1.m1). Repeat to create markers between all vertebrae (i.e. from Marker ".World.Winston_C1.m1" to ".World.Winston_L5.m24"). The locations of all these markers are given in Table F.2 in Appendix F.

Step 4.7: Create a Marker for the joint connection to Lower Torso

Create a marker below L5 vertebrae and above the Sacrum of Lower Torso. Rename the marker .World.Winston_Lower_Torso.m25

Step 4.8: Create the ribs and sternum to replace the torso segment

All other segments that belong to the Upper Torso must also be defined as separate bodies. Set the segment name to Ribs. Pick the CM Location at the center of the torso and set the Orientation as (0, 0, 0). Select "Estimate Mass Properties with Ellipsoids" and check "Default Human Tissue Density" and bounding ellipsoid of x-length = 310, y-length = 350, z- length = 200. For the graphics, select existing geometry of .World.Winston_Upper_Torso.Skel_ribs. Select Apply.

Set the segment name to Sternum. Pick the CM Location at the center of the sternum and set the Orientation to (0, 0, 0). Select "Estimate Mass Properties with Ellipsoids" and check "Default Human Tissue Density" and bounding ellipsoid of x-length = 1, y-length = 1, z- length = 1. For the graphics, select existing geometry of .World.Winston_Upper_Torso.Skel_sternum. Select Apply.

Step 5: Reassigning muscle attachment points

All muscles associated with the discretized spine must be re-assigned. The original base segments for Neck, Upper Torso and Central Torso are then deleted.

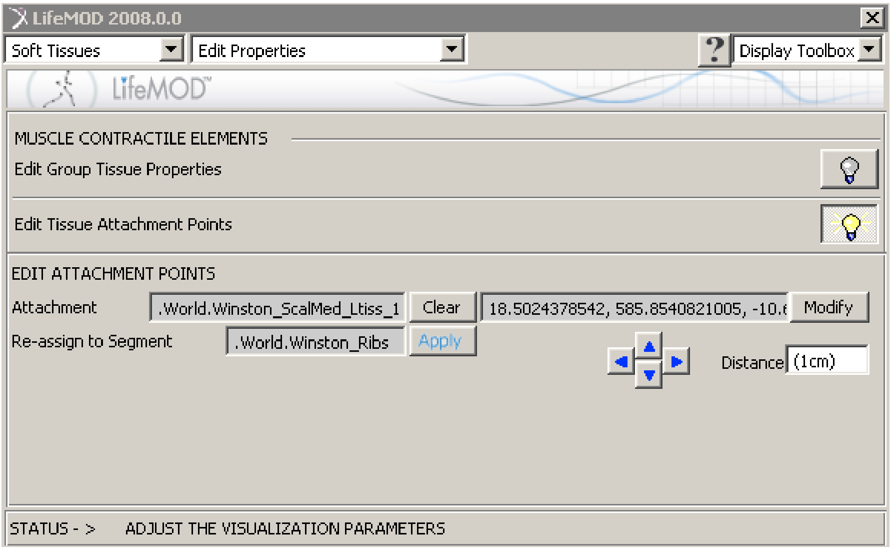

Attachment .World.Winston_ScalMed_Ltiss_1 18.5024378542, 585.8540821005, -10.

Re-assign to Segment .World.Winston_Ribs

Distance (1cm)

STATUS - > ADJUST THE VISUALIZATION PARAMETERS

Figure B. 10 Panel for editing and reassigning attachment points

The muscles are attached to the respective bones based on geometric landmarks on the bone graphics. With the new vertebra segments created, the muscle attachments to the original segment must be reassigned to be more specific to the new vertebra segments. The physical attachment locations will remain the same.

Step 5.1: Bring up the soft tissues edit panel

Select SOFT TISSUES in the main-menu and EDIT PROPERTIES in the submenu. Select "Edit Tissue Attachment Points".

Step 5.2: Reassign muscles

In EDIT ATTACHMENT POINTS, under "Attachment" right click and browse to search for the relevant muscle and select it. Select attachment 1. Under "Re-assign to Segment" type the corresponding new segment name as given in the Table F.3 in Appendix F. Select Apply. Repeat for attachment 2 of the same muscle.

- Repeat for Right and Left side.
- Repeat for all muscles.

Step 5.3: Bring up the segments delete panel

Select SEGMENTS from the main menu and DELETE from the submenu. Check the Neck, Upper_Torso and Central_Torso to delete the original base segments.

Step 6: Recreating Joints between Scapular and Ribs

Upon deleting the original thoracic segment, the joint between Scapula and Ribs has been removed too. Therefore first of all, it is required to recreate the Scapula joint.

Step 6.1: Bring up the panel to create single joint

Select JOINTS from the main menu and CREATE INDIVIDUAL JOINT from the submenu.

Step 6.2: Rename Marker

From the Main Toolbar, go to Edit → Rename → World → Winston_Left_Scapula (Part) → Upper_Torso (Marker), select this Upper_Torso marker and rename it World.Winston_Ribs.L_Torso. Perform the same procedure for Right Scapula and rename the Upper_Toso marker as .World.Winston_Ribs.R_Torso.

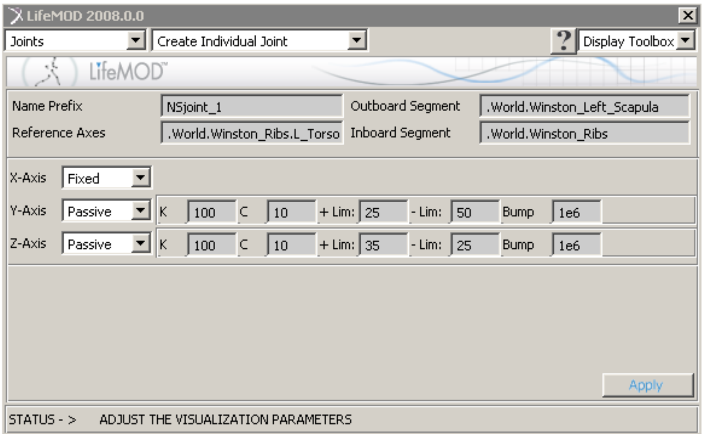

Name Prefix: NSjoint_1
Outboard Segment: .World.Winston_Left_Scapula
Reference Axes: .World.Winston_Ribs.L_Torso
Inboard Segment: .World.Winston_Ribs

X-Axis	Fixed										
Y-Axis	Passive	K	100	C	10	+ Lim:	25	- Lim:	50	Bump	1e6
Z-Axis	Passive	K	100	C	10	+ Lim:	35	- Lim:	25	Bump	1e6

STATUS - > ADJUST THE VISUALIZATION PARAMETERS

Figure B. 11 Panel to create a single joint between Scapula and Ribs

Step 6.3: Create a joint between left scapula and ribs

Set the inboard segment to .World.Winston_Ribs and the outboard segment to World.Winston_Left_Scapula and the reference axis to .World.Winston_Ribs.L_Torso. Set Sagittal axes to fixed, Transverse and Frontal axes to passive stiffness (k) of 100 and damping value (c) 10. Set the limits of Transverse axes as +Lim 25, -Lim 50 and limits of Frontal axes as +Lim 35, -Lim 25. Perform the same procedures to create joint between Right Scapula and Ribs.

Step 6.4: Create a fixed joint between sternum and ribs

Set the inboard segment to .World.Winston_Ribs and the outboard segment to .World.Winston_Sternum and the reference axis to .World.Winston_Ribs.CM. Set X, Y and Z axes to fixed joint. Select Apply.

Step 6.5: Create a fixed joint between ribs and T6

Set the inboard segment to .World.Winston_T6 and the outboard segment to .World.Winston_Ribs and the reference axis to .World.Winston_T6.CM. Set X, Y and Z axes to fixed joint. Select Apply.

Step 7: Creating individual spine joints between vertebrae

It is necessary to create individual non-standard joints between each newly created vertebra. The spinal joints are modeled as torsional springs and the passive 3 DOF jointed action can be defined with user-specified stiffness, damping, angular limits and limit stiffness values. These values can be referenced in Table F.4 and F.5 in Appendix F.

Figure B. 12 displays the inboard/outboard relationship when creating individual joints between segments. The most inboard segment is the pelvis. When adjusting the posture or position of the human model, the inboard segment of the joint will not translate/rotate, only the outboard segment will translate/rotate. As such when creating the spinal joints between each vertebra, the inboard/outboard relationship has to be defined sequentially starting from the head followed by the corresponding vertebra along cervical, thoracic and lumbar spine. Ultimately, the pelvis has to be defined as the most inboard segment to ensure that the rest of the body segments are movable.

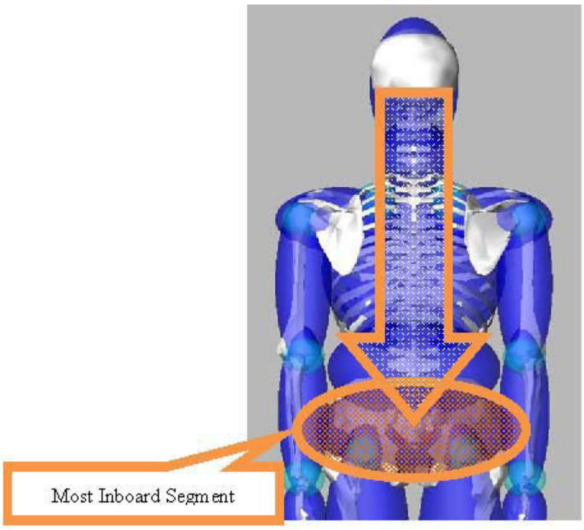

Figure B. 12 Inboard/Outboard segment relationship

The single joint may be specified with the kinematic parameters as shown in Figure B. 13 when creating the spinal joint between the C1 and C2 vertebrae. The angle limits specified for the x-axis, y-axis and z-axis represents the flexion/extension, torsion and lateral bending of spinal motion respectively.

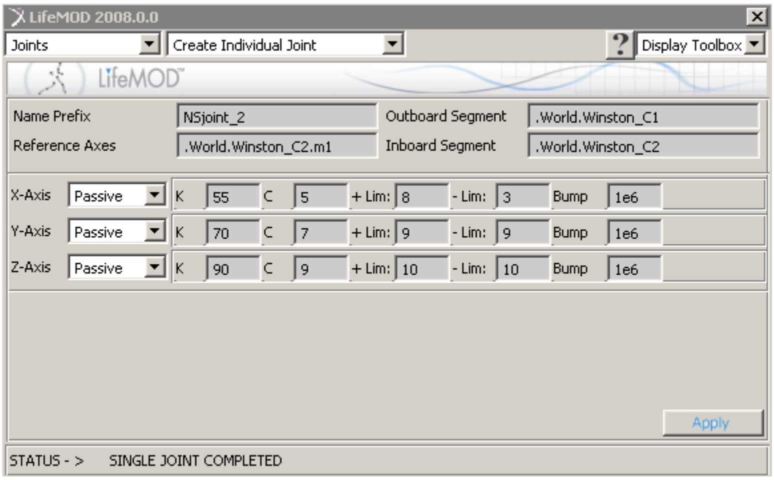

Name Prefix: NSjoint_2
Reference Axes: .World.Winston_C2.m1
Outboard Segment: .World.Winston_C1
Inboard Segment: .World.Winston_C2

		K	C	+ Lim:	- Lim:	Bump
X-Axis	Passive	55	5	8	3	1e6
Y-Axis	Passive	70	7	9	9	1e6
Z-Axis	Passive	90	9	10	10	1e6

STATUS - > SINGLE JOINT COMPLETED

Figure B. 13 Joint creation

Set the inboard segment to .World.Winston_C1 and the outboard segment to .World.Winston_Head and the reference axis to .World.Winston_C1.m1. Set X, Y and Z axes passive stiffness (K) and damping value (C) according to Table F.3. Set the limits of Sagittal, Transverse and Frontal axes according to the segmental range of motion in Tables F.4. Perform the same procedures to create joints for the entire spine column.

Step 8: Creating ligament tissue

Ligaments are passive spring/dampers and are not included in the generic full body tissue set. Between every two vertebra, six ligaments (interspinous, ligementum flavum, anterior/posterior longitudinal and joint capsule) are created, with user defined stiffness, damping and preload. The purpose of ligaments is to guide segment motion and contribute to spinal stability.

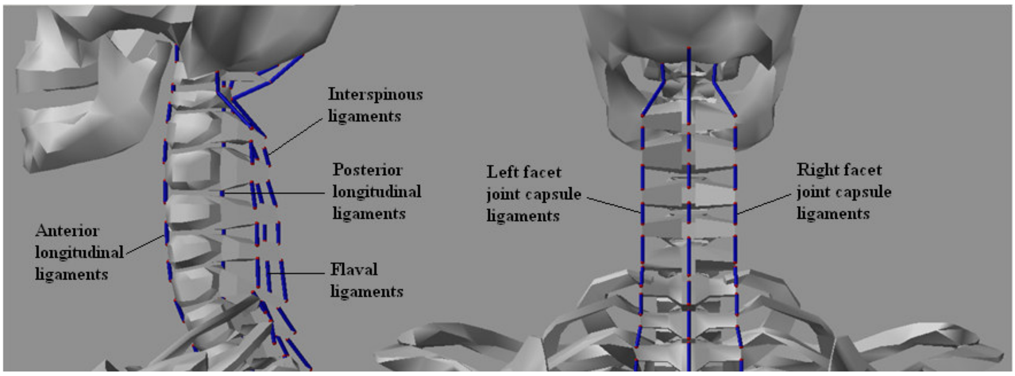

Figure B. 14 Ligament locations on the spine model

Step 8.1: Bring up the soft tissue panel

Select SOFT TISSUES on the mainmenu and CREATE INDIVIDUAL TISSUE on the submenu. Select Ligament/Tendon tissues on the drop down menu.

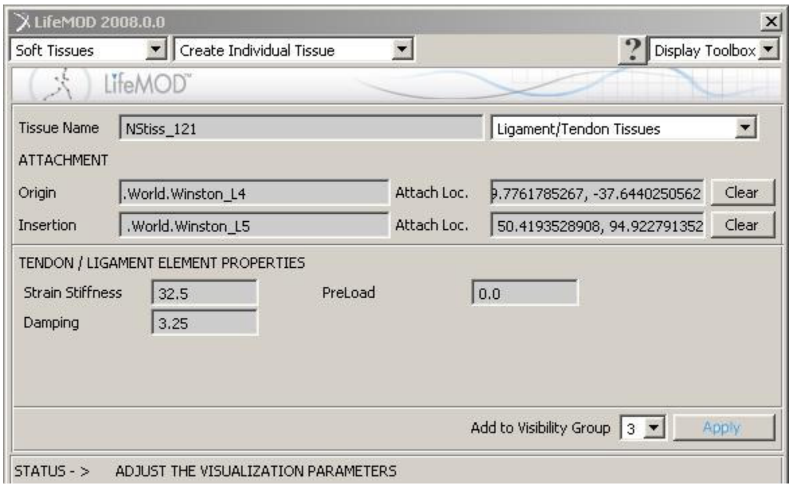

Tissue Name: NStiss_121
Ligament/Tendon Tissues

ATTACHMENT

Origin: .World.Winston_L4 — Attach Loc.: .7761785267, -37.6440250562

Insertion: .World.Winston_L5 — Attach Loc.: 50.4193528908, 94.922791352

TENDON / LIGAMENT ELEMENT PROPERTIES

Strain Stiffness: 32.5
PreLoad: 0.0
Damping: 3.25

Add to Visibility Group: 3

STATUS - > ADJUST THE VISUALIZATION PARAMETERS

Figure B. 15 Panel for creating ligaments

Step 8.2: Create the interspinous, flaval and anterior longitudinal ligaments

Use the panel above to create the ligaments. Set the stiffness according to Tables F.6 and F.7 in Appendix F and the damping is 10% of the stiffness value. For the present model, cervical stiffness values are also used for the thoracic region. Bring up the rectangular working grid and set the Global Origin, Global YZ for location and orientation respectively. Attach the ligaments to the Origin and Insertions by snapping the locations on the working grid, connecting the superior vertebra to the inferior vertebra. Select Apply.

Step 8.3: Create the facet joint capsule ligaments

Remove the working grid and connect the ligaments to the vertices of the two corresponding vertebrae articular process.

Step 9: Implementing lumbar back muscles

Select SOFT TISSUES on the main menu and CREATE INDIVIDUAL TISSUE on the submenu. Select “Recording Muscles” on the drop down menu.

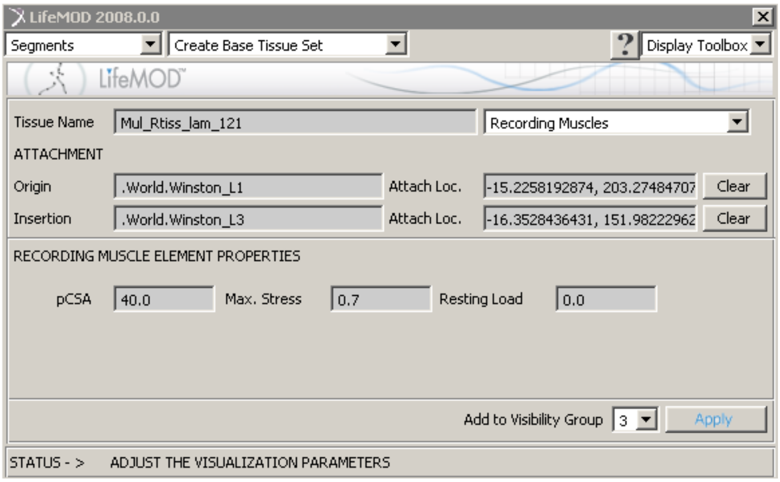

Tissue Name: Mul_Rtiss_lam_121
Recording Muscles

ATTACHMENT

Origin: .World.Winston_L1 — Attach Loc.: -15.2258192874, 203.27484707

Insertion: .World.Winston_L3 — Attach Loc.: -16.3528436431, 151.98222962

RECORDING MUSCLE ELEMENT PROPERTIES

pCSA: 40.0
Max. Stress: 0.7
Resting Load: 0.0

Add to Visibility Group: 3

STATUS - > ADJUST THE VISUALIZATION PARAMETERS

Figure B. 16 Panel for creating muscles

Step 9.1: Adding multifidus muscle

Set the attachment points and mechanical properties of each muscle according to Table F.8 and F.9 in Appendix F respectively for the right side. Select “Apply”. Repeat for the muscles on the left side with X coordinates are opposite to those of the right side.

Step 9.2: Adding erector spinae muscle

Perform the same procedure as mentioned in step 9.1 using Table F.10 and F.11 in Appendix F.

Step 9.3: Adding psoas major muscle

Perform the same procedure as mentioned in step 9.1 using Table F.12 and F.13 in Appendix F.

Step 9.4: Adding quadratus lumborum muscle

Perform the same procedure as mentioned in step 9.1 using Table F.14 and F.15 in Appendix F.

Step 10: Adding abdominal muscles

Step 10.1: Importing the rectus sheath

Select SEGMENTS on the main-menu and CREATE INDIVIDUAL SEGMENT on the sub-menu. Select “Calculate Mass Properties Based on Material”. Set CM location to (0, 0, 0) and Orientation to (0, 0, 0). Set Material Type to .World.Rectus_Material. Select “Import parasolids geometry”. Select Rectus Sheath.x_t for File.

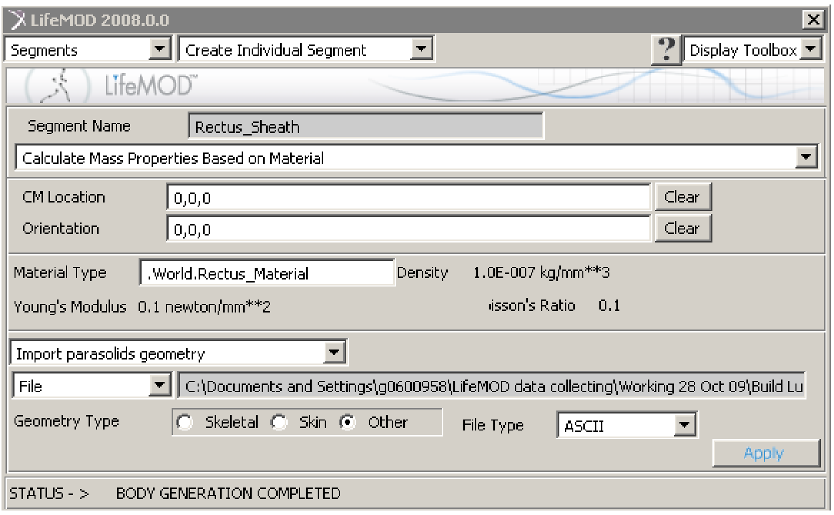

Segments
Create Individual Segment
Segment Name: Rectus_Sheath
Calculate Mass Properties Based on Material
CM Location: 0,0,0
Orientation: 0,0,0
Material Type: .World.Rectus_Material
Density 1.0E-007 kg/mm**3
Young's Modulus 0.1 newton/mm**2
isson's Ratio 0.1
Import parasolids geometry
File: C:\Documents and Settings\g0600958\LifeMOD data collecting\Working 28 Oct 09\Build Lu
Geometry Type: ○ Skeletal ○ Skin ● Other
File Type: ASCII
STATUS - > BODY GENERATION COMPLETED

Figure B. 17 Import Rectus sheath

Step 10.2: Adding obliquus externus and obliquus internus

Perform the same procedure as mentioned in step 9.1 using Table F.16 and F.17 in Appendix F.

Step 11: Adding intra-abdominal pressure

Select icon “Bush” on Main Box. Choose Winston_Ribs as first body and Winston_Lower_Torso as second body. Set Location to (0.0, 110.0, 40.0). Set the stiffness value of the bushing element as found in Appendix C.

APPENDIX C

CALCULATING INTRA-ABDOMINAL PRESSURE

Step 1: Finding abdominal volume and mean section area

Initially, the volume V_{L1L5} occupying from L1 to L5 needs to be determined. Using SolidWorks, the value of V_{L1L5} is 1994099.78 mm^3.

Next, the surface areas of 5 circuits can also be determined in SolidWorks as follow: $S_1 = 22808.09\ mm^3$, $S_2 = 18497.33\ mm^3$, $S_3 = 16070.55\ mm^3$, $S_4 = 13649.48\ mm^3$, $S_5 = 13263.93\ mm^3$.

Therefore, mean surface area S_{mean} can be obtained as follow:

$$S_{mean} = \frac{\sum_n S_i}{n} = \frac{84289.38}{5} = 16857.876\ (mm^3)$$

where n is number of closed circuits.

Step 2: Computing stiffness values of the spring structure

The height of lumbar spine region h_{L1L5} is computed by the following equation:

$$h_{L1L5} = \frac{V_{L1L5}}{S_{mean}} = \frac{1994099.78}{16857.876} = 118.2889\ (mm)$$

So, the height of the abdomen h is calculated as below:

$$h = \frac{3}{2} h_{L1L5} = \frac{3}{2} * 118.2889 = 177.433\ (mm)$$

The length of the spring structure a is determined as:

$$a = \sqrt{S_{mean}} = \sqrt{16857.876} = 129.837\ (mm)$$

In the literature (Cobb et al. 2005), the normal intra-abdominal pressure of healthy adults found is 20 mmHg. Hence, the translational stiffness K_y is computed as:

$$k_y = \frac{1}{2} P a^2 = \frac{1}{2} * 20 * 13570 * 10^{-9} * 9.81 * 129.837^2 = 22.44\ (N/mm)$$

Using the similar procedure, the translational stiffnesses K_x and K_z can be determined by the following equation:

$$k_x = k_z = \frac{1}{2} Pah = \frac{1}{2} * 20 * 13570 * 10^{-9} * 9.81 * 129.837 * 177.433 = 30.667\ (N/mm)$$

To calculate torsional stiffnesses of the spring structure, a small rotational angle of 1 degree about a specific axis is given. In this case, the lower surface attaching to the pelvis is fixed. Hence, the relative translation in y direction Δy is expressed as follow:

$$\Delta y = \frac{\pi a}{360} = \frac{\pi * 129.837}{360} = 1.133$$

Since the lengths in x and z directions are equal, the moments M_x, Mz are given as:

$$M_x = M_z = k_y \frac{\pi}{180} a^2 = 22.44 * \frac{\pi}{180} * 129.837^2 = 6602.329\ (N.mm/\deg)$$

Similarly, the torsional stiffness M_y is determined as follow:

$$M_y = k_x \frac{\pi}{180} a^2 = k_z \frac{\pi}{180} a^2 = 30.667 * \frac{\pi}{180} * 129.837^2 = 9022.888 \ (N.mm/\deg)$$

Step 3: Using an equivalent bushing element

Bushing element is a six-degrees-of-freedom joint that allows translational and rotational motions. Hence, the translational and rotational stiffnesses of the bushing element are specified in the following expressions:

$$k_x^{'} = k_z^{'} = 4k_x = 4k_z = 4 * 30.667 = 122.668 \ (N/mm)$$

$$k_y^{'} = 4k_y = 4 * 22.44 = 89.76 \ (N/mm)$$

$$M_x^{'} = M_z^{'} = k_y \frac{\pi}{180} a^2 = 6602.329 \ (N.mm/\deg)$$

$$M_y^{'} = k_x \frac{\pi}{180} a^2 = k_z \frac{\pi}{180} a^2 = 9022.888 \ (N.mm/\deg)$$

APPENDIX D

DYNAMIC DATABASE OF THE SPINE MODEL IN LIFEMOD

Due to space constraint, dynamic database of the spine model under external forces applying onto vertebrae from T1 to T2 is extracted here.

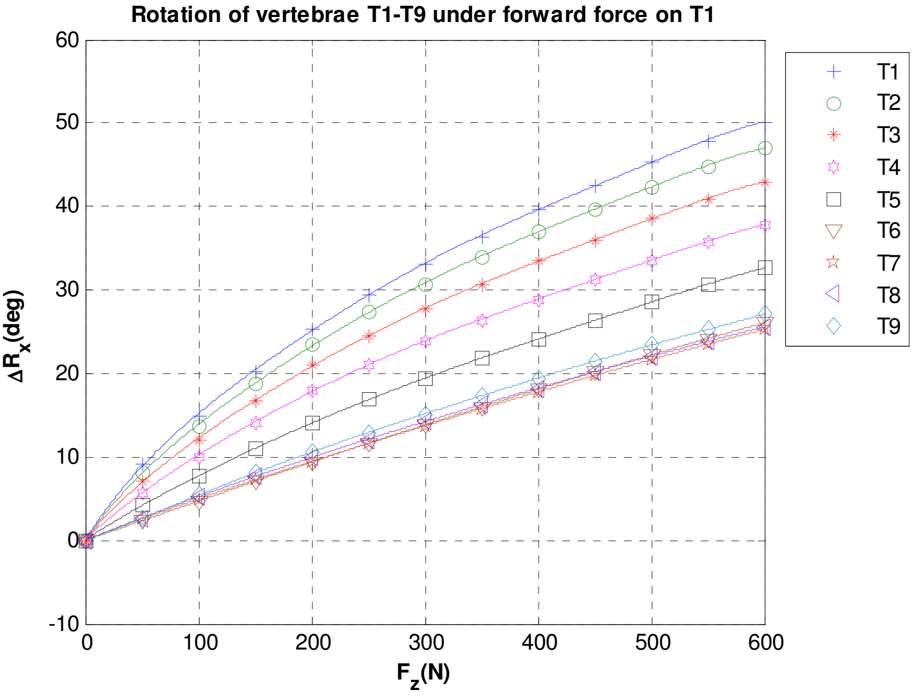

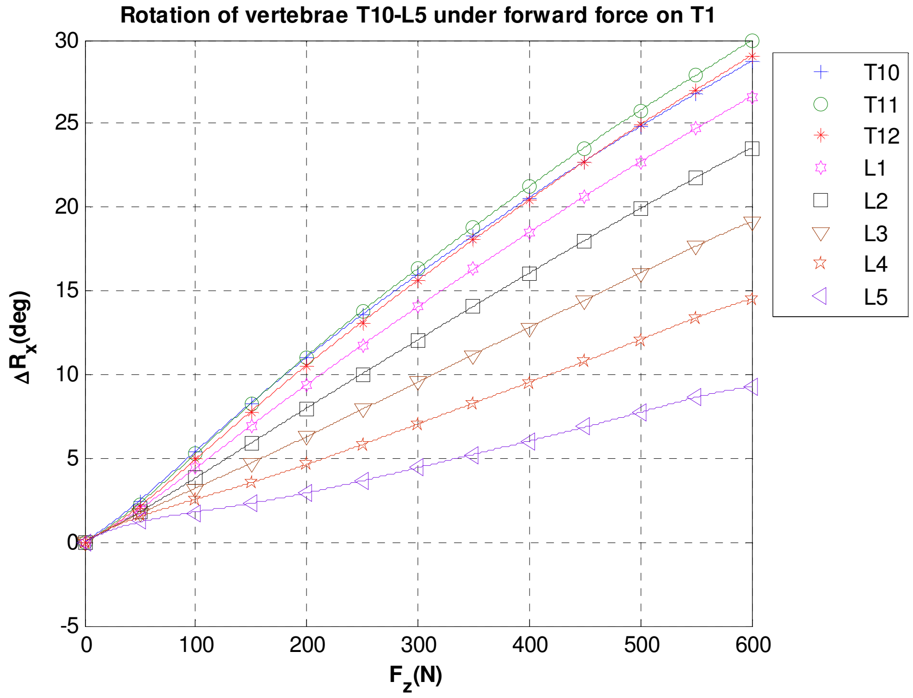

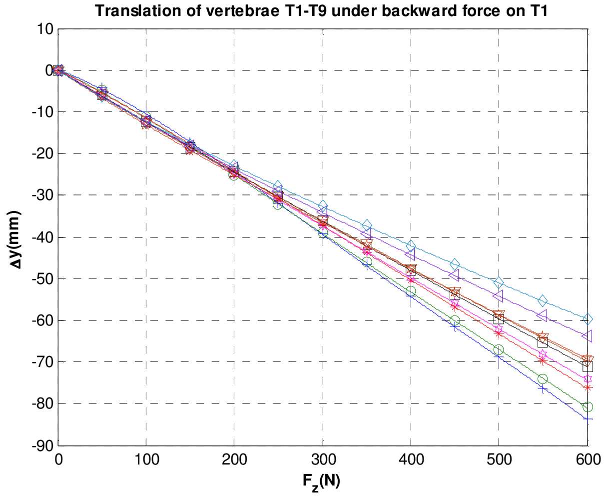
Translation of vertebrae T1-T9 under backward force on T1

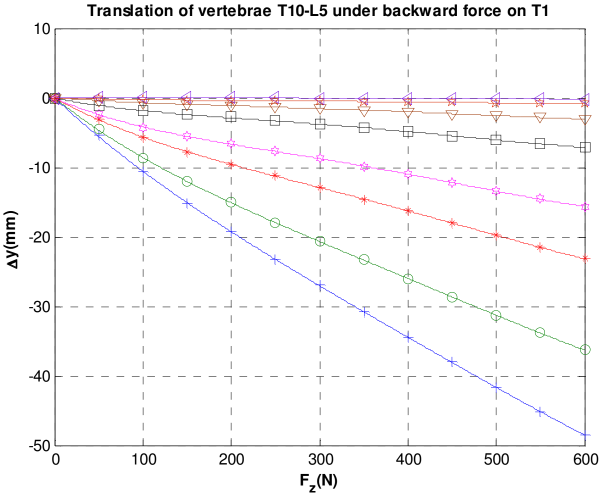
Translation of vertebrae T10-L5 under backward force on T1

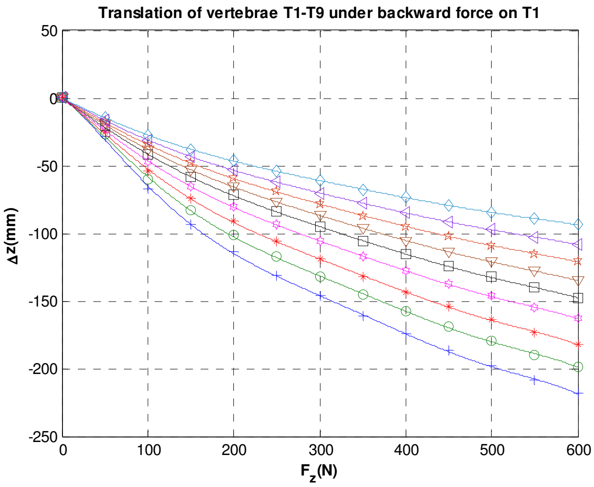
Translation of vertebrae T1-T9 under backward force on T1

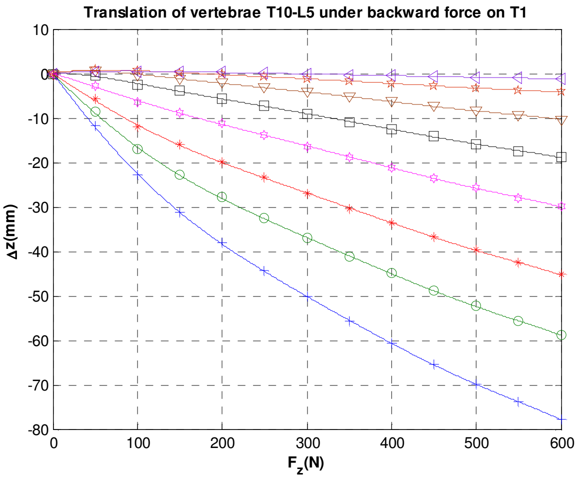
Translation of vertebrae T10-L5 under backward force on T1

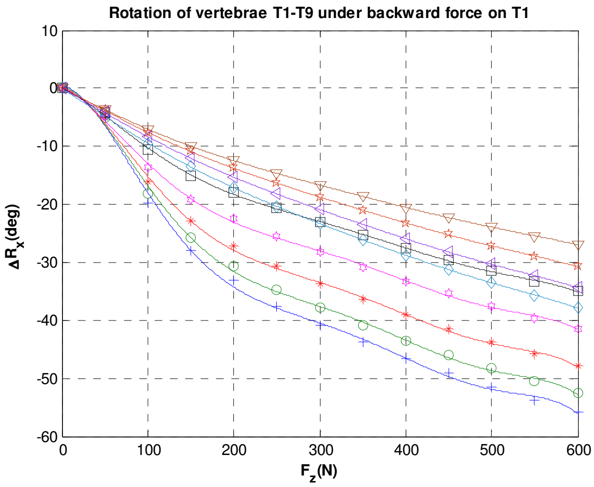
Rotation of vertebrae T1-T9 under backward force on T1

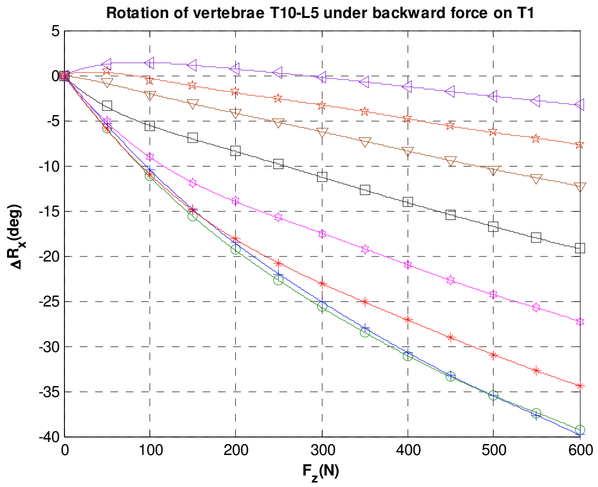
Rotation of vertebrae T10-L5 under backward force on T1

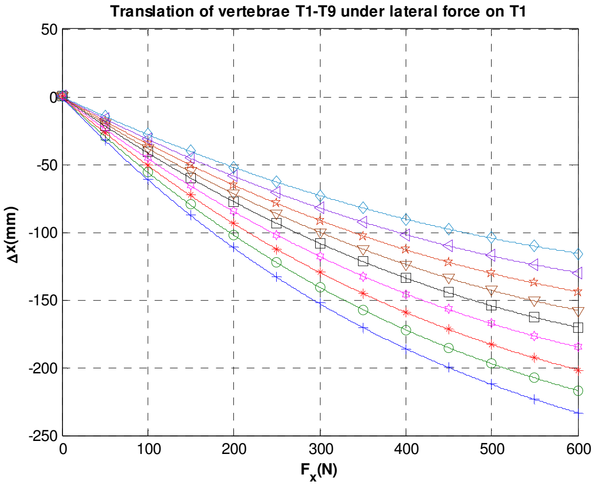
Translation of vertebrae T1-T9 under lateral force on T1

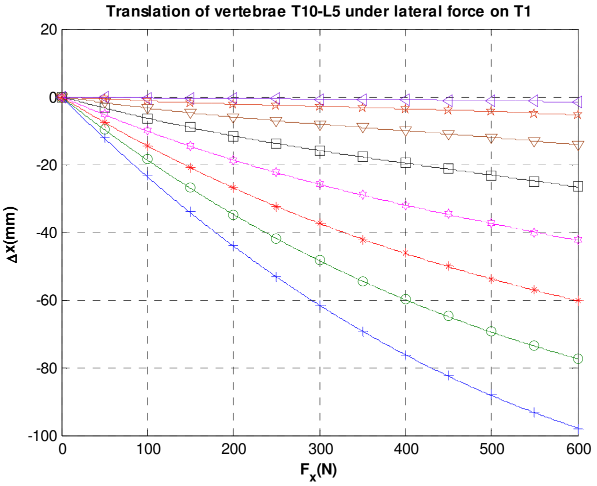
Translation of vertebrae T10-L5 under lateral force on T1

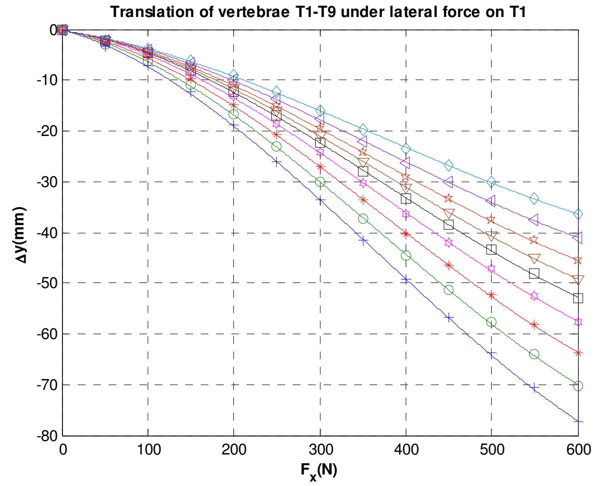
Translation of vertebrae T1-T9 under lateral force on T1

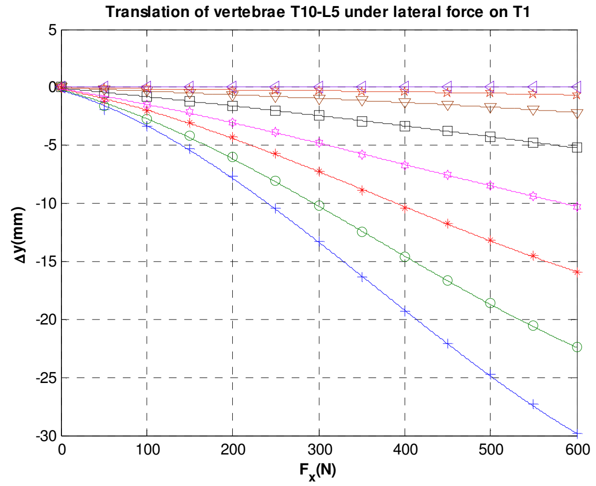
Translation of vertebrae T10-L5 under lateral force on T1

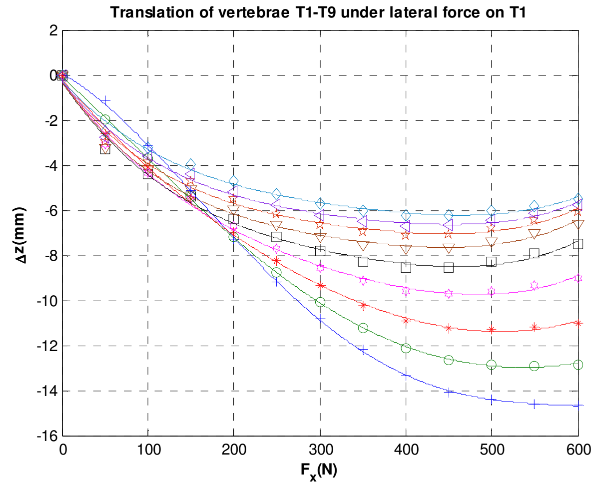
Translation of vertebrae T1-T9 under lateral force on T1

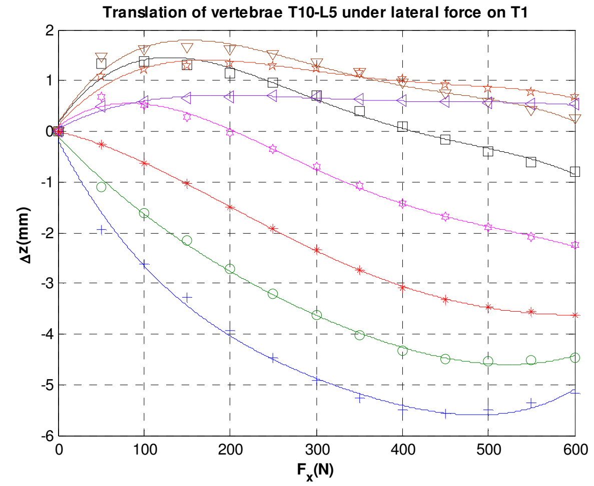
Translation of vertebrae T10-L5 under lateral force on T1

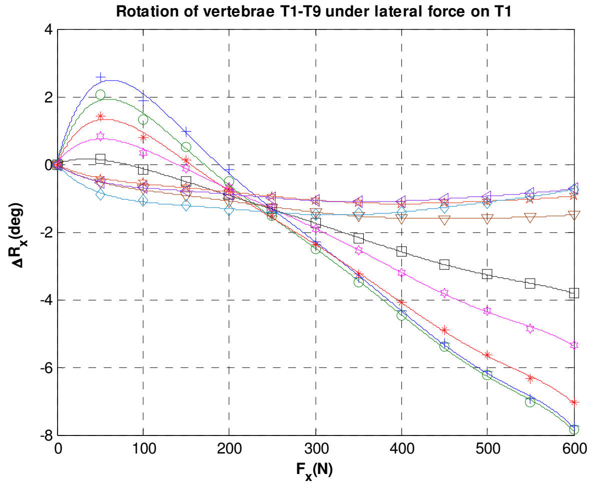
Rotation of vertebrae T1-T9 under lateral force on T1

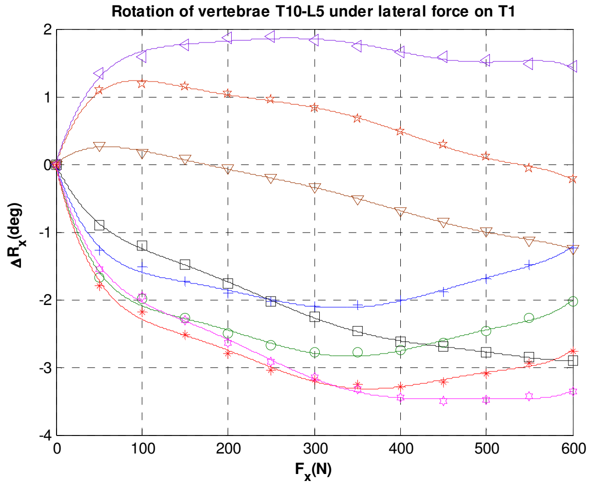
Rotation of vertebrae T10-L5 under lateral force on T1

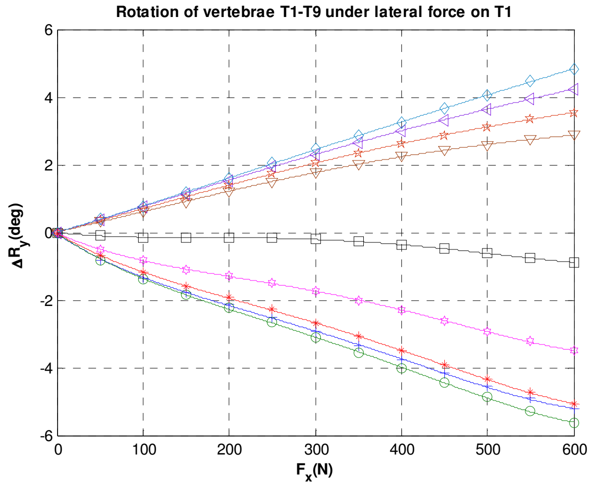
Rotation of vertebrae T1-T9 under lateral force on T1

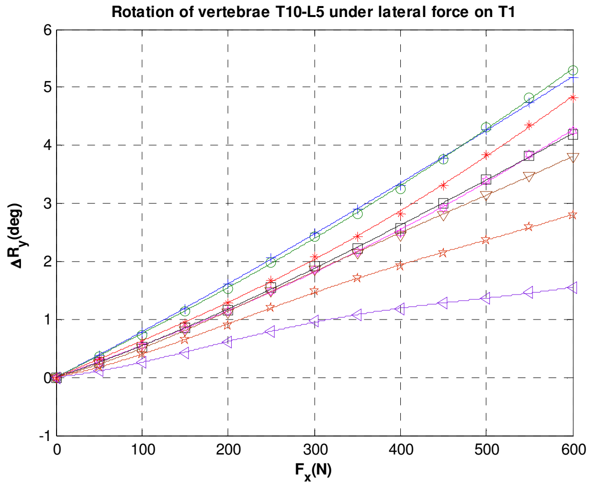
Rotation of vertebrae T10-L5 under lateral force on T1

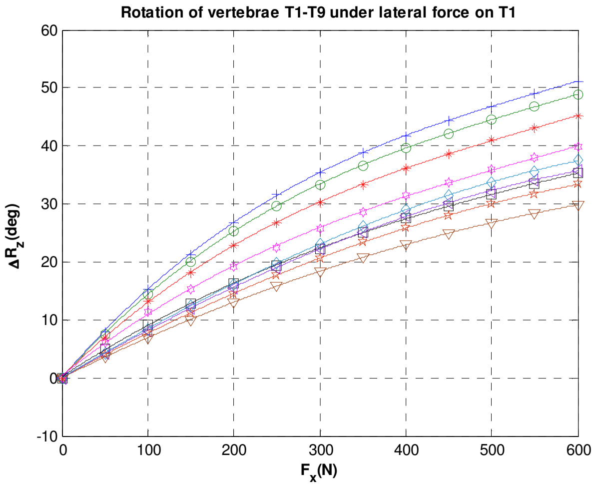
Rotation of vertebrae T1-T9 under lateral force on T1

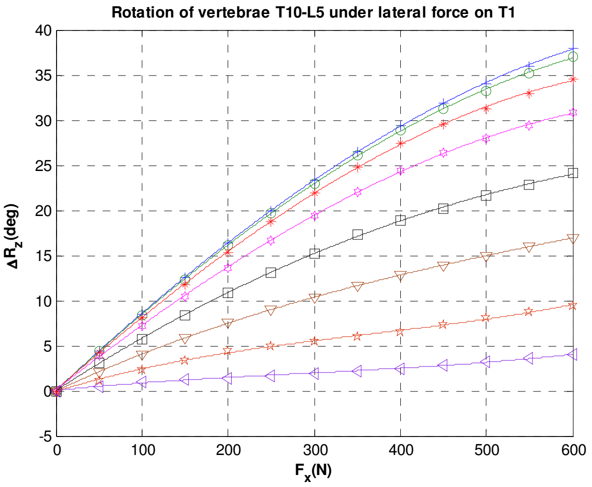
Rotation of vertebrae T10-L5 under lateral force on T1

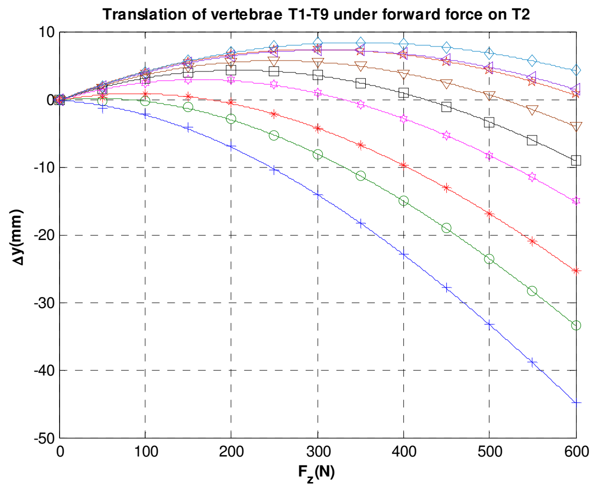
Translation of vertebrae T1-T9 under forward force on T2
Δy(mm)
10
0
-10
-20
-30
-40
-50
0
100
200
300
400
500
600
F_z(N)

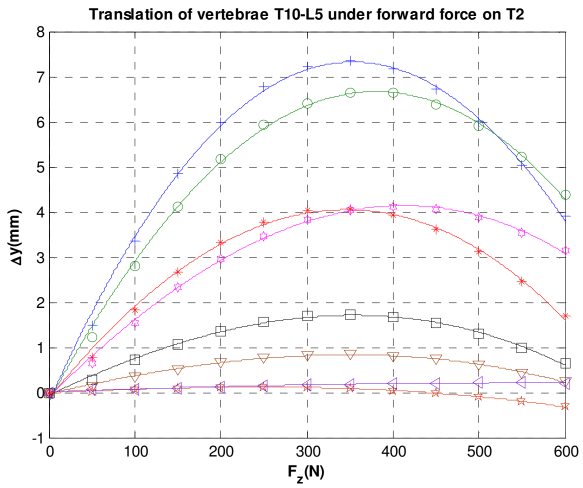
Translation of vertebrae T10-L5 under forward force on T2
Δy(mm)
8
7
6
5
4
3
2
1
0
-1
0
100
200
300
400
500
600
F_z(N)

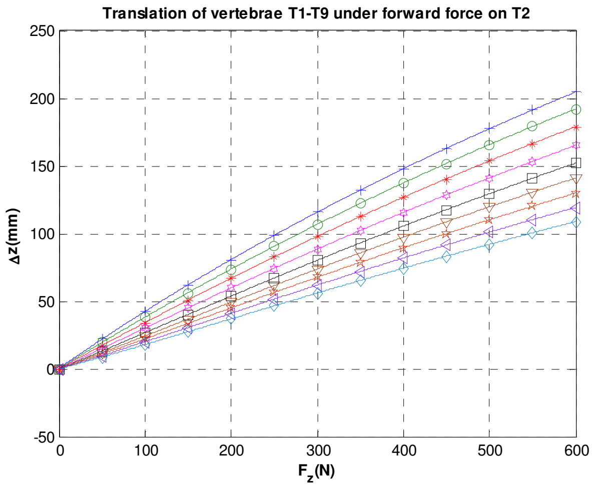
Translation of vertebrae T1-T9 under forward force on T2
Δz(mm)
250
200
150
100
50
0
-50
0
100
200
300
400
500
600
F_z(N)

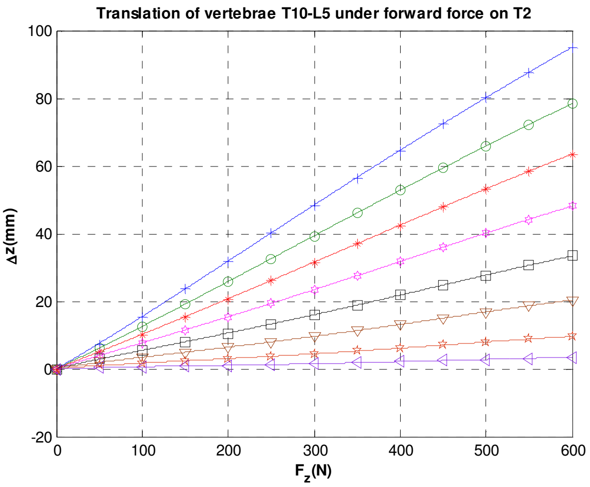
Translation of vertebrae T10-L5 under forward force on T2
Δz(mm)
100
80
60
40
20
0
-20
0
100
200
300
400
500
600
F_z(N)

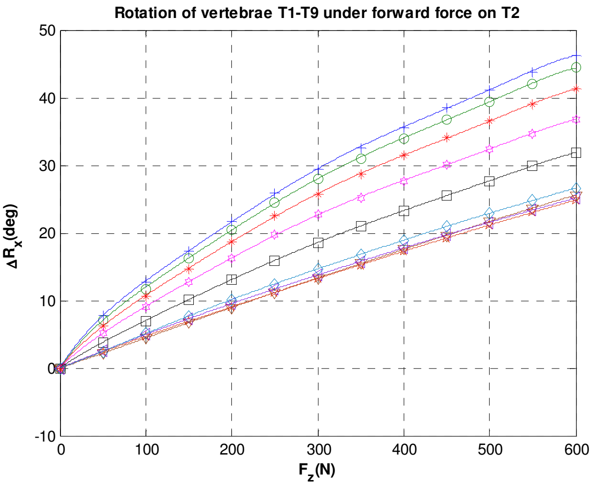
Rotation of vertebrae T1-T9 under forward force on T2
ΔR_x(deg)
50
40
30
20
10
0
-10
0
100
200
300
400
500
600
F_z(N)

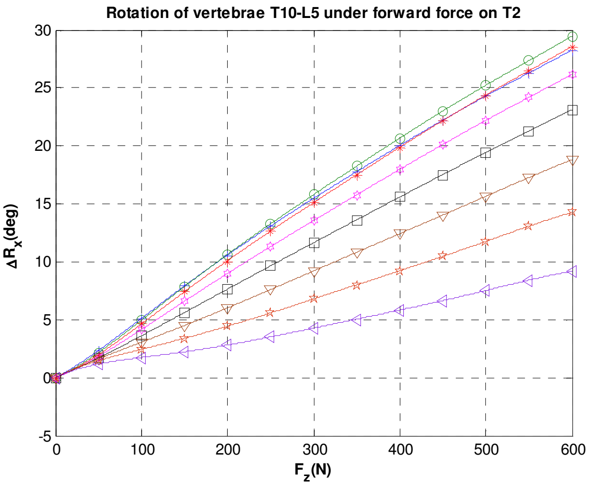
Rotation of vertebrae T10-L5 under forward force on T2
ΔR_x(deg)
30
25
20
15
10
5
0
-5
0
100
200
300
400
500
600
F_z(N)

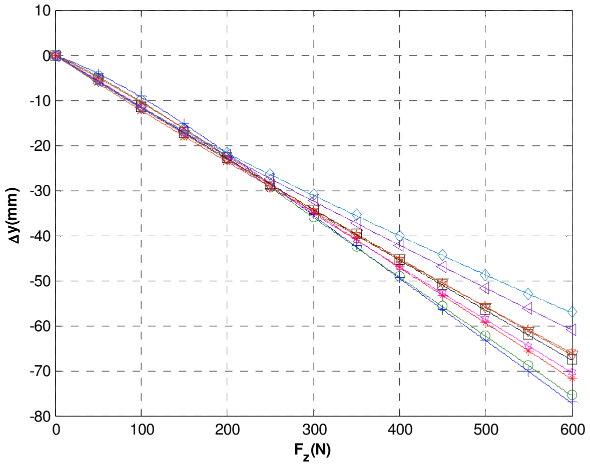
Translation of vertebrae T1-T9 under backward force on T2

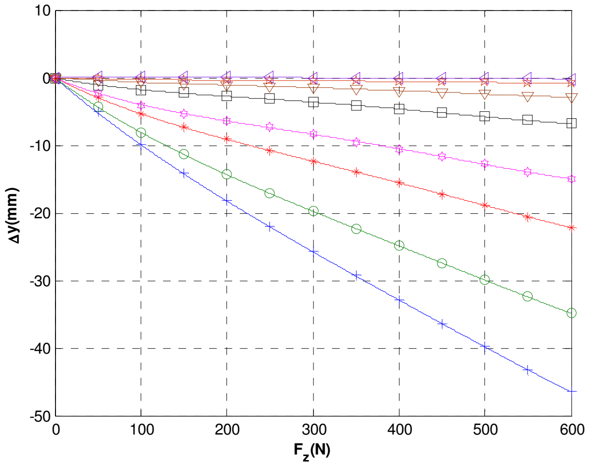
Translation of vertebrae T10-L5 under backward force on T2

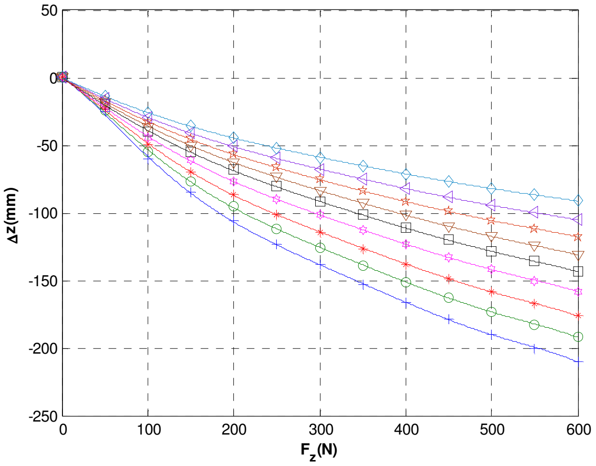
Translation of vertebrae T1-T9 under backward force on T2

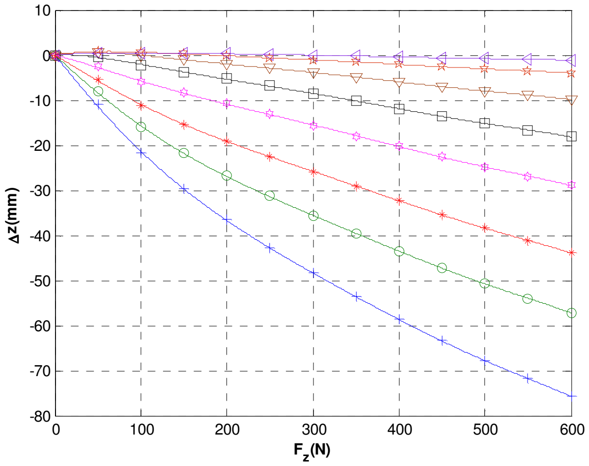
Translation of vertebrae T10-L5 under backward force on T2

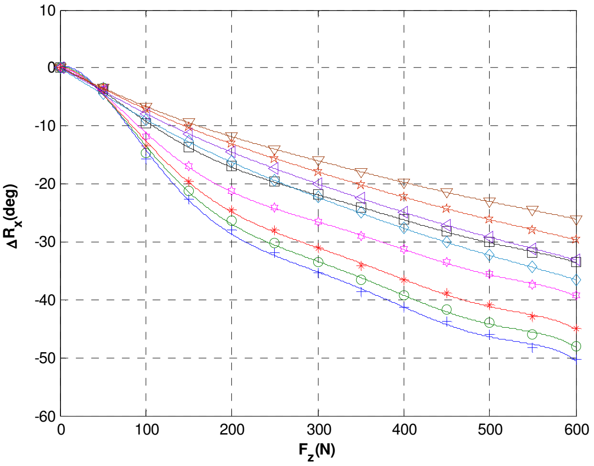
Rotation of vertebrae T1-T9 under backward force on T2

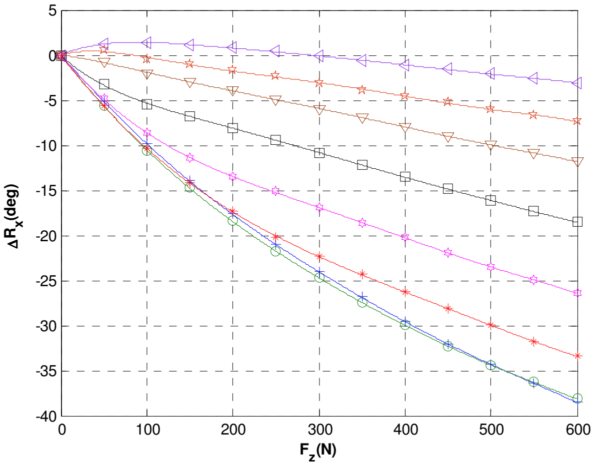
Rotation of vertebrae T10-L5 under backward force on T2

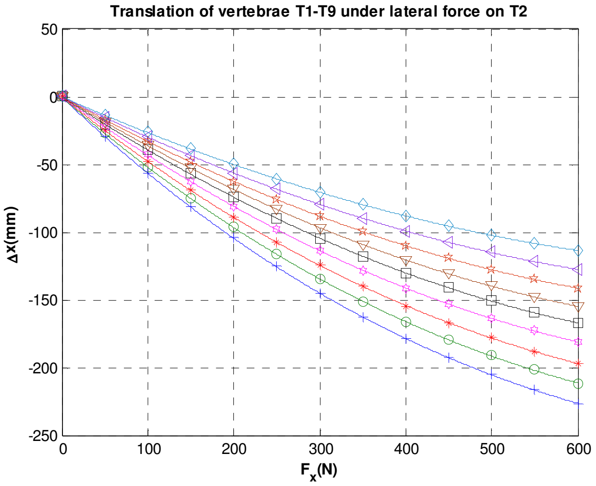
Translation of vertebrae T1-T9 under lateral force on T2
Δx(mm)
50
0
-50
-100
-150
-200
-250
0
100
200
300
400
500
600
F_x(N)

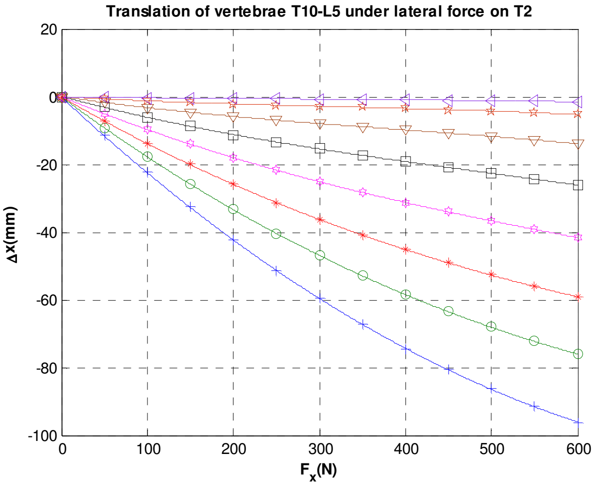
Translation of vertebrae T10-L5 under lateral force on T2
Δx(mm)
20
0
-20
-40
-60
-80
-100
0
100
200
300
400
500
600
F_x(N)

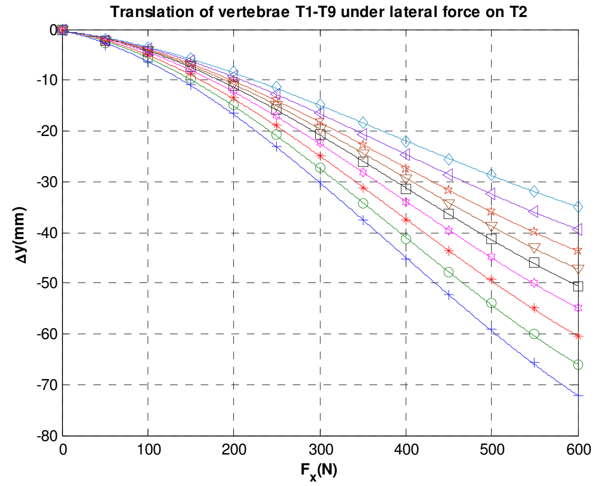
Translation of vertebrae T1-T9 under lateral force on T2
Δy(mm)
0
-10
-20
-30
-40
-50
-60
-70
-80
0
100
200
300
400
500
600
F_x(N)

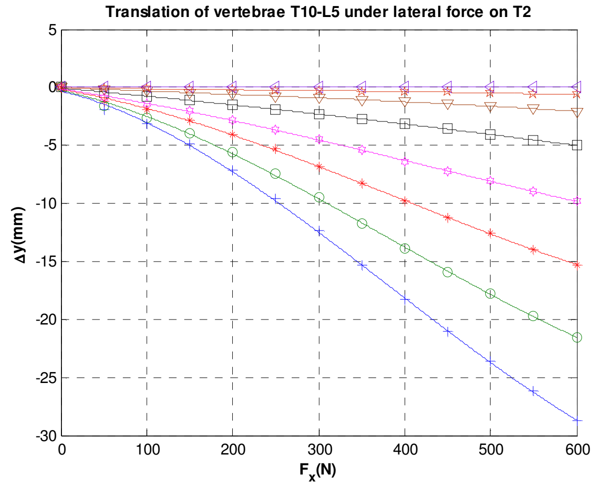
Translation of vertebrae T10-L5 under lateral force on T2
Δy(mm)
5
0
-5
-10
-15
-20
-25
-30
0
100
200
300
400
500
600
F_x(N)

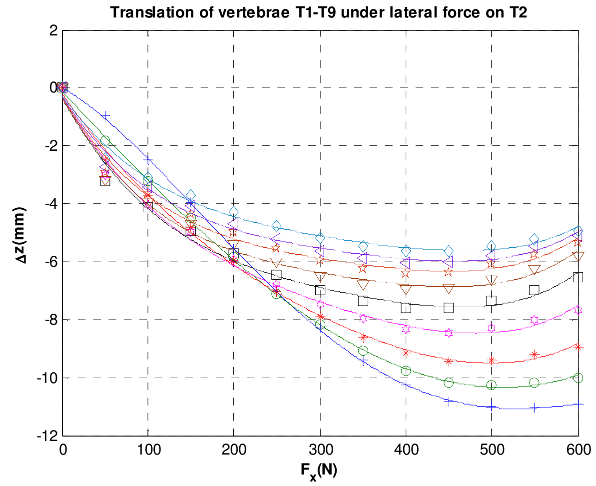
Translation of vertebrae T1-T9 under lateral force on T2
Δz(mm)
2
0
-2
-4
-6
-8
-10
-12
0
100
200
300
400
500
600
F_x(N)

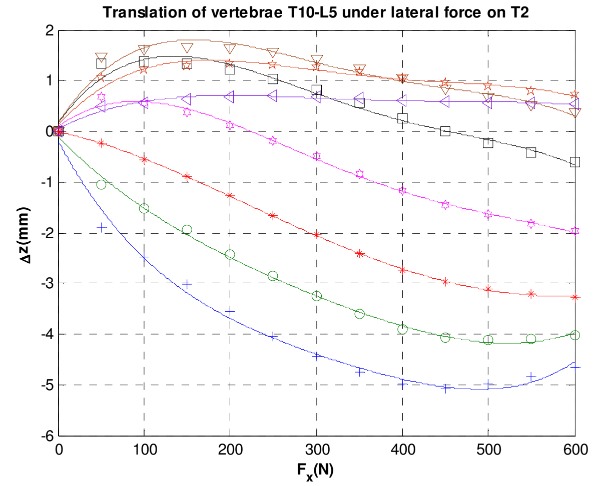
Translation of vertebrae T10-L5 under lateral force on T2
Δz(mm)
2
1
0
-1
-2
-3
-4
-5
-6
0
100
200
300
400
500
600
F_x(N)

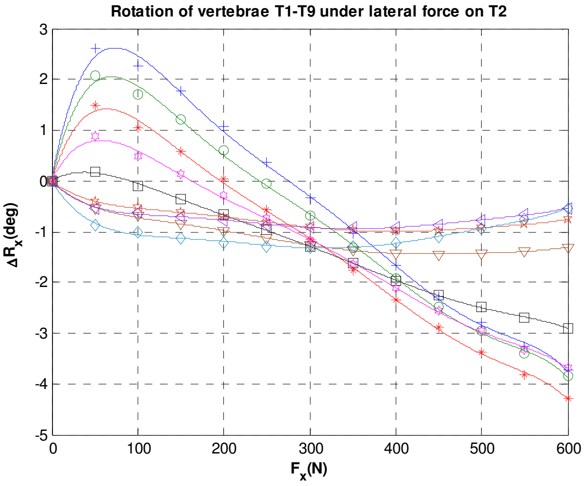
Rotation of vertebrae T1-T9 under lateral force on T2
ΔR_x(deg)
F_x(N)
3
2
1
0
-1
-2
-3
-4
-5
0
100
200
300
400
500
600

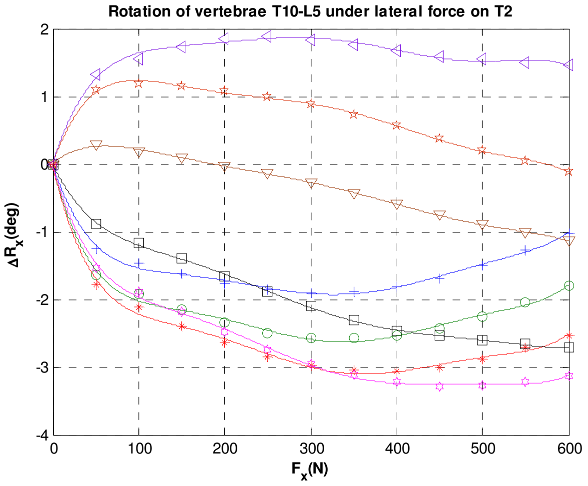
Rotation of vertebrae T10-L5 under lateral force on T2
ΔR_x(deg)
F_x(N)
2
1
0
-1
-2
-3
-4
0
100
200
300
400
500
600

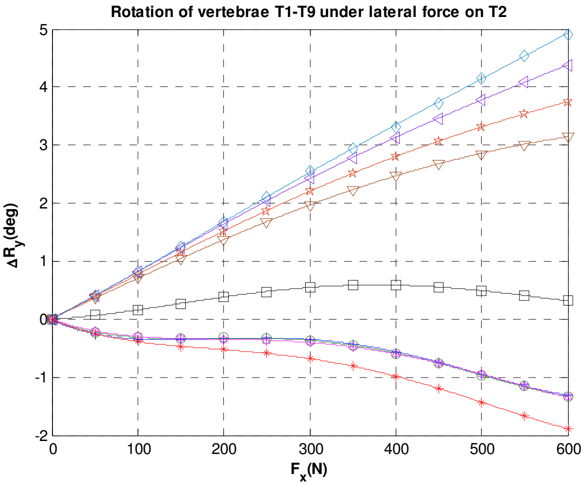
Rotation of vertebrae T1-T9 under lateral force on T2
ΔR_y(deg)
F_x(N)
5
4
3
2
1
0
-1
-2
0
100
200
300
400
500
600

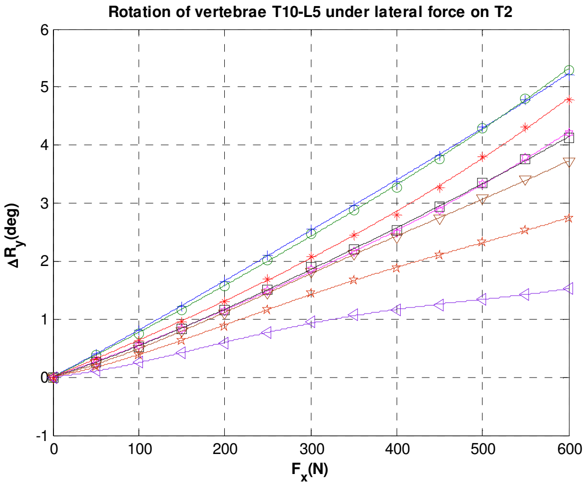
Rotation of vertebrae T10-L5 under lateral force on T2
ΔR_y(deg)
F_x(N)
6
5
4
3
2
1
0
-1
0
100
200
300
400
500
600

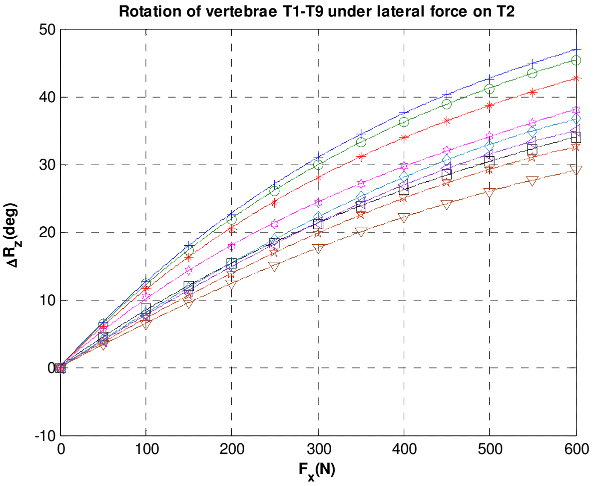
Rotation of vertebrae T1-T9 under lateral force on T2
ΔR_z(deg)
F_x(N)
50
40
30
20
10
0
-10
0
100
200
300
400
500
600

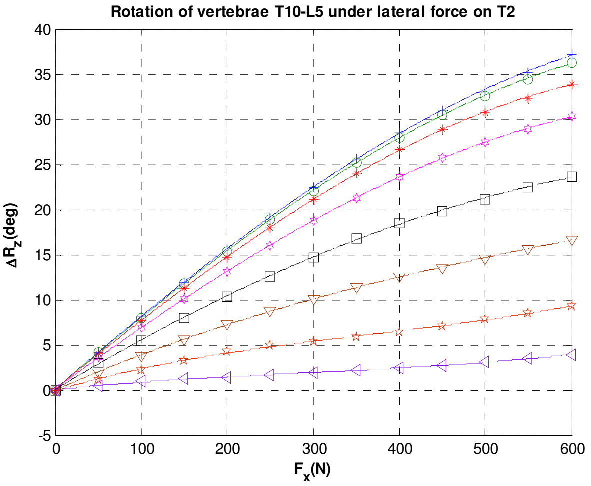
Rotation of vertebrae T10-L5 under lateral force on T2
ΔR_z(deg)
F_x(N)
40
35
30
25
20
15
10
5
0
-5
0
100
200
300
400
500
600

APPENDIX E

RELATIVE DISPLACEMENTS OF ALL PAIRS OF VERTEBRAE UNDER EXTERNAL FORCES IN X- AND Z-AXIS DIRECTIONS

Due to space constraint, dynamic database of the spine model under external forces applying onto vertebrae from T2 to T3 is extracted here.

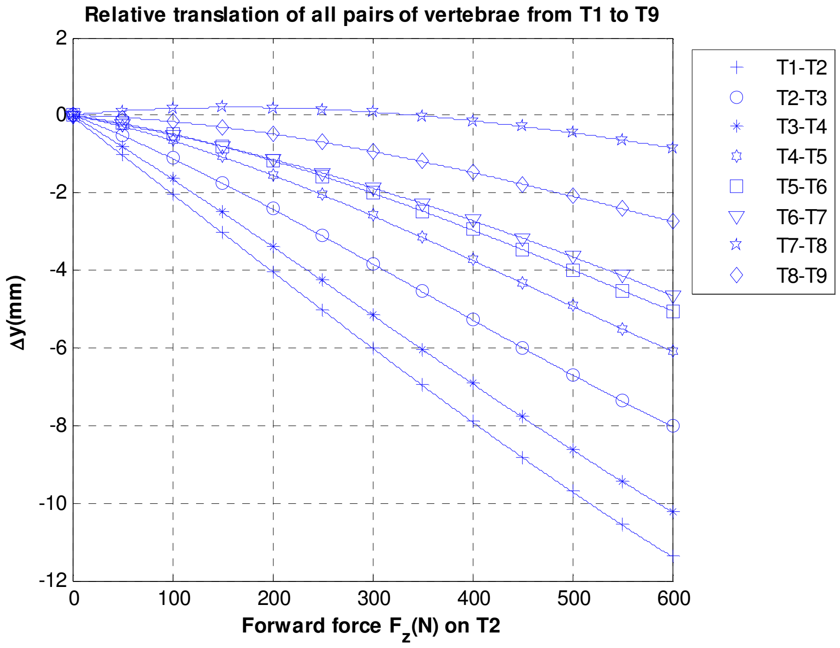

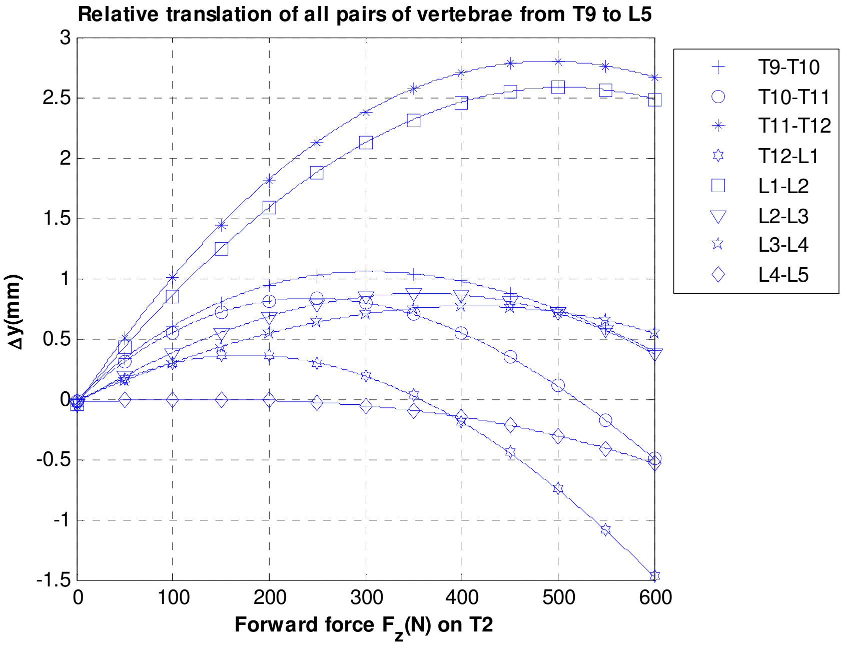

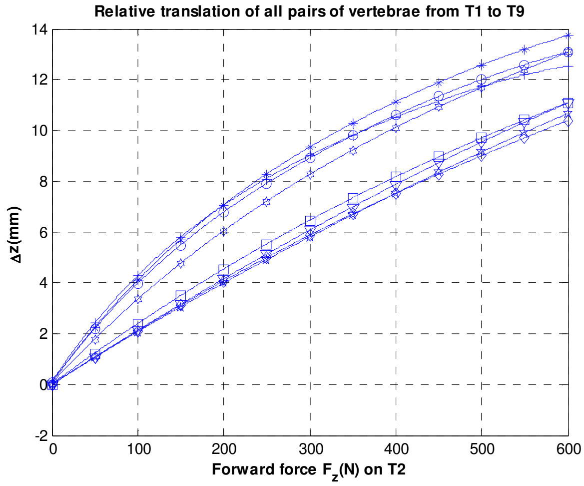
Relative translation of all pairs of vertebrae from T1 to T9

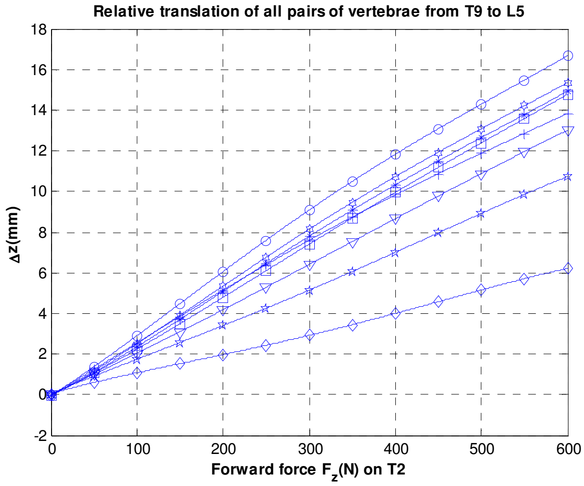
Relative translation of all pairs of vertebrae from T9 to L5

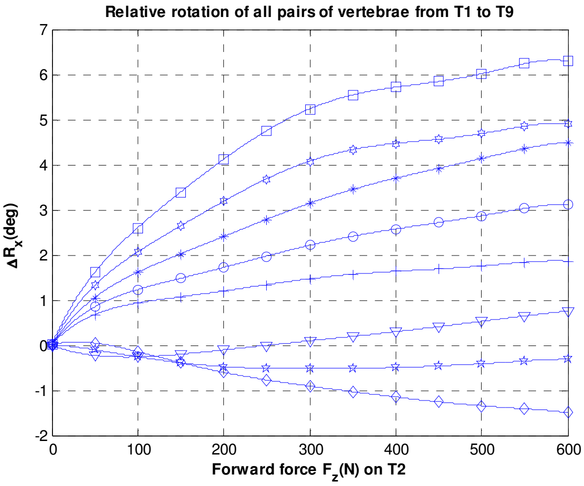
Relative rotation of all pairs of vertebrae from T1 to T9

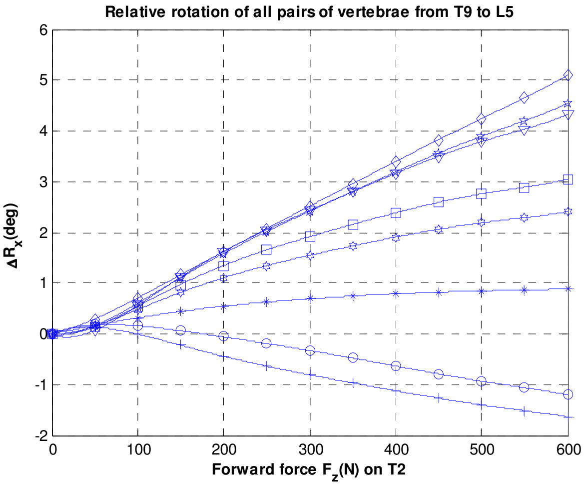
Relative rotation of all pairs of vertebrae from T9 to L5

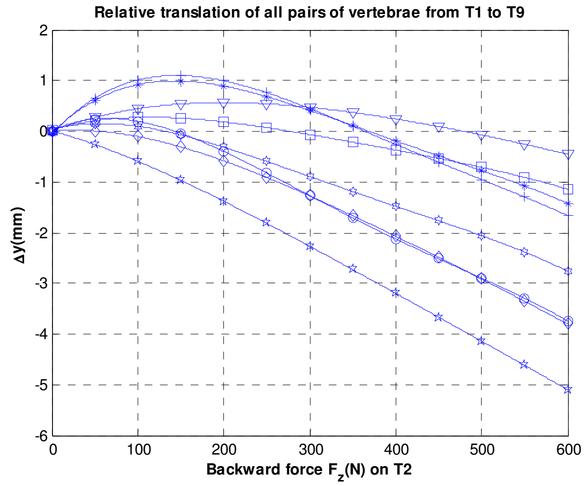
Relative translation of all pairs of vertebrae from T1 to T9

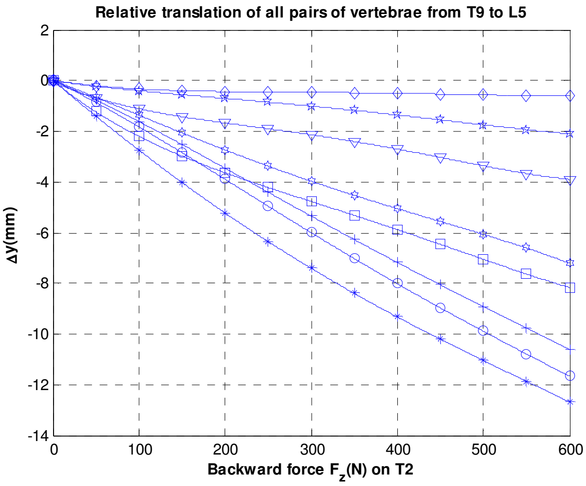
Relative translation of all pairs of vertebrae from T9 to L5

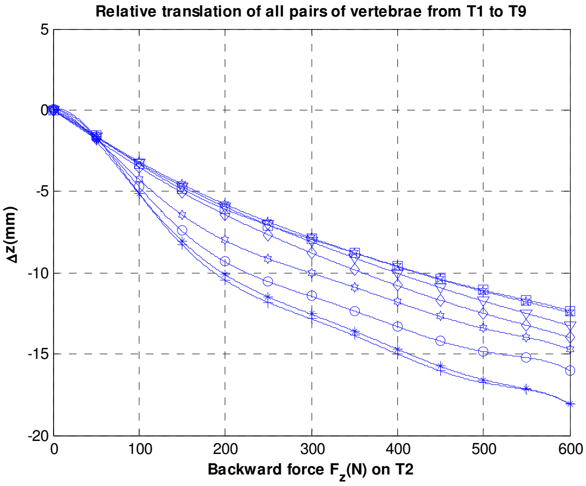
Relative translation of all pairs of vertebrae from T1 to T9
Δz(mm)
5
0
-5
-10
-15
-20
0
100
200
300
400
500
600
Backward force F_z(N) on T2

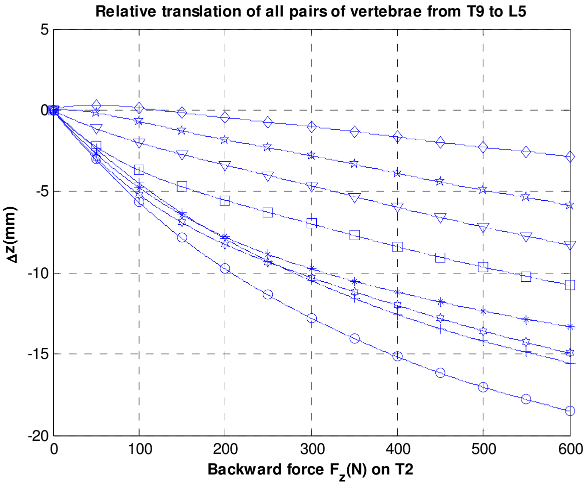
Relative translation of all pairs of vertebrae from T9 to L5
Δz(mm)
5
0
-5
-10
-15
-20
0
100
200
300
400
500
600
Backward force F_z(N) on T2

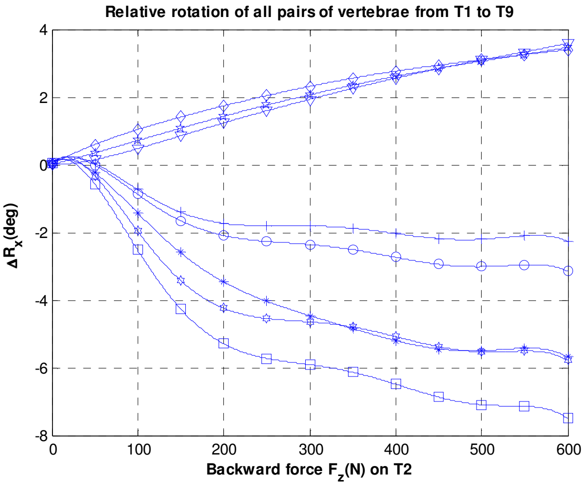
Relative rotation of all pairs of vertebrae from T1 to T9
ΔR_x(deg)
4
2
0
-2
-4
-6
-8
0
100
200
300
400
500
600
Backward force F_z(N) on T2

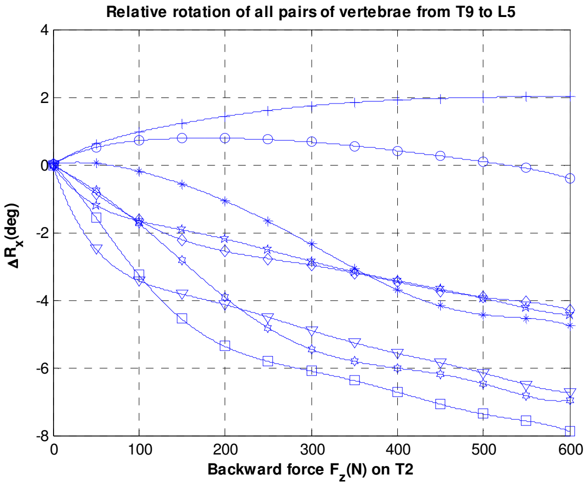
Relative rotation of all pairs of vertebrae from T9 to L5
ΔR_x(deg)
4
2
0
-2
-4
-6
-8
0
100
200
300
400
500
600
Backward force F_z(N) on T2

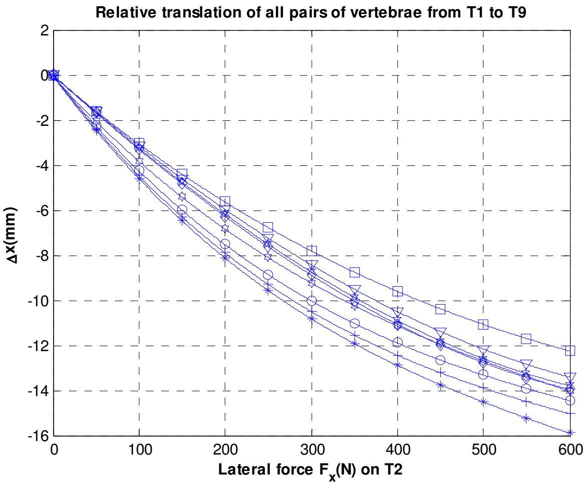
Relative translation of all pairs of vertebrae from T1 to T9
Δx(mm)
2
0
-2
-4
-6
-8
-10
-12
-14
-16
0
100
200
300
400
500
600
Lateral force F_x(N) on T2

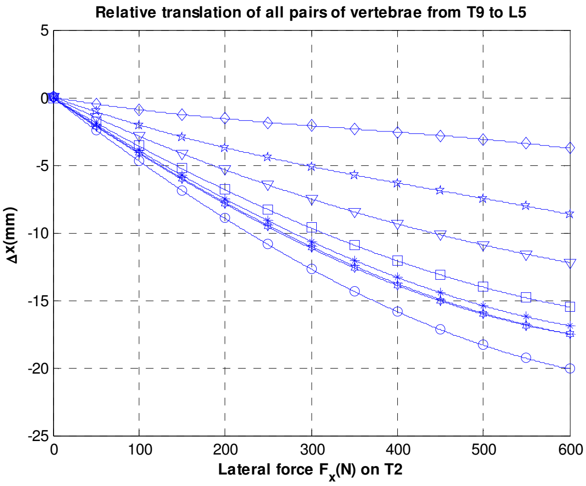
Relative translation of all pairs of vertebrae from T9 to L5
Δx(mm)
5
0
-5
-10
-15
-20
-25
0
100
200
300
400
500
600
Lateral force F_x(N) on T2

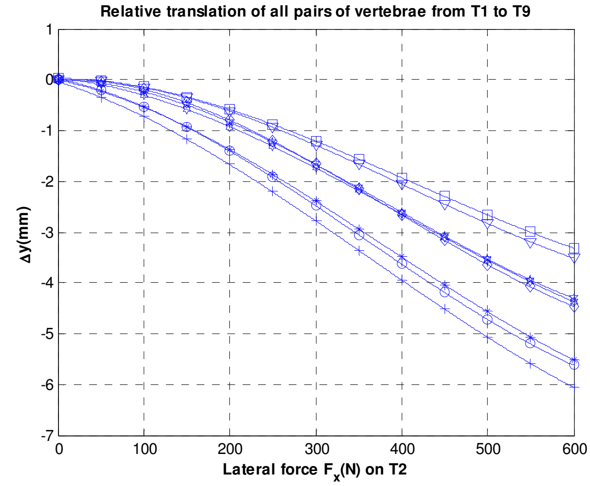
Relative translation of all pairs of vertebrae from T1 to T9

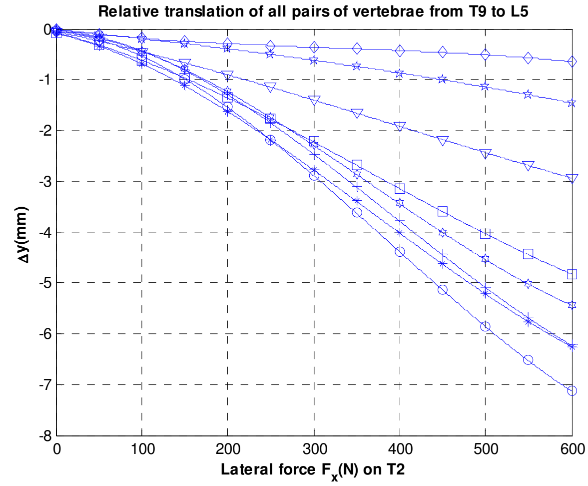
Relative translation of all pairs of vertebrae from T9 to L5

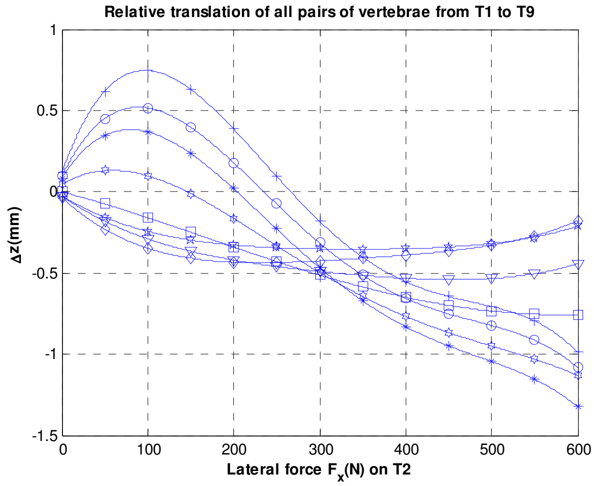
Relative translation of all pairs of vertebrae from T1 to T9

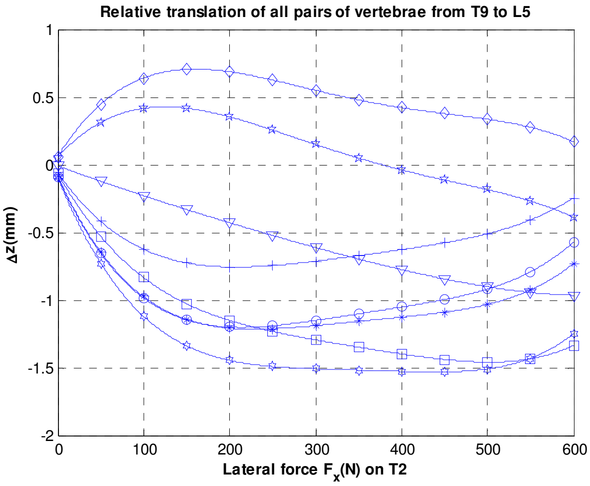
Relative translation of all pairs of vertebrae from T9 to L5

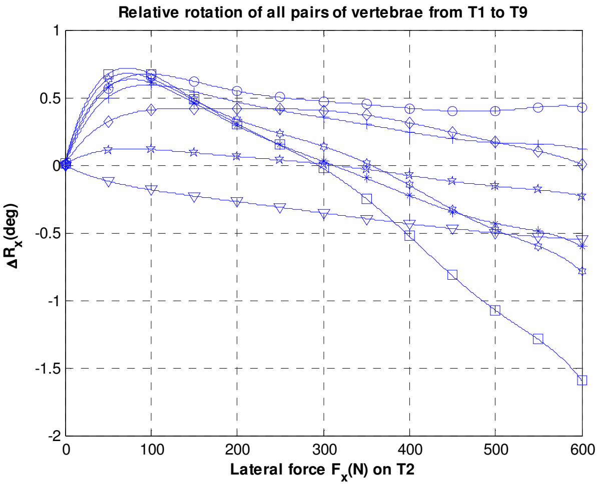
Relative rotation of all pairs of vertebrae from T1 to T9

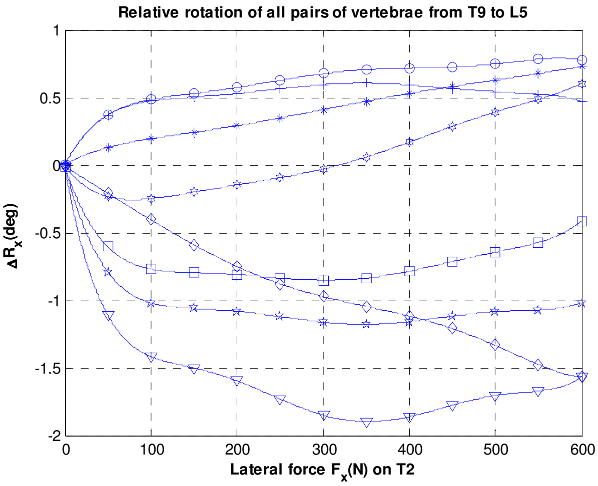
Relative rotation of all pairs of vertebrae from T9 to L5

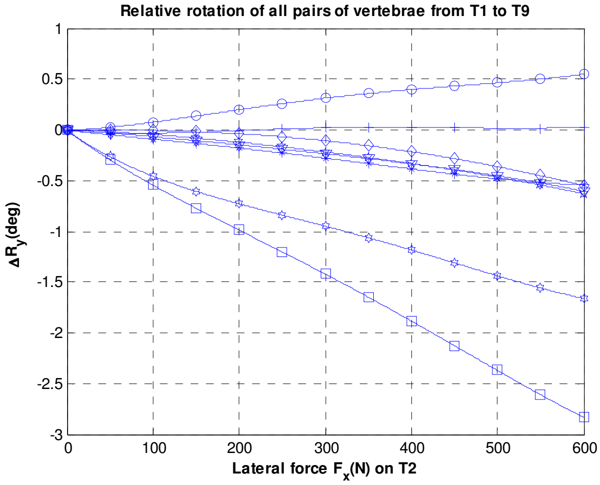
Relative rotation of all pairs of vertebrae from T1 to T9

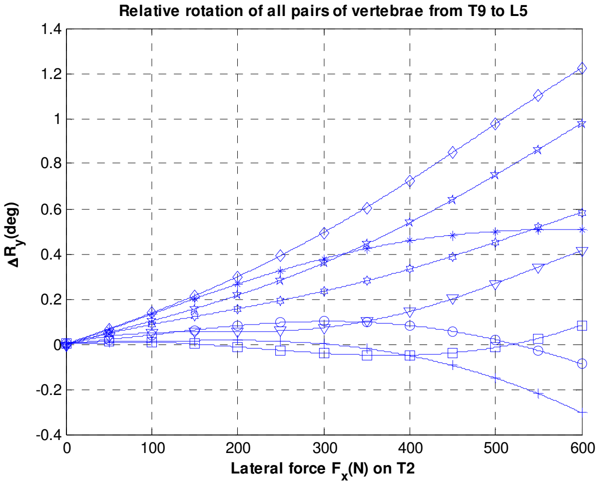
Relative rotation of all pairs of vertebrae from T9 to L5

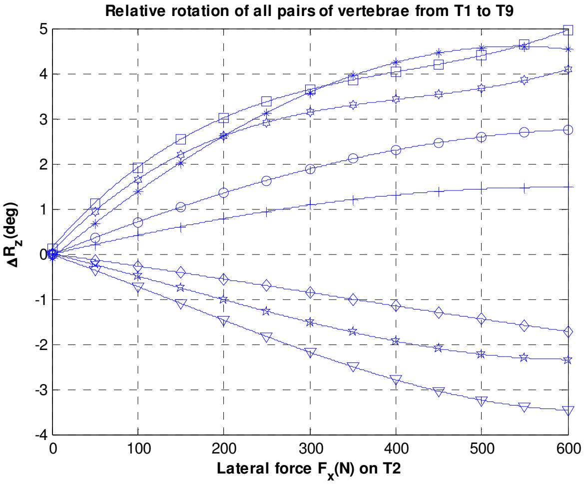
Relative rotation of all pairs of vertebrae from T1 to T9

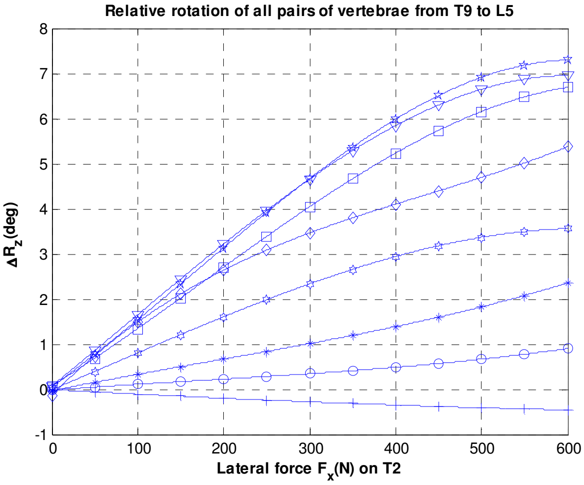
Relative rotation of all pairs of vertebrae from T9 to L5

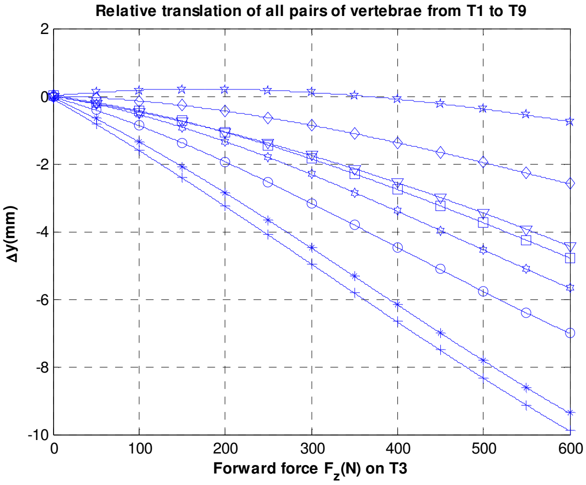
Relative translation of all pairs of vertebrae from T1 to T9

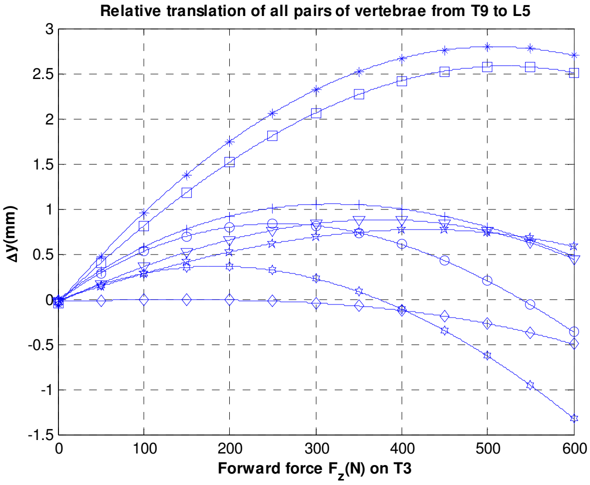
Relative translation of all pairs of vertebrae from T9 to L5

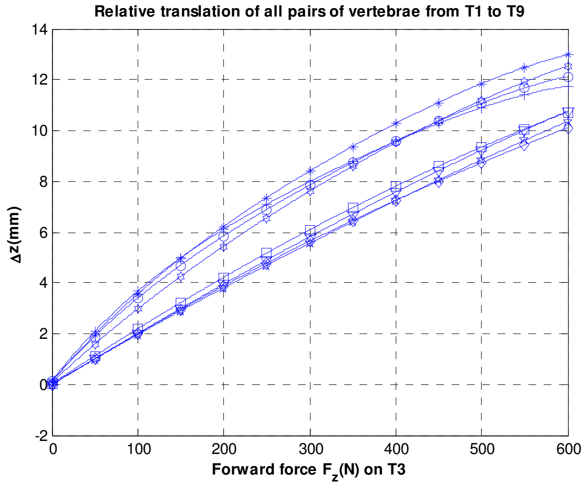
Relative translation of all pairs of vertebrae from T1 to T9

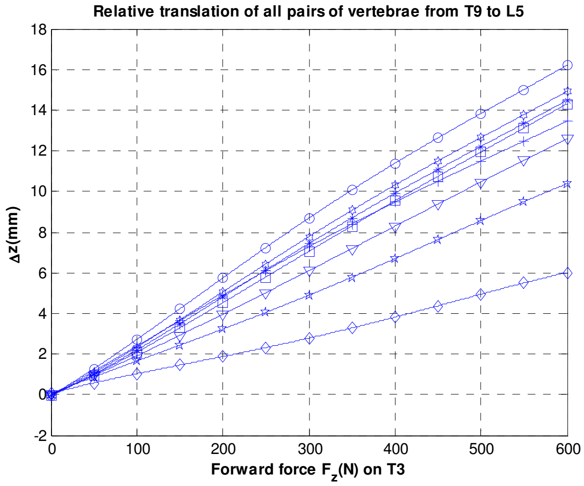
Relative translation of all pairs of vertebrae from T9 to L5

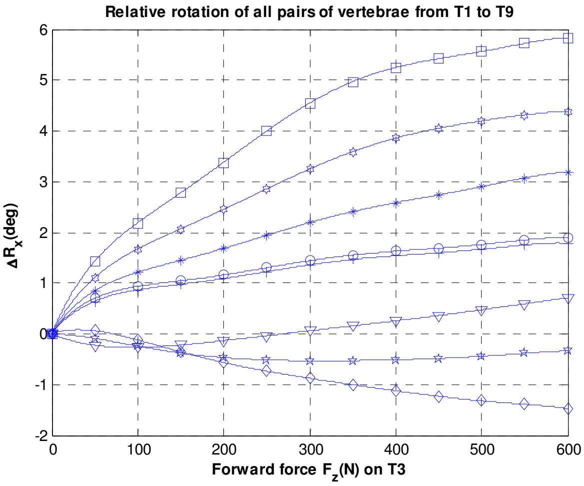
Relative rotation of all pairs of vertebrae from T1 to T9

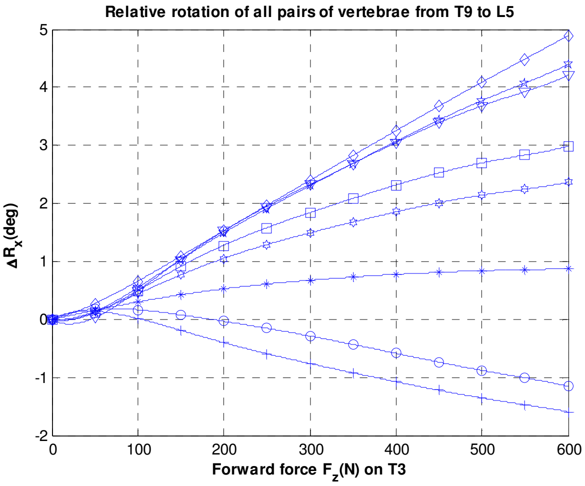
Relative rotation of all pairs of vertebrae from T9 to L5

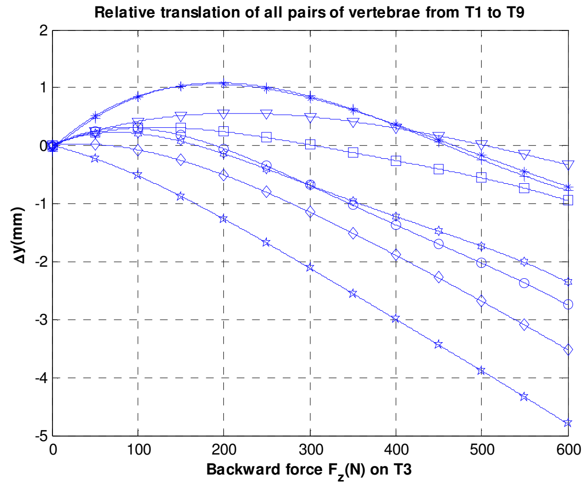
Relative translation of all pairs of vertebrae from T1 to T9

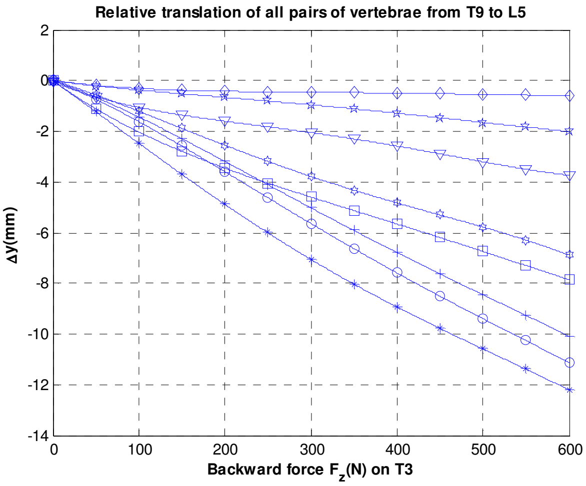
Relative translation of all pairs of vertebrae from T9 to L5

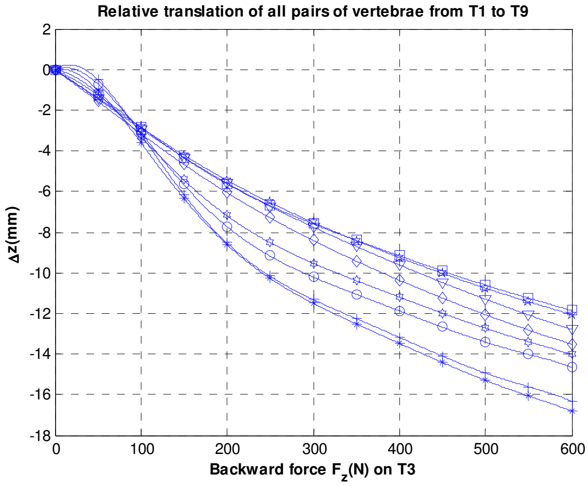
Relative translation of all pairs of vertebrae from T1 to T9

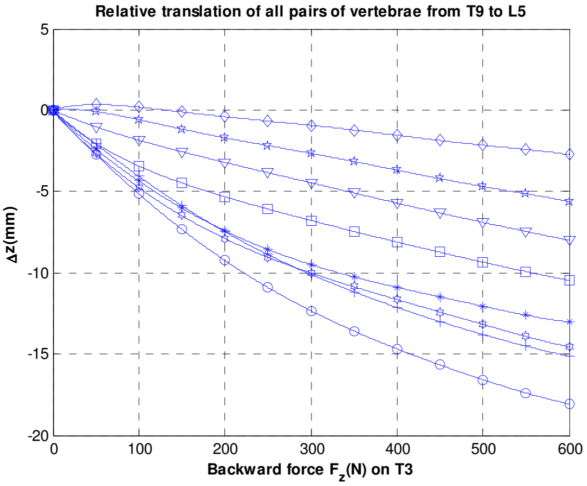
Relative translation of all pairs of vertebrae from T9 to L5

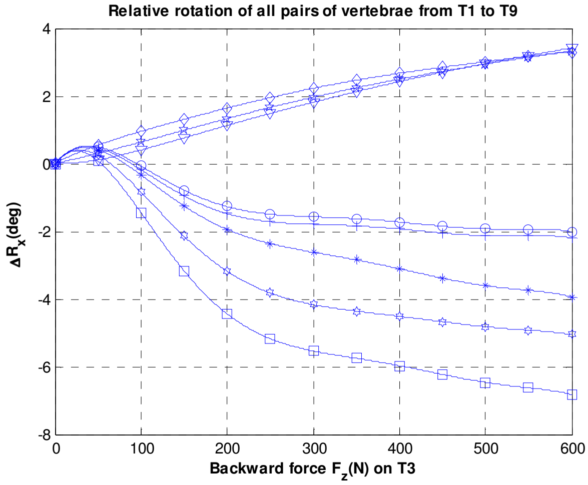
Relative rotation of all pairs of vertebrae from T1 to T9

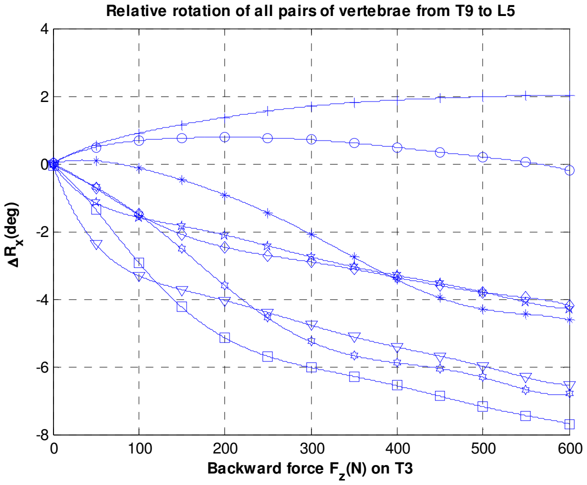
Relative rotation of all pairs of vertebrae from T9 to L5

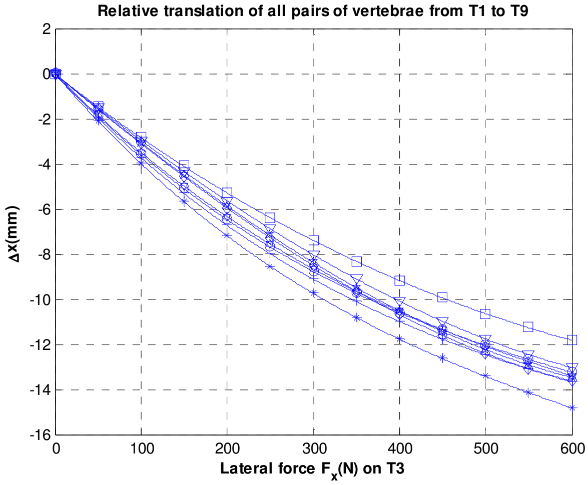
Relative translation of all pairs of vertebrae from T1 to T9

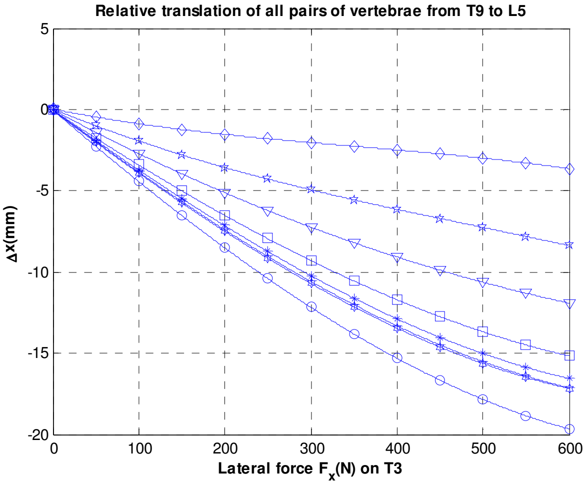
Relative translation of all pairs of vertebrae from T9 to L5

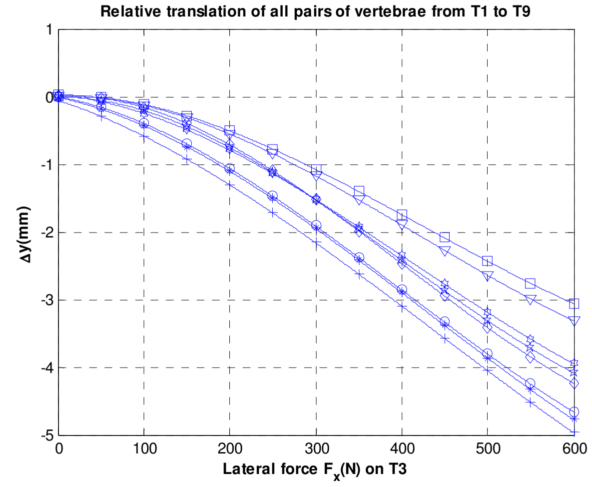
Relative translation of all pairs of vertebrae from T1 to T9
Δy(mm)
1
0
-1
-2
-3
-4
-5
0
100
200
300
400
500
600
Lateral force F_x(N) on T3

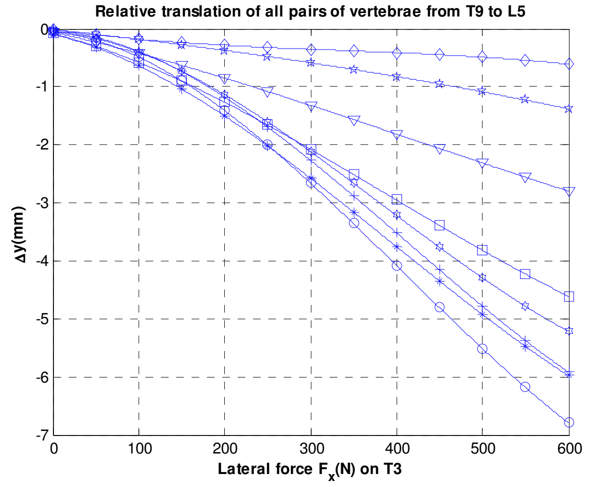
Relative translation of all pairs of vertebrae from T9 to L5
Δy(mm)
0
-1
-2
-3
-4
-5
-6
-7
0
100
200
300
400
500
600
Lateral force F_x(N) on T3

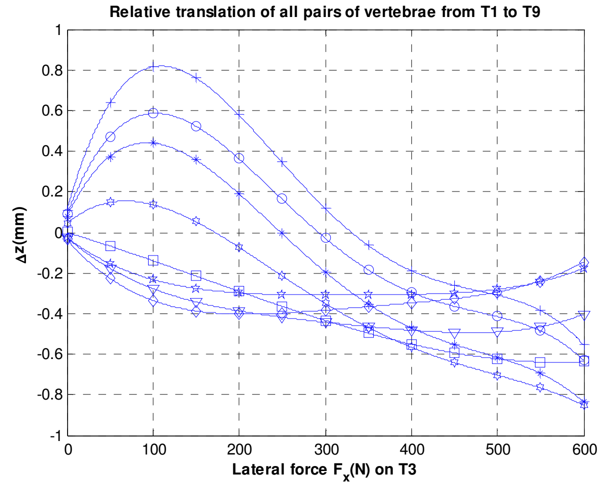
Relative translation of all pairs of vertebrae from T1 to T9
Δz(mm)
1
0.8
0.6
0.4
0.2
0
-0.2
-0.4
-0.6
-0.8
-1
0
100
200
300
400
500
600
Lateral force F_x(N) on T3

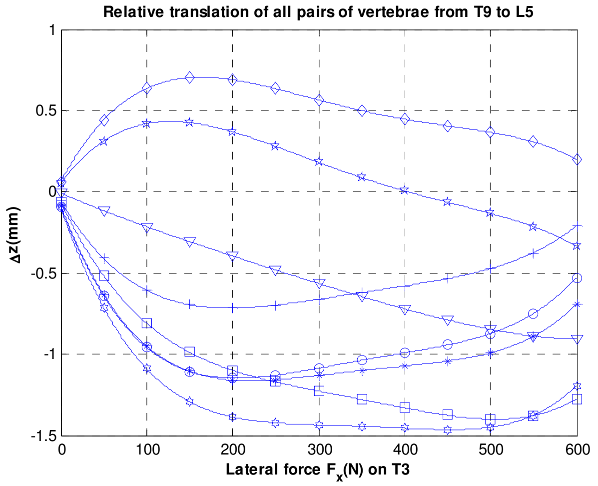
Relative translation of all pairs of vertebrae from T9 to L5
Δz(mm)
1
0.5
0
-0.5
-1
-1.5
0
100
200
300
400
500
600
Lateral force F_x(N) on T3

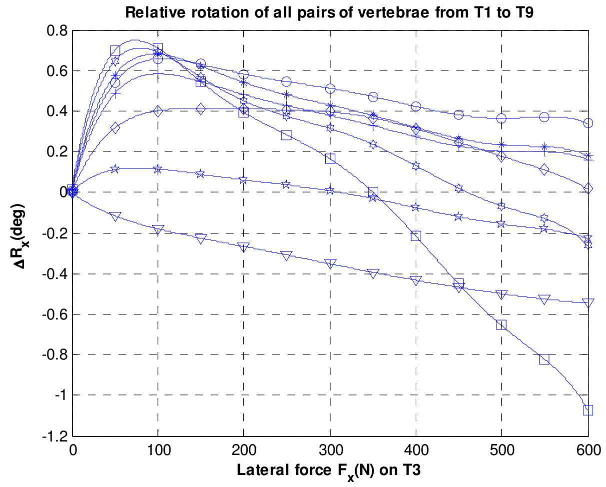
Relative rotation of all pairs of vertebrae from T1 to T9
ΔR_x(deg)
0.8
0.6
0.4
0.2
0
-0.2
-0.4
-0.6
-0.8
-1
-1.2
0
100
200
300
400
500
600
Lateral force F_x(N) on T3

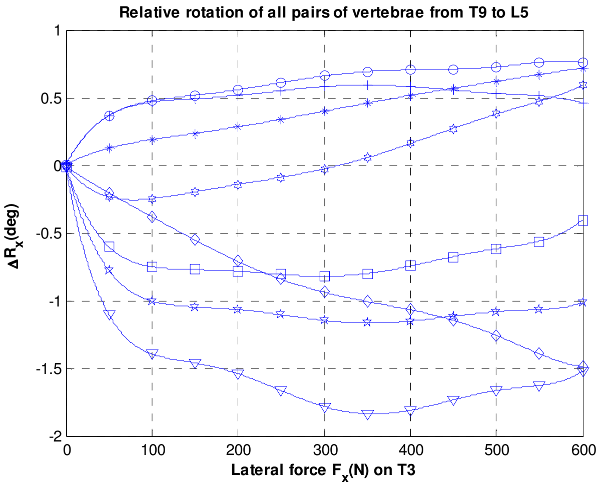
Relative rotation of all pairs of vertebrae from T9 to L5
ΔR_x(deg)
1
0.5
0
-0.5
-1
-1.5
-2
0
100
200
300
400
500
600
Lateral force F_x(N) on T3

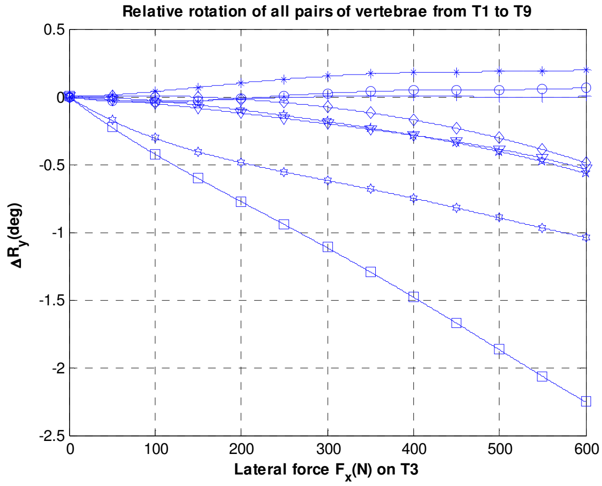
Relative rotation of all pairs of vertebrae from T1 to T9

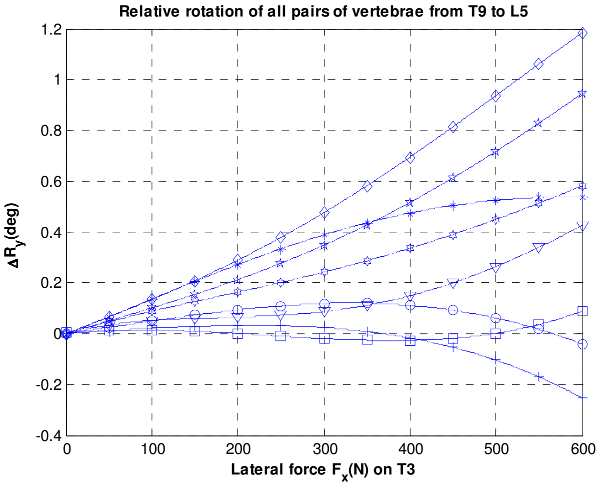
Relative rotation of all pairs of vertebrae from T9 to L5

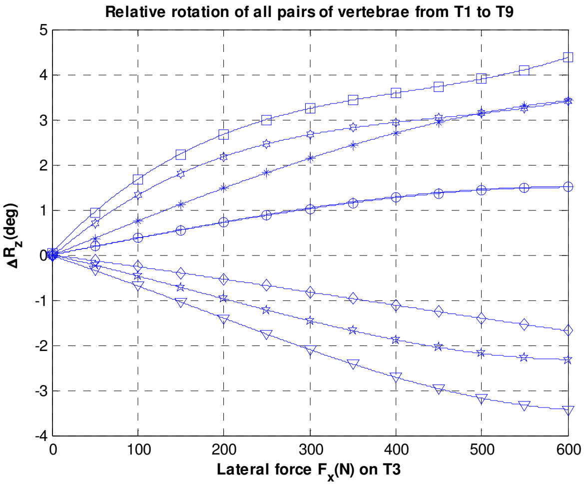
Relative rotation of all pairs of vertebrae from T1 to T9

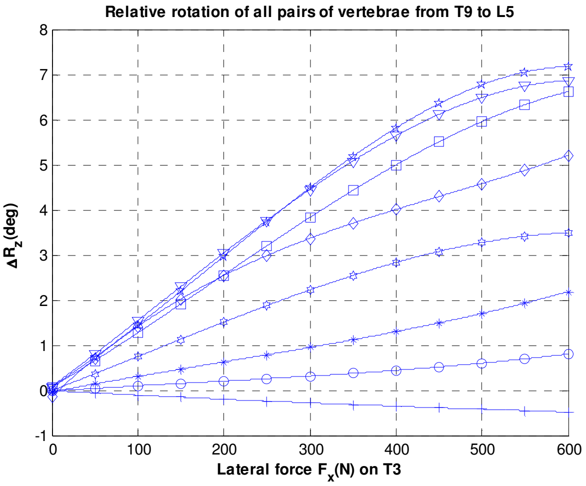
Relative rotation of all pairs of vertebrae from T9 to L5

APPENDIX F

SUPPLEMENTAL DATA

Table F.1 CM location of all vertebrae (mm and degree)

Segment Name	CM Location	Orientation
C1	0.0, 675.0, -20.0	0.0, 0.0, 0.0
C2	0.0, 659.5, -16.5	0.0, 0.0, 0.0
C3	0.0, 640.0, -22.5	0.0, 0.0, 0.0
C4	0.0, 615.0, -24.0	0.0, 0.0, 0.0
C5	0.0, 590.0, -24.0	0.0, 0.0, 0.0
C6	0.0, 568.0, -28.0	0.0, 0.0, 0.0
C7	0.0, 548.0, -24.0	0.0, 0.0, 0.0
T1	0.0, 524.0, -31.5	0.0, 0.0, 0.0
T2	0.0, 503.5, -39.0	0.0, 0.0, 0.0
T3	0.0, 483.0, -43.0	0.0, 0.0, 0.0
T4	0.0, 459.0, -51.0	0.0, 0.0, 0.0
T5	0.0, 435.0, -55.0	0.0, 0.0, 0.0
T6	0.0, 411.0, -60.0	0.0, 0.0, 0.0
T7	0.0, 384.0, -65.0	0.0, 0.0, 0.0
T8	0.0, 359.5, -61.5	0.0, 0.0, 0.0
T9	0.0, 335.5, -62.0	0.0, 0.0, 0.0
T10	0.0, 307.5, -54.0	0.0, 0.0, 0.0
T11	0.0, 275.0, -46.5	0.0, 0.0, 0.0
T12	0.0, 247.5, -34.0	0.0, 0.0, 0.0
L1	0.0, 215.5, -30.0	0.0, 0.0, 0.0
L2	0.0, 183.0, -18.0	0.0, 0.0, 0.0
L3	0.0, 148.0, -13.0	0.0, 0.0, 0.0
L4	0.0, 112.0, -8.5	0.0, 0.0, 0.0
L5	0.0, 84.0, -12.0	0.0, 0.0, 0.0

Table F.2: Location of markers for joints connecting vertebrae (mm)

Joint Number	Location	X, Y, Z Coordinates	Marker ID
NSJoint_5	Head-C1	0.0, 684.0, -12.0	.m1
NSJoint_6	C1-C2	0.0, 666.0, -15.0	.m2
NSJoint_7	C2-C3	0.0, 651.0, -18.0	.m3
NSJoint_8	C3-C4	0.0, 630.0, -15.0	.m4
NSJoint_9	C4-C5	0.0, 603.0, -18.0	.m5
NSJoint_10	C5-C6	0.0, 579.0, -18.0	.m6
NSJoint_11	C6-C7	0.0, 558.0, -15.0	.m7
NSJoint_12	C7-T1	0.0, 534.0, -21.0	.m8
NSJoint_13	T1-T2	0.0, 510.0, -30.0	.m9
NSJoint_14	T2-T3	0.0, 492.0, -36.0	.m10
NSJoint_15	T3-T4	0.0, 468.0, -42.0	.m11
NSJoint_16	T4-T5	0.0, 447.0, -48.0	.m12
NSJoint_17	T5-T6	0.0, 423.0, -54.0	.m13
NSJoint_18	T6-T7	0.0, 396.0, -57.0	.m14

NSJoint_19	T7-T8	0.0, 372.0, -57.0	.m15
NSJoint_20	T8-T9	0.0, 348.0, -57.0	.m16
NSJoint_21	T9-T10	0.0, 324.0, -54.0	.m17
NSJoint_22	T10-T11	0.0, 294.0, -48.0	.m18
NSJoint_23	T11-T12	0.0, 264.0, -36.0	.m19
NSJoint_24	T12-L1	0.0, 231.0, -24.0	.m20
NSJoint_25	L1-L2	0.0, 201.0, -15.0	.m21
NSJoint_26	L2-L3	0.0, 168.0, -3.0	.m22
NSJoint_27	L3-L4	0.0, 129.0, 0.0	.m23
NSJoint_28	L4-L5	0.0, 93.0, 0.0	.m24
NSJoint_29	L5-S1	0.0, 63.0, -9.0	.m25

Table F.3: Muscle re-attachment points

Muscle	Attach Proximal (attachment 1)	Attach Distal (attachment 2)
Rectus Abdominis	Sternum	Pelvis
Obliquus Externus	Ribs	Pelvis
Scalenus Medius	C5	Ribs
Scalenus Anterior	C5	Ribs
Erector Spinae 1	T7	Pelvis
Erector Spinae 2	L2	Pelvis
Erector Spinae 3	T7	L2
Scalenus Posterior	C5	Ribs
Splenius Cervicis	Head	C7
Splenius Capitis	Head	T1
Pectoralis Minor 3	Scapula	Ribs
Pectoralis Minor 2	Scapula	Ribs
Pectoralis Minor 1	Ribs	Unchanged
Trapezius 1	C7	Scapula
Trapezius 2	T6	Scapula
Latissimus Dorsi 1	T7	Unchanged
Pectoralis Major 2	Ribs	Unchanged
Pectoralis Major 3	Ribs	Unchanged
Trapezius 3	Scapula	L2
Latissimus Dorsi 2	Unchanged	L1
Pectoralis Minor 1	Scapula	Ribs
Trapezius 4	C6	Scapula
Subclavious	Sternum	Scapula
Psoas Major	L3	Unchanged

Table F.4: Average torsional stiffness values for adult human spines (N.mm/deg)

Spine level	Flexion/Extension	Lateral bending	Axial torsion
Occ-C1	40/20	90	60
C1-C2	60/50	90	70
C2-C7	400/700	700	1200
T1-T12	2700/3300	3000	2600
L1-L5	1400/2900	1600	6900
L5-S1	2100/3000	3600	4600

Table F.5: Average segmental ranges of motion at each spine level (degree)

Level	Flexion	Extension	Lateral bending	Torsion
Occ-C1	13	13	8	0
C1-C2	10	9	0	47
C2-C3	8	3	10	9
C3-C4	7	9	11	11
C4-C5	10	8	13	12
C5-C6	10	11	15	10
C6-C7	13	5	12	9
C7-T1	6	4	14	8
T1-T2	5	3	2	9
T2-T3	4	4	3	8
T3-T4	5	5	4	8
T4-T5	4	4	2	8
T5-T6	5	5	2	8
T6-T7	5	5	3	8
T7-T8	5	5	2	8
T8-T9	4	4	2	7
T9-T10	3	3	2	4
T10-T11	4	4	3	2
T11-T12	4	4	3	2
T12-L1	5	5	3	2
L1-L2	8	5	6	1
L2-L3	10	3	6	1
L3-L4	12	1	6	2
L4-L5	13	2	3	2
L5-S1	9	5	1	1

Table F.6: Stiffness properties of cervical spine ligaments (N/mm)

Cervical spine region	Interspinous Ligament (ISL)	Ligament Flavum (LF)	Anterior Longitudinal Ligament (ALL)	Posterior Longitudinal Ligament (PLL)	Joint Capsule (JC)
Stiffness	7	23.3	17	24.2	32.5

Table F.7: Stiffness properties of lumbar spine ligaments (N/mm)

Lumbar spine region	Interspinous Ligament (ISL)	Ligament Flavum (LF)	Anterior Longitudinal Ligament (ALL)	Posterior Longitudinal Ligament (PLL)	Joint Capsule (JC)
Stiffness	11.5	27.2	33	20.4	33.9

Note: For thoracic spine ligaments, stiffness properties are mean values of those in the cervical and lumbar spine regions.

Table F.8: Attach locations of multifidus muscles on the right-side body (mm)

Muscle	Attach Proximal	Location	Attach Distal	Location
NStiss_121	L1	-15.2, 203.3, -48.4	L3	-16.4, 152.0, -32.0
NStiss_122	L1	-4.2, 186.0, -57.0	L4	-17.1, 119.0, -30.7

NStiss_123	L1	-4.2, 181.0, -64.3	L5	-17.7, 94.1, -31.9
NStiss_124	L1	-4.2, 181.0, -64.3	Sacrum	-19.3, 64.9, -46.3
NStiss_125	L1	-4.2, 181.0, -64.3	Iliac	-39.1, 50.2, -73.6
NStiss_126	L2	-15.9, 171.9, -34.3	L4	-17.1, 119.0, -30.7
NStiss_127	L2	-4.22, 154.5, -45.0	L5	-17.7, 94.1, -31.9
NStiss_128	L2	-4.2, 149.8, -55.7	L5	-17.7, 94.1, -31.9
NStiss_129	L2	-4.2, 149.8, -55.7	Sacrum	-19.3, 64.9, -46.3
NStiss_130	L2	-4.2, 149.8, -55.7	Iliac	-32.0, 36.0, -71.5
NStiss_131	L3	-16.6, 141.3, -30.8	L5	-17.7, 94.1, -31.9
NStiss_132	L3	-4.2, 126.0, -45.0	Sacrum	-19.3, 64.9, -46.3
NStiss_133	L3	-4.2, 124.2, -56.8	Iliac	-32.6, 17.3, -63.3
NStiss_134	L4	-17.3, 109.0, -30.1	Sacrum	-19.3, 64.9, -46.3
NStiss_135	L4	-4.2, 96.0, -45.0	Sacrum	-20.3, 33.3, -66.0
NStiss_136	L4	-4.2, 95.7, -55.2	Iliac	-22.9, 10.0, -62.0
NStiss_137	L5	-17.9, 84.0, -32.7	Sacrum	-13.0, 46.5, -70.0
NStiss_138	L5	-4.2, 73.5, -46.5	Sacrum	-13.0, 46.5, -70.0
NStiss_139	L5	-4.2, 72.2, -55.8	Iliac	-10.0, 33.0, -76.0

Note: For the multifidus muscles on the left-side body, x coordinates of the muscles are opposite to those shown above.

Table F.9: The mechanical properties of multifidus muscles (mm^2 and N/mm^2)

Muscle	pCSA	Max Stress	Muscle	pCSA	Max Stress
NStiss_121	40	0.7	NStiss_131	54	0.7
NStiss_122	40	0.7	NStiss_132	157	0.7
NStiss_123	42	0.7	NStiss_133	157	0.7
NStiss_124	36	0.7	NStiss_134	186	0.7
NStiss_125	60	0.7	NStiss_135	186	0.7
NStiss_126	39	0.7	NStiss_136	186	0.7
NStiss_127	39	0.7	NStiss_137	90	0.7
NStiss_128	39	0.7	NStiss_138	90	0.7
NStiss_129	99	0.7	NStiss_139	90	0.7
NStiss_130	99	0.7			

Table F.10: Attach locations of erector spinae muscles on the right-side body (mm)

Muscle	Attach Proximal	Location	Attach Distal	Location
NStiss_140	L1	-42.0, 208.5, -57.0	Iliac crest	-54.0, 52.5, -58.0
NStiss_141	L2	-44.0, 177.0, -43.0	Iliac crest	-60.0, 78.0, -44.0
NStiss_142	L3	-46.0, 147.0, -39.0	Iliac crest	-66.0, 90.0, -36.0
NStiss_143	L4	-48.0, 114.0, -38.0	Iliac crest	-72.0, 97.5, -28.0
NStiss_144	L1	-26.0, 208.0, -52.0	Iliac crest	-54.0, 52.5, -58.0
NStiss_145	L2	-26.0, 175.5, -39.0	Iliac crest	-50.0, 58.5, -60.0
NStiss_146	L3	-26.0, 147.0, -34.5	Iliac crest	-46.0, 64.5, -68.0
NStiss_147	L4	-26.0, 114.0, -33.0	Iliac crest	-42.0, 70.5, -75.0
NStiss_148	L5	-26.0, 90.0, -34.5	Iliac crest	-36.0, 76.5, -79.0

Note: For the erector spinae muscles on the left-side body, x coordinates of the muscles are opposite to those shown above.

Table F.11: The mechanical properties of erector spinae muscles (mm^2 and N/mm^2)

Muscle	pCSA	Max Stress	Muscle	pCSA	Max Stress
NStiss_140	107	0.7	NStiss_145	91	0.7
NStiss_141	154	0.7	NStiss_146	103	0.7
NStiss_142	182	0.7	NStiss_147	110	0.7
NStiss_143	189	0.7	NStiss_148	116	0.7
NStiss_144	79	0.7			

Table F.12: Attach locations of psoas major muscles on the right-side body (mm)

Muscle	Attach Proximal	Location	Attach Distal	Location
NStiss_149	L1 VB	-28.22, 223.13, -32.03	Femur	-68.0, -30.0, 6.0
NStiss_150	L1 TP	-12.0, 210.0, -39.0	Femur	-68.0, -30.0, 6.0
NStiss_151	L1-L2 IVD	-28.0, 199.5, -18.0	Femur	-68.0, -30.0, 6.0
NStiss_152	L2 TP	-12.0, 178.5, -25.5	Femur	-68.0, -30.0, 6.0
NStiss_153	L2-L3 IVD	-30.0, 166.5, -4.0	Femur	-68.0, -30.0, 6.0
NStiss_154	L3 TP	-28.0, 147.5, -24.0	Femur	-68.0, -30.0, 6.0
NStiss_155	L3-L4 IVD	-30.0, 129.0, 0.0	Femur	-68.0, -30.0, 6.0
NStiss_156	L4 TP	-28.0, 117.0, -22.5	Femur	-68.0, -30.0, 6.0
NStiss_157	L4-L5 IVD	-30.0, 94.5, -2.0	Femur	-68.0, -30.0, 6.0
NStiss_158	L5 TP	-32.0, 90.0, -26.0	Femur	-68.0, -30.0, 6.0
NStiss_159	L5 VB	-32.0, 75.0, -8.0	Femur	-68.0, -30.0, 6.0

Note: For the psoas major muscles on the left-side body, x coordinates of the muscles are opposite to those shown above.

Table F.13: The mechanical properties of psoas major muscles (mm^2 and N/mm^2)

Muscle	pCSA	Max Stress	Muscle	pCSA	Max Stress
NStiss_149	211	0.7	NStiss_155	191	0.7
NStiss_150	61	0.7	NStiss_156	120	0.7
NStiss_151	211	0.7	NStiss_157	119	0.7
NStiss_152	101	0.7	NStiss_158	36	0.7
NStiss_153	161	0.7	NStiss_159	79	0.7
NStiss_154	173	0.7			

Table F.14: Attach locations of quadratus lumborum muscles on the right-side body (mm)

Muscle	Attach Proximal	Location	Attach Distal	Location
NStiss_160	T12	-50.0, 237.0, -57.0	Iliac crest	-90.0, 123.0, -13.5
NStiss_161	L1	-38.0, 214.5, -47.0	Iliac crest	-90.0, 123.0, -13.5
NStiss_162	L2	-38.0, 181.5, -34.0	Iliac crest	-90.0, 123.0, -13.5
NStiss_163	L3	-40.0, 151.5, -27.5	Iliac crest	-90.0, 123.0, -13.5
NStiss_164	L4	-42.0, 117.0, -25.5	Iliac crest	-90.0, 123.0, -13.5

Note: For the quadratus lumborum muscles on the left-side body, x coordinates of the muscles are opposite to those shown above.

Table F.15: The mechanical properties of quadratus lumborum muscles (mm^2 and N/mm^2)

Muscle	pCSA	Max Stress	Muscle	pCSA	Max Stress
NStiss_160	52	0.7	NStiss_163	52	0.7
NStiss_161	52	0.7	NStiss_164	52	0.7
NStiss_162	52	0.7			

Table F.16: Attach locations of external oblique muscles on the right-side body (mm)

Muscle	Attach Proximal	Location	Attach Distal	Location
NStiss_165	Ribs	-74.0, 213.0, -48.0	Lower-Torso	-112.0, 114.0, 0.0
NStiss_166	Ribs	-112.0, 199.5, -4.0	Lower-Torso	-122.0, 109.0, 5.5
NStiss_167	Ribs	-116.0, 196.5, 72.0	Rectus-Sheath	-26.0, 121.5, 72.0
NStiss_168	Ribs	-126.0, 225.0, 82.0	Rectus-Sheath	-22.0, 139.5, 76.0
NStiss_169	Ribs	-118.0, 262.5, 90.0	Rectus-Sheath	-18.0, 159.0, 80.0
NStiss_170	Ribs	-116.0, 301.5, 78.0	Rectus-Sheath	-14.0, 180.0, 84.0

Note: For the external oblique muscles on the left-side body, x coordinates of the muscles are opposite to those shown above.

Table F.17: The mechanical properties of external oblique muscles (mm^2 and N/mm^2)

Muscle	pCSA	Max Stress	Muscle	pCSA	Max Stress
NStiss_165	397.4	0.7	NStiss_168	243.2	0.7
NStiss_166	273	0.7	NStiss_169	231.7	0.7
NStiss_167	234.4	0.7	NStiss_170	195.7	0.7

Table F.18: Attach locations of internal oblique muscles on the right-side body (mm)

Muscle	Attach Proximal	Location	Attach Distal	Location
NStiss_171	Ribs	-109.0, 204.0, -12.0	Lower-Torso	-100.0, 121.5, -7.5
NStiss_172	Ribs	-122.0, 208.5, 36.0	Lower-Torso	-128.0, 97.5, 12.0
NStiss_173	Ribs	-132.0, 237.0, 56.0	Lower-Torso	-132.0, 90.0, 16.0
NStiss_174	Lower-Torso	-138.0, 67.5, 28.0	Rectus-Sheath	-26.0, 90.0, 66.0

NStiss_175	Lower-Torso	-138.0, 57.0, 34.0	Rectus-Sheath	-22.0, 69.0, 62.0
NStiss_176	Lower-Torso	-138.0, 45.0, 38.0	Rectus-Sheath	-18.0, 49.5, 58.0

Note: For the internal oblique muscles on the left-side body, x coordinates of the muscles are opposite to those shown above.

Table F.19: The mechanical properties of internal oblique muscles (mm^2 and N/mm^2)

Muscle	pCSA	Max Stress	Muscle	pCSA	Max Stress
NStiss_171	207.2	0.7	NStiss_174	226	0.7
NStiss_172	235	0.7	NStiss_175	224.3	0.7
NStiss_173	267.6	0.7	NStiss_176	185.3	0.7